On the Reinforcement of Rubber by Fillers and Strain-Induced Crystallization

Von der Naturwissenschaftlichen Fakultät der
Gottfried Wilhelm Leibniz Universität Hannover

zur Erlangung des Grades

Doktor der Naturwissenschaften
Dr. rer. nat.

genehmigte Dissertation
von

Jan Bernhard Plagge, M.Sc.

2018

Referent: Prof. Dr. Manfred Klüppel

Korreferent: Prof. Dr. Jürgen Caro

Weiterer Korreferent: Prof. Dr. Gert Heinrich

Tag der Promotion: 02.11.2018

Preface

The presented thesis collects thoughts and experimental results I obtained during my Ph.D. studies at the German Institute of Rubber Technology (DIK) in the group of Prof. Manfred Klüppel from May 2014 to May 2018. Within this period I worked on several projects, both publicly and privately funded. I started my studies with a project aiming to improve the wear properties of rubber rollers ("Verbesserung der Gebrauchs- und Verschleißeigenschaften von gummierten Walzen in der Druckindustrie") which granted me great scientific freedom and the possibility to learn the basics about rubber compounding and characterization. Then a privately funded projects named "Ozone Protection of Tire Side Walls by Paraffin Waxes" followed, teaching me that there is room for optimization in every detail of modern technology. The next project, funded by a big tire company, was called "DIK Material Model" and dealt with the improvement of a micromechanical material model for filled elastomers developed at the DIK. Up to the completion of this thesis I worked on the privately funded community project "Reinforcement Mechanisms of NR/Silica Composites". The latter two titles outline the scope of this work: Understanding and modeling the interplay of nanoscopic fillers and polymer, as well as self reinforcement occurring in natural rubber (NR).

The main results are written down in 5 publications, all but one authored by me as first author. In chapter 3 a series of two articles investigating basic mechanisms of filler reinforcement is presented. The first article is about a new material model developed by myself. It fits a variety of different compounds at different temperature and speeds and I hope that it will be used for finite element calculations in the future. The second article in chapter 3 is about the interaction of polymer-analogue gases with common fillers used in rubber industry. While I developed the whole data treatment and presentation, I want to thank F. Fleck for the extensive amount of experimental data he left to me. In chapter 4 I present a series of 3 articles investigating strain induced crystallization in natural rubber. The first one lays the foundations for online calorimetric measurements of strain induced crystallization. It was written in large parts by T. Spratte, an excellent Bachelor student supervised by me and M. Wunde. In the second publication I worked out these foundations towards a reliable, fast and mature method. The last article is about a micromechanical theory of strain induced crystallization in natural rubber. Although based on relatively simple physical concepts it takes aspects into account which were probably overlooked by previous authors. The theory answers some of the open questions regarding the thermodynamics of crystallization in NR.

Acknowledgments

My thesis would not have been possible without the help of many people and institutions. I am deeply thankful to my supervisor Prof. Manfred Klüppel who granted me a wealth of freedom to do creative research while pushing me in the right direction whenever necessary. He always had an open ear for easy questions in the beginning and more advanced concepts in the end, at every time willing to interrupt his own work for the sake of his students. His experience and guidance contributed a large part to this work.

The AiF grant 18079 is acknowledged for financial support during the first two years of my work at DIK. Additionally, I would like to thank the current and former members of my department "Material Concept and Modeling": Frank Fleck, who introduced me into the institute and gas adsorption machine, Patrick Stratmann, who was always willing to discuss the more complex matters, Andrej Lang being part of the departments backbone and Matthias Wunde, who was a wonderfully uncomplicated and helpful office colleague.

Of course, all members of DIK contributed to this thesis by providing conditions which always let me come to work with a sense of energy. Kevin Krauses, Nils Krögers and Marvin Ludwigs company is appreciated for not only rubber related discussion. Moreover, I would like to thank all my family and friends for their support.

Finally, I am deeply thankful to Irina, who bravely endured numerous mood swings during the production of this thesis.

Thesis advisor: Prof. Dr. rer. nat. habil. Manfred Klüppel Jan Plagge

On the Reinforcement of Rubber by Fillers and Strain-Induced Crystallization

Abstract

This thesis is dedicated to reinforcement mechanisms in filled and strain-crystallizing elastomers. First of all, a constitutive model for filled elastomers is presented. It is based on the non-affine tube model whose length measure is heterogeneously constraint by the filler particles. The model successfully describes a variety of compounds for different deformation modes, speeds and temperatures. When increasing crosslink density or amount of filler systematically, the parameters evolve in a physically reasonable manner. Moreover an extension and simplification of the model is presented, greatly improving its performance in Finite-Element applications. To further support the modeling hypothesis the interaction of different industrial grade carbon blacks and silicas with polymer-analogue gases is analyzed by means of static gas adsorption. The isotherms are deconvolved into a surface energy distribution using a specifically designed algorithm. Probing the samples with different gases reveals the different polar- and dispersive interaction capabilities of silica and carbon black. Chain desorption from the fillers surface is identified as a possible origin of mechanical hysteresis at large strains. Self reinforcement due to strain-induced crystallization (SIC) in natural rubber is analyzed by comparing the measured temperature increase upon deformation with a hypothetical temperature calculated from the mechanical response. The difference of both temperatures is attributed to crystallization. The method is applied to differently crosslinked and filled compounds and is shown to deliver fast, easy and reproducible results. Incorporation of filler changes the behavior of crystallization in accordance with the assumption of heterogeneous strain amplification. Cyclic loading at elevated strains reveals vanishing hysteresis in the degree of crystallinity, which is indicative of a different crystallization mechanism. Additionally, a theory of SIC is derived which relates mechanical response, crystal size and degree of crystallization using a minimal set of parameters. It takes into account the entropy loss due to attaching a chain to a crystal and naturally explains the constant crystal length and constant crystallization strain onset observed by many authors. The reinforcing effect of SIC is attributed to an intrinsic strain regulation mechanism.

Keywords: rubber reinforcement, static gas adsorption, filler-polymer interaction, constitutive modeling, strain-induced crystallization

Betreuer: Prof. Dr. rer. nat. habil. Manfred Klüppel Jan Plagge

On the Reinforcement of Rubber by Fillers and Strain-Induced Crystallization

Kurzfassung

Das Thema dieser Arbeit sind Verstärkungseffekte in gefüllten und dehnungskristallisierenden Elastomeren. Zunächst wird ein konstitutives Modell für gefüllte Elastomere präsentiert. Es basiert auf dem nicht-affinen Röhrenmodell, dessen Längenmaß heterogen durch Füllstoffpartikel verstärkt wird. Das Modell reproduziert das mechanische Verhalten verschiedener Mischungen bei verschiedenen Deformationsmoden, Geschwindigkeiten und Temperaturen. Bei variierender Vernetzungsdichte oder Füllstoffanteil verhalten sich die Modellparameter physikalisch sinnvoll. Zusätzlich wird eine Erweiterung des Modells gezeigt, die eine Nutzung in Finite-Elemente-Programmen vereinfacht. Zur Stützung der Modellhypothesen wird die Wechselwirkung verschiedener industriell genutzter Ruße und Silicas mit polymeranalogen Gasen mittels statischer Gasadsorption analysiert. Aus den Adsorptionsisothermen konnte mit Hilfe eines für diesen Zweck geschaffenen Algorithmus eine Oberflächenenergieverteilung errechnet werden. Durch die Messung mit verschiedenen Gasen wurde die Oberflächenenergie bezüglich polarer und disperser Anteile untersucht. Es zeigt sich, dass Kettendesorption von der Füllstoffoberfläche eine Ursache für mechanische Hysterese bei großen Dehnungen sein könnte. Selbstverstärkung durch Dehnungskristallisation in Naturkautschuk wird untersucht, indem die durch Deformation hervorgerufene Temperaturänderung mit einer aus der mechanischen Antwort errechneten hypothetischen Temperatur verglichen wird. Die Temperaturdifferenz wird Kristallisation zugeschrieben. Die Methode wird an verschieden vernetzten und gefüllten Mischungen validiert und liefert auf einfache Weise reproduzierbare Ergebnisse. Füllstoffe verändern das Kristallisationsverhalten in einer Weise, die sich im Rahmen von heterogener Verstärkung verstehen lässt. Bei zyklischer Belastung um hohe Dehnungen verschwindet die Hysterese im Kristallisationsgrad, was auf eine Veränderung des Kristallisationsmechanismus schließen lässt. Weiterhin wird eine Theorie der Dehnungskristallisation entwickelt, die mechanische Antwort, Kristallgröße und Kristallisationsgrad über ein minimales Set von Parametern in Verbindung setzt. Die Theorie zeigt, dass ein Polymer allein durch die Anbindung an den Kristall einen großen Teil seiner Entropie einbüßt. Dieser Effekt erklärt auf natürliche Weise die konstante Kristallgröße und die von der Vernetzungsdichte unabhängige kritische Dehnung, bei der Kristallisation in Naturkautschuk beginnt. Der Verstärkungseffekt der Dehnungskristallisation wird einem intrinsischen Dehnungsregulierungsmechanismus zugeschrieben.

Stichwörter: Verstärkte Elastomere, statische Gasadsorption, Füllstoff-Polymer Wechselwirkung, konstitutive Modellierung, dehnungsinduzierte Kristallisation

Abbreviations

BET	Brunauer Emmett Teller
BR	Butadiene Rubber
CB	Carbon Black
CCA	Cluster-Cluster Aggregation
DC	Direct Current
DFM	Dynamic Flocculation Model
DIK	Deutsches Institut für Kautschuktechnologie e. V.
DMA	Dynamic-Mechanical Analysis
DSC	Dynamic Scanning Calorimetry
EPDM	Ethylene Propylene Diene Rubber
FE	Finite Element
HNBR	Hydrogenated Nitrile Butadiene Rubber
MORPH	Model of Rubber Phenomenology
NR	Natural Rubber
SAXS	Small Angle X-Ray Scattering
SBR	Styrene Butadiene Rubber
SIC	Strain-Induced Crystallization
WAXS	Wide Angle X-Ray Scattering

Contents

1 INTRODUCTION 2
1.1 Setting the Scene . . . 2
1.2 Technical Elastomers . . . 3
1.3 Polymer Crosslinking . . . 5
1.4 Reinforcing Fillers . . . 5
1.5 Stress Softening . . . 7

2 MODELING OF ELASTOMERS 10
2.1 Some Continuum Mechanics . . . 10
2.2 The Gauss Chain Model . . . 11
2.3 The Neo-Hooke Model . . . 15
2.4 The Mooney Rivlin Model . . . 16
2.5 The Extended Non-Affine Tube Model . . . 17
2.6 The Dynamic Flocculation Model . . . 18

3 INVESTIGATION AND MODELING OF FILLER REINFORCEMENT 23
3.1 Introduction . . . 23
3.2 Publication 1: A Physically Based Model of Stress Softening and Hysteresis of Filled Rubber Including Rate- and Temperature Dependency . . . 26
3.3 Publication 2: Investigation of Carbon Black and Silica Surface Structure by Static Gas Adsorption with Various Gases . . . 50
3.4 Outlook and Supplementary Information . . . 61

4 SELF-REINFORCEMENT DUE TO STRAIN-INDUCED CRYSTALLIZATION 68
4.1 Introduction . . . 68
4.2 Publication 3: Investigation of Strain-Induced Crystallization of Carbon Black and Silica Filled Natural Rubber Composites based on Mechanical and Temperature Measurements . . . 72
4.3 Publication 4: Determining Strain-Induced Crystallization of Natural Rubber Composites by Combined Thermography and Stress-Strain Measurements . . . 81
4.4 Publication 5: A Theory Relating Crystal Size, Mechanical Response, and Degree of Crystallization in Strained Natural Rubber . . . 88
4.5 Outlook and Supplementary Information . . . 99

5 CONCLUSION AND OUTLOOK 101

REFERENCES 113

APPENDIX A 114
A.1 Curriculum Vitae . . . 115
A.2 Own Literature . . . 116
A.3 Contributions to Conferences . . . 117

1

Introduction

1.1 Setting the Scene

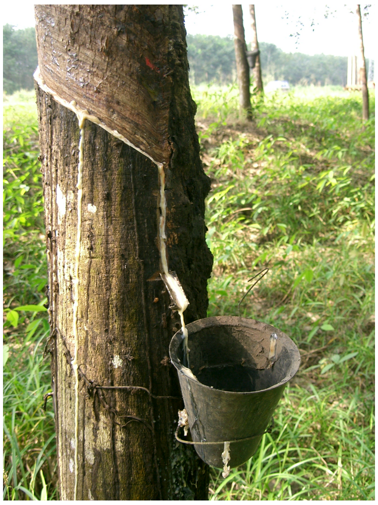

Figure 1.1: A tapped *Hevea* tree, cameroon.

Rubber and mankind have a long history. The first reports of rubber usage date back several thousands of years to mesoamerican cultures, where the latex coming from the *Hevea* tree was used for making sports balls [1]. After discovery of the new world, in 1770 Joseph Priestly showed that the material was ideal to rub off pencil from paper and thus invented the term "rubber". Industrial use of rubber started 1832 in Peru, based in large parts on the exploitation of native american population [2]. Several attempts to increase rubber production using *Hevea* plantations failed, because the fungus *Microcyclus ulei* infested the trees. In 1876 the englishman Henry Wickham smuggled about 70000 *Hevea* seeds to England. Many small trees grown from the seeds were shipped to Malaysia, but only 8 survived. These 8 trees are the ancestors of all rubber plantations in asia today [3]. Around this time rubber was mainly used for waterproof clothing and shoes, but it had an essential drawback: At high temperature it became sticky and at low temperature stiff. This problem was resolved by Charles Goodyear in 1839, who accidentally discovered vulcanization by trying to dissolve rubber in boiling sulfur, allowing the production of shape conserving rubber articles of great strength [3]. Driven by the success of automobiles, in 1909 the first synthetic rubber was invented by Fritz Hofmann. During World War II almost all natural rubber was under control of the axis powers, forcing the US army to develop an alternative supply. The result was styrene-butadiene rubber, a copolymer which is still very important today.

Nowadays, elastomers are omnipresent in everyday life – be it tires, seals, floors, rubber bands or several other products. Each product class has its own set of requirements and specifications, ranging from chemical-environmental stability over biocompatibility and non-toxicity to mechanical toughness or elasticity, in most cases a combination of them. This thesis mostly deals with the latter field of properties.

Mechanical durability of elastomers can be obtained by selecting a polymer which is able to withstand high mechanical loads. Indeed, vulcanized natural rubber is extremely elastic and durable, unmatched by almost every synthetic polymer. The reason for that is still under discussion, but believed to be due to an effect called strain-induced crystallization: By stretching, the material is microscopically aligned, facilitating the formation of crystals which in turn locally increase the materials toughness. This complex interplay of phase transition and mechanical properties is one of the main topics of the thesis.

Another possibility to increase mechanical strength is to add nanoscopic particles, called fillers. In fact, most technical rubber is black because of up to 50 vol. % carbon black. In the last 20 years, silica (silicon dioxide) increasingly replaced carbon black as filler in car tires, because it decreases viscoelastic losses while simultaneously increasing wet grip, paving the way for environmental friendly "green" tires. Under loading the finely dispersed particles locally increase strain of the surrounding polymer matrix in consequence of their occupied volume. Additionally, if particle concentration is high enough, they form a secondary, comparably stiff network, greatly increasing the materials' stiffness and, in the case of carbon based fillers, conductivity. The largest contribution to mechanical strength probably originates from reorganization of filler clusters, slippage of polymer chains or, more general, local breaking points which locally limit stress before it becomes too high. Again, the exact mechanism is not clear, even though there is a great variety of theories. This thesis aims to give an overview and offers an explanation by a physically motivated model which can be used in finite element simulations.

1.2 Technical Elastomers

1.2.1 Polymers and Polymer Types

The term polymer is greek and means "many parts". Thus, it denotes a macromolecule made up of many primary units joined together, called monomers. Most industrial monomers are relatively simple organic compounds mainly made up of carbon and hydrogen, even though there are some famous exceptions like Teflon (which replaces hydrogen by fluorine) or silicone rubber (where silicon and oxygen make up the polymers backbone). In this thesis we mainly deal with three polymers which are in wide industrial use: Natural rubber, ethylene propylene diene rubber and styrene-butadiene rubber. In this section the chemical structure and physicochemical properties of each polymer will be briefly explained.

Natural Rubber As the name suggests, natural rubber is harvested by tapping *Hevea* trees, mostly growing in south asia. It was the first rubber to be used and still has up around 40 % market share [4].

From a chemical point of view natural rubber (NR) is polyisoprene, consisting of many isoprene units covalently linked together as shown in Fig. 1.2a. The linking can be done in two ways: In *cis*-conformation both neighboring monomers are on the same side, resulting in straight chains and

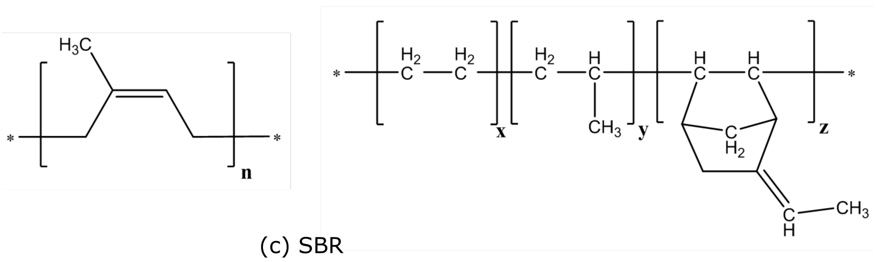
(a) *cis*-1,4-polyisoprene (NR)

(b) EPDM

(c) SBR

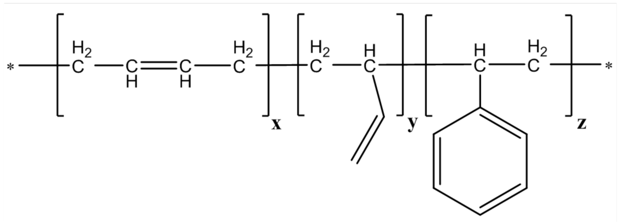

Figure 1.2: Chemical structure of the polymers used in this work. (a) *cis*-1,4-polyisoprene, the main constituent of natural rubber. (b) Ethylene Propylene Diene (EPDM) rubber. The x and y indicate the content of ethylene and propylene, respectively. The diene component (z) is added to allow sulfur vulcanization using the double C-C bond. (c) Styrene-Butadiene Rubber (SBR). The x and y indicate the content of butadiene in different conformations. The styrene component (z) is added to control viscoelastic properties.

highly flexible materials. The *trans*-conformation occurs, when they are on opposite sides, creating chains resembling a sawtooth with inferior elastic bulk properties. Most synthetic isoprene has up to 98 % *cis* content, while natural rubber consists of more than 99.9 % *cis* [5]. Due to its unsaturated double bond in the backbone natural rubber has relatively low chemical and thermal resistance [4]. The mechanical and wear properties of NR are outstanding, making it the polymer of choice for heavy duty articles like truck tires or conveyor belts.

ETHYLENE PROPYLENE DIENE RUBBER (EPDM) is polymerized from three different monomers, a so-called terpolymer as shown in Fig. 1.2b. The ethylene content varies from 45% to 85% and controls the polymers ability to crystallize. EPDM with less than 55% of ethylene is called amorphous. At high ethylene content there are large crystalline domains, inducing thermoplastic behavior. Typically 2.5% to 12.5% dienes are used to add carbon double bonds, which are crucial for sulfur vulcanization. Because of its saturated backbone, EPDM is chemically and thermally resistant, while maintaining a good elasticity. It is used e. g. for seals, hoses, tubing and electrical insulation [4].

STYRENE BUTADIENE RUBBER (SBR) is a copolymer made from 1.3-butadiene and styrene. The ring-shaped styrene visible in Fig. 1.2c induces strong internal friction, such that the styrene content is used to control the viscoelastic properties of the material. SBR can be made from emulsion, called E-SBR or from solution, named S-SBR. Historically, polymerization by emulsion came first, creating highly branched macromolecules. In contrast, solution polymerization creates linear molecules of almost uniform size, making it a good choice for automobile tires where elasticity is of major importance [6]. Generally, it is more stable concerning environmental influences than NR but performs worse than EPDM [4].

1.3 Polymer Crosslinking

Even though raw natural rubber resembles a solid body it is, in a physical sense, a liquid made up of highly entangled macromolecules. Thus, it will flow on very long timescales. Its liquid-like nature comes to light at elevated temperatures. The discovery of vulcanization was probably the greatest milestone in rubber history, because polymer chains are connected during the process. These connections, called crosslinks, prevent flowing of the system and transform the liquid-like polymer melt into a solid body.

In the tradition of Charles Goodyear, most diene rubbers are still vulcanized via sulfur or sulfur based accelerators. The diene component is a requirement for sulfur vulcanization, because crosslinks are established by addition of sulfur to the dienes double bond. The diene may occur in the polymers backbone, e. g. in SBR and NR, or in a side chain as is the case in EPDM. Elementary sulfur usually has the shape of S_8-rings. Before vulcanization can start the rings have to open which takes a long time, prevents industrial use of pure sulfur and consequently motivated the development of a great series of accelerators [7]. Sulfur based vulcanizates have good mechanical properties, but their thermal resistance is limited due to the dissociation energy of sulfur-sulfur bridges of 251 kJ/mol [4].

Peroxide vulcanization does not require carbon double bonds. During the process a peroxide molecule dissociates thermally into radicals which are transferred to the polymer via substitution of hydrogen atoms or addition to the carbon double bond. The polymer radical may react further in terms of crosslinking or chain scission, depending on the chemical composition of the polymer [8–10]. Peroxide vulcanizates have good thermal resistance and less compression set, but exhibit poorer mechanical properties [4].

1.4 Reinforcing Fillers

In general, the terminus filler denotes insoluble particles which are added in a significant amount to a matrix material. This is done to change the properties of the composites or for cost savings, because fillers are often less expensive than the matrix material. In rubber industry a great variety of fillers are in use, ranging from relatively large particles like chalk or silicate over nanoscopic silica and carbon black to new generation fillers like carbon nanotubes and graphenes. Large particles have a comparably low relative surface area which yields low interaction with the matrix. For this reason, this class of fillers is called inactive and is mainly used for cost savings [4]. Nevertheless, the platelet-like shape of some silicates reduces gas permeability significantly [4]. Nanoscopic particles, predominantly carbon black and silica, are in wide use in a variety of rubber articles. By correct composition they greatly increase mechanical properties, reduce swelling in solvents and improve UV-stability. Additionally, carbon black allows for electrical conductivity [11] which is especially important to lead away quasistatic load in cars via the tires. The mechanical reinforcement is shown exemplary using carbon black filled EPDM in Fig. 1.3. Tensile strength increases almost by an order of magnitude by adding 20 vol. % of carbon black. The corresponding recipe can be found in Tab. 1 of publication 1. The mechanism of mechanical reinforcement is still under discussion. Nevertheless, it is well known that the specific surface area of a filler, usually measured in m^2/g [12],

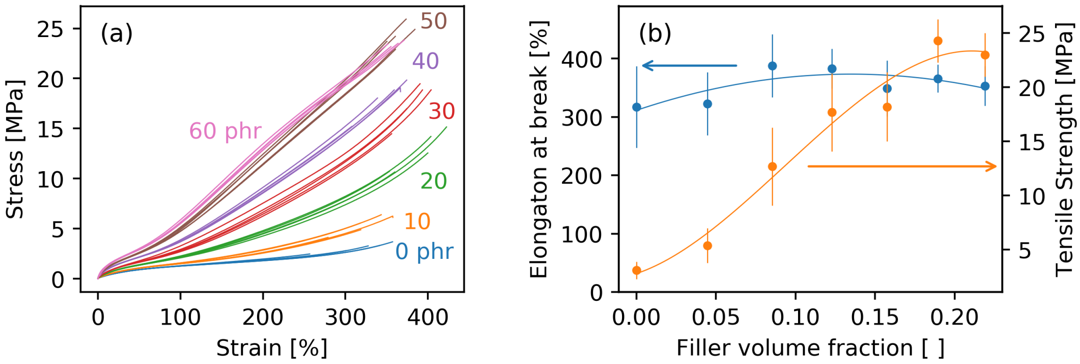

Figure 1.3: (a) Exemplary experimental data showing the improvement of tensile strength and elongation at break in the case of carbon black filled EPDM. (b) Evaluation of the curves presented in (a) in terms of elongation of break and tensile strength. The solid lines are guides for the eyes.

as well as the fillers structure, usually measured by the amount of oil a given amount of carbon black can absorb [13], can be positively correlated to mechanical reinforcement. In both cases this is attributed to increased physical polymer-filler interaction [14]. Additionally, active fillers tend to build mechanically stable and, in the case of carbon based fillers highly conductive, secondary network. The breakdown of this network is responsible for the Payne effect, a pronounced decrease in stiffness after small (periodic) deformation, as discussed in chapter 1.5.1. Even at high strains ($> 100\%$), filled elastomers continue to soften. This observation, called Mullins effect, is explained by the slipping of polymer chains or the successive breakdown of carbon black network structure, see chapter 1.5.2.

The introduction of silica as a filler for passenger car tires can be regarded as the last milestone in tire development. Up to this point, tires were filled almost exclusively with carbon black, restricting tire manufacturers to balance physical properties within the famous magic triangle: rolling resistance, wet traction and abrasion. The emerging silica technology allowed to decrease rolling resistance and increase wet traction while maintaining sufficient abrasion resistance. This was achieved by chemical coupling of the silica particles to S-SBR using appropriate silanes. The majority of energy efficient tires is similar to this original Michelin formulation [15]. Nevertheless, silica technology fails in combination with the mechanically unmatched natural rubber, preventing energy efficient truck tires.

1.4.1 Rubber Mixing

A requirement for good mechanical properties is a sufficient dispersion of the filler into the matrix. Most fillers tend to form larger structures due to cohesive forces which have to be broken during mixing. For carbon black, the mixing process can be split up into three parts. In the first one, called the *subdivision* process, larger chunks of filler are broken down mechanically by the mixer into smaller parts, called agglomerates. After this stage polymer is able to penetrate into the filler. Being highly viscous, the polymer transfers large shear forces into the agglomerates, forcing them to break up into smaller aggregates. The latter process is called *disperse mixing.* Aggregates represent the smallest unbreakable entity of carbon black within the scope of forces acting in rubber materials. Thus, the following step is a mere displacement of aggregates, ideally up to a state of equal distribution, called *distributive mixing* [4, 14].

1.5 STRESS SOFTENING

1.5.1 THE PAYNE EFFECT

Highly filled elastomers, which have never been deformed before, are very stiff. This is attributed to the formation of a percolated and comparably stiff filler network. When increasing strain above a threshold of about 0.1 %, the modulus strongly decreases with deformation amplitude, corresponding to the breakdown of the filler network. It was named after A. R. Payne, who was the first to give a detailed description of the phenomenon for carbon black [16]. The Payne effect is fully reversible on the timescale of hours to days [17]. First works assumed direct contact of filler aggregates [18] or short ranged Van-der-Waals interaction [19]. More recent works identified glassy polymer bridges within the filler particles [20]. The phenomenon was also discussed in the context of jamming transitions [21]. In the popular Kraus model [22] the rate of carbon-carbon contact breakage is assumed to be proportional to the number of contacts and to a powerlaw increasing with amplitude. In contrast, the rate of contact formation is set proportional to the number of broken contacts and antiproportional to the same powerlaw. Identifying the number of contacts with G' and the rate of contact breakage with G'' Kraus is able to successfully describe the behavior of both moduli with increasing amplitude, although the physical foundations of the model are disputed. Recently, Paynes work was investigated and extended by Hentschke, who introduced scaling arguments about filler morphology into the model [23].

The physical picture of breaking and reaggregating carbon black structures was also investigated by dielectric measurements carried out by Steinhauser et al., showing that aggregation happens according to Cluster-Cluster-Aggregation (CCA) mechanisms [14, 24, 25]. Moreover, Tunnicliffe et al. have shown that surface deactivation of carbon black via graphitization strongly increases filler networking. The authors confirmed the well known result that Payne effect decreases with increasing temperature. The latter is more pronounced for graphitized samples [26]. It was shown recently that the development of these networks, called flocculation, can be understood qualitatively by employing models from game theory [27].

1.5.2 THE MULLINS EFFECT

For filled elastomers, the low strain stress softening is rather well understood in terms of the Payne effect. At large strains, after the breakdown of the percolated filler network, the material continues to soften. This effect was first observed by Bouasse [28] and coworkers and later investigated by Mullins who gave his name to the phenomenon [29, 30]. Apart from filled elastomers also some semicrystalline and strain-crystallizing polymers exhibit this property [31, 32]. Softening is usually most pronounced after surpassing the maximum previous load for the first time. Consecutive loading cycles further reduce the materials stiffness. Although many authors assume complete softening after 5 to 10 cycles, experimental data on mechanical relaxation at fixed load suggests that softening will not stop on timescales usually investigated in mechanical experiments [33]. An example

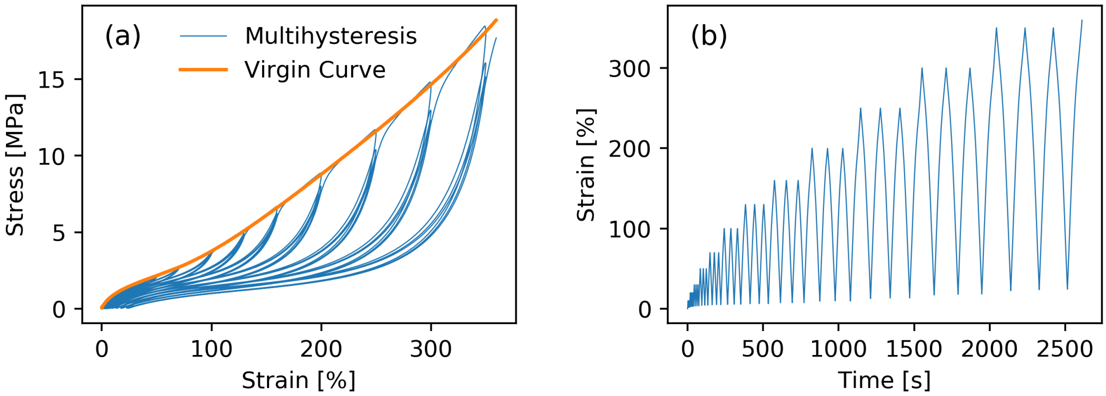

Figure 1.4: (a) Example of a material experiencing Mullins effect: 40 phr carbon black (N339) filled, sulfur cured EPDM. Continuous stretching (virgin curve) and multihysteresis experiment, consisting of repeated loading of increasing strain levels. (b) Corresponding strain protocol.

showing Mullins effect in 40 phr carbon black filled EPDM rubber is given in Fig. 1.4. The recipe can be found in Tab. 1 of publication 1. It is clearly visible that the material becomes softer when strain surpasses the previous maximum. Moreover, the high-strain cycles have residual strain at zero stress. Studies on filled silicone rubber have repeatedly shown that Mullins effect is anisotropic [34–36]. The authors exposed a large sample to uniaxial strain. Afterwards, smaller uniaxial samples were cut from the large sample and tested again. Samples cut orthogonal to the previous stretching direction showed almost no softening effect. Diani and coworkers found, the mechanical response of carbon black filled SBR previously exposed to 200 % strain recovers completely after 17 hours at 80 °C in vacuo [37]. A similar result was found for carbon black filled NR heated to 95 °C in vacuo by Lara-Abbes et al. [38]. In contrast, storage of carbon black filled rubber over 4 weeks at room temperature induces only minor recovery [39]. Thus, at room temperature Mullins effect is often considered to be irreversible damage. It was found that Mullins effect may also be influenced by filler surface modification. In the group of M. Klüppel ionic liquids [40] were used on highly reinforcing carbon blacks. Depending on polymer polarity an increase or decrease in stiffness and hysteresis could be achieved. In the same group the effect of carbon black deactivation via surface graphitization on the dielectric and mechanical properties was investigated [11]. Graphitized blacks yielded less reinforcement and higher elongation at break.

The origin of the Mullins effect is still not clear [37]. For this reason a variety of physical concepts exists:

- Some of the first works tried to explain Mullins softening by the breakage of polymer chains or crosslinks due to overstretches of shorter chains between filler particles [41, 42]. More than 40 years later, chain scission was found in filled SBR using electron spin resonance [43].
- The idea of breaking links does not fit the result that Mullins effect is reversible. Therefore, Houwink et al. [44] proposed that polymer chains slide on the fillers surface and rearrange at reduced network stress. A combination of permanent link breakage and reversible links is used also in modern approaches [45]. In fact, very recent molecular dynamics simulations on

large filler polymer networks have revealed that chain sliding may be one of the main reasons for Mullins softening [46].

- Another class of models focuses on the breakdown or rearrangement of local carbon black structure [22, 47], which decreases geometric constraints imposed on the polymer matrix and results in softening the material. The rearrangement and recovery of the carbon black network during deformation was shown to occur via dielectric spectroscopy [24] and online Direct-Current (DC)-measurements [48]. Moreover, structural changes of the filler network in silica filled SBR during deformation was measured by means of Ultra-Small-Angle X-Ray Scattering (USAXS) [49]. Similar results were found using molecular dynamics simulations [46, 50]. The same authors observed rotation of anisotropic aggregates under load. X-ray photon correlation spectroscopy (XPCS) has shown that uncoupled silica particle diffusion velocity in strained samples is more than one order of magnitude larger than for comparable carbon black filled samples [33]. The velocity profile of carbon black particles could be interpreted in terms of carbon black rotation, too. Filler particle diffusion in entangled polymer melts was investigated theoretically by Cai et al. [51], who investigated different timescales corresponding to hopping, diffusion and caging. Moreover, it was experimentally shown that diffusivity greatly reduces with an increase in particle to mesh size ratio [52]. These findings indicate that filler mobility in the matrix might play a key role for the understanding of Mullins effect.

- Disentanglement phenomena might play a role.

- Recently, a rather abstract model proposed by Wulf and Ihlemann [53] attributes reinforcement and softening to less local emergent phenomena, e. g. larger scale reorganization.

While most models give a simple answer to the increase in modulus, e. g. by local overstretches of the polymer matrix due to adsorption on filler or hydrodynamic/volume exclusion effects, physical ideas about the increase in elongation at break and tensile strength are rare. This is astonishing, as both quantities are closely related to the durability of the material.

2

Modeling of Elastomers

2.1 Some Continuum Mechanics

The upcoming rubber models involve continuum mechanical quantities. For this reason some foundations are briefly reviewed here.

The undeformed (reference) coordinates of a material point inside a continuum shall be denoted X_i. After deformation the material point is displaced to coordinates x_i. If the current state is in equilibrium the current position vector $\mathbf{x}$ is a function solely dependent on the reference configuration $\mathbf{X}$. This is written as

$$\mathbf{x} = \mathbf{x}(\mathbf{X}) \tag{2.1}$$

In particular it has to be kept in mind that $\mathbf{x}(\mathbf{X})$ is a *function* of $\mathbf{X}$ [54, 55]. Assuming that the x_i are continuous we can express the differential change in position x_i in terms of the undeformed coordinates X_j as

$$\mathrm{d}x_i = \sum_j \frac{\partial x_i}{\partial X_j}\,\mathrm{d}X_j \tag{2.2}$$

This can be rewritten as

$$\mathrm{d}\mathbf{x} = \mathbf{F}\,\mathrm{d}\mathbf{X} \qquad \text{with} \qquad F_{ij} = \frac{\partial x_i}{\partial X_j} \tag{2.3}$$

The tensor $\mathbf{F}$ is called deformation gradient and measures the change in length of infinitesimal line segments. The goal of this chapter will be the derivation of a free energy density which characterizes the energy stored in the continuum at given strain. In classical mechanics potential energy is usually expressed, to first order, as quadratic in length scales. This motivates the usage of the left Cauchy Green tensor

$$\mathbf{B} = \mathbf{F}\mathbf{F}^{\mathrm{T}} \tag{2.4}$$

as a strain measure. It is symmetric by construction and can be shown to be positive definite, guaranteeing positive eigenvalues [54, 55]. As they are positive, the eigenvalues can be written as λ_i^2 which is the square of the so-called principal stretch λ_i.

The left Cauchy Green tensor **B** is a symmetric second order tensor and has three principal invariants, which do not change upon change of the coordinate system. These are

$$\begin{aligned} I_1 &= \lambda_1^2 + \lambda_2^2 + \lambda_3^2 \quad \text{(trace)} \\ I_2 &= \lambda_1^2\,\lambda_2^2 + \lambda_2^2\,\lambda_3^2 + \lambda_1^2\,\lambda_3^2 \quad \text{(trace of adjoint)} \\ I_3 &= \lambda_1^2\,\lambda_2^2\,\lambda_3^2 \quad \text{(determinant)} \end{aligned} \tag{2.5}$$

Thus, if a material is isotropic its free energy density W has to depend solely on these invariants. The first invariant I_1 can be envisioned as the squared length of a hypothetical vector inside the continuum. Accordingly, the second invariant I_2 may be interpreted as being proportional to the average area spanned by the components of the vector. The third invariant measures the change in volume of the corresponding hypothetical cuboid. In rubber, the change in volume with respect to stretch is usually negligible, such that $I_3 \approx 1$. The latter approximation may be dropped, if a material model is used for high pressure simulations or stems from compressible materials (e.g. foamed rubber).

From the free energy density a variety of mathematically equivalent stress measures can be calculated. Two of them are especially important and shall be explained briefly.

CAUCHY STRESS (or true stress) measures stress with respect to an area in the *deformed* configuration. It is a symmetric tensor and is often denoted σ. For compressible isotropic materials it can be calculated from the free energy density W using

$$\sigma_{ij} = \sum_{n=1}^{3} \frac{\lambda_n}{\lambda_1\,\lambda_2\,\lambda_3} \frac{\partial W}{\partial \lambda_n}\, b_i^{(n)}\, b_j^{(n)} \tag{2.6}$$

where $\mathbf{b}^{(n)}$ denotes the n-th eigenvector of the left Cauchy Green tensor **B** [55].

FIRST PIOLA KIRCHHOFF STRESS (or engineering stress) measures stress with respect to an area in the *undeformed* configuration. It is often used, because in experiments the undeformed configuration (e.g. undeformed cross section of the sample) is easier to access than the deformed configuration. In contrast, it is difficult to process in FE-code as it is an unsymmetric tensor [55]. It is often denoted as **P** and can be calculated from Cauchy stress via

$$\mathbf{P} = J\,\mathbf{F}^{-1} \cdot \sigma \tag{2.7}$$

with $J = \det(\mathbf{F}) = \sqrt{I_3} = \lambda_1\lambda_2\lambda_3$ quantifying volume changes and **F** being the deformation gradient.

2.2 THE GAUSS CHAIN MODEL

The physical behavior of polymers emerges from the collective motion of all linked monomers. The degrees of freedom of a monomer can be split into two categories. The first one collects random

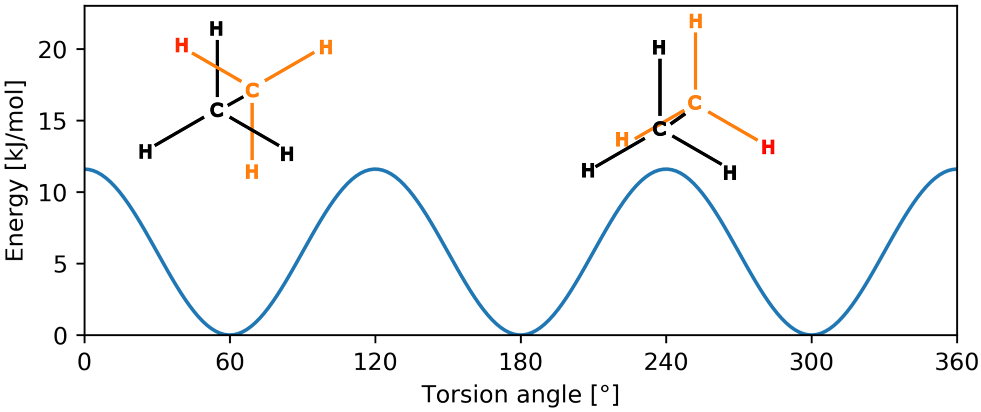

Figure 2.1: Visualization of the bond rotation potential of ethane [56]. Configurations that maximize hydrogen distance are energetically favorable. The red marked hydrogen is an indicator for the torsion angle.

motion and fluctuation around bond potentials which only allows minor changes of the overall structure and thus will be ignored. The second category contains larger structural changes due to change of potential minima. This happens, because most monomers contain single carbon-carbon bonds which can be freely rotated around the axes. Nevertheless, not every rotational position is energetically favorable, because the distance of the remaining parts of the monomers constituents changes. For example, hydrogen-hydrogen interaction is repulsive, such that potential minima are defined by states with maximum hydrogen distance. This is visualized for the example of ethane in Fig. 2.1. At low temperatures, the rotational angles of lowest energy will be chosen, whereas at high temperatures thermal energy $k_\mathrm{B}T$ increases and thermal fluctuation competes potential driving force, allowing access to higher energy states.

Following these thoughts, the orientations of consecutive monomers are correlated due to the limitations in bond rotation. By adding more and more monomers, the orientation of the starting monomer will be “forgotten”, or more precisely, the orientations *decorrelate*. By introducing a coordinate along the polymers contour l and the corresponding tangent vector $\mathbf{e}(l)$ we define the correlation function

$$K(\Delta l) = \langle \mathbf{e}(l)\mathbf{e}(l+\Delta l)\rangle_l \simeq \exp\left(-\Delta l/l_p\right) = \langle \cos\theta(\Delta l)\rangle_l \tag{2.8}$$

where the angular brackets $\langle\cdot\rangle_l$ denote an average over the whole contour. $\theta(\Delta l)$ is the angle enclosed by monomers with spacing Δl. The persistence length l_p is the length scale on which segment orientation decorrelates. This is visualized for a hypothetical polymer, whose monomers always enclose an angle of 30° in Fig. 2.2.

For the sum of N decorrelated, or statistically independent, quantities X_i we can use the central limit theorem on a random variable Y defined as

$$Y = \sum_{i=1}^{N} X_i \tag{2.9}$$

If all X_i are distributed according to the same probability distribution P_X and N is large, the prob-

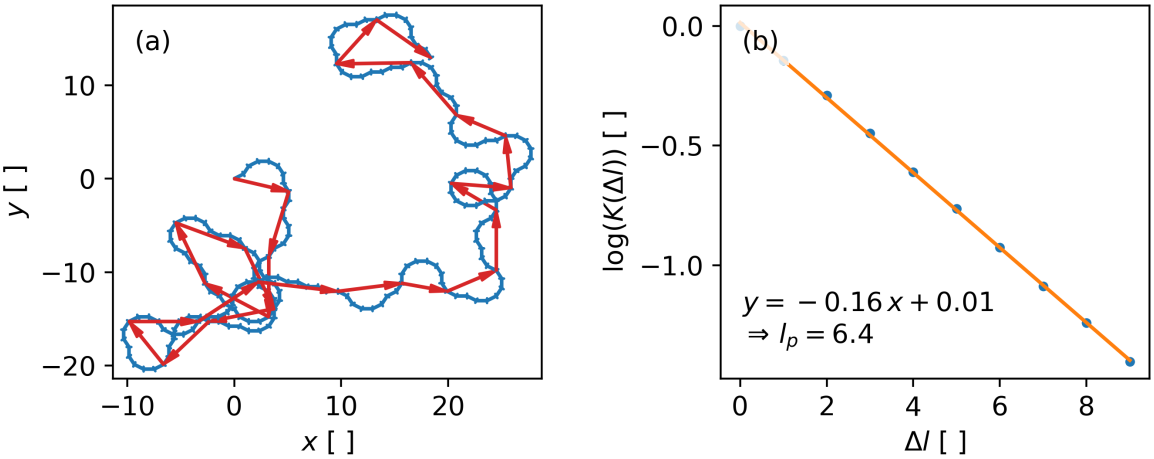

Figure 2.2: (a) Example of the decorrelation described via Eq. (2.8). Successive monomers (blue) always enclose an angle of $\pm 30°$. After about six monomers the connecting vector (red) is decorrelated, meaning that the angle between two vectors can be arbitrary. (b) Visualization of the decorrelation function corresponding to (a) and exponential fit.

ability distribution P_Y will always converge to a gaussian with defined shape [57]

$$P_Y(Y) = \frac{1}{\sqrt{2\pi\, \sigma_Y^2}} \exp\left[-\frac{1}{2\sigma_Y^2}(Y - \bar{Y})^2\right] \tag{2.10}$$

where $\sigma_Y^2 = N\, \sigma_X^2$ and $\bar{Y}$ are the variance and mean value of Y, respectively. The X_i are now identified with the step length of statistically independent polymer segments of Kuhn length $b = 2\, l_p$ [58], which will be explained later. By combining n of them we obtain the probability density of the end-to-end vector r as the product of three random walks, one in each direction of space

$$P(r) = \left(\frac{3}{2\pi\, n\, b^2}\right)^{3/2} \exp\left(-\frac{3}{2}\frac{\mathbf{r}^2}{n\, b^2}\right) \tag{2.11}$$

This is derived in more detail in many textbooks [57]. Eq. (2.11) holds for all polymers irrespective of their microstructure, the only assumption being the decorrelation of segment orientation. Take into account that there is a finite probability for all r, even for rs larger than the contour size $L = n\, b$, which is physically impossible. This error occurs, because segments are not statistically independent anymore, if the contour becomes straight. It can be corrected using Lagrange multipliers, forcing the total contour length to be equal L, which leads to the famous Langevin statistics [59].

From Eq. (2.11) the entropy of a Gauss chain can be derived via $S = k_\mathrm{B} \log \Omega$. The total number of conformations Ω is expressed as the (normalized) probability distribution $P(\mathbf{r})$ multiplied by number of realizations of the undeformed chain. The latter is given by the number of possible conformations of the statistical segment c_1 to the power of the number of segments n. Moreover, it is antiproportional to the discretization of phase space $\mathcal{V}$. The entropy is then given as

$$S = k_\mathrm{B} \log \Omega = k_\mathrm{B} \log\left(\frac{c_1^n}{\mathcal{V}}\, P(r)\right) \simeq k_\mathrm{B}\left(n\, c_2 - \log \mathcal{V} + \frac{3}{2}\log\left(\frac{3}{2\pi\, n\, b^2}\right) - \frac{3}{2}\frac{r^2}{n\, b^2}\right) \tag{2.12}$$

where $c_2 = \log(c_1)$. Within the present modeling there are no internal energy contributions. Then, the mechanical response is calculated from the free energy $F = -T\,S$. By taking the derivative with respect to r we get a retracting force

$$f = -\frac{\mathrm{d}F}{\mathrm{d}r} = -3\,k_\mathrm{B}T\,\frac{r}{n\,b^2} \tag{2.13}$$

The temperature proportionality in Eq. (2.13) tells us about a property inherent to all polymers, called entropy elasticity: Polymers retract, because stretched conformations are less likely to occur than coiled conformations. Of course, the proportionality in temperature fails below crystallization- or glass temperature. Entropy elasticity is fundamentally different from elasticity in most other materials, where force results from displacements in interatomic potentials (e. g. in steel). Bond potentials in technical elastomers contribute in a similar way to elasticity, but their effect is limited: In most technical polymers like SBR and NR the contribution of bond potentials ranges from 0 to 20 % [60]. In technical elastomers with many additives and additional ingredients (especially fillers) the behavior is much more complex and entropy elasticity may be superimposed by additional effects.

For many purposes it is interesting to know about the mean length of the polymers end-to-end vector. As the average $\langle r \rangle$ vanishes due to isotropy we have to rely on the mean squared displacement $\langle r^2 \rangle$. This can be calculated as the second moment of Eq. (2.11):

$$r_{\langle\rangle}^2 := \langle r^2 \rangle = \int_0^\infty r^2\,P(r)\,4\pi r^2\,\mathrm{d}r = b^2\,n \tag{2.14}$$

where $r_{\langle\rangle} = b\sqrt{n}$ is the mean displacement. As shown in Fig. 2.3 it is close to the maximum of the probability distribution $P(r)$ for scalar r, when increase in phase space volume (sphere shell $\propto r^2$) is taken into account. Thus, it is also a measure of the most probable distance of the polymers end from its beginning. For this reason it is commonly used to define the size of a polymer coil.

Werner Kuhn used Eq. (2.14) to define the Kuhn length b: It is the step length of the random walk constructing the polymer. It is closely related to the persistence length via $b = 2\,l_p$ [58]. This is not surprising, because the persistence length quantifies the length scale at which polymer orientation decorrelates which is a prerequisite for random walk statistics.

Moreover, Eq. (2.14) may be used to heuristically derive an expression for the average spacing between junctions in a network made up of connected Gauss chains. The connection of two chains can be either physical, e.g. by entanglements or weak physical interactions, or chemical, e.g. by chemical crosslinks. At the present stage we treat every network junction as permanent and ignore its specific nature. We have seen, that the end of a chain of N segments of length b is, most probably, located in distance $r_{\langle\rangle}(N) = \sqrt{N}b$ of its origin. As we assume statistically independent segments, this relation holds also for every (gaussian) subchain with $n < N$. After triggering the crosslink-

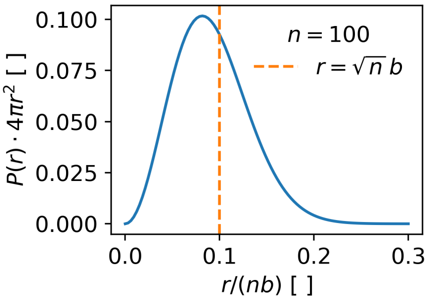

Figure 2.3: Probability to find the end of the polymer coil in a sphere shell with radius r.

ing process (e. g. by temperature), the crosslinking process is taking place by randomly connecting polymers with respect to space and time. After crosslinking, the network node is, in a first approximation, fixed in space. As the polymer subchain is most probably the distance $r_{\langle\rangle}(n)$ away from the last junction when crosslinking happens, we can state, that the average distance between two crosslinks is $r_0 = r_{\langle\rangle}(n) = \sqrt{n}\, b$, with subchains of n segments between them. This relation will prove useful in the upcoming chapters.

2.3 THE NEO-HOOKE MODEL

In this section the Gauss chain model is extended to a simple network. The network is represented by a parallel connection of Gauss chains of arbitrary spatial orientation with n statistical segments and end-to-end distance distributed according to gaussian statistics. Formally, the free energy of a single Gauss chain is averaged over all possible chain configurations. In reality, these Gauss chains can be identified with subchains between two network nodes. Interaction between subchains is neglected. The affinely deformed end-to-end vector of a chain can be expressed in terms of spherical coordinates as

$$\mathbf{r}_\lambda = \begin{pmatrix} \lambda_1 & 0 & 0 \\ 0 & \lambda_2 & 0 \\ 0 & 0 & \lambda_3 \end{pmatrix} \begin{pmatrix} \cos\theta\cos\varphi \\ \cos\theta\sin\varphi \\ \sin\varphi \end{pmatrix} r \tag{2.15}$$

where the λ_i denote the macroscopic deformation ratio in i-direction. Eq. (2.15) states that the orientation vector of the chain will deform in the same way as the whole sample. This is called affine deformation and is a rough, but the most simple approximation. If isotropic conditions are assumed the orientation in the network will be random, thus we have to average over all possible directions θ and φ as well as the vector length r. The latter is distributed according to $P(r)$ as given in Eq. (2.11). The free energy of a single chain $F = -T\,S$ can be expressed by the entropy given in Eq. (2.12). Finally, the averaged free energy per chain is scaled by the number of elastically active chains in the material ν_c. Altogether we have

$$W_{\mathrm{NH}} = \nu_c \langle F \rangle_{\mathbf{r}_\lambda} \equiv \nu_c \left\langle k_{\mathrm{B}}T \, \frac{3}{2} \frac{r^2}{n\, b^2} \right\rangle_{\mathbf{r}_\lambda} \tag{2.16}$$

$$= \nu_c \frac{3\, k_{\mathrm{B}}T}{2\, n\, b^2} \int_0^\infty \mathrm{d}r\, P(r) \int_0^\pi \mathrm{d}\varphi \int_0^{2\pi} \sin\theta \mathrm{d}\theta\, r^2 \left(\lambda_1^2 \cos^2\theta\cos^2\varphi + \lambda_2^2\cos^2\theta\sin^2\varphi + \lambda_3^2\sin^2\theta\right)$$

$$= \frac{\nu_c}{2} k_{\mathrm{B}}T(\lambda_1^2 + \lambda_2^2 + \lambda_3^2) = \frac{\nu_c}{2} k_{\mathrm{B}}T\, I_1 = \frac{G}{2}\, I_1 \tag{2.17}$$

where "≡" means that we omitted all terms independent of r, because they will vanish after differentiation with respect to stretch. $I_1 = \lambda_1^2 + \lambda_2^2 + \lambda_3^2$ is the first invariant of the left Cauchy Green deformation tensor [55]. The quantity $G = \nu_c\, k_{\mathrm{B}}T$ is called the modulus of the material, measuring the magnitude of the materials mechanical response. It is proportional to temperature T, reflecting the entropy elasticity of the underlying polymer chains. Eq. (2.17) is the energy density of a Neo Hookean material, the most basic rubber model available. Nevertheless, it is still in wide use in FE codes because of its efficiency, stability and simplicity.

The most common way to characterize the mechanical response of rubber is a uniaxial stretching test. Rubber is almost incompressible which means that the volume of a hypothetical cuboid with dimensions λ_i has constant volume, so $\lambda_1 \, \lambda_2 \, \lambda_3 \approx 1$. By setting $\lambda_1 = \lambda$ and requiring symmetry with respect to the two other dimensions, we find

$$\lambda_1 = \lambda \qquad \text{and} \qquad \lambda_2 = \lambda_3 = 1/\sqrt{\lambda} \tag{2.18}$$

By putting Eq. (2.18) into Eq. (2.17) we can easily derive stress by differentiation with respect to stretch*

$$P_{\mathrm{NH}} = \frac{\mathrm{d}W_{\mathrm{NH}}}{\mathrm{d}\lambda} = G\left(\lambda - \frac{1}{\lambda^2}\right) \tag{2.19}$$

where P_{NH} is the first Piola Kirchhoff stress, also known as engineering stress, which measures stress with respect to the cross section of the undeformed sample (see section 2.1).

2.4 The Mooney Rivlin Model

From Eq. (2.17) we see that the transition from one chain to an affinely deformed networks yields a free energy density solely dependent on the first invariant I_1 of the left Cauchy Green deformation tensor $\mathbf{B}$. As explained in section 2.1 this may be understood intuitively, because $I_1 = \lambda_1^2 + \lambda_2^2 + \lambda_3^2$ is the norm of a hypothetical length measure (elongation of a chain) within the sample. For isotropic systems a well-defined free energy density may depend on all invariants of $\mathbf{B}$. Keeping in mind that $I_3 \approx 1$, the famous Mooney-Rivlin material law [61] for incompressible rubber is given as a linear superposition of I_1 and I_2:

$$W_{\mathrm{MR}} = C_1\,(I_1 - 3) + C_2\,(I_2 - 3) \tag{2.20}$$

The “-3” occurring after both invariants ensures that the energy stored in an undeformed material is zero. It shall be noted here that the experimentally accessible physical quantity is stress which is the derivative of energy. Thus, an arbitrary additive constant (e. g. $-3\,(C_1 + C_2)$) does not change physics and is commonly done to adhere to conventions.

Engineering stress for uniaxial deformation is calculated by plugging in Eq. (2.18) and differentiating with respect to λ

$$P_{\mathrm{MR}} = 2C_1\left(\lambda - \frac{1}{\lambda^2}\right) + 2C_2\left(1 - \frac{1}{\lambda^3}\right) \tag{2.21}$$

The Mooney Rivlin model describes uniaxial test data for small strains ($\lambda \leq 3$) rather good, but overestimates stress for biaxial loading [62]. If Eq. (2.21) is directly fitted to experimental data, there is great uncertainty in the numerical value of C_2. As can be seen from the formula, this is due to the effect that the C_2 related stress term only changes significantly at low strains. For an equally weighted fitting measure over the whole strain range the model is linearized by dividing stress by $\lambda - 1/\lambda^2$:

$$\frac{P_{\mathrm{MR}}}{\lambda - \lambda^{-2}} = 2C_1 + 2C_2\,\frac{1}{\lambda} \tag{2.22}$$

---

[*] The “simple” differentiation method (differentiating with respect to λ after plugging in a parameterized first invariant) has to be used with care. It fails for more advanced material laws, e. g. Eq. (2.25). For a general concept to derive stresses from free energy densities the reader is referred to section 2.1 or a continuum mechanics book [55].

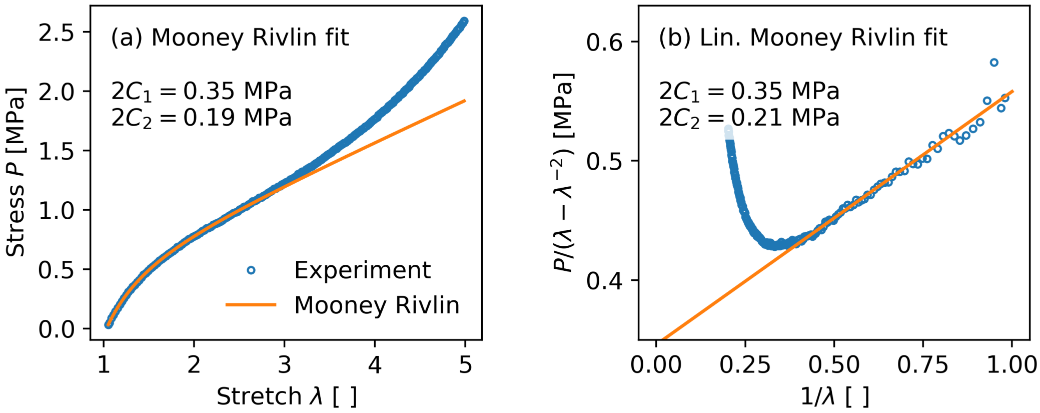

Figure 2.4: (a) Mooney Rivlin fits of a uniaxially stretched, sulfur cured NR at 60 °C. (b) Linearized Mooney Rivlin fit. Only data up to $\lambda = 2.5$ was used for fitting in both cases.

Plotting $P_{\mathrm{MR}}/(\lambda - \lambda^{-2})$ vs. $1/\lambda$ allows to directly read $2C_1$ from the offset and $2C_2$ from the slope of the fitted line. An example is shown in Fig. 2.4.

By comparing $2C_1$ with the modulus $G = \nu_c k_{\mathrm{B}} T = 2C_1$ of the Neo-Hooke model the Mooney Rivlin fit is often used to determine the number of elastically active chains ν_c, which is a measure for crosslink density [63]. The C_2 term is attributed to the effect of physical chain entanglements. Although being an established procedure for easy quantification of crosslink density of unfilled rubbers, the model neglects fluctuations of crosslinks. This is corrected for by the phantom model [57] or more advanced approaches, which allow to calculate crosslink fluctuations by means of entanglement- and crosslink contributions [64, 65].

2.5 The Extended Non-Affine Tube Model

The previously presented Neo-Hooke model includes the assumption that chains are not interacting and can slip through each other, called phantom chains [66–69]. Topological constraints exist only in terms of rigid crosslinks. First attempts to explain the C_2 term of the successful Mooney-Rivlin model included the assumption of constraints acting on the fluctuating crosslinks [65, 70, 71]. The knowledge about the equivalence of stochastic processes and path integrals occurring in quantum mechanics allowed the formulation of constraints acting on all polymer segments [72], called tube constraint. Within that framework a variety of tube models emerged [73–79]. The non-affine tube model [80, 81] presented here was validated by various experimental techniques [81]. It is derived using statistical mechanical methods on the hamiltonian

$$\frac{H}{kbT} = \frac{3}{2b} \int_0^L \mathrm{d}s \left(\frac{\partial \mathbf{r}(s)}{\partial s} \right)^2 + \sum_i \int_0^L \mathrm{d}s\, \Omega_i^2 \left(r_i(s) - R_i(s) \right)^2 \tag{2.23}$$

where the first integral generates gaussian chain statistics and the sum represents the tube constraints. It is crucial to note here that a polymer network is a quenched system, requiring to average the free energy of a hypothetical chain over all possible conformations. As lined out for the gaussian chain in Eq. (2.16) this requires averaging over the logarithm of the partition function Z. In many cases, the calculation is feasible only using the famous replica trick [78]. For the detailed calculation we refer the reader to one of the references [80, 81]. The potential scaling parameter in i-direction can be related to the tube diameter d_i and statistical segment length b via $\Omega_i = \sqrt{b}\, d_i^{-2}$. In the principal axis system, the tube diameter is expressed in terms of the principal stretches λ_i and equilibrium tube diameter d_0

$$d_i = d_0\, \lambda_i^{\alpha\beta} \tag{2.24}$$

The first exponent $\alpha = 1/2$ defines the non-affine relation of stretch and tube diameter. With the second exponent $\beta = 0 \ldots 1$ the model can be adjusted to the swelling and network defect degree as well as relaxation level of the tube. For sufficiently crosslinked samples it was found to be $\beta \approx 1$ [80, 81]. Moreover, the model was extended to reproduce strain hardening by Vilgis [81, 82]. The total free energy of the non-affine tube model is then

$$W(\bar{I}_1, \bar{I}^*) = \frac{G_\mathrm{c}}{2}\left[\frac{\left(1-\frac{1}{\hat{n}}\right)\bar{I}_1}{1-\frac{1}{\hat{n}}\bar{I}_1} + \log\left(1-\frac{1}{\hat{n}}\bar{I}_1\right)\right] + 2G_\mathrm{e}\,\bar{I}^*(-\beta) \tag{2.25}$$

$$\bar{I}_1 := I_1 - 3 = \lambda_1^2 + \lambda_2^2 + \lambda_3^2 - 3 \tag{2.26}$$

$$\bar{I}^*(\beta) := \frac{1}{\beta^2}\left(\lambda_1^\beta + \lambda_2^\beta + \lambda_3^\beta - 3\right) \tag{2.27}$$

where the generalized invariant $I^*(\beta)$ is introduced. For small strains and $\beta = 2$ the model reproduces the Mooney-Rivlin model. The quantities G_c and G_e are crosslink- and entanglement modulus, respectively. They can be expressed in terms of molecular quantities as follows

$$G_\mathrm{c} = A_c\, \nu_c\, k_\mathrm{B} T \tag{2.28}$$

$$G_\mathrm{e} = \frac{\beta^2}{4\sqrt{6}}\, \nu_\mathrm{s}\, k_\mathrm{B} T \left(\frac{b}{d_0}\right)^2 = \beta^2\, G_\mathrm{e}^* \tag{2.29}$$

where A_c is a microstructural factor quantifying the constraints acting on crosslinks. For $A_\mathrm{c} = 1$, crosslinks are fixed (affine model), while for $A_\mathrm{c} = 1/2$ crosslinks are allowed to fluctuate freely (phantom model limit). The statistical segment density can be expressed as $\nu_\mathrm{s} = M_\mathrm{s}/(\rho\, N_\mathrm{A})$, with segment molar mass M_s and density ρ. A plot showing a fit of the non-affine tube model to natural rubber for different β is shown in Fig. 2.5. Marckmann and Verron performed extensive benchmarking on a variety of phenomenological and physically-derived rubber models [62]. The non-affine tube model turned out to be the best compromise of fitting quality, predictive capability and number of parameters.

2.6 THE DYNAMIC FLOCCULATION MODEL

Most models are valid only for the pure polymer matrix. However, most technical rubber articles contain fillers which greatly increase the materials complexity as outlined in chapter 1.4. The Dynamic Flocculation Model (DFM) [47] aims to capture the additional phenomena occuring in filled rubber: stress softening, increased hysteresis and permanent set. The polymer matrix is described by the non-affine tube model given by Eq. (2.25). Filler is assumed to interact with the polymer

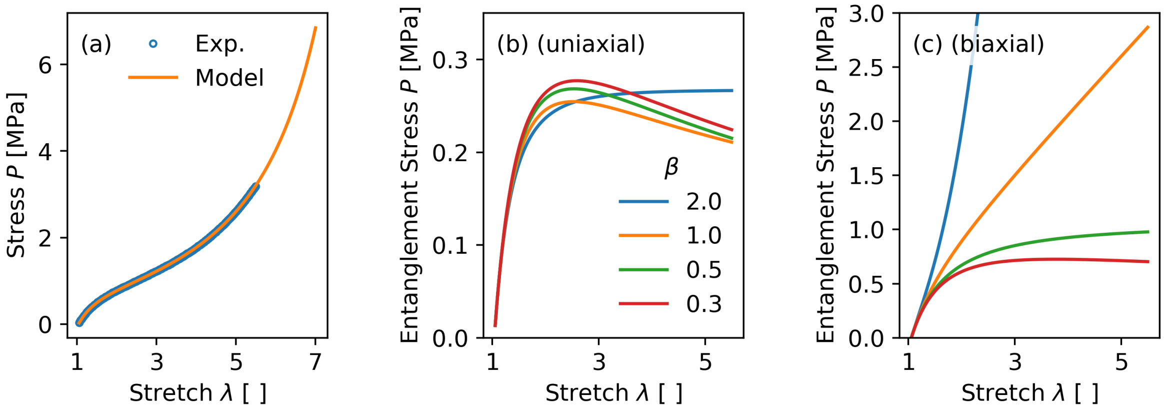

Figure 2.5: Fit of the non-affine tube model to sulfur cured NR at 60 °C, giving $G_\mathrm{c} = 0.31$ MPa, $G_\mathrm{e} = 0.27$ MPa and n=104. The high temperature is chosen to suppress crystallization. (a) Uniaxial fit ($\beta = 1$). (b) Entanglement stress contribution for uniaxial loading. The different curves correspond to variation of β. The special (but unphysical) case of $\beta = 2$ gives identical stress as the $C2$ term of the Mooney-Rivlin model. (c) Same plot for biaxial loading.

matrix in two different ways. Stiff filler clusters consisting of several aggregates increase local strain by hydrodynamic amplification. If stress surpasses a cluster-dependent critical load, the cluster breaks apart into aggregates and has a greatly reduced amplifying effect. At low strains, the broken clusters are assumed to reaggregate into loser soft clusters which do not amplify but take over the network stress. When stress gets large enough the soft clusters break, too, dissipating their energy. The latter process causes hysteresis.

The free energy is defined as the sum of an elastic contribution of the rubber matrix W_R given by the free energy density of the non-affine tube model (Eq. (2.25)) and the contribution from soft filler clusters W_A.

$$W_\mathrm{DFM}(\varepsilon_\mu, \varepsilon_{\mu,\mathrm{min/max}}) = (1 - \Phi_\mathrm{eff})\, W_\mathrm{R}(\varepsilon_\mu, \varepsilon_{\mu,\mathrm{min/max}}) + \Phi_\mathrm{eff}\, W_\mathrm{A}(\varepsilon_\mu, \varepsilon_{\mu,\mathrm{min/max}}) \tag{2.30}$$

where Φ_eff is the effective filler volume fraction which is larger than the true filler volume fraction due to occluded rubber [47]. The $\varepsilon_{\mu,\mathrm{min/max}} = \lambda_{\mu,\mathrm{min/max}} - 1$ measure the maximum and minimum deformation in each direction of space μ. Hydrodynamic strain amplification is implemented by assuming that the macroscopic stretch λ_μ translates into an amplified microscopic stretch κ_μ:

$$\lambda_\mu = 1 + \varepsilon_\mu \qquad \rightarrow \qquad \kappa_\mu = 1 + X_\mu\, \varepsilon_\mu \tag{2.31}$$

via a hydrodynamic amplification factor X_μ in direction μ. The requirement of rubber incompressibility holds for macroscopic as well as microscopic stretches, such that $\prod_\mu \lambda_\mu = \prod_\mu \kappa_\mu = 1$. This poses constraints on X_μ that can be fulfilled by rewriting

$$\kappa_\mu = \lambda_\mu^r \qquad \text{with} \qquad r = \log(1 + X_\mathrm{max}\, \varepsilon_f) / \log(1 + \varepsilon_f) \tag{2.32}$$

where X_max and ε_f refer to the respective values in the direction of maximum strain (in principal axes system). Note that Eq. (2.32) implicitly assumes the remaining two dimension to deform iden-

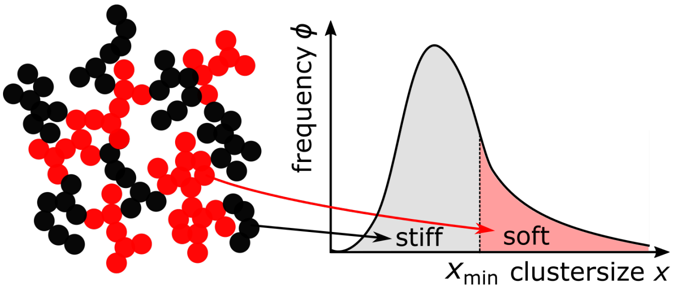

Figure 2.6: Cluster size distribution $\phi(x)$ as defined in Eq. (2.34). Black clusters have never been broken (called stiff or virgin clusters) and are assumed to amplify the material. Red clusters (called soft or broken) have already been broken and are responsible for hysteresis.

tically. Additionally, it may induce discontinuities when the direction of maximum principal strain changes (e.g. in two sided shear experiments). The amplification factor X_{max} depends on the all-time maximum and minimum strain, and on the details of the cluster structure within the network

$$X_{\mathrm{max}} = 1 + c\,\Phi_{\mathrm{eff}}^{\frac{2}{3-d_{\mathrm{f}}}} \left[\int\limits_{0}^{x_{1,\mathrm{min}}} x^{d_{\mathrm{w}}-d_{\mathrm{f}}} \phi(x)\,\mathrm{d}x + \int\limits_{x_{1,\mathrm{min}}}^{\infty} \phi(x)\,\mathrm{d}x \right] \tag{2.33}$$

where $c = 2.5$ is a constant motivated by the Einstein relation for spherical inclusions [83] and Φ_{eff} is the effective filler volume fraction. The latter is larger than the real filler volume fraction Φ mainly due to rubber occluded from mechanical deformation. The quantities $d_{\mathrm{w}} \approx 3.1$ and $d_{\mathrm{f}} \approx 1.8$ are anomalous diffusion coefficient and fractal dimension of filler clusters respectively [47, 84]. $x_{1,\mathrm{min}}$ is the size of the largest cluster which survived the maximum previous strain given in units of primary particle size. The cluster size distribution $\phi(x)$ in Eq. (2.33) is chosen as a Smoluchowski type, because it reflects the outcome of cluster-cluster aggregation (CCA) occuring during carbon black flocculation inside the rubber matrix [85]:

$$\phi(x) = \frac{4x}{x_0^2} \exp\left(-2\frac{x}{x_0}\right) \tag{2.34}$$

with x_0 being the average cluster size. The distribution is sketched in Fig. 2.6. Using Eq. (2.34) and approximating $d_{\mathrm{w}} - d_{\mathrm{f}} \approx 1$ the integral in Eq. (2.33) can be carried out analytically [47]. The size of the largest surviving cluster $x_{1,\mathrm{min}}$ is calculated via

$$x_{\mu,\mathrm{min}} = \frac{s_{\mathrm{v}}}{\hat{\sigma}_{\mathrm{R},\mu}(\varepsilon_{\mu,\mathrm{max}}; \varepsilon_{\mu,\mathrm{min}})} \tag{2.35}$$

where s_{v} is the strength of virgin (never broken) filler-filler bonds which are assumed to consist of glassy polymer bridges. The denominator is the maximum relative stress the sample has ever experienced within its deformation history. It is defined by

$$\hat{\sigma}_{\mathrm{R},\mu}(\varepsilon_{\mu}; \varepsilon_{\mu,\mathrm{min}}) = \sigma_{\mathrm{R},\mu}(\kappa_{\mu}) - \sigma_{\mathrm{R},\mu}(\kappa_{\mu,\mathrm{min}}) \tag{2.36}$$

where σ_R is the first Piola-Kirchhoff stress derived from the free energy density of the non affine tube model given by Eq. (2.25). In order to adhere to the nomenclature used in most works on the

DFM [40, 47, 86] the first Piola Kirchhoff stress is denoted “σ” instead of “P” here. The occurrence of the minimum stress allows additional stress softening when changing the deformation direction, e. g. during two-sided shear deformation.

Hysteresis is generated by already broken soft clusters, see Fig. 2.6. Soft clusters are assumed to be in mechanical equilibrium with their elastic surrounding and correspondingly store energy. Upon stretching, soft clusters in stretching direction μ break down and dissipate the stored energy. During sample relaxation these clusters reaggregate, while the lateral dimension is expanded and induces lateral cluster breaking. The soft clusters' stress contribution in direction ν is given as

$$\sigma_{A,\nu} = \sum_{0}^{\partial\varepsilon_\mu/\partial t>0} = \hat{\sigma}_{\mathrm{R},\mu}(\varepsilon_\mu;\varepsilon_{\mu,\mathrm{min}}) \int_{x_\mu(\varepsilon_{\mu,\mathrm{max}},\varepsilon_{\mu,\mathrm{min}})}^{x_\mu(\varepsilon_\mu,\varepsilon_{\mu,\mathrm{min}})} \frac{\mathrm{d}\varepsilon_\mu}{\mathrm{d}\varepsilon_\nu}\phi(x)\mathrm{d}x \tag{2.37}$$

where $\mathrm{d}\varepsilon_\mu/\mathrm{d}\varepsilon_\nu$ transforms the stress contributions from lateral directions into axial direction. For uniaxial load ($\lambda_1 = \lambda$, $\lambda_2 = \lambda_3 = 1/\sqrt{\lambda}$), this can be expressed as

$$\frac{\mathrm{d}\varepsilon_\mu}{\mathrm{d}\varepsilon_\nu} = -\frac{1}{2}(1+\varepsilon_1)^{-3/2} \tag{2.38}$$

The integral boundaries x_μ define the fraction of intact soft clusters. They are defined as

$$x_\mu(\varepsilon_\mu,\varepsilon_{\mu,\mathrm{min}}) = \frac{s_\mathrm{d}}{\hat{\sigma}_{\mathrm{R},\mu}(\varepsilon_\mu;\varepsilon_{\mu,\mathrm{min}})} \tag{2.39}$$

in analogy to Eq. (2.35), but with a lower bonding strength $s_\mathrm{d} < s_\mathrm{v}$ for the already broken clusters. The sum selects the direction where strain is increasing. The total energy is then expressed as

$$\sigma_\nu = (1-\Phi_\mathrm{eff})\,\sigma_{\mathrm{R},\nu}(\kappa_\nu) + \Phi_\mathrm{eff}\,\sigma_{A,\nu} + \sigma_\mathrm{set} \tag{2.40}$$

where stress was split up into matrix- and filler contribution according to their contribution to total volume. Residual stress is introduced via σ_set and has to be adjusted by empirical functions. If temperature dependence is neglected a convenient functional form is

$$\sigma_\mathrm{set} = s_{\mathrm{set},0}\left(\sqrt{\varepsilon_\mathrm{max}} - \sqrt{|\varepsilon_\mathrm{min}|}\right) \tag{2.41}$$

A fitting example is presented in Fig. 2.7. The 5th cycle of each strain step was extracted and used for fitting to guarantee equilibrated conditions. The model fits uniaxial data up to 140 % strain rather well. At larger strains the model deviates from experiment.

Viscoelasticity and continuous damage was recently added to the model by Ragunath et al. [86]. It shall be noted, that the free energy density of the DFM shown in Fig. 2.30 has to be seen as a starting point for the calculations in this chapters. It does not represent the free energy stored in the material, because amplified strain is inserted *after* the stress functional is calculated from the free energy density.

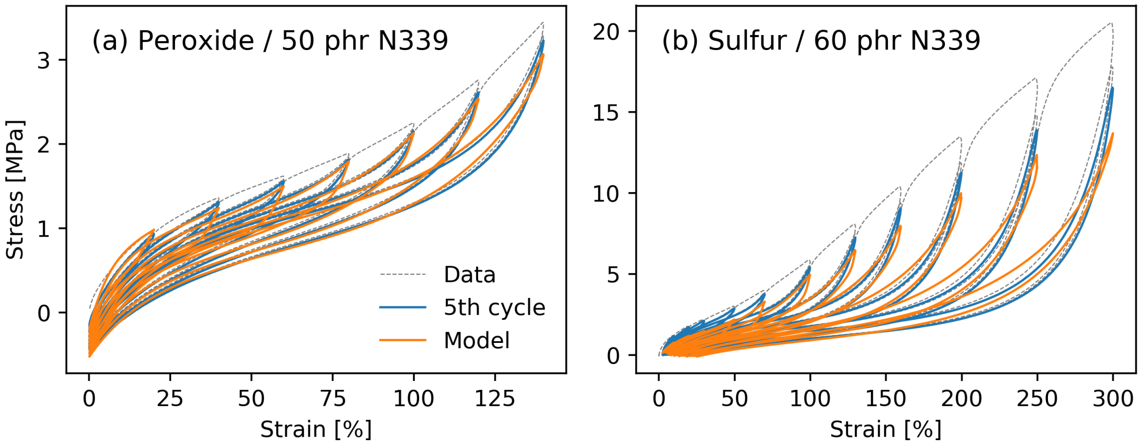

Figure 2.7: (a) Fit of the DFM to EPDM sample P/CB of publication 3.2 measured at 20 mm/min and 23 °C. Parameters are $G_\mathsf{c} = 0.32$ MPa, $G_\mathsf{e} = 1.36$ MPa, $\Phi_\mathsf{eff} = 0.32$, $x_0 = 14.5$, $s_\mathsf{v} = 38.0$ MPa, $s_\mathsf{d} = 37.3$ MPa, $n = 17.3$ and $s_{\mathsf{set,0}} = 0.45$. (b) Fit to EPDM sample S/CB of publication 3.2 measured at 20 mm/min and 23 °C. Parameters are $G_\mathsf{c} = 0.63$ MPa, $G_\mathsf{e} = 1.66$ MPa, $\Phi_\mathsf{eff} = 0.35$, $x_0 = 5.1$, $s_\mathsf{v} = 68.3$ MPa, $s_\mathsf{d} = 50.9$ MPa, $n = 20.3$ and $s_{\mathsf{set,0}} = 0.50$.

With four parameters I can fit an elephant, and
with five I can make him wiggle his trunk.
John von Neumann

3

Investigation and Modeling of Filler Reinforcement

3.1 INTRODUCTION

This chapter deals with the understanding and modeling of filler reinforcement. For a review on the physics and modeling approaches of rubber amplification the reader is referred to chapters 1 and 2.

In the first of the upcoming publications a physically plausible but still efficient material model for filled elastomers is developed. Thus, the paradigms are twofold: (1) The model shall be built on physical principles which are simple enough to capture the main effects of the arbitrarily complex filler-polymer interplay, but allow a compact mathematical description. This approach deliberately neglects the details of microscopic interactions and focuses on their emergent behavior. (2) Some compromises are done to keep the mathematics suitable for FE-codes. This involves application of the strain amplification concept to a frame-independent local strain measure.

In that sense, the model may be placed in between phenomenological models like the Model of Rubber Phenomenology (MORPH) [87], being a collection of formulas without physical reference, and physically derived ones like the Dynamic Flocculation Model (DFM) [88] which are often mathematically inconsistent in a continuum mechanical sense. Reinforcement is modeled by introducing differently strain-amplified polymer-filler domains, corresponding to a microscopically inhomogeneously material. The material softens, when the most amplified domains break down and reform less amplified. The heterogeneity in amplification is explicitly taken into account and is not averaged-out as done in the DFM (see section 2.6) [47]. Hysteresis is introduced via a dynamic breakdown and reaggregation mechanism, which is described by driven diffusion out of a potential well. This mechanism is sensitive to deformation rate and temperature. Again, the details of the structures breaking down and reaggregating are not specified. The publication shows that the model is able to capture the behavior of filled rubber at different deformation modes with a relatively small set of 7 physically motivated fitting parameters. With two additional parameters it is able to describe the effect of temperature and varying deformation rate. Recently, the hyperelastic

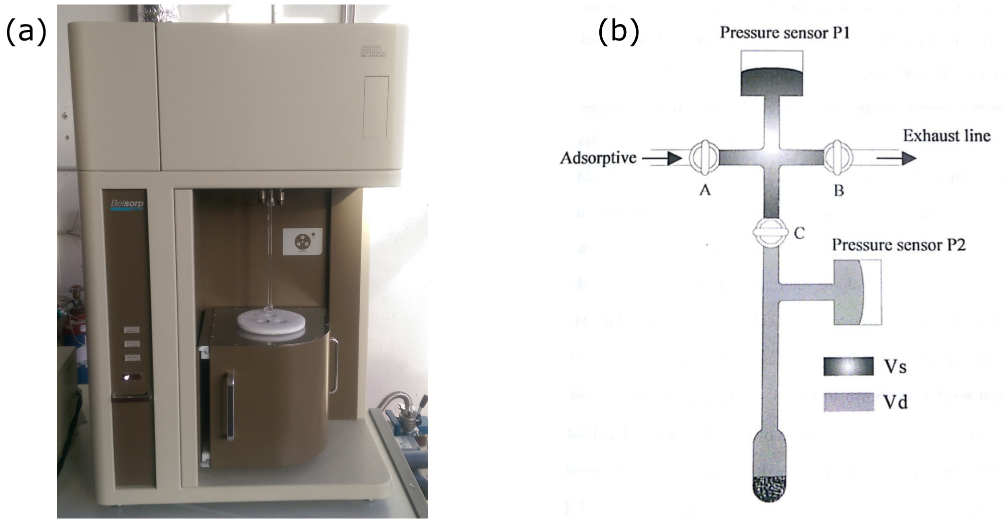

Figure 3.1: (a) Photograph of the BELSORP Max adsorption automaton used in this work and (b) scheme of its internal structure [91]: After gas input through valve A the molar amount of gas inside Vs is calculated from an appropriate equation of state. Then valve C is opened and the gas adsorbs on the samples surface. After equilibration the adsorbed amount of gas is calculated from pressure P2, Vs and Vd and the equation of state. This is procedure is repeated, successively increasing pressure P2.

part of the model was implemented in the commercial FE software Abaqus [89] and has proven to be efficient and easy to handle. Nevertheless, the model contains some uncommon mathematical concepts which are replaced in this thesis after presentation of the publications.

The results of model fitting happening in publication 1 show that the deformation-driven breakdown and reaggregation mechanism is characterized by energy barriers around 100 kJ/mol and length scales of about 5 nm. These values suggest the polymer-filler interface to be the origin of hysteresis. For this reason the second publication deals with the investigation of polymer-filler interaction via static gas adsorption[*] using different polymer-analogue gases, carbon blacks and silicas. Static gas adsorption is a well established method for surface characterization, especially known for the BET surface area per gram of sample [12]. The BET surface area is obtained by giving gaseous nitrogen to a sample of defined mass and measuring the amount sticking to the surface using the remaining gas pressure. After saturation of the surface its area is calculated from the adsorbed molar amount of nitrogen and the corresponding surface occupation per mole. This is done using the BET equation, named after its inventors Brunauer, Emmett and Teller [90]. The adsorbed amount of gas in dependence of pressure at constant temperature is called adsorption isotherm and is used to characterize filler morphology in two ways: (1) The surface area accessible to the adsorptive. It can be assumed to decrease for larger gas molecules, because they are unable to penetrate small cavities. (2) The interaction energy of adsorptive and adsorbate, which depends on the polar and dispersive components of each reactant. Generally, it will increase for larger gas molecules, because they have a larger contact area. The ratio of interaction energy and surface occupation of each gas molecule may be regarded as indicative for the interaction of the molecules constituents with the corresponding filler. Measurements are performed using a BELSORP-max (BEL Japan) adsorption automaton as shown in Fig. 3.1. The publication will show that the difference in (dispersive) polymer-filler interaction alone is not able to explain the vastly different behavior of silica and carbon black in a polymer matrix.

---

[*] The terminus *adsorption* means that particles (the adsorptive) are attached to a surface (adsorbate) while *absorption* means particle incorporation into a solid.

Moreover, the adsorption energies can be compared to the energy barrier of around 100 kJ/mol related to mechanical hysteresis obtained from model fitting. The polymer is an amorphous EPDM† consisting of 52 wt. % ethylene and 4.3 wt. % dienes. For a rough calculation it will be assumed that it consists by half of ethylene and propylene. The adsorption energies of ethane‡ and propene (propylene) on carbon black are found in publication 2 as 18.5 kJ/mol and 20.4 kJ/mol, respectively, giving 19.5 kJ/mol for an average monomer. Thus, if we assume polymer adsorption and desorption to be responsible for hysteresis, $100/19.5 \approx 5$ monomers define the typical length of desorbed subchains. Given the length of a C-C bond of about 0.12 nm [92] and approximately 2.5 bonds per monomer, the chain segments have a length of $5 \cdot 2.5 \cdot 1.2\,\mathrm{nm} = 1.5\,\mathrm{nm}$. This roughly corresponds to the length of statistical segments for many polymers [93]. The calculation shows that physical chain adsorption and desorption on the scale of single statistical segments may be the predominant reason for mechanical hysteresis.

---

† Trade name Keltan 4450.

‡ Ethane is sufficiently similar to ethylene for a simple estimate.

International Journal of Plasticity 89 (2017) 173–196

Contents lists available at ScienceDirect

International Journal of Plasticity

journal homepage: www.elsevier.com/locate/ijplas

A physically based model of stress softening and hysteresis of filled rubber including rate- and temperature dependency

J. Plagge*, M. Klüppel

Deutsches Institut für Kautschuktechnologie e.V., Eupener Str. 33, 30519, Hannover, Germany

A R T I C L E I N F O

Article history:
Received 5 September 2016
Received in revised form 21 November 2016
Accepted 24 November 2016
Available online 28 November 2016

Keywords:
Microstructures
Finite strain
Rate-dependent material
Viscoelastic material
Constitutive behavior

A B S T R A C T

A novel physically based material model is presented that describes the complex stress-strain behavior of filled rubbers under arbitrary deformation histories in a constitutive manner. The polymer response is considered by the extended non-affine tube model. Stress softening is taken into account via the breakdown of highly stressed polymer-filler domains under load and homogenization of the medium. Set stress and hysteresis are introduced via a continuous reformation mechanism, characterized by a single critical stress parameter. The latter is predicted to be dependent on temperature and deformation rate by means of Kramers escape rate. This is confirmed for a wide range of temperatures and speeds by fitting to multihysteresis measurements carried out in a heat chamber. Fitting parameters reveal that the mechanism responsible for hysteresis and set stress takes place on the nanometer scale with energies of roughly 100 kJ/mol. The behavior of the fitting parameters is analyzed for varying filler loadings and crosslinker concentrations in EPDM. Simulations of the stress-strain response for several deformation modes are in good agreement with experiments and its mathematical simplicity makes it very promising for applications with Finite Element Methods (FEM).

© 2016 Elsevier Ltd. All rights reserved.

1. Introduction

Reinforced elastomers consisting of a polymer and a nano-structured filler like carbon black or silica are present almost everywhere in our lives. The most prominent example is automotive tires, where its incredible wear- and fatigue properties are still unmatched. An unfilled elastomer is almost ideally hyperelastic, e.g. exhibiting small hysteresis and weak rate dependency. The incorporation of fillers greatly toughens and stiffens the polymer, but also creates memory-like material properties as increased hysteresis and stress softening. For small dynamic deformations the latter effect is known as Payne-Effect (Payne, 1962) and is attributed to the irreversible breakdown of a stiff, percolated filler network (Rendek and Lion, 2010). This effect was extensively described by Payne and investigated by Kraus (1984) and Medalia (1978). A similar phenomenon can be observed for larger deformations, which was investigated by Mullins and Tobin (1965): The greater the deformation the material was subject to, the softer the materials response. The change in the response is not immediate, but requires several cycles to reach a steady state. The explanation for this effect is the complex interplay and structural rearrangement of filler particles and the polymer network, as reviewed in Vilgis et al. (2009). In particular, a breakdown or slippage of adsorbed polymer chains at the filler surface (Dannenberg, 1975; Bueche, 1960) and disentanglement of chains

---

* Corresponding author.
E-mail address: jan.plagge@DIKautschuk.de (J. Plagge).

http://dx.doi.org/10.1016/j.ijplas.2016.11.010
0749-6419/© 2016 Elsevier Ltd. All rights reserved.

Reproduced with permission from
International Journal of Plasticity, 2017, 89, 173-196.
https://doi.org/10.1016/j.ijplas.2016.11.010

adsorbed at the filler surface (Hamed and Hatfield, 1989) or a rearrangement of network junctions in filled systems (Payne and Kraus, 1965) has been proposed. A constitutive model of stress-induced desorption of chains from the filler surface has been derived by Govindjee and Simo based on a statistical mechanics approach (Govindjee and Simo, 1991, 1992). This idea was recently extended to include deformation of filler aggregates as well, allowing the calculation of hysteresis (Dargazany and Itskov, 2013). Reese (2003) built a material model on the basis of the Neo-Hooke material model, taking into account breaking and reforming of chains by using several assumptions about chain distribution to arrive at a continuum level description. Similarly, a FE multiphase computational model was developed, explicitly embedding filler particles into a rubber matrix. The model is able to reproduce Mullins effect on a macroscopic level (Sodhani and Reese, 2014). A more general yet abstract approach was chosen by Wulf and Ihlemann (2015), who did computer simulations of a minimal rubber material on a molecular scale. In their work a small collection of generalized interactions was sufficient to generate typical rubber stress-strain data. In addition to these physical approaches, there exists a wealth of phenomenological models. For example, Amin et al. (2006) modeled the material by decomposing the deformation gradient into elastic and inelastic parts, using the concept of the Zener model. From experiment, they find that both overstress as well as deformation measures are necessary to accurately describe rubber viscosity.

However, experimental investigations of the DC-conductivity of cyclically loaded carbon black filled rubbers indicate that the stress softening effect is closely related to a rearrangement or breakdown of filler clusters which strongly depends on the interaction strength between polymer and filler (Stübler et al., 2011; Geberth and Klüppel, 2012; Geberth, 2013). An example for carbon black filled natural rubber is shown in Fig. 1, where the electrical resistance increases over 2 orders of magnitude by increasing strain up to 100%. Like the mechanical data, resistance shows hysteresis and approaches a steady cycle after repeated identical deformation.

The so called Dynamic-Flocculation-Model (DFM) derived by Klüppel at al. (Klüppel and Schramm, 2000; Klüppel, 2003; Klüppel et al., 2005) states that the underlying mechanism of stress softening is hydrodynamic reinforcement by stiff filler clusters, which immobilize a certain amount of polymer. By increasing the load, more and more filler clusters are broken, decreasing the geometric constraints imposed on the polymer matrix. The hydrodynamic amplification factor is obtained by integrating over a physically reasonable clusters size distribution with an upper boundary depending on the maximum strain. In addition, the broken clusters are dynamically re-aggregating and breaking during repeated loading up to a certain strain level, thereby causing hysteresis which is a further typical effect found in experiments. The DFM was shown to be in good agreement with experimental data for various elastomer nano-composites with carbon black or silica/silane filler systems at different deformation modes (Lorenz et al., 2010; Lorenz and Klüppel, 2012). Recently, the aging behavior and the polymer-filler interphase dynamics were successfully investigated by a DFM parameter study (Plagge and Klüppel, 2015; Fleck et al., 2014). In addition, the temperature dependence of quasi-static stress-strain cycles could be well described by a simple, physically based extension of the model (Lorenz et al., 2012) and the strain rate and amplitude dependency was formulated in finite viscoelasticity (Raghunath et al., 2016). Due to the complexity of the DFM, the breakdown and re-aggregation mechanism could only be formulated in the main axis system which makes it difficult to implement into a finite element code or to calculate more complex deformation modes. So far, this could only be achieved by applying the so-called concept of representative directions (Lorenz et al., 2012; Freund et al., 2011) but this requires large computation times. Therefore it makes sense to simplify the breakdown and re-aggregation mechanism of the filler network in strained elastomers by referring to a semi-empirical approach that generates the observed stress softening and hysteresis effects in a similar manner.

In this paper a model of stress softening and hysteresis is presented, which is built on physical principles and can easily be calculated for arbitrary stress-strain histories and any complex deformation modes. The hyper-elastic rubber matrix is modeled by the extended non-affine tube model (Heinrich and Kaliske, 1997; Klüppel and Schramm, 2000), and the underlying mechanism of stress softening is considered to be hydrodynamic amplification of the rubber matrix by highly

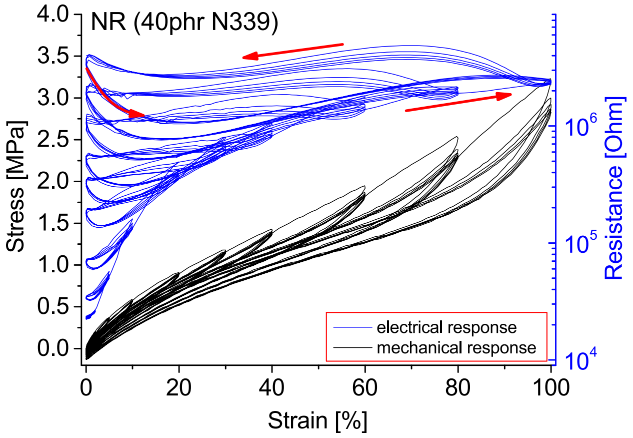

Fig. 1. Mechanical stress and electrical resistance of a multihysteresis experiment with increasing strain level measured with a dumbbell sample. Taken from (Geberth, 2013).

constraint domains. The latter is described by considering a power law distribution of amplification factors with an upper boundary depending on the maximum value of the first deformation invariant. The hysteresis is modeled by a generalized network model with dynamically opening links which immediately close at zero stress. The critical stress is then found to be the key quantity for an extension of the model regarding rate- and temperature dependent effects. Finally a constitutive formulation of the model is given and the global energy dissipation is discussed. In the second part of the paper the developed concepts are then tested by a variety of experiments under uniaxial, equibiaxial and pure shear deformation for various elastomer composites with different filler loadings and curing states.

2. Theory

2.1. Hydrodynamic amplification

For the elastic response the interaction between filler and polymer is implemented via the concept of hydrodynamic amplification. The main idea can be traced back to Einstein who calculated the increase of viscosity in a viscous liquid due to the presence of rigid spheres (Einstein, 1906). Smallwood used the analogy of the equations to identify spheres with filler particles and liquid with the polymer matrix (Smallwood, 1944). Mathematically this is implemented via a hydrodynamic amplification factor X, such that in linear theory

$$\sigma_{\text{filled}} = X\sigma_{\text{unfilled}} = XG_{\text{unfilled}}\varepsilon \tag{1}$$

where G_{unfilled} is the modulus of the unfilled material and ε is engineering strain. When deriving this expression, it turns out that the amplification factor X consists of a stress amplification factor a_s and a strain amplification factor a_d, that both depend on the filler volume fraction φ. For the energy density of the filled elastomer W_{filled} it can be shown (Einstein, 1906; Domurath et al., 2012), that

$$W_{\text{filled}}(\varepsilon) = a_s W_{\text{unfilled}}\left(a_d^2\varepsilon\right) \tag{2}$$

$$\text{with} \quad a_d = \frac{1}{1-\varphi} \quad \text{and} \quad a_s = 1 + \frac{\varphi}{2} \tag{3}$$

such that in the linear regime with $W_{\text{unfilled}}(\varepsilon) = \frac{1}{2}G_{\text{unfilled}}\varepsilon^2$ the total amplification X as defined in Eq. (1) can be calculated as

$$X = a_d^2 a_s = \frac{1+\frac{\varphi}{2}}{(1-\varphi)^2} = 1 + 2.5\varphi + 4\varphi^2 + \mathcal{O}\left(\varphi^3\right) \tag{4}$$

Eqs. (2) and (4) hold for perfectly spherical, evenly distributed spheres of arbitrary radius, which are hydrodynamically decoupled. Strain amplification a_d represents the increase in local strain as a consequence of a reduced deformable volume. Hence, its origin is purely geometrical. Stress amplification a_s results from attractive filler-polymer boundary conditions and their influence on the hydrodynamic equations. From this point of view it is reasonable, that the former one directly impacts the local strain, while the latter one acts on the energy.

In the rubber community hydrodynamic amplification is often considered as pure strain amplification. This is in fact a good approximation as the following calculation shows.

Solving Eq. (4) for φ and omitting the unphysical solutions gives

$$\varphi = 1 - \frac{\sqrt{24X+1}-1}{4X} \tag{5}$$

Using this expression, we can express a_d and a_s via Eq. (3) in terms of X:

$$a_d = \frac{1}{6}\left(\sqrt{24X+1}+1\right) \quad \text{and} \quad a_s = \frac{1+12X-\sqrt{24X+1}}{8X} \tag{6}$$

For $X \approx 1$ these expressions can be approximated as

$$a_{d,1} \approx \sqrt{X} \quad \text{and} \quad a_{s,1} \approx 1 \tag{7}$$

The asymptotic behavior for large X reads

$$a_{d,\infty} \approx \frac{\sqrt{24}}{6}\sqrt{X} \quad \text{and} \quad a_{s,\infty} \approx \frac{3}{2} - \frac{\sqrt{24}}{8}\frac{1}{\sqrt{X}} \tag{8}$$

Take into account, that both approximations are compatible with Eq. (4), because in both cases $X = a_d^2 a_s$ holds. In the following we are interested in a power-law approximation of the strain- and stress amplification factor for small X, so the first approximation is chosen. From Fig. 2 it can be seen, that the approximation is reasonable. The result shows, that stress amplification is of minor importance, especially for large X (or filler concentration φ).

2.2. Elastic energy density

The base of the elastic response is the physically motivated non-affine tube model developed by Heinrich et al. (Heinrich et al., 1988). In a review by Marckmann and Verron it was compared to physical as well as non-physical rubber models and shown to accurately describe several deformation modes, even allowing to calculate biaxial and pure shear data from uniaxial fits (Marckmann and Verron, 2006). Its energy density is given by

$$W\left(\bar{I}_1,\bar{I}^*\right) = \frac{G_c}{2}\left[\frac{\left(1-\frac{1}{n}\right)\bar{I}_1}{1-\frac{1}{n}\bar{I}_1} + \log\left(1-\frac{1}{n}\bar{I}_1\right)\right] + 2G_e\bar{I}^*(-\beta) \tag{9}$$

$$\bar{I}_1 = \lambda_1^2 + \lambda_2^2 + \lambda_3^2 - 3 \tag{10}$$

$$\bar{I}^*(\beta) = \frac{1}{\beta^2}\left(\lambda_1^{-\beta} + \lambda_2^{-\beta} + \lambda_3^{-\beta} - 3\right) \tag{11}$$

The quantity $\bar{I}_1 = I_1 - 3$ is the first invariant of the left Cauchy Green tensor (Holzapfel, 2000), but shifted such that it is zero at zero strain. It can be physically interpreted as a squared length deformation measure. $\bar{I}^*(\beta)$ is a generalized invariant taking into account the non-affine tube constraints imposed by neighboring polymer chains. The parameter β is supposed to be between 0 and 1 and is a measure for the relaxation state of these constraints. It has been shown, that $\beta = 1$ is reasonable for sufficiently crosslinked samples (Klüppel and Schramm, 2000; Vilgis et al., 2009; Klüppel and Heinrich, 1994), hence it will be fixed to this value. Recently, the extended non-affine tube model has been reviewed by Behnke et al. (2011), whereby also non.equilibrium branches were considered and thermo-mechanically coupled FEM problems were addressed. This demonstrates, that the energy density given by Eq. (9) represents a fundamental framework for rubber elastic material behavior up to large strains.

The first bracket term of Eq. (9) considers the elastically effective network junctions (cross-links and trapped entanglements) with an elastic modulus G_c proportional to the density of network junctions. The second term describes topological tube constraints in dense networks (packing effects), whereby the tube constraint modulus G_e is proportional to the entanglement density of the polymer chains. The parenthetical expression in the first term refers to a non-Gaussian extension of the tube model (Heinrich and Kaliske, 1997). It is taking into account the finite chain extensibility of the polymer network with n being the number of statistical chain segments between two successive network junctions. For the limiting case $n = \bar{I}_1$, the free energy density Eq. (9) exhibits a singularity, which is reached when the chains between successive network junctions are stretched, totally. For the moduli G_c and G_e, the following relations regarding molecular material parameters hold:

$$G_c = A_c \nu_c k_B T \quad G_e = \frac{\beta^2}{\sqrt{6}} \nu_e k_B T \tag{12}$$

Here, ν_c and ν_e are the inter-junction- and inter-entanglement chain densities, respectively, A_c is a micro-structure factor that describes the fluctuations of network junctions (A_c 0.67; Klüppel and Heinrich (1994)), k_B the Boltzmann constant and T

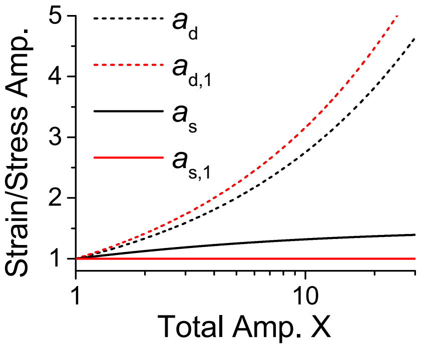

Fig. 2. Plot of the split-up of the total amplification factor X into strain (a_d) and stress (a_s) amplification and corresponding power-law approximations $a_{d,1}$ and $a_{s,1}$.

the absolute temperature. The linear increase of the moduli G_c and G_e with temperature T reflects the entropic origin of rubber elasticity. We want to amplify global strain $\sqrt{\bar{I}_1} = \sqrt{\lambda_1^2 + \lambda_2^2 + \lambda_3^2 - 3}$ linearly, as was already outlined in (Bergstrom and Boyce, 1999). This is in contrast to previous works, where the microscopic strain in a specific (principal) direction is amplified (Lorenz and Klüppel, 2012). This new definition is independent of direction and avoids problems occurring from rotating coordinate systems and changes in maximum strain directions within deformation history. Additionally, it ensures constant volume. Entanglements and tube constraints (I^*) are amplified in the same way. This can be explained by looking at the expansions of both invariants of an incompressible material with $\lambda_3 = 1/(\lambda_1\lambda_2)$ around $\lambda_1 = \lambda_2 = 1$ up to second order:

$$\bar{I}_1 = 4\Big((\lambda_1 - 1)^2 + (\lambda_2 - 1)^2 + (\lambda_1 - 1)(\lambda_2 - 1)\Big) + \mathcal{O}\Big((\ldots)^3\Big)$$

$$\bar{I}^* = (\lambda_1 - 1)^2 + (\lambda_2 - 1)^2 + (\lambda_1 - 1)(\lambda_2 - 1) + \mathcal{O}\Big((\ldots)^3\Big)$$

In consequence both invariants coincide by a multiplicative factor of 4, justifying a similar treatment for low strains.

According to Einstein (1906); Domurath et al. (2012) energies are amplified using the strain and stress amplification factors a_d and a_s according to Eq. (2). Taking into account the approximation given by Eq. (7) we can replace

$$W\left(\bar{I}_1, \bar{I}^*\right) \rightarrow a_s W\left(a_d^2 \bar{I}_1, a_d^2 \bar{I}^*\right) \approx W\left(X\bar{I}_1, X\bar{I}^*\right) \tag{13}$$

The consistency of this idea can be shown by the example of an incompressible Neo-Hooke material for uniaxial strain, which is in fact the linear expansion of Eq. (9):

$$W_{\mathrm{NH}} = \frac{C_1}{2}\bar{I}_1 \rightarrow W_{\mathrm{NH}} = \frac{C_1}{2}X\bar{I}_1 \tag{14}$$

which results in a first Piola-Kirchhoff-stress of

$$P_{11,\mathrm{NH}} = C_1\left(\lambda_1 - \lambda_1^{-2}\right) \rightarrow P_{11,\mathrm{NH}} = XC_1\left(\lambda_1 - \lambda_1^{-2}\right) \tag{15}$$

So the resulting stress is amplified linearly (which isn't surprising because differentiation is a linear operation). In fact, the amplification concept is valid in linear elasticity only, but it is assumed to describe hyperelastic behavior as well.

Filled elastomers are a highly heterogeneous material. In this model it is assumed, that there are heavily amplified stiff domains coexisting with softer domains, represented by larger and smaller amplification factors. At a certain stress, stiff domains break up and reorganize in an energetically more favorable state with a smaller amplification factor X. We assume a power law amplification-factor distribution, which can be motivated from percolation theory and is always normalized to 1 in the interval $[X_{\min}, X_{\max}]$:

$$P_X(X) = X^{-\chi} \cdot \frac{\chi - 1}{X_{\min}^{1-\chi} - X_{\max}^{1-\chi}} \tag{16}$$

Indeed, in percolation theory a power law distribution of particles numbers per cluster is realized close to the percolation threshold $P_s \sim s^{-\tau}$, with exponent $\tau = 1 + d/d_f$ (Stauffer and Aharony, 1994). Substitution of the cluster size $\xi \sim s^{d_f}$ then gives for the distribution of cluster sizes $P_\xi \sim \xi^{-\tau/d_f}$. For $d = 3$ the fractal dimension is $d_f = 2.5$ yielding $\tau = 2.2$ and $\tau/d_f = 0.9$. The Huber-Vilgis approach of hydrodynamic amplification (Huber and Vilgis, 1999) connects the cluster size ξ with the amplification factor X of strongly interpenetrating clusters, $X \sim \xi^{d_w - d_f}$ with $d_w = 3.8$ being the anomalous diffusion exponent of the percolated system. For the amplification factor distribution $P_X \sim X^{-\tau/(d_f(d_w - d_f))}$ this delivers an exponent equal to 0.68. The amplification factor distribution $P_X(X)$ is fully defined by the slope χ and upper and lower borders $X_{\min}$ and $X_{\max}$. The lower border is set to 1

$$X_{\min} = 1$$

because, thinking of differently amplified domains, there should be regions within the elastomer which aren't amplified at all (e.g. because there is no filler present).

From Eq. (9) it is obvious that the energy density of the non-affine tube model diverges at $\bar{I}_1 = n$. Physically, this corresponds to fully stretched polymer chains. As we have replaced $\bar{I}_1$ by $X\bar{I}_1$ we have to solve

$$X_{\text{div}}\bar{I}_{1,\max} = n \rightarrow X_{\text{div}} = \frac{n}{\bar{I}_{1,\max}} \tag{17}$$

to get, at given $\bar{I}_{1,\max}$, the amplification factor at which the energy density diverges. The largest amplification factor present in the compound has to be below X_{div}. The function relating the maximum amplification factor $X_{\max}$ to the deformation history is chosen to be

$$X_{\max} = \max\left(X_{\min}, \frac{n}{\bar{I}_{1,\max} + \gamma}\right) < \max(X_{\min}, X_{\text{div}}) \tag{18}$$

where $\bar{I}_{1,\max}$ is the largest value of the first invariant within the deformation history. The free parameter γ determines the maximum amplification factor of the system before any deformation $X_{\max}(\bar{I}_{1,\max} = 0) = n/\gamma$. With this definition of $X_{\max}$ the material is always isotropic. Note that $X_{\max}$ immediately decreases when increasing maximum strain. Thus, there are no continuous damage effects implemented up to now. A relaxation mechanism for $X_{\max}$ is under investigation.Now we want to do the average of the amplified energy density according to the power law amplification factor distribution (Eq. (16)). This can be understood as a superposition of the stress response of differently amplified domains, as visualized in Fig. 3. Remember that $X_{\max} = X_{\max}(\bar{I}_{1,\max})$ is the quantity determining stress-softening via the breakdown and reorganization of highly amplified domains. Doing the average we obtain

$$W_X\left(\bar{I}_1, \bar{I}^*, X_{\max}\right) = \int_{X_{\min}}^{X_{\max}} \mathrm{d}X\, P_X(X) W\left(X\bar{I}_1, X\bar{I}^*\right) \tag{19}$$

The integration can be carried out in closed form and is discussed in Appendix A. Take into account, that the averaging by integration corresponds to a parallel connection of all domains. This is questionable, but data on macroscopic moduli of heterogeneous materials is scarce and a parallel connection is the easiest mathematical implementation. In previous works by Klüppel (Klüppel et al., 2005; Lorenz et al., 2012) an internal average $W_X \sim W(\langle X \rangle)$ was used to take the diversity of microscopic structure into account. Here, the average is external $W_X \sim \langle W(X) \rangle$ and thus allows the distinct effects (like upturn) of the most amplified domains to come to light. Altogether, the Mullins effect is implemented in the following way:

- Before any deformation, $X_{\max}(\bar{I}_{1,\max} = 0) = n/\gamma$ is large and the materials contains many domains of highly amplified rubber.
- Increasing the strain yields increasing invariants, resulting in the breakdown of the most amplified domains.
- The broken down domains reorganize less amplified. This is implemented naturally via the normalization of $P_X(X)$ to 1, resulting in equipartition of the broken down domains in the interval $[X_{\min}, X_{\max}]$.
- Subsequent cycles with $\bar{I}_1 < \bar{I}_{1,\max}$ don't change $X_{\max}$ anymore.

2.3. Elastic stress

The elastic component of first Piola-Kirchhoff stress is calculated as

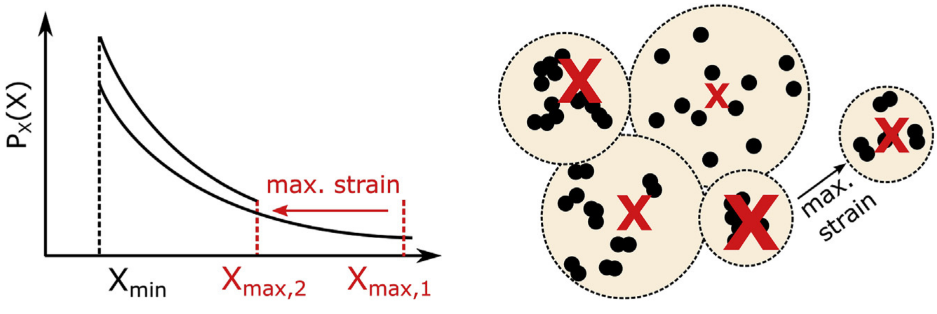

(a) (b)

Fig. 3. (a) Amplification factor distribution $P_X(X)$ for different upper borders. Lowering the upper border increases the average height of the distribution. (b) Visualization of the inhomogeneous distribution of amplification factors (red X), depending on local filler structure (black particles). By increasing load, highly constrained domains break down and reorganize less amplified. (For interpretation of the references to colour in this figure legend, the reader is referred to the web version of this article.)

$$\boldsymbol{P}_{\text{el}} = J\boldsymbol{\sigma}_{\text{el}}\boldsymbol{F}^{-T} \tag{20}$$

with $J = \sqrt{\det(\boldsymbol{B})}$. The left Cauchy-Green Tensor is defined as $\boldsymbol{B} = \boldsymbol{F}^T\boldsymbol{F}$. The deformation gradient $(\boldsymbol{F})_{ij} = \mathrm{d}x_i/\mathrm{d}X_j$ is a measure for the change of the original coordinates X_j to new coordinates x_i due to deformation (Holzapfel, 2000). The elastic Cauchy stress is calculated according to the formula

$$(\boldsymbol{\sigma}_{\text{el}})_{ij} = \sum_{n=1}^{3} \frac{\lambda_n}{\lambda_1\lambda_2\lambda_3}\frac{\partial W_X}{\partial \lambda_n}\mathbf{b}_i^{(n)} \otimes \mathbf{b}_j^{(n)} \tag{21}$$

where $\mathbf{b}^{(n)}$ are the eigenvectors of the left Cauchy-Green Tensor $\boldsymbol{B}$ and W_X is given by Eq. (19).

The principal strains for the three most simple deformation states are

$$\begin{aligned} &\text{Uniaxial}: \quad \lambda_1 = \lambda \quad \lambda_2 = 1\big/\sqrt{\lambda} \quad \lambda_3 = 1\big/\sqrt{\lambda} \\ &\text{Pure Shear}: \quad \lambda_1 = \lambda \quad \lambda_2 = 1 \quad \lambda_3 = 1/\lambda \\ &\text{Equibiaxial}: \quad \lambda_1 = \lambda \quad \lambda_2 = \lambda \quad \lambda_3 = 1\big/\lambda^2 \end{aligned} \tag{22}$$

In these cases the vectors $\mathbf{b}^{(n)}$ represent the cartesian coordinate system and the material is assumed to be incompressible.

2.4. Hysteresis and set stress

Besides Mullins effect, pronounced hysteresis and set stress are properties characteristic for filled rubbers. Both phenomena have the same origin and shall be modeled by one simple mechanism in the following. It is assumed, that polymer-filler structures inside the rubber are successively breaking down on average at a certain force and immediately rebind at zero stress. This is visualized in Fig. 4. When increasing strain this mechanism generates an additional force component, thus increasing the total force. On the way back it decreases the total force, generating hysteresis. Set stress is created by the remaining stressed structures at zero strain. At this point it is worth mentioning, that the rebinding process is assumed to be reorganization on a microscopic scale, while the breakdown and reorganization of domains as described in Section 2.2 takes place on much larger energy and time scales. Variables corresponding to a single energetically and spatially well defined structure shall be denoted by the superscript ~ from now on. The rebinding process can be formulated as

$$\tilde{f}_{\text{hys}} = f_{\text{el}}(\varepsilon) - \sum_j \theta\left(f_{\text{el}} - f_{\text{el},j}\right)\left[f_{\text{el},j} - f_{\text{el},j-1}\right] \tag{23}$$

where $f_{\text{el},j}$ denotes the force imposed on the structure by the elastic rubber matrix at the j-th breaking point and $\theta(x)$ is the Heaviside step function. Take into account, that $\tilde{f}_{\text{hys}}$ becomes zero if $f_{\text{el}} = f_{\text{el},j}$ $\forall j$. Assuming that the rebinding occurs completely random, but on average at a critical stress of $\tilde{f}_c = \langle f_{\text{el},j} - f_{\text{el},j-1}\rangle_j$, the intervals between two rebinding events

$$\Delta_j = f_{\text{el},j} - f_{\text{el},j-1}$$

are distributed exponentially according to

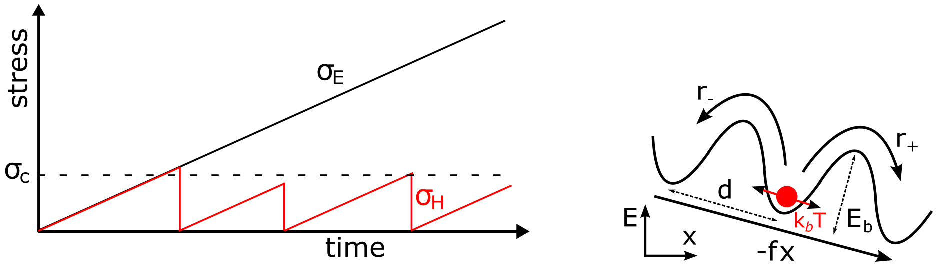

(a) (b)

Fig. 4. (a) Scheme of the proposed hysteresis mechanism: Rubber-filler structures are stretched up to a critical force (σ_c) at which they are on average breaking down. Then they immediately rebind and can be stretched again. The residual stress of these structures at zero strain creates set stress. (b) The rebinding process can be modeled as diffusion in a periodical potential driven by an external force f.

$$P_{\Delta}(\Delta) = \frac{1}{\tilde{f}_c} \mathrm{e}^{-\Delta/\tilde{f}_c} \tag{24}$$

This assumption is in accordance with the statistical nature of the rebinding events, see Fig. 4. By rewriting Eq. (23) in terms of Δ_j and doing the average according to P_{Δ} in Fourier space we can express Eq. (23) in a convolution-like manner

$$\tilde{f}_{\mathrm{hys}} = \int_{-\infty}^{\varsigma} \mathrm{d}\varsigma' \mathrm{e}^{-(\varsigma-\varsigma')/\tilde{f}_c} \frac{\mathrm{d}f_{\mathrm{el}}(\varsigma')}{\mathrm{d}\varsigma'} \quad \text{with} \quad \varsigma = \int |\mathrm{d}f_{\mathrm{el}}| = \int_{-\infty}^{t} \mathrm{d}t' \left| \dot{f}_{\mathrm{el}}(t') \right| \tag{25}$$

where we introduced the intrinsic time ς, which is monotonically increasing but stays constant when elastic stress is constant. The derivation is lengthy, but can be found in Appendix B. Eq. (25) can also be understood intuitively: Having an ensemble of randomly rebinding structures with same $\tilde{f}_c$, there will be structures which are highly stressed (large Δ) and slightly stressed (small Δ) present at the same time, weighted by Eq. (24). So on average, the response will be the force history, weighted by an exponential memory kernel which is a direct consequence of Eq. (24).

In reality there won't be just one critical force $\tilde{f}_c$ within the material, because of its geometric and energetic complexity. So the kernel isn't necessarily an exponential as in Eq. (25) but could be any function decreasing sufficiently fast resulting from an average over the single critical force $\tilde{f}_c$. In general, this can be expressed by introducing the kernel $k_{\langle \tilde{f}_c \rangle}(\varsigma)$.

$$f_{\mathrm{hys}} = \int_{-\infty}^{\varsigma} \mathrm{d}\varsigma' k_{\langle \tilde{f}_c \rangle}(\varsigma - \varsigma') \frac{\mathrm{d}f_{\mathrm{el}}(\varsigma')}{\mathrm{d}\varsigma'} \tag{26}$$

2.4.1. *Memory Kernel - averaging over microscopic structure*

Now we assume, that there is a typical energy scale E_b (e.g. a monomer-filler or filler-filler bond energy) which has to be overcome to break a rubber-filler structure. This energy has to be equal to the work done on the structure. Introducing the critical stress $\tilde{\sigma}_c = \tilde{f}_c/\tilde{A}$ we get:

$$E_b = \tilde{f}_c \tilde{d} = \tilde{\sigma}_c \tilde{A} \tilde{d} = \tilde{\sigma}_c \tilde{V} \rightarrow \tilde{\sigma}_c = \frac{E_b}{\tilde{V}}$$

where $\tilde{A}$ represents the molecular cross section, $\tilde{d}$ the force-induced displacement and $\tilde{V}$ the excited volume of the structure. We choose an exponential distribution of the excitation volumes with average volume V to ensure a converging kernel. The energy barrier E_b is assumed to have a characteristic constant value, which can be considered as the average of a peaked distribution. Integrating over the exponential (single critical stress) kernel results in a power-law kernel

$$k_{\langle \tilde{f}_c \rangle}(\varsigma) = \int_0^{\infty} \mathrm{d}\tilde{V} \frac{1}{V} \mathrm{e}^{-\frac{\tilde{V}}{V}} \mathrm{e}^{-\varsigma \frac{\tilde{V}}{E_b}} = \frac{1}{V} \int_0^{\infty} \mathrm{d}\tilde{V} \mathrm{e}^{-\tilde{V}\left(\frac{\varsigma}{E_b} + \frac{1}{V}\right)} = \frac{1}{1 + \frac{\varsigma V}{E_b}} = \frac{1}{1 + \frac{\varsigma}{\sigma_c}}$$

where we introduced the average critical stress $\sigma_c = \frac{V}{E_b}$. Finally, the hysteretic part of the stress can be expressed as

$$f_{\mathrm{hys}} = \int_{-\infty}^{\varsigma} \mathrm{d}\varsigma' \frac{1}{1 + \frac{\varsigma - \varsigma'}{\sigma_c}} \frac{\mathrm{d}f_{\mathrm{el}}(\varsigma')}{\mathrm{d}\varsigma'} \quad \text{with} \quad \varsigma = \int |\mathrm{d}f_{\mathrm{el}}| = \int_{-\infty}^{t} \mathrm{d}t' \left| \dot{f}_{\mathrm{el}}(t') \right| \tag{27}$$

Up to here it remains unclear which continuum mechanical stress measure corresponds to f_{el}. The first Piola Kirchhoff stress is calculated with respect to the reference cross section, thus being similar to a force. Additionally, the physical idea is based on reforming entities, such that the force affecting an entity should not depend on the strain dependence of its cross section. It is better understood as an ensemble of springs rather than a continuum. For these reasons, we identify f_{el} with a scalar measure of the first Piola Kirchhoff stress

$$f_{\mathrm{el}} = P_{\mathrm{el}} \tag{28}$$

2.4.2. *Temperature- and rate dependency*

We can imagine the breaking and rebinding mechanism as a stress-induced hopping over a (in first approximation periodical) potential barrier, as visualized in Fig. 4b. The crossing of the potential barrier E_b is driven by an external force f. If no force is present, there should be the same amount of un- and rebinding events. According to Kramer the hopping rate can be approximated as (Hänggi et al., 1990)

$$r_{\pm} = \frac{D}{2\pi k_B T}\sqrt{|U''(a)||U''(b)|}\mathrm{e}^{-\frac{E_b \mp fd}{k_B T}}$$

with diffusion constant D and second spatial derivatives of the potential U in the minimum $x = a$ and maximum $x = b$. E_b is the barrier height and d the average distance between two minima. The force f can be calculated once again as $f = \sigma_c A$, with the average molecular area of the structure A. Again we introduce the average excited volume

$$V = Ad$$

In fluids and polymers on length scales below the distance of network nodes the diffusion constant is $D \propto k_B T$, so we simplify the equation to

$$r_{\pm} = r_0 \mathrm{e}^{-\frac{E_b \mp \sigma_c V}{k_B T}}$$

with r_0 being the jump rate without any potential (athermal limit). The net jump rate in force direction is the difference of hopping forward and hopping backward rate

$$r = r_+ - r_- = r_0 \mathrm{e}^{-\frac{E_b}{k_B T}}\left(\mathrm{e}^{+\frac{\sigma_c V}{k_B T}} - \mathrm{e}^{-\frac{\sigma_c V}{k_B T}}\right) = 2r_0 \mathrm{e}^{-\frac{E_b}{k_B T}}\sinh\left(\frac{\sigma_c V}{k_B T}\right) \tag{29}$$

From Eq. (29) it is obvious, that an increase in the applied critical stress σ_c yields a larger escape rate. But σ_c was defined to be the average stress at which the hysteresis generating structures break down. So the formula should be interpreted the other way: σ_c has to be chosen such that the escape rate or escape timescale is the same as the rate of deformation or timescale of deformation, respectively. The timescale of deformation can be expressed as $r_d = aR_d$, where $R_d\left[\frac{\%}{\mathrm{s}}\right]$ is the deformation rate from the sample and $a\left[\frac{1}{\%}\right]$ is an unknown proportionality factor.

Given that, we can solve for σ_c

$$\sigma_c(R_d, T) = \frac{k_B T}{V}\sinh^{-1}\left(\frac{aR_d}{2r_0}\mathrm{e}^{\frac{E_b}{k_B T}}\right) \tag{30}$$

$$\approx \frac{1}{V}\left(E_b + k_B T \log(aR_d/r_0)\right) \tag{31}$$

where the approximation holds if the forces $\sigma_c V \gg k_B T$ are much larger than thermal energy. The logarithmic dependence already indicates that the hysteresis part is only weakly dependent on deformation rate R_d. Equation (30) relates set stress and hysteresis to temperature and rate via 3 parameters, V, E_b and a/r_0, which can be determined on one single sample with multihysteresis experiments at different rates and temperatures. We want to point out, that this mechanism relies on a constant-velocity v deformation on a microscopic scale, where the hopping timescale τ and the hopping distance d are related by $v = d/\tau = dr$. It doesn't capture the relaxation of a stressed non-equilibrium state into the energy minimum (force induced hopping in the time domain).

2.5. Total stress

The hysteretic stress is calculated using the elastic Piola Kirchhoff stress. With Eq. (27) we get

$$\left(\boldsymbol{P}_{\mathrm{hys}}\right)_{ij} = \int_{-\infty}^{\varsigma} \mathrm{d}\varsigma' \frac{1}{1 + \frac{\varsigma_{ij} - \varsigma'_{ij}}{\sigma_c}} \frac{\mathrm{d}(\boldsymbol{P}_{\mathrm{el}})_{ij}\left(\varsigma'_{ij}\right)}{\mathrm{d}\varsigma'} \quad \text{with} \quad \varsigma_{ij} = \int_{-\infty}^{t} \mathrm{d}t' \left|\left(\dot{\boldsymbol{P}}_{\mathrm{el}}\right)_{ij}(t')\right| \tag{32}$$

with $\boldsymbol{P}_{\mathrm{el}}$ defined by Eq. (20) and Eq. (21). The total stress is the weighted sum of both contributions

$$\boldsymbol{P} = (1 - \phi)\boldsymbol{P}_{\mathrm{el}} + \phi \boldsymbol{P}_{\mathrm{hys}} \tag{33}$$

ϕ is a fitting parameter, which should be proportional to the true filler volume fraction φ. It measures the fraction of the composite material responsible for elastic or hysteretic response. An example is shown in Fig. 5. Due to the convolution in Eq. (32) the model is not coaxial.

2.6. Energy dissipation

Energy dissipation can be calculated straightforward at every given point in stress-strain history. As the structure breaking is driven by the external force, the breaking energy has to be equal to the mechanical work applied to the hysteretic part. In fact, this is not entirely true but a good approximation: From the averaging done to Eq. (27) it is clear, that some of the structures are assumed to have breaking stresses larger than the applied stress. These structures contribute elastically. Tt can be calculated using the contraction of the dissipative component of the first Piola-Kirchhoff stress $\boldsymbol{P}_{\mathrm{hys}}$ and the deformation gradient $\boldsymbol{F}$ (Holzapfel, 2000)

$$\mathrm{d}W_{\mathrm{hys}} = \left(\boldsymbol{P}_{\mathrm{hys}}\right)_{ij}\mathrm{d}\boldsymbol{F}_{ji} = \left(J\boldsymbol{F}^{-1}\boldsymbol{\sigma}_{\mathrm{hys}}\right)_{ij}\mathrm{d}\boldsymbol{F}_{ji} \tag{34}$$

The other dissipative component is a consequence of the Mullins-effect. The energy lost by breaking the fraction of highly stressed polymer-filler domains in the amplification factor range $[X_{\max} - \mathrm{d}X_{\max}, X_{\max}]$ is, up to first order

$$\mathrm{d}W_{\mathrm{mul}} = -\int_{X_{\max}-\mathrm{d}X_{\max}}^{X_{\max}} \mathrm{d}X' P(X') W\left(X'\bar{I}_1, X'\bar{I}^*\right) = -P(X_{\max}) W\left(X_{\max}\bar{I}_1, X_{\max}\bar{I}^*\right)\mathrm{d}X_{\max} \tag{35}$$

Using Eq. (18) we can express $\mathrm{d}X_{\max}$ in terms of the change of the maximum of the first invariant, which can be directly related to the strain tensor, so we get

$$\mathrm{d}W_{\mathrm{mul}} = P(X_{\max}) W\left(X_{\max}\bar{I}_1, X_{\max}\bar{I}^*\right) \frac{n}{\left(\gamma + \bar{I}_1\right)^2}\mathrm{d}\bar{I}_{1,\max} \tag{36}$$

The total dissipated energy is the sum of both contributions

$$\mathrm{d}W_{\mathrm{diss}} = \mathrm{d}W_{\mathrm{hys}} + \mathrm{d}W_{\mathrm{mul}} \tag{37}$$

An example is presented in Fig. 6. There, the dissipated energy is compared to the stored energy corresponding to the work integral $W_{\mathrm{mech}} = \int_0^t \mathrm{d}t'\sigma(t')\dot{\lambda}(t')$ which is equal to the dissipated energy at the closure of each cycle. Take into account, that it looks like there is energy production at the turning points of each cycle. This is due to the energy stored in robust structures,

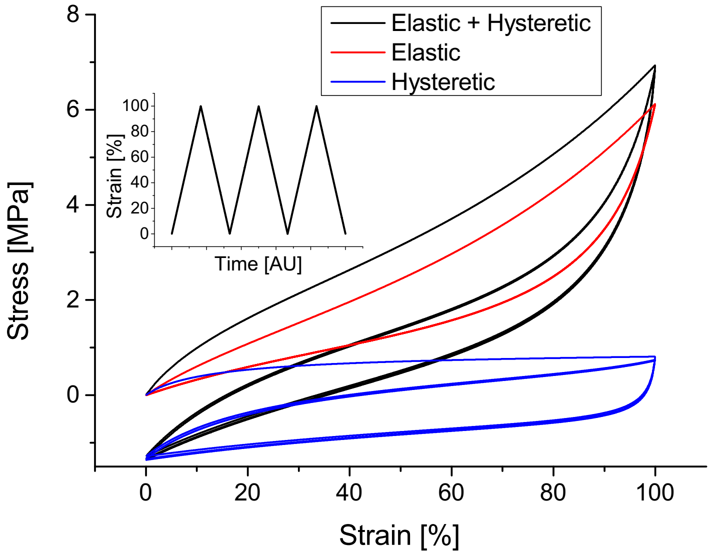

Fig. 5. Example with arbitrary model parameters. The elastic part (red) shows stress softening and stays on the same curve after the first cycle. The hysteretic part (blue) exhibits a stress-offset generating set stress. (For interpretation of the references to colour in this figure legend, the reader is referred to the web version of this article.)

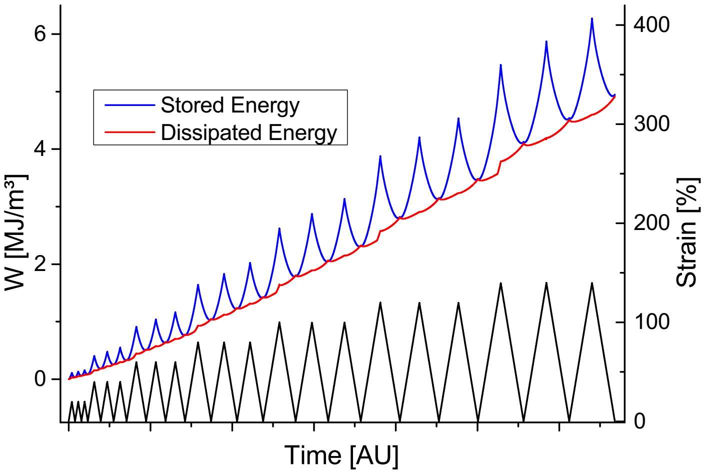

Fig. 6. Stored (blue) and dissipated (red) energy of material P/CB (see Fig. 11) according to Eq. (37) for the shown strain protocol. As expected stored energy and dissipated energy coincide at the closure of each cycle. (For interpretation of the references to colour in this figure legend, the reader is referred to the web version of this article.)

which haven't been broken within the cycle and are naturally included by spacial- and temporal averages over the primitive (exponential) memory kernel given in Eq. (25). Although this effect is rather small it prevented us from doing a rigorous thermodynamic validation via the Clausius-Duhem inequality, because this elastic contribution cannot clearly be separated from the hysteretic part.

2.7. Parameter overview

In total the basic model is defined by 7 fitting parameters, all of which have physical meaning.

- G_c is the crosslink modulus, a measure for the chemical and physical crosslink contribution to the total modulus. The crosslink modulus scales the upturn (high strain) part of the stress-strain curve.
- G_e measures the contribution of trapped (non resolvable) entanglements to the modulus. This contribution is visible at small strains.
- n is the distance, measured in segment lengths, between two trapped entanglements. It can be regarded as an inverse measure of network density. In the original tube model $n \approx 40$ for sufficiently crosslinked samples. Physically, the stress-strain curve diverges when chains become fully stretched, such that a small n yields an early diverging stress-strain curve.
- γ defines the all time maximum amplification factor via $X_{\max}(\bar{I}_{1,\max} = 0) = n/\gamma$.
- ϕ scales elastic and hysteretic stress contributions and thus the amount of hysteresis. In this theory all inelastic effects are attributed to the presence of filler, such that this quantity should scale with filler content.
- χ is the exponent of the amplification factor distribution. With rising filler content it should decrease, because more filler results in more constrained domains. A smaller exponent also yields a more pronounced Mullins effect.
- σ_c is the average critical stress at which rubber-filler structures break down and reform. It scales the amplitude dependency of the hysteretic stress component.

3. Experimental methods

3.1. Sample preparation

To identify model parameters and check the foundations of the model several model compounds were made. Carbon black (CB, grade N339) as well as silane (Si-266) coupled silica was used (Si, grade U7000) together with different rubbers, i. e. amorphous Ethylene Propylene Diene Rubber (EPDM, trade name Keltan 4450) and Styrene Butadiene Rubber (SBR). Sulfur (S) curing with accelerator CBS (*N*-Cyclohexyl-2-benzothiazole sulfenamide) and coactivator DPG (Diphenyl Guanidine) as well as Dicumyl Peroxide curing (DCP) in combination with Triallyl Isocyanurate (TAIC) was used. For aging protection *N*-Isopropyl-N′-phenyl-*p*-phenylenediamine (IPPD) or 2,2,4-Trimethyl-1,2-Dihydroquinoline (TMQ) was added to sulfur or peroxide compounds, respectively. The complete compounds in units of phr (parts per hundred rubber) are given in Table 1. Compounding was carried out using an internal mixer (Werner and Pfleiderer GK 1,5E) at 50 rpm. After a relaxation period of at least 16 h samples were vulcanized up to $t_{90\%}$ time (measured with a vulcameter) at temperatures of 150 °C (sample SBB), 160 °C (sample S/CB, S/Si) and 170 °C (sample P/CB).

Table 1
Composition of the investigated model compounds in phr (per hundred rubber).

Short name	Polymer		Filler		ZNO	St.Ac.	X-Link/Accel.			Anti-Age
	EPDM	S-SBR/BR	N339	U7000/Si-266			S	CBS	DPG	IPPD
S/CB	100		50		3	1	1.8	2.4	1.5	1.5
S/Si	100			50/5	3	1	1.8	2.4	1.5	1.5
SBB		85/15	60		3	1	1.7	2.5		1.5
							DCP	TAIC 70%		TMQ
P/CB	100		50				1.5	1.5		1.0

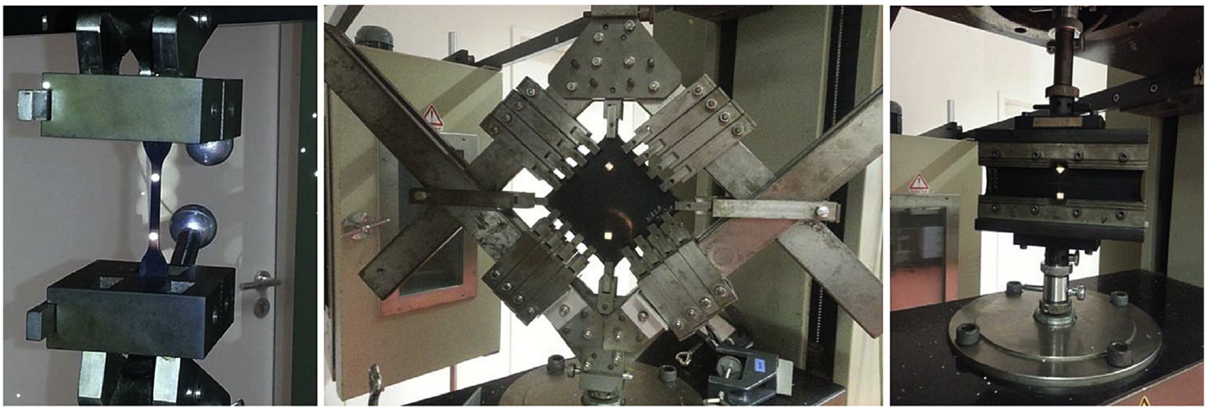
(a) (b) (c)

Fig. 7. Measurement setup for uniaxial (S2 sample) deformation (a), equibiaxial deformation (b) and pure shear (c). In the background of (b) and (c) the heat chamber used for measurement at elevated temperatures is visible.

Table 2
List of speeds and temperatures together with corresponding σ_c fitting results for all samples.

$R_c\left[\frac{\mathrm{mm}}{\mathrm{min}}\right]$	T [$^{\circ}$C]	σ_c [10^{-1} MPa]		
		S/CB	S/Si	P/CB
20	23	1.43	2.17	4.10
	50	1.10	1.29	2.20
	70	0.82	1.15	1.53
	110	0.65	0.89	0.93
100	23	1.52	2.69	4.86
	70	0.95	1.09	1.94
	90	0.74	1.16	1.58
	110	0.74	0.88	1.1
500	23	1.88	3.11	5.95
	50	1.56	2.11	3.67
	70	1.22	1.77	2.63
	110	0.88	1.67	1.63

3.2. *Measurement procedure*

Multihysteresis measurements were carried out using a Zwick 1445 universal testing facility. Multihysteresis means, that a sample is stretched/compressed to different strain levels several times (mostly 3 to 5 times) with a constant rate of displacement. Axially symmetric dumbbell samples (15 mm diameter) or flat S2 samples were used for uniaxial testing. S2, pure shear and equibiaxial samples and the measurement gear can be seen in Fig. 7. Strain was recorded with an optical system, tracking two reflecting points on the samples surface.

To check Eq. (30) uniaxial multihysteresis tests are performed from at least 0%–60% strain in a heat chamber after at least 1 h of heating time. Sometimes large strains couldn't be tested, because some samples collapsed. The three compounds were measured at rates and temperatures given in Table 2. Every data point was obtained using a fresh dumbbell-sample.

4. Results and discussion

4.1. Variation of materials and deformation modes

The model was fitted to Eq. (33) via an unconstrained Marquardt-Levenberg Algorithm. Except for resampling the data to 10,000 points to ensure monotonically increasing/decreasing strains no pretreatment was done. Dependent on the sample the data points defining a new maximum strain level (virgin curve) were excluded from fitting.

Several fits are presented in Fig. 11, showing very good agreement with experiment. The model isn't able to reproduce continuous damage effects, hence there is an almost immediate transition from the virgin curve (before stress softening) to a steady cycle. The fits of sulfur and peroxide cured EPDM stress-strain data, shown in Fig. 11a and b, were done on data obtained by measurements on dumbbell samples. At zero strain there is a residual set stress, which is underestimated by the fit (see inset). Except of this, fit quality at larger strains is very good. Fig. 11c was obtained using a dumbbell sample, too, but measured in stretching, compression and internal cycles (decreasing strain levels). Except of the additional stress softening in compression, all characteristics including internal cycles are captured well by the model. In Fig. 11d a flat S2-sample was used. In the graph this is visible, because the down cycle stops at zero stress to avoid a bending of the sample. The fit successfully reproduces the measurement up to 400% strain. The inset shows, that there are deviations at strains below 40%.

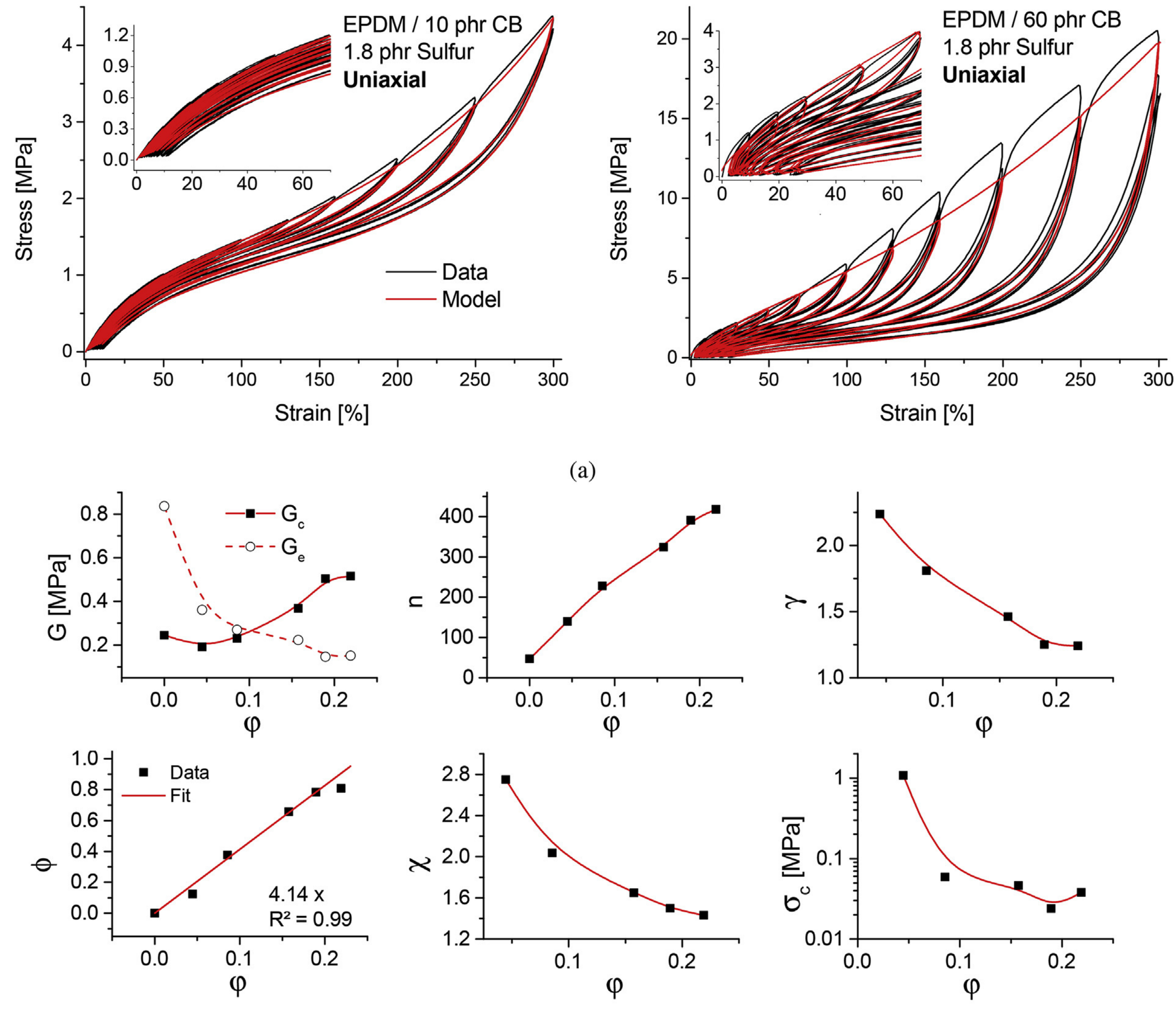

(a)

(b)

Fig. 8. (a) Fits of uniaxial stress-strain measurements of EPDM samples with 10 phr and 60 phr N339 carbon black. (b) Corresponding fit parameters of samples with 0, 10, 20, 40, 50 and 60 phr carbon black against the true filler volume fraction φ.

As described in Section 3.1 samples with 0, 10, 20, 40, 50 and 60 phr carbon black were prepared. All samples could be stretched up to at least 300%. Fitting was done up to 300% using the same set of starting parameters for all samples. For the unfilled rubber the non-affine tube model with $\beta = 1$ was used, see Eq. (9). In Fig. 8 fits for the 10 phr and 60 phr samples are shown, together with the fitting parameters for all samples. The crosslink-modulus G_c is increasing with increasing amount of carbon black. This is expected due to the additional crosslinking points provided by the fillers surface. Neglecting the unfilled sample, the entanglement modulus G_e is more robust with regard to carbon black concentration but decreasing with increasing filler load. Probably filler particles are preventing entanglements. The distance between network nods n as well as the weighting parameter ϕ are increasing almost linearly with filler content. The increase of the latter can be understood intuitively, because all hysteresis is attributed to the presence of filler. The linear increase of n will be discussed later. The distribution exponent χ is decreasing with filler content, which is reasonable because a greater amount of filler will create a wider distribution of amplification factors. The parameter γ determining the global maximum amplification factor via $X_{\max}(\bar{I}_{1,\max} = 0) = n/\gamma$ is decreasing with filler content, increasing the maximum amplification factor. Additionally, γ determines the occurrence of the upturn. It can be predicted by setting $\bar{I}_1 = \gamma$ (see Eq. (18)). For the sample with 10 phr carbon black this yields $\lambda \approx 2.1$, for the 60 phr filled sample $\lambda \approx 1.75$, which roughly fits the visual impression in Fig. 8a. The critical stress of breaking structures σ_c decreases with increasing filler load. An interpretation is difficult, because the exact molecular origin is not known. Probably hysteresis for slightly filled samples is due to softer rubbery structures while at larger filler volume fractions more brittle filler dominated structures are the main source of hysteresis.

Additionally, samples with varying amount of curatives were prepared. As before, an amorphous EPDM filled with 50 phr N339 carbon black with sulfur amount between 0.3 and 1.8 phr was used. Accelerators were scaled proportionally, see Table 1. In addition to uniaxial tests pure shear and equibiaxial measurements were carried out for each curing agent level. Fitting was done to all deformation modes at once (see Eq. (22)), thus generating one universal parameter set. Examples for weakly and strongly crosslinked compounds are shown in Fig. 9. The set of fitting parameters is rather robust against variation of initial parameters and the most physical set almost always gives the best fit. This may be due to the physical basis of the model, being a strong argument for the correctness of the assumptions. Fitting parameters for all compounds are presented in Fig. 10. The crosslink modulus is monotonically increasing with sulfur concentration. In contrast, the entanglement modulus is rather

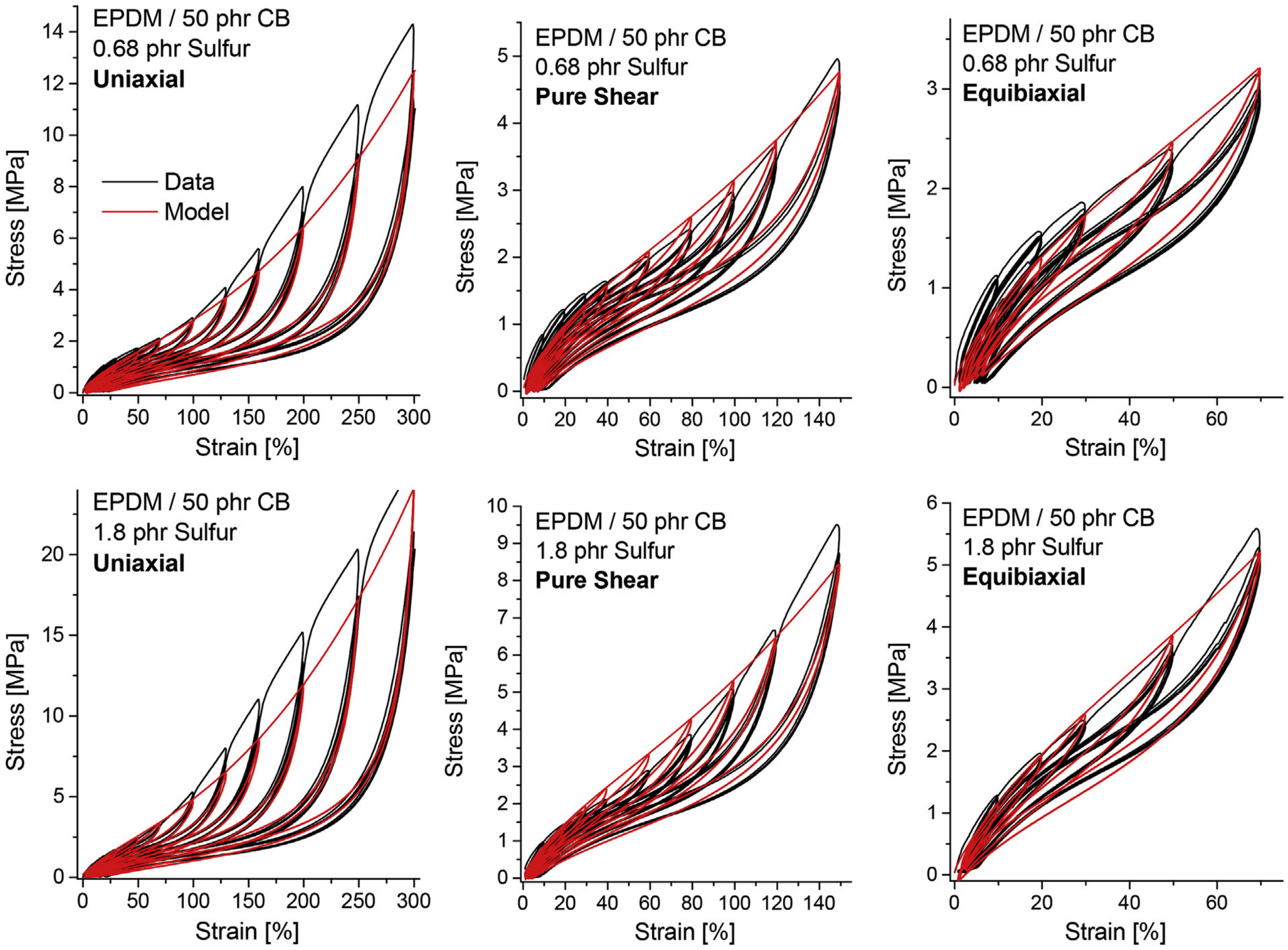

Fig. 9. Fit to several simple deformation modes for a weakly crosslinked sample (0.68 phr sulfur) and strongly crosslinked sample (1.8 phr sulfur).

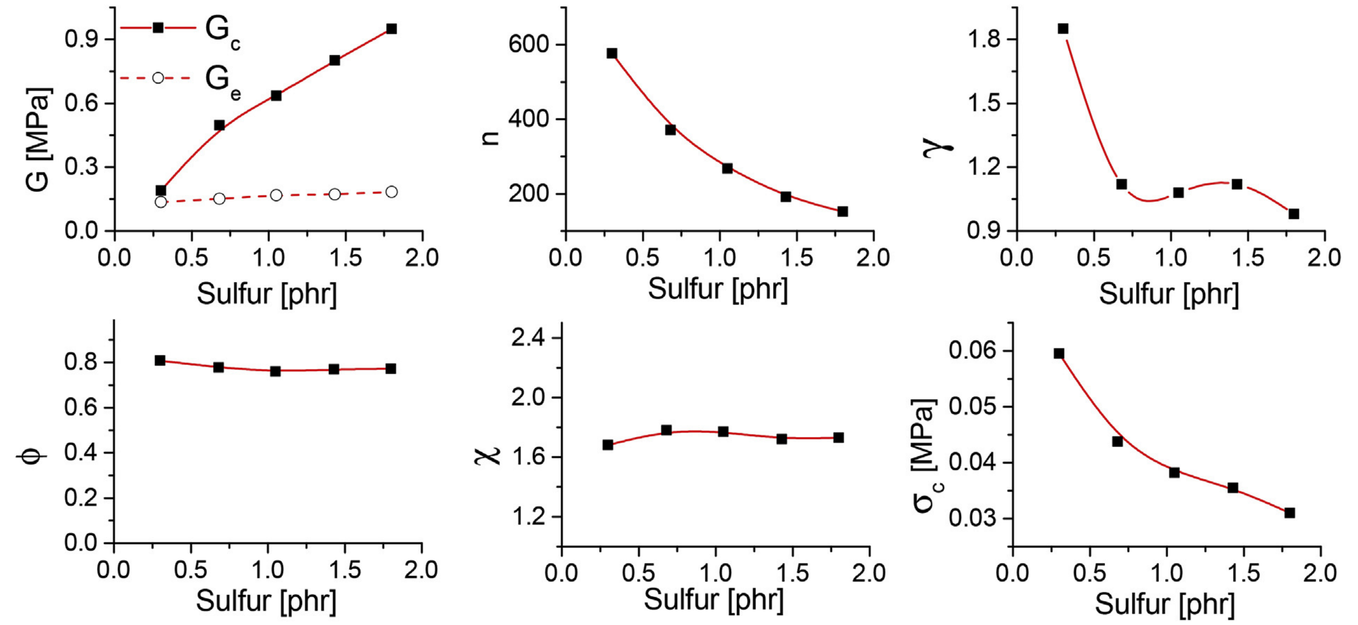

Fig. 10. Fitting parameters of parallel fitting to uniaxial, pure shear and equibiaxial measurements. The EPDM compound is filled with 50 phr N339 carbon black. Accelerators (DPG, CBS) are scaled proportionally.

constant. The distance between network nods n is monotonically decreasing, as can be expected from physics. ϕ is almost constant, matching the constant filler volume fraction. The exponent of the amplification distribution χ as well as γ are almost constant, too, probably for the same reason. Critical stress σ_c is decreasing, corresponding to looser, probably almost viscous structures at less dense networks. All parameters with an intuitive response to a denser network show the expected behavior.

In general, the parameter ϕ scaling the elastic and inelastic part is too large to identify it with a filler volume fraction. Nevertheless, it has been shown, that a proportionality of true filler volume fraction and ϕ can be found.

From Fig. 11 it can be seen, that fitting parameters crucially depend on fitting range and/or deformation mode (e. g. compression in 11c). In particular, the moduli are larger and n is smaller for low strain fits, e. g. $n \approx 15$ for Fig. 11a and b in contrast to $n \geq 100$ for large strain fits as given by Figs. 11 and 8b. This indicates, that simple uniaxial measurements to low strains probably don't provide enough information to fully describe the materials mechanical behavior. Fits of the non-affine tube model to unfilled sufficiently crosslinked rubbers result in $n \approx 20 \ldots 60$ (Syed et al., 2016; Klüppel et al., 2001) (depending on rubber type), being far lower than n obtained from large strain fits with the new model. So another interpretation may be appropriate: Looking at the energy density Eq. (9) it can be seen, that, from a mathematical point of view, amplification can be envisioned as modulus amplification and network condensing

$$G_c \to XG_c \quad G_e \to XG_e \quad n \to n/X$$

With this more general idea in mind the large fitted n is just the distance between entanglements of the least amplified domains. In fact, Ducrot et al. found that superimposing differently prestretched networks greatly enhances the polymers toughness and adds pronounced stress softening, comparable to the presence of filler (Ducrot et al., 2014). Their claim is, that the most prestretched (minority) subnetwork are limiting stress by successively breaking down with increasing load, whereas the lesser stretched (majority) networks prevent crack formation. This mechanism, although supposed here to be induced by filler, is formally implemented via the breakdown and reorganization of domains described by Eq. (18). Moreover, hysteresis can be found in unfilled polymers as well, e. g. crystallizing polymers (e. g. natural rubber) and thermoplastics (Srivastava et al., 2010). Especially in the latter case it can be attributed to a rearrangement of structure induced by external force. This is formally similar to the hysteresis mechanism proposed here.

The new interpretation is also more compatible with findings of Rault (Rault et al., 2006) who has shown by means of NMR, that microscopic strain amplification alone isn't able to explain the great increase in modulus (macroscopic amplification factor). He concludes, that additional filler induced crosslinks make up for the missing part of the modulus, which is implemented here as the increase in crosslink modulus G_c.

Wulf and Ihlemann (2015), (Wulf, 2016) presented simulations of a self organizing abstract rubber model, where stress softening and hysteresis arise naturally as an emergent phenomenon on the basis of a small set of physical interactions. The model presented here implements the same ideas in an analytically treatable manner, although a splitting of macroscopic reorganizations (breakdown and reorganization of domains) and microscopic reorganizations (breakdown and rebinding of smaller structures) had to be done.

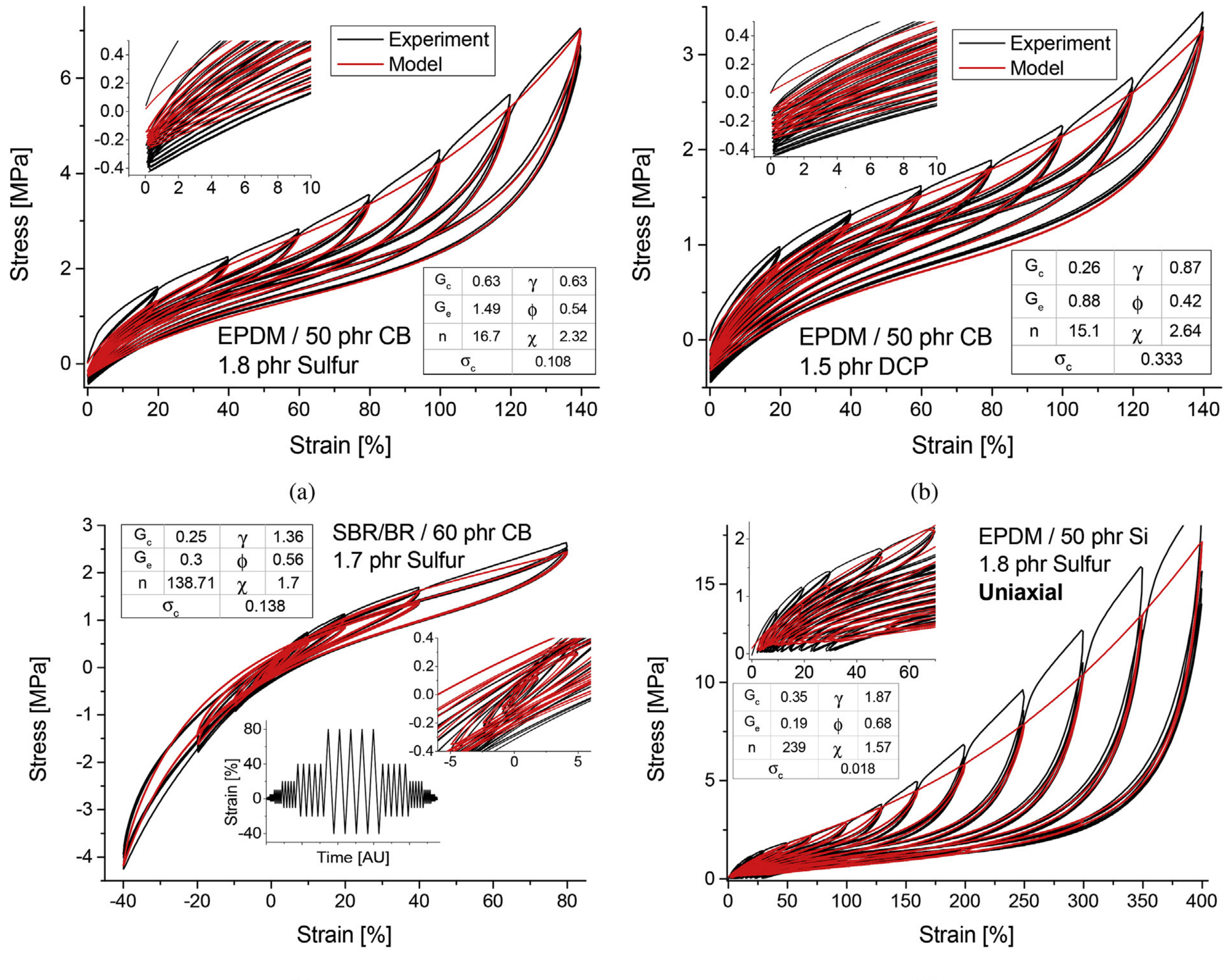

(a) (b)

(c) (d)

Fig. 11. Fit of the model to several uniaxial measurements. (a) Sulfur-cured EPDM/carbon black, measured on a dumbbell. (b) Peroxide-cured EPDM/carbon black, measured on a dumbbell. (c) Sulfur-cured SBR/BR/carbon black with compression and with internal cycles (decreasing strain levels), measured on a dumbbell. (d) Sulfur-cured EPDM/silica, measured on a S2-sample. Fitting parameters are shown in the insets. The influence of every parameter on the fitted curves is explained in Section 2.7.

4.2. Temperature and rate dependency

To check the validity of Eq. (30) several dumbbell samples of compound S/CB, S/Si and P/CB were investigated at different temperature and strain rates (see Table 2). Before stress-strain measurement, samples S/Si and P/CB were stored at 120 °C for 8 h in an air ventilated oven to ensure that every major chemical reaction occurring below 120 °C has taken place. Samples S/CB were stored at 130 °C for 20 h. From the theory described in Section 2.4.2 temperature and rate effects are implemented only via $\sigma_c(R_d, T)$, see Eq. (30). To check the validity of this idea, all parameters which are assumed to be independent on temperature and rate are fixed to isolate the effect of temperature and rate on σ_c. These are n, γ, χ, ϕ. Crosslink- and entanglement modulus G_c and G_e can be temperature dependent, so they are left free for fitting. The fixed parameters are determined by performing a completely free fit of data sets measured at 100 mm/min and temperatures of 23 °C, 70 °C and 110 °C and taking the average of the fit parameters. They are given in Table 3. Some samples showed significantly reduced elongation at break at elevated temperatures. For this reason all samples of type S/CB were fitted up to 60% strain, samples S/Si up to 80% and samples P/CB up to 140% strain. Thermal expansion was taken into account by using an thermal expansion coefficient of $5.5 \cdot 10^{-4} \frac{1}{K}$, which represents an average value for moderately filled elastomers (Mark, 2007).

In Fig. 12 a constrained fit with fixed parameters n, γ, χ and ϕ for sample P/CB is presented, showing very good agreement with data over a wide range of temperatures and deformation rates. It can be seen, that hysteresis decreases with increasing temperature and lower deformation rates. The free fitting parameters G_c, G_e and n are given in Fig. 13. The fit of Eq. (30) to σ_c obtained from fits to different rates and temperatures is shown for sample P/CB and S/CB in Fig. 13a. Detailed numerical data is

Table 3

Fitting results of Eq. (30) to data given in Table 2. Average G_e and line fit data of G_c from Fig. 13b as well as set of fixed parameters for all samples.

	S/CB	S/Si	P/CB
V [nm^3]	375 ± 77	182 ± 53	106 ± 26
$V^{1/3}$ [nm]	7.2 ± 0.5	5.7 ± 0.6	4.7 ± 0.4
E_b [kJ/mol]	104 ± 23	83 ± 26	118 ± 31
$\log(r_0/a)$[]	30 ± 6	25 ± 8	38 ± 10
R^2 []	0.920	0.804	0.896
G_e [MPa]	2.35	1.44	0.94
a [MPa]	−0.201	−0.236	−0.057
b [MPa/K]	0.0022	0.0018	0.0012
G_c [MPa]	$a+bT$		
ϕ[]	0.55	0.37	0.42
γ[]	0.41	0.87	1.26
χ[]	2.43	2.51	2.79
n []	7.92	10.8	14.4

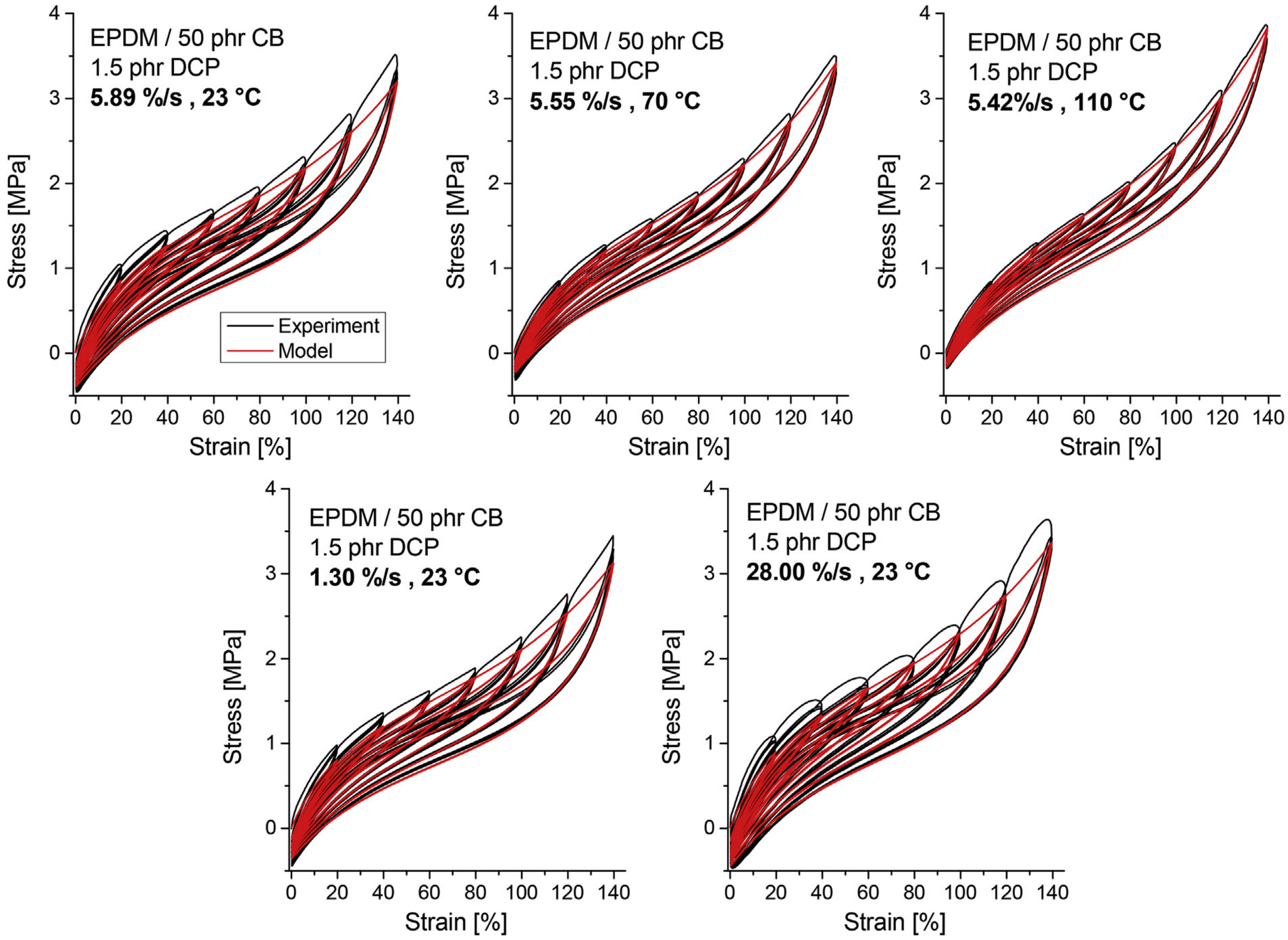

Fig. 12. Constrained fits of sample P/CB for different speeds and amplitudes. $\gamma = 1.26$, $\phi = 0.42$, $n = 14.4$ and $\chi = 2.79$ were kept fixed at the average values obtained from previous fits. Hysteresis decreases with increasing temperature and increases with larger deformation rate. Free fitting parameters are presented in Fig. 13.

given in Table 2. It turns out, that σ_c increases with strain rate and decreases with temperature. With $R^2 = 0.896$ for P/CB and $R^2 = 0.920$ for S/CB the model describes the experiment well, given the simplicity of the assumptions. The moduli are presented in Fig. 13b with G_e being rather temperature insensitive and G_c showing a significant trend towards larger values with increasing temperature. The increase of the cross-link modulus G_c is in line with the entropic character of rubber elasticity as given by Eq. (12). However, for the topological constraint modulus G_e, which should also scale linear with the absolute temperature T, a second effect showing the opposite trend plays a role, which delivers the apparent temperature

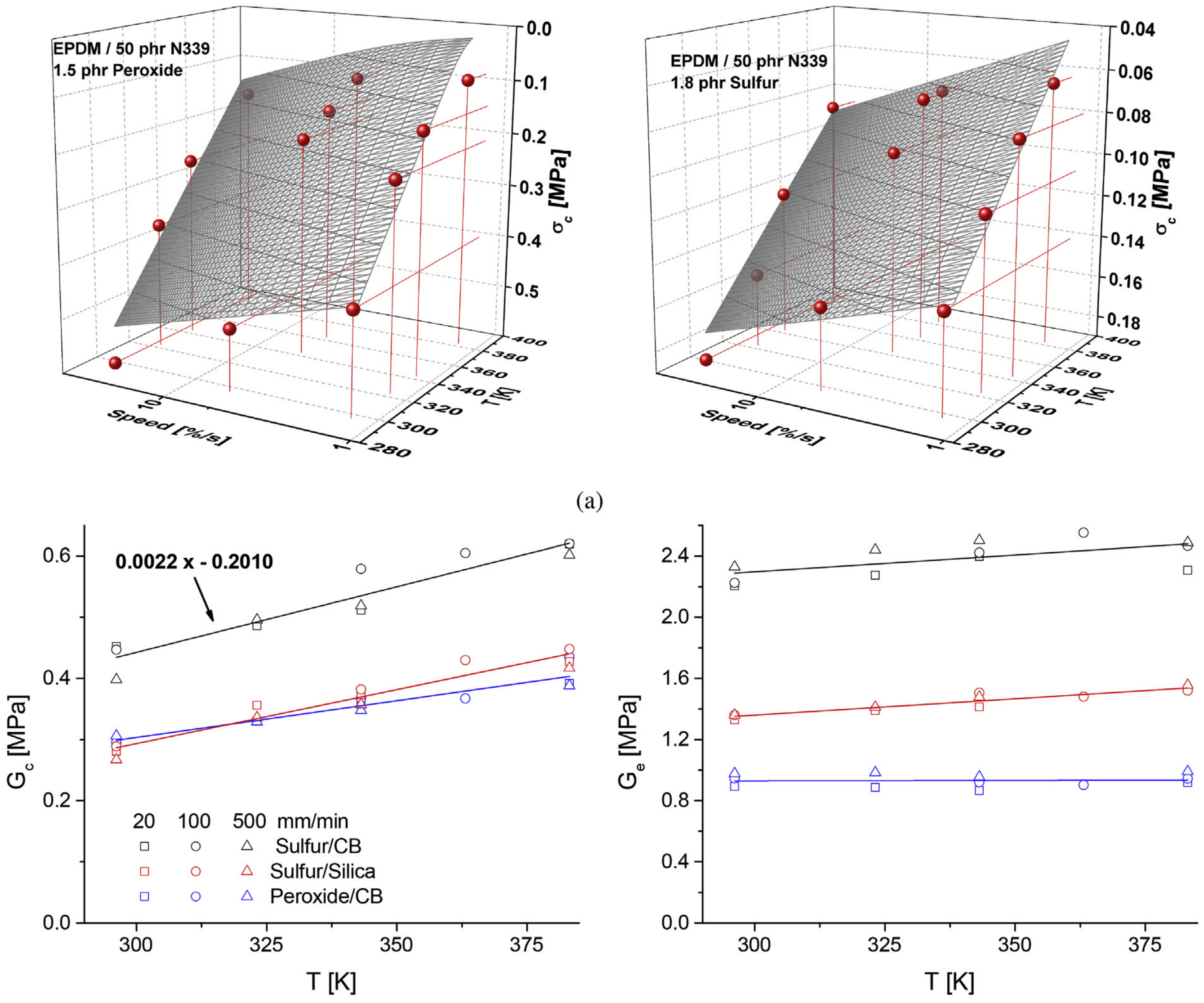

(a)

(b)

Fig. 13. (a) Fit of Eq. (30) to σ_c obtained from measurements at different rates and temperatures for sample P/CB (left) and S/CB (right). (b) Crosslink and entanglement modulus G_c and G_e of the same measurements. G_c is significantly dependent on temperature, whereas G_e is not. The dependence on rate (stacked symbols) is less pronounced and less systematic.

independency. This so-called constraint release effect is described by the parameter β in Eq. (12) and considers long-time relaxations of the network, which are more pronounced at high temperatures (Heinrich et al., 1988). It appears that this parameter, which can assumed to be close to $\beta = 1$ for sufficiently cross-linked networks, decreases slightly with increasing temperature delivering the observed temperature dependence of G_e. Additionally, there could be thermal effects acting on the amplifying filler network, which aren't modeled and thus are taken into account by a variation of the moduli.

The fitting results including the active volume V, the length scale $V^{1/3}$, the barrier height E_b and the logarithm of the modified stress-free jump rate $\log(r_0/a)$, which can be viewed as a measure for the mobility of the particles in question are given in Table 3. It turns out that the length scale is near 5 nm, which may be identified with the average size of filler-filler contacts. The barrier energy of all samples is around 100 kJ/mol, which is close to the adsorption energy of small hydrocarbon molecules. In particular the adsorption energy of 1-butene on carbon black is about 24 kJ/mol (Klüppel et al., 2016), such that the result hints toward rebinding events of small chain segments on the filler particles. Alternatively, it could be identified with the adhesion energy of filler-filler contacts. Note, that these contacts are mediated by strongly bound polymer chains at the filler surface forming some kind of immobilized polymer bridges between adjacent filler particles (Vilgis et al., 2009; Klüppel, 2003). It has to be mentioned, that the results are weakly dependent on fitting range and the choice of fixed parameters. Nevertheless it is remarkable, that all parameters with an obvious physical meaning have plausible values.

To show the ability to describe temperature- and rate dependent rubber behavior simulations of the response of sample S/CB are shown in Fig. 14. There, only the fixed set of parameters, the σ_c model function (Eq. (30)) and the linear approximation

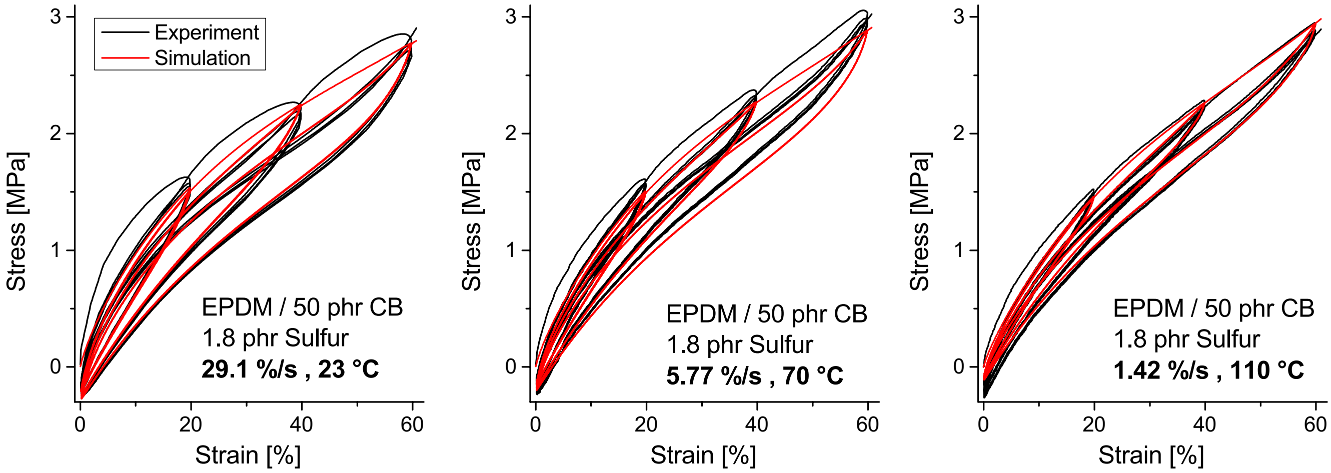

Fig. 14. Simulation of sample S/CB at selected rates and temperatures using the parameter set given in Table 3 i. e. the model function in Fig. 13a and the denoted linear fit of G_c shown in 13b.

to G_c was used. As for the other systems S/Si and P/CB overall agreement to experiment is very good. The deviations in the central 70 °C plot originate from an outlier in Fig. 13b.

5. Conclusion and outlook

A new model has been developed that accurately describes stress-strain data for various compounds and deformation states, even up to large strains/compressions and internal cycles. An energy functional including stress-softening is provided, which greatly simplifies calculations and allows to use the model for methods requiring stored energy. Hysteresis and set-stress are included via a rate- and temperature dependent rebinding mechanism. It is implemented using a convolution operation, which is inherently stable and performant. It's speed, accuracy and stability make the model suitable for FE-implementation.

The model has been derived using physical plausible assumptions about the materials microstructure. This approach guarantees the consistency of the equations and ensures, that fitting parameters show an expectable and physically reasonable behavior. This has been proven by successively increasing filler content or curing agent level while fixing all other quantities. The former yields a rising crosslink modulus, larger fraction of hysteretically active material and an overall more amplified material. The latter mainly results in an increase of crosslink modulus and a decrease of the distance between network nods while quantities describing the condition of the filler network stay constant.

Finally it was shown, that temperature and rate dependency can be modeled by a simple force driven diffusion process, interrelating both parameters on a basic physical level. Fitting results indicate, that hysteresis is generated on the nanometer scale at energy levels of around 100 kJ/mol. The results show, that upcoming modeling approaches should incorporate this close connection of rate (or time) and temperature rather than modeling both phenomena separately.

The fitting parameter determining the average spacing of network knots n turns out to be far larger than expected. This can be explained by assuming domains to be differently "crosslinked" in contrast to be differently amplified, which fits concepts explaining toughening and stress softening by the assumption of "sacrificing entities" (Ducrot et al., 2014). This is also in accordance with recent simulations viewing rubber behavior dominated by emergent reorganization effects rather than being explainable by averaging microscopic structure (Wulf and Ihlemann, 2015; Wulf, 2016).

It should be possible to generalize rate and temperature-dependency of hysteresis and set stress to a more general relaxation mechanism in the time domain formulated by differential equations also taking into account continuous damage effects. The foundations are already worked out and will be addressed in an upcoming publication. Additionally, anisotropic stress softening shall be included, which is a distinct feature of particle-reinforced elastomers (Machado et al., 2012). Mullins effect is known to be reversible at elevated temperatures (Diani et al., 2009). Since hysteresis was shown to be temperature sensitive as well, both phenomena probably can be modeled by the same physical process, but on different scales. Given that, description of the whole spectrum of rubber characteristics by an underlying universal mechanism should be possible.

Acknowledgement

We thank Rathan Ragunath (DIK e.V.) for experimental assistance and Dr. Hagen Lorenz for experimental data shown in Fig. 11c. The Arbeitsgemeinschaft industrieller Forschungsvereinigungen (AiF) grant 18079 BG is appreciated for financial support.

Appendix A. Energy density

Following Eq. (9)

$$W_X\left(\bar{I}_1,\bar{I}^*,X_{\max}\right)=\int_{X_{\min}}^{X_{\max}}\mathrm{d}X\,P_X(X)W\left(X\bar{I}_1,X\bar{I}^*\right)$$

$$=\frac{\chi-1}{X_{\min}^{1-\chi}-X_{\max}^{1-\chi}}\int_{X_{\min}}^{X_{\max}}\mathrm{d}X\,X^{-\chi}\left(\frac{G_c}{2}\left[\frac{(1-\frac{1}{n})X\bar{I}_1}{1-\frac{1}{n}X\bar{I}_1}+\log\left(1-\frac{1}{n}X\bar{I}_1\right)\right]+2G_eX\bar{I}^*(-\beta)\right) \tag{A.1}$$

$$=\frac{\chi-1}{X_{\min}^{1-\chi}-X_{\max}^{1-\chi}}(\mathcal{W}(X_{\max})-\mathcal{W}(X_{\min})) \tag{A.2}$$

Here the term before the integral is the normalization of the X-distribution function $P_X(X)$, $\mathcal{W}$ denotes the antiderivative of the integrand, which is given as

$$\mathcal{W}(X)=G_c\frac{X^{1-\chi}}{2(\chi-2)(\chi-1)^2}\Bigg[(\chi-2)(\chi(n-1)-n)+(\chi-2)\Bigg((\chi+n-\chi n)_2F_1\left(1,1-\chi,2-\chi,\frac{\bar{I}_1X}{n}\right)-(\chi-1)\log\Bigg(1 \\ -\frac{\bar{I}_1X}{n}\Bigg)\Bigg)\Bigg]+G_e\frac{2\bar{I}^*X^{2-\chi}}{2-\chi} \tag{A.3}$$

${}_2F_1(a,b,c,z)$ is a hypergeometric function, as defined in (Weisstein, 2016):

$${}_2F_1(a,b,c,z)=\frac{\Gamma(c)}{\Gamma(b)\Gamma(c-b)}\int_0^1\frac{t^{b-1}(1-t)^{c-b-1}}{(1-tz)^a}\mathrm{d}t \tag{A.4}$$

$$\text{with}\quad \mathrm{Re}(c)>\mathrm{Re}(b)>0\wedge|\arg(1-z)|<\pi$$

with the Gamma function $\Gamma(x)$. From parameter comparison of Eq. (A.3) and Eq. (A.4) it is easy to see, that

$$a=1\quad b=1-\chi\quad c=2-\chi\quad z=\frac{1}{n}X\bar{I}_1$$

For this parameter combination the definition Eq. (A.4) becomes

$${}_2F_1(1,1-\chi,2-\chi,z)=(1-\chi)\int_0^1\frac{t^{-\chi}}{1-tz}\mathrm{d}t$$

The derivative respective z can then be simplified by product integration

$$\frac{\mathrm{d}}{\mathrm{d}z}{}_2F_1(1,1-\chi,2-\chi,z)=(1-\chi)\int_0^1\frac{t^{1-\chi}}{(1-tz)^2}\mathrm{d}t=(1-\chi)\frac{1}{z(1-z)}-(1-\chi)\int_0^1\frac{1}{z(1-tz)}(1-\chi)t^{-\chi}\mathrm{d}t$$

$$=\frac{1-\chi}{z}\left(\frac{1}{1-z}-{}_2F_1(1,1-\chi,2-\chi,z)\right)$$

With this identity the integrand in Eq. (A.2) follows from Eq. (A.3) by differentiation.

Appendix B. Derivation of the exponential convolution from discrete rebinding events

We define the Fourier transform to be symmetric

$$\tilde{f}(\omega) = \mathcal{F}[f(t)](\omega) = \frac{1}{\sqrt{2\pi}} \int\limits_{-\infty}^{\infty} \mathrm{d}t\, f(t) \mathrm{e}^{i\omega t} \tag{B.1}$$

$$f(t) = \mathcal{F}^{-1}\left[\tilde{f}\right](t) = \frac{1}{\sqrt{2\pi}} \int\limits_{-\infty}^{\infty} \mathrm{d}\omega\, \tilde{f}(\omega) \mathrm{e}^{-i\omega t} \tag{B.2}$$

$$\mathcal{F}^{-1}\left[\tilde{f}\cdot\tilde{g}\right](t) = \frac{(f*g)(t)}{\sqrt{2\pi}} \tag{B.3}$$

where the latter equation is called the convolution theorem. For better readability, the ~ is omitted and fourier transforms are identified by the argument. We start off with a general analytical expression for a variable $\bar{x}(t)$, which is evolving as externally prescribed by $x(t)$, but is set to zero at coordinates $\{t_j\}$, where t shall denote a monotonincally increasing, time-like coordinate

$$\bar{x}(t) = x(t) + \sum_j \theta(t - t_j)\left[x(t_{j-1}) - x(t_j)\right] \tag{B.4}$$

with the step function $\theta(t{-}t_j)$. The most obvious example would be a spring, where the zero elongation position is shifted at $\{t_j\}$ such, that the stress/strain is zero at this point. It corresponds to the special case of Eq.(23) by setting $x(t) = t$.

This expression can be Fourier-transformed[1]

$$\bar{x}(\omega) = x(\omega) + \sum_j \frac{i}{\sqrt{2\pi}\omega} \mathrm{e}^{it_j\omega} \frac{1}{\sqrt{2\pi}} \int\limits_{-\infty}^{\infty} \mathrm{d}\omega' x(\omega')\left[\mathrm{e}^{-it_{j-1}\omega'} - \mathrm{e}^{-it_j\omega'}\right] \tag{B.5}$$

$$= x(\omega) + \frac{i}{2\pi\omega} \sum_j \int\limits_{-\infty}^{\infty} \mathrm{d}\omega' x(\omega')\left[\mathrm{e}^{it_j\omega - it_{j-1}\omega'} - \mathrm{e}^{it_j(\omega-\omega')}\right] \tag{B.6}$$

Next we assume, that the rebinding events occur completely random. When randomly placing N events on a rod with length $N\tau = t$, then the probability density of event-spacings Δ is given as

$$P(\Delta) = \frac{1}{\tau}\mathrm{e}^{-\Delta/\tau} \tag{B.7}$$

where τ is the average spacing between rebinding events.

Now we can easily construct the t_j from a collection of positive intervals $\{\Delta_j\}$

$$t_j = \mathrm{sgn}(t_j)\sum_{k=1}^{j}\Delta_k \tag{B.8}$$

where $t = 0$ can be set arbitrary. The goal is now to get an average expression of Eq. (B.6) in terms of over the intervals $\{\Delta_j\}$, like

$$\langle\bar{x}(\omega)\rangle_\Delta = x(\omega) + \frac{i}{2\pi\omega} \sum_j \int\limits_{-\infty}^{\infty} \mathrm{d}\omega' x(\omega')\left[\langle \mathrm{e}^{it_j\omega - it_{j-1}\omega'}\rangle_\Delta - \langle \mathrm{e}^{it_j(\omega-\omega')}\rangle_\Delta\right] \tag{B.9}$$

To do so, let's take a closer look at a single averaged exponential

$$\langle \mathrm{e}^{it_j\omega}\rangle_\Delta = \langle \exp\left(i\omega\,\mathrm{sgn}(t_j)\sum_{k=1}^{j}\Delta_k\right)\rangle_\Delta = \langle\prod_{k=1}^{j}\exp(i\omega\,\mathrm{sgn}(t_j)\Delta_k)\rangle_\Delta \tag{B.10}$$

---

[1] In fact, a $\delta(\omega)$ term coming from the Fourier transform of the step function is omitted here. It turns out to be zero after doing the average, as can easily be seen by analogous calculation.

$$= \prod_{k=1}^{j} \int_0^\infty \mathrm{d}\Delta_k P(\Delta_k) \exp\left(i\omega \operatorname{sgn}(t_j)\Delta_k\right) \tag{B.11}$$

$$= \left[\int_0^\infty \mathrm{d}\Delta \frac{1}{\tau} \exp\left(i\omega \operatorname{sgn}(t_j)\Delta - \frac{\Delta}{\tau}\right)\right]^j = \left[\frac{1}{1 - i\omega\tau \operatorname{sgn}(t_j)}\right]^j \tag{B.12}$$

The calculation is now straightforward, going on from Eq. (B.9). Using $t_{j-1} = t_j - \Delta_j$

$$\langle \overline{x}(\omega)\rangle_\Delta = x(\omega) + \frac{i}{2\pi\omega} \sum_j \int_{-\infty}^{\infty} \mathrm{d}\omega' x(\omega') \left[\langle \mathrm{e}^{it_j(\omega-\omega')}\rangle_\Delta \langle \mathrm{e}^{i\Delta_j\omega'}\rangle_\Delta - \langle \mathrm{e}^{it_j(\omega-\omega')}\rangle_\Delta\right] \tag{B.13}$$

$$= x(\omega) + \frac{i}{2\pi\omega} \sum_j \int_{-\infty}^{\infty} \mathrm{d}\omega' x(\omega h') \left[\left(\frac{1}{1 - i(\omega - \omega h')\tau \operatorname{sgn}(t_j)}\right)^j \left(\frac{1}{1 - i\omega'\tau}\right) - \right. \tag{B.14}$$

$$\left. \left(\frac{1}{1 - i(\omega - \omega')\tau \operatorname{sgn}(t_j)}\right)^j \right] \tag{B.15}$$

Let's now take a closer look at the expressions in the []-bracket. We start by noticing, that there are infinitely many rebinding events before and after $t = 0$, because we assume a stationary infinite process. Afterwards the geometric series $\sum_{n=0}^{N} a^n = \frac{1-a^N}{1-a}$ is used

$$\sum_j \left(\frac{1}{1 - i(\omega' - \omega)\tau \operatorname{sgn}(t_j)}\right)^j = \lim_{N\to\infty} \sum_{j=1}^{N} \Bigg[\tag{B.16}$$

$$= \lim_{N\to\infty} \frac{1}{i(\omega' - \omega)\tau} \left(\left(\frac{1}{1 - i(\omega' - \omega)\tau}\right)^{N-1} - \left(\frac{1}{1 + i(\omega' - \omega)\tau}\right)^{N-1}\right) \tag{B.17}$$

The two terms in the brackets just differ in the sign of the complex number. Hence, they can be rewritten in polar form, yielding

$$= \lim_{N\to\infty} \frac{2}{(\omega' - \omega)\tau\left(1 + ((\omega' - \omega)\tau)^2\right)^{\frac{N-1}{2}}} \sin((N-1)\arctan((\omega' - \omega)\tau)) \tag{B.18}$$

The prefactor has the shape $\lim\limits_{N\to\infty} \frac{1}{x(1+x^2)^N}$, becoming zero for every $x \neq 0$. Therefore, the expression can be expanded up to linear order in $(\omega' - \omega)\tau$. Using $\arctan(x) \approx x$ this exactly results in the sinc-representation of the Dirac δ-distribution

$$= \lim_{N\to\infty} \frac{2}{(\omega' - \omega)\tau} \sin(N(\omega' - \omega)\tau) \tag{B.19}$$

$$= 2\pi\delta((\omega' - \omega)\tau) = \frac{2\pi}{\tau}\delta(\omega' - \omega) \tag{B.20}$$

The relation derived above can now be used to greatly simplify Eq. (B.15). We end up with the surprisingly simple result

$$\langle \overline{x}(\omega)\rangle_\Delta = x(\omega) + \frac{i}{2\pi\omega} x(\omega) \left(\frac{2\pi}{\tau} \frac{1}{1 - i\omega\tau} - \frac{2\pi}{\tau}\right) \tag{B.21}$$

$$= \frac{i\omega\tau}{i\omega\tau - 1} x(\omega) \tag{B.22}$$

which is a product of a Maxwell-like element with the original data. In time-space, the product can be translated into a convolution

$$\langle\overline{x}(\omega)\rangle_{\Delta}=\left(\frac{\tau}{1-i\omega\tau}\right)\cdot(-i\omega x(\omega))\Rightarrow\langle\overline{x}(t)\rangle_{\Delta}=\frac{\left[\sqrt{2\pi}\mathrm{e}^{-t/\tau}\theta(t)*\dot{x}\right](t)}{\sqrt{2\pi}}=\int\limits_{-\infty}^{t}\mathrm{d}t'\mathrm{e}^{-\frac{t-t'}{\tau}}\frac{\mathrm{d}x}{\mathrm{d}t'} \tag{B.23}$$

being exactly the generalization of Eq. (25).

References

Amin, A., Lion, A., Sekita, S., Okui, Y., 2006. Nonlinear dependence of viscosity in modeling the rate-dependent response of natural and high damping rubbers in compression and shear: experimental identification and numerical verification. Int. J. Plast. 22 (9), 1610–1657.

Behnke, R., Dal, H., Kaliske, M., 2011. An extended tube model for thermo-viscoelasticity of rubberlike materials: theory and numerical implementation. In: Constitutive Models for Rubber VII. Taylor & Francis Group London, pp. 87–92.

Bergstrom, J., Boyce, M.C., 1999. Mechanical behavior of particle filled elastomers. Rubber Chem. Technol. 72 (4), 633–656.

Bueche, F., 1960. Molecular basis for the mullins effect. J. Appl. Polym. Sci. 4 (10), 107–114.

Dannenberg, E., 1975. The effects of surface chemical interactions on the properties of filler-reinforced rubbers. Rubber Chem. Technol. 48 (3), 410–444.

Dargazany, R., Itskov, M., 2013. Constitutive modeling of the mullins effect and cyclic stress softening in filled elastomers. Phys. Rev. E 88 (1), 012602.

Diani, J., Fayolle, B., Gilormini, P., 2009. A review on the mullins effect. Eur. Polym. J. 45 (3), 601–612.

Domurath, J., Saphiannikova, M., Gilles, A., Heinrich, G., 2012. Modelling of stress and strain amplification effects in filled polymer melts. J. Newt. Fluid Mech. 171, 8–16.

Ducrot, E., Chen, Y., Bulters, M., Sijbesma, R.P., Creton, C., 2014. Toughening elastomers with sacrificial bonds and watching them break. Science 344 (6180), 186–189.

Einstein, A., 1906. Eine neue Bestimmung der Moleküldimensionen. Ann. Phys. 324, 289–306.

Fleck, F., Froltsov, V., Klüppel, M., 2014. Polymer-filler interphase dynamics and reinforcement of elastomer nanocomposites. Soft Mater. 12 (Suppl. 1), S121–S134.

Freund, M., Lorenz, H., Juhre, D., Ihlemann, J., Klüppel, M., 2011. Finite element implementation of a microstructure-based model for filled elastomers. Int. J. Plast. 27 (6), 902–919.

Geberth, E., 2013. Analyse der Füllstoffkopplung von gefüllten Elastomeren unter mechanischer Belastung. Ph.D. thesis. Wilhelm Leibniz Universität Hannover.

Geberth, E., Klüppel, M., 2012. Effect of carbon black deactivation on the mechanical and electrical properties of elastomers. Macromol. Mater. Eng. 297 (9), 914–922.

Govindjee, S., Simo, J., 1991. A micro-mechanically based continuum damage model for carbon black-filled rubbers incorporating mullins' effect. J. Mech. Phys. Solids 39 (1), 87–112.

Govindjee, S., Simo, J., 1992. Transition from micro-mechanics to computationally efficient phenomenology: carbon black filled rubbers incorporating mullins' effect. J. Mech. Phys. Solids 40 (1), 213–233.

Hamed, G.R., Hatfield, S., 1989. On the role of bound rubber in carbon-black reinforcement. Rubber Chem. Technol. 62 (1), 143–156.

Hänggi, P., Talkner, P., Borkovec, M., 1990. Reaction-rate theory: fifty years after kramers. Rev. Mod. Phys. 62 (2), 251.

Heinrich, G., Kaliske, M., 1997. Theoretical and numerical formulation of a molecular based constitutive tube-model of rubber elasticity. Comput. Theor. Polym. Sci. 7 (3/4), 227–241.

Heinrich, G., Straube, E., Helmis, G., 1988. Rubber elasticity of polymer networks: Theories. In: Polymer Physics. Springer, pp. 33–87.

Holzapfel, G.A., 2000. Nonlinear Solid Mechanics, p. 24.

Huber, G., Vilgis, T.A., 1999. Universal properties of filled rubbers: mechanisms for reinforcement on different length scales. Kautsch. Gummi Kunstst. 52 (2), 102–107.

Klüppel, M., 2003. The role of disorder in filler reinforcement of elastomers on various length scales. In: Filler-reinforced Elastomers/Scanning Force Microscopy. Springer, pp. 1–86.

Klüppel, M., Heinrich, G., 1994. Network structure and mechanical properties of sulfur-cured rubbers. Macromolecules 27 (13), 3596–3603.

Klüppel, M., Meier, J., Dämgen, M., 2005. Modeling of stress softening and filler induced hysteresis of elastomer materials. In: Constitutive Models for Rubber, vol. 4. Balkema, p. 171.

Klüppel, M., Menge, H., Schmidt, H., Schneider, H., Schuster, R., 2001. Influence of preparation conditions on network parameters of sulfur-cured natural rubber. Macromolecules 34 (23), 8107–8116.

Klüppel, M., Möwes, M., Lang, A., Plagge, J., Wunde, M., Fleck, F., Karl, C., 2016. Characterization and Application of Graphene Nanoplatelets in Elastomers. Springer Berlin Heidelberg, Berlin, Heidelberg, pp. 1–42.

Klüppel, M., Schramm, J., 2000. A generalized tube model of rubber elasticity and stress softening of filler reinforced elastomer systems. Macromol. Theory Simul. 9 (9), 742–754.

Kraus, G., 1984. Mechanical losses in carbon-black-filled rubbers. J. Appl. Polym. Sci. Appl. Polym. Symp. 39, 75–92.

Lorenz, H., Klüppel, M., 2012. Microstructure-based modelling of arbitrary deformation histories of filler-reinforced elastomers. J. Mech. Phys. Solids 60 (11), 1842–1861.

Lorenz, H., Klüppel, M., Heinrich, G., 2012. Microstructure-based modelling and FE implementation of filler-induced stress softening and hysteresis of reinforced rubbers. ZAMM 92 (8), 608–631.

Lorenz, H., Meier, J., Klüppel, M., 2010. Micromechanics of internal friction of filler reinforced elastomers. LNACM (51).

Machado, G., Chagnon, G., Favier, D., 2012. Induced anisotropy by the mullins effect in filled silicone rubber. Mech. Mater. 50, 70–80.

Marckmann, G., Verron, E., 2006. Comparison of hyperelastic models for rubber-like materials. Rubber Chem. Technol. 79 (5), 835–858.

Mark, J.E., 2007. Physical Properties of Polymers Handbook, vol. 1076. Springer.

Medalia, A., 1978. Effect of carbon black on dynamic properties of rubber vulcanizates. Rubber Chem. Technol. 51 (3), 437–523.

Mullins, L., Tobin, N., 1965. Stress softening in rubber vulcanizates. part i. use of a strain amplification factor to describe the elastic behavior of filler-reinforced vulcanized rubber. J. Appl. Polym. Sci. 9 (9), 2993–3009.

Payne, A., 1962. The dynamic properties of carbon black-loaded natural rubber vulcanizates. part i. J. Appl. Polym. Sci. 6 (19), 57–63.

Payne, A., Kraus, G., 1965. Reinforcement of Elastomers. Interscience, New York, p. 69.

Plagge, J., Klüppel, M., 2015. Application of a micro-structure based model to thermally aged filler reinforced elastomer compounds. In: Constitutive Models for Rubber IX, p. 29.

Raghunath, R., Juhre, D., Klüppel, M., 2016. A physically motivated model for filled elastomers including strain rate and amplitude dependency in finite viscoelasticity. Int. J. Plast. 78, 223–241.

Rault, J., Marchal, J., Judeinstein, P., Albouy, P., 2006. Stress-induced crystallization and reinforcement in filled natural rubbers: ^{2}H NMR study. Macromolecules 39 (24), 8356–8368.

Reese, S., 2003. A micromechanically motivated material model for the thermo-viscoelastic material behaviour of rubber-like polymers. Int. J. Plast. 19 (7), 909–940.

Rendek, M., Lion, A., 2010. Amplitude dependence of filler-reinforced rubber: experiments, constitutive modelling and fem–implementation. Int. J. Solids Struct. 47 (21), 2918–2936.

Smallwood, H., 1944. Limiting law of the reinforcement of rubber. J. Appl. Phys. 15 (11), 758–766.

Sodhani, D., Reese, S., 2014. Finite element based micro-mechanical modeling of interphase in filler reinforced elastomers. Soft Mater. 12 (Suppl. 1), S152–S161.

Srivastava, V., Chester, S.A., Anand, L., 2010. Thermally actuated shape-memory polymers: experiments, theory, and numerical simulations. J. Mech. Phys. Solids 58 (8), 1100–1124.

Stauffer, D., Aharony, A., 1994. Introduction to percolation theory. CRC press.

Stübler, N., Fritzsche, J., Klüppel, M., 2011. Mechanical and electrical analysis of carbon black networking in elastomers under strain. Polym. Eng. Sci. 51 (6), 1206–1217.

Syed, I.H., Stratmann, P., Hempel, G., Klüppel, M., Saalwächter, K., 2016. Entanglements, defects and inhomogeneities in nitrile butadiene rubbers: macroscopic vs microscopic properties. Macromolecules (submitted).

Vilgis, T.A., Heinrich, G., Klüppel, M., 2009. Reinforcement of Polymer Nano-composites: Theory, Experiments and Applications. Cambridge University Press.

Weisstein, E.W., 04 2016. Wolfram Math World - Hypergeometric Function. http://mathworld.wolfram.com/HypergeometricFunction.html.

Wulf, H., 2016. Modellierung und Simulation von Selbstorganisationsprozessen in belasteten technischen Gummiwerkstoffen. Ph.D. thesis. Technische Universität Chemnitz.

Wulf, H., Ihlemann, J., 2015. Simulation of mullins effect and relaxation due to self-organization processes in filled rubber. In: Constitutive Models for Rubber IX, vol. 305.

Reproduced with permission from Rubber Chemistry and Technology 2018, 91(2), 509-519.
Copyright 2018 American Chemical Society. https://doi.org/10.5254/rct-18-82628
The manuscript is corrected for editorial mistakes.

INVESTIGATION OF CARBON BLACK AND SILICA SURFACE STRUCTURE BY STATIC GAS ADSORPTION WITH VARIOUS GASES

J. Plagge,* M. Klüppel

Deutsches Institut für Kautschuktechnologie e.V., Eupener Str. 33, 30519 Hannover, Germany

RUBBER CHEMISTRY AND TECHNOLOGY, Vol. 91, No. 2, pp. 509–519 (2018)

ABSTRACT

The surface of various carbon black and silica grades is characterized via static gas adsorption using different gases. From decomposition of the adsorption isotherm into distinct energetic contributions, the adsorption energy distribution as well as the surface area are obtained. The decomposition is done by an iterative expectation maximization algorithm specifically designed for this problem. It is found that the adsorption isotherms of the various gases differ significantly in the low-pressure regime, leading to characteristic energy distributions with distinct maxima. As expected, the mean adsorption energy generally increases with the cross section of the gases, and systematic deviations are found reflecting the polar and dispersive interaction characteristics of silica and carbon black, respectively. The surface fractal dimension of two different carbon black grades is estimated using the yardstick method. The obtained values 2.6 and 2.7 agree with previous findings that the carbon black surface morphology is very rough. The adsorption of CO_2 on both carbon blacks delivers unexpectedly low values of the monolayer coverage or specific surface area, indicating that mainly high energetic sites of the surface are covered. In consequence, compared with N_2, a relatively high value of the mean adsorption energy is found. For both investigated silicas, the mean adsorption energy scales with the quadrupole moments of CO_2 and N_2, which is indicative of a large polar contribution to interaction energy. [doi:10.5254/rct-18-82628]

INTRODUCTION

Carbon black and silica are widely used filling materials in the rubber industry, greatly improving the toughness and wear resistance of elastomers. The latter, in particular, has become more important in recent years as a crucial component of environmentally friendly tires. This is related to a tailor-made polymer–filler interaction via silane coupling or covering agents,[1] which allows the control of viscoelastic hysteresis losses for improved rolling resistance and wet traction of tires. The reinforcement mechanism of fillers is still under discussion. Lorenz et al.[2] assume the filler network stores and dissipates energy by constantly breaking down and reforming, while other authors treat fillers as binding points, allowing the elastomer to attach and detach under load.[3] Some other works treat the filler–polymer interaction in a less specific way, describing it as a large-scale reorganization phenomenon.[4,5] The low-strain amplification was shown to mainly depend on filler structure.[6] In most approaches, the affinity of polymer and filler particles is an important ingredient that can be quantified by the filler's specific surface area and surface activity (e.g., binding energy of filler and polymer). Both quantities control polymer–filler phase bonding and the strength of the filler–filler interaction. For carbon black, they are affected by the surface roughness on small-length scales and the energy site distribution in relation to the polymer matrix under consideration.[7] While this is generally true also for silica, the surface chemistry (especially silanol groups) may be regarded as the key factor determining the polymer–filler interaction.[8,9] It was demonstrated by equilibrium gas-adsorption measurements on different carbon black grades that the surface roughness, characterized by the surface fractal dimension, is similar for all carbon blacks irrespective of their specific surface area and DBP number.[10] These results confirm previous findings that all furnace black grades adsorb the same amount (or number) of polymer chains per unit surface area.[11] Therefore, the contribution of the surface roughness cannot explain specific reinforcing effects caused by different carbon black grades, and more attention is given to energetic contributions of the surface activity in explaining mechanical and electrical properties of carbon black–filled elastomers. Nonequilibrium inverse gas-chromatography investigations performed in the 1990s[12] indicate a relationship between the dispersive surface energy contribution and the primary particle size and deliver hints for a heterogeneous surface energy distribution. In addition, (grafted) silica was investigated,[9,13] highlighting the difference in adsorption of unpolar hydrocarbons and polar probes such as benzene. Another way to characterize surface activity is contact angle measurements. Using the Wilhelmy method, silica samples exhibit large polar surface energy components, while carbon black interacts almost purely dispersively.[8]

---

*Corresponding author. Email: plagge.jan@gmail.com

Previous studies on carbon black[10] and graphenes[14] have shown that equilibrium gas adsorption is able to give information about specific surface area and surface activity as well as about energetic and morphological roughness. In this work, we want to provide an overview of this method and focus on the influence of different gases on the adsorption characteristics of various silica and carbon black grades. The difference between silica and carbon black with respect to their more or less dispersive and polar interaction characteristics is especially highlighted. The gases vary in size (molecular area) and polarity. They are chosen to give information about the dispersive and polar interaction characteristics of adsorbed polymer chains on carbon black and silica, respectively.

THEORY

A simple theory describing adsorption of multiple gas layers on energetically homogeneous surfaces is the extended BET theory named after its inventors Brunauer Emmet and Teller. It is given by

$$\theta(h,W)=\frac{N}{N_\mathrm{m}}=\frac{1}{1-h}-\frac{1}{1+(K_\mathrm{FG}(W,\theta)\,p_0-1)\,h}\qquad \text{with}\qquad h=p/p_0 \tag{1}$$

where $\theta(h, W)$ is called the surface coverage ranging from 0 (no coverage) over 1 (monolayer) to values >1 for multilayer adsorption. N is the adsorbed molar amount of gas per unit pass of sample. Accordingly, N_m is the molar capacity of a gas monolayer per unit mass given in mol/g. The pressure p_0 (given in kPa) is the saturation pressure, so $h=p/p_0$ is called the dimensionless relative pressure. The constant K_FG (given in 1/kPa) is defined in terms of the Langmuir constant K_L, which can be approximated[15] as

$$K_L(W)=\frac{N_\mathrm{A}\sigma\tau}{\sqrt{2\pi\, mRT}}\exp\left(\frac{W}{RT}\right) \tag{2}$$

with Avogadro's number N_A, ideal gas constant R, sample temperature T (given in K), molar mass m, molecular cross section σ (in nm^2), and mean adsorption time $\tau \approx 10^{-12}$s.[16] W denotes the binding energy of surface and gas molecules. The original BET theory assumes zero interaction between neighboring adsorbed molecules. Fowler and Guggenheim[17] included this interaction by introducing

$$K_\mathrm{FG}(W,\theta)=K_L(W)\exp\left(\frac{\theta\, z\,\Omega}{RT}\right) \tag{3}$$

Here, z is the coordination number (e.g., the number of neighbors), which was set to $z=4$ in this work. The interaction energy of two neighboring adsorbed molecules $\Omega=H_v/(4z)$ (in kJ/mol) is estimated using the enthalpy of vaporization H_v.[17] Equation 1 depends on surface coverage θ itself but has to be plugged into Eq. 1 to determine surface coverage, such that numerical methods are required to solve for θ.

In reality, few surfaces are energetically homogeneous. Heterogeneities can be of chemical origin (e.g., in terms of polarity) or of morphological origin (i.e., cavities or "summits"). A well-established approach is to reconstruct the isotherm N_{exp} obtained by experiment by a model isotherm N_{mod}, defined as a superposition of BET isotherms with different adsorption energies W (see Eq. 1):

$$N_{\mathrm{exp}}(h) \simeq N_{\mathrm{mod}}(h) = \int_0^\infty \theta(h, W) F(W)\, \mathrm{d}W \tag{4}$$

where the integral limits implicitly include the assumption of purely attractive interaction. Note that the left-hand side given in mol/g is the data from the machine, which has to be reproduced as good as possible by the model isotherm N_{mod}, which is constructed as the sum of many BET isotherms $\theta(h, W)$ with different adsorption energies W. The function $F(W)$ is the surface energy distribution and is not normalized. This is the quantity of interest. Unfortunately, the integral cannot be inverted analytically to solve for $F(W)$, such that numerical methods have to be employed. An algorithm specifically designed for the solution of this equation is an expectation maximization algorithm given by Stanley and Guiochon.[18] The iteration scheme for the kth iteration step of $F(W)$ is

$$F^{k+1}(W_i) = F^k(W_i) \frac{\sum\limits_j \theta(h_j, W_i) \frac{N_{\mathrm{exp}}(h_j)}{N_{\mathrm{mod}}(h_j)}}{\sum\limits_j \theta(h_j, W_i)} \qquad \text{for all } i \tag{5}$$

with h_i and W_i being the discretized relative pressure and adsorption energy, respectively. After sufficient iterations, the experimental isotherm $N_{\mathrm{exp}}(h_j) \simeq N_{\mathrm{mod}}(h_j)$ for all j. Then, $\frac{N_{\mathrm{exp}}(h_j)}{N_{\mathrm{mod}}(h_j)} \simeq 1$, such that the left and right side of the equation coincide and a fixed point of iteration is reached. The surface area is hidden in the normalization constant of $F(W)$ and can be identified with the global monolayer capacity $N_{\mathrm{m,g}}$. The normalized energy distribution reads

$$f(W) = \frac{F(W)}{N_{\mathrm{m,g}}} \qquad \text{with} \qquad N_{\mathrm{m,g}} = \int_0^\infty F(W)\, \mathrm{d}W \tag{6}$$

The specific surface area S (in m^2/g) and mean adsorption energy $\langle W \rangle$ (in kJ/mol) are then given as

$$S = N_{\mathrm{m,g}} N_{\mathrm{A}}\, \sigma \qquad \text{and} \qquad \langle W \rangle = \int_0^\infty W f(W)\, \mathrm{d}W \tag{7}$$

where the molecular area σ is calculated from liquid bulk density ρ at adsorption temperature and molar mass m according to[16,19]

$$\sigma = 2\sqrt{3} \left(\frac{m}{4\sqrt{2} N_{\mathrm{A}}\, \rho} \right)^{2/3} \tag{8}$$

By continuing iteration of Eq. 5, the experimental isotherm can be reproduced to almost arbitrary precision up to the point where measurement errors are reproduced as well, generating artifacts in the energy distribution. A frequently used method is to keep iterating until the deviation of model and data is of the same order as the experimental error. Unfortunately, this cannot be done here, because machine precision is not exactly known and model deviations due to neglected effects (e.g., capillary condensation at high pressures) introduce systematic errors. Therefore, we start with a flat distribution $F(W) = \mathit{const.}$ and perform 1000 iterations each time.

In addition, the data were evaluated following the classical BET approach as outlined in, for example, Adamson and Gast.[16] For this purpose, Eq. 1 without the Fowler–Guggenheim correction is rewritten in its linear form

$$y = \frac{1}{N(1/h-1)} = \frac{c-1}{N_\mathrm{m}\, c} h + \frac{1}{N_\mathrm{m}\, c} = A\, h + B \qquad (9)$$

$$\text{with} \quad h = p/p_0 \quad \text{and} \quad c = K_L\, p_0$$

where c is called the BET constant. We want to point out that the Fowler–Guggenheim correction has a strong impact on surface area as well as interaction energy. Nevertheless, it is neglected for the classical BET evaluation to allow comparison with other literature. When plotting the linearized data (y vs h), the data are usually linear for pressures $h = p/p_0 \simeq 0.05 \ldots 0.20$. Doing a linear fit in this regime according to $y = A\ h + B$, the BET surface area is calculated as

$$N_\mathrm{m} = \frac{1}{A+B} \qquad (10)$$

$$S_\mathrm{BET} = N_\mathrm{m}\, N_\mathrm{A}\, \sigma \qquad (11)$$

where N_m is the monolayer capacity of a hypothetical energetically homogeneous surface.

EXPERIMENTAL

Gas adsorption measurements were carried out using a BELSORP-max (BEL Japan Inc., Osaka, Japan) volumetric adsorption machine from 0.1 Pa up to atmospheric pressure, corresponding to $h = 10^{-6} \ldots 1$. Adsorptives are N_2, CO_2, ethane, propene, and 1-butene. The latter three are rather unpolar hydrocarbons and resemble in this respect most polymers. Standard carbon black grades N339 and N550 and silicas VN2 and Z1165, which are in wide technical use (e.g., in tire treads) were investigated. To clean the filler surfaces of impurities, all carbon black and silica samples were heated in a vacuum for 3 h at 300 °C and 100 °C, respectively. Adsorption measurements started at low pressure after reaching a pressure of $\sim 10^{-8}$ bar, which was achieved by using a turbo molecular pump for at least 12 h. The leakage rate without pumping was $\sim 10^{-7}$ bar/min. During measurement, the sample glass with filler inside was kept at a condensation temperature of the gas using a thermostat (ethane, propene, and 1-butene), a liquid nitrogen bath (N_2), or an acetone bath filled with dry ice (CO_2).

RESULTS AND DISCUSSION

Figure 1 shows normalized adsorption isotherms and fitted isotherms for all samples and gases against the relative pressure $h = p/p_0$. The pressure p_0 is 101.3 kPa at temperatures 77.2 K, 194.7 K, 184.6 K, 225.5 K, and 266.9 K for N_2, CO_2, ethane, propene, and 1-butene, respectively. It can be seen that the adsorption automaton delivers reliable results for pressures $p/p_0 \gtrsim 5 \cdot 10^{-6}$ such that the lower fit limit was set to this pressure. The overall fitting quality is good for all gases and samples. It is worth mentioning here that the slope of the curves cannot be taken as a direct measure for the interaction, as the molar mass and molecular area of the gases influence the Langmuir constant (which is the initial slope; see Eq. 2).

The surface area of the sample is directly influenced by the molecular area of the gas. For all gases except CO_2, the molecular area was calculated via Eq. 8. The surface area of CO_2 varies strongly in the literature,[20,21] mostly being in the range of ~ 0.17 nm^2. Here, $\sigma(CO_2) = 0.178$ nm^2 from the latter reference is chosen, because it is close to the value $\sigma(CO_2) = 0.179$ nm^2 calculated

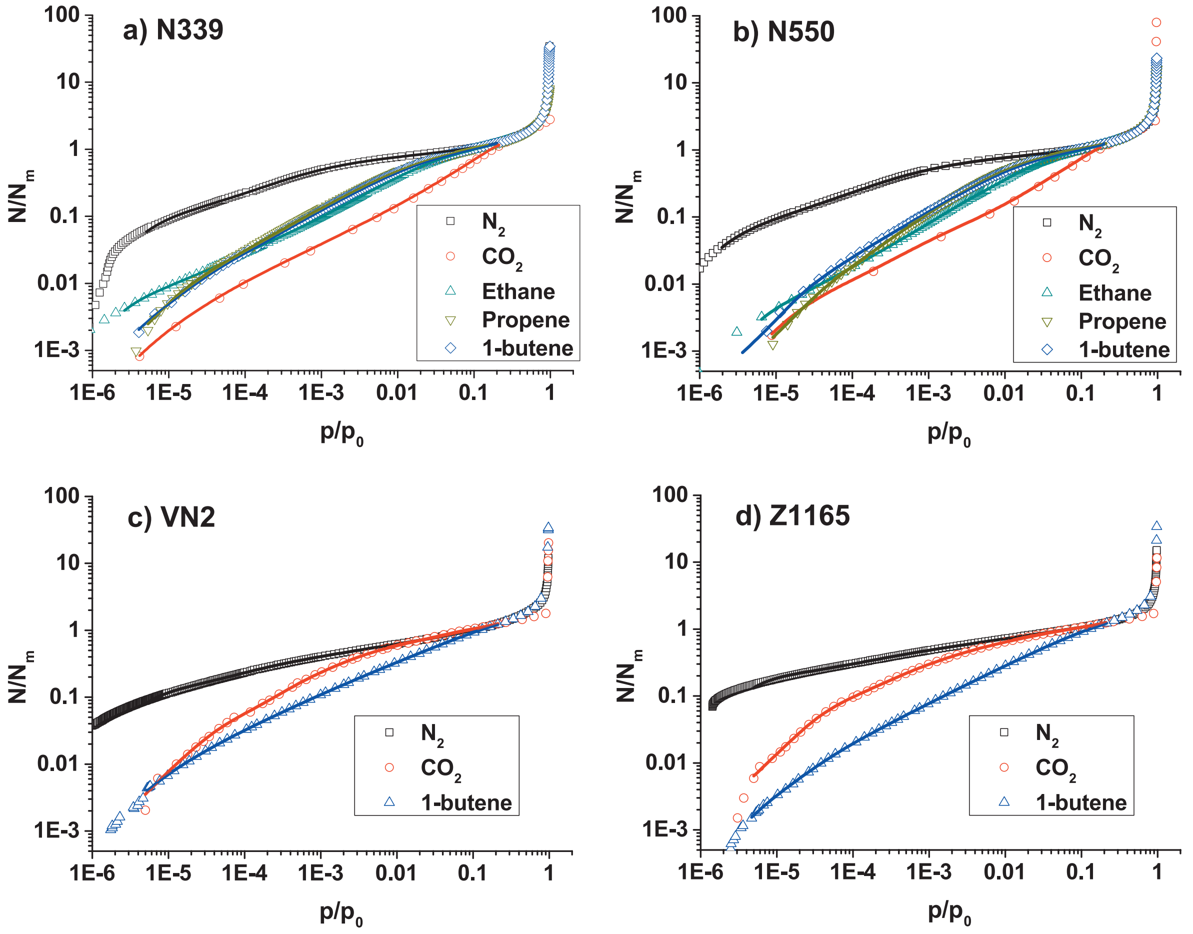

FIG. 1. — Normalized adsorption isotherms (symbols) and fitted model isotherms (solid lines) for all samples and gases investigated. For the two carbon blacks N339 (a) and N550 (b), the CO_2 isotherm is clearly below all other gases. This is not the case for silica samples VN2 (c) and Z1165 (d), where CO_2 is between 1-butene and N_2.

from Eq. 8 when using the density of liquid CO_2 at the lowest pressure allowing a liquid state (517 kPa).

Specific surface area S, BET surface area S_{BET}, and mean adsorption energy $\langle W \rangle$ (see Eq. 7) are shown in Table I. Remember that the BET surface area is calculated without Fowler–Guggenheim self-interaction, which may change the surface area if adsorbant self-interaction plays an important role (e.g., due to weak interaction with the filler). As expected, the surface area of N550 is always smaller compared with N339, and the BET surface areas S_{BET} obtained with nitrogen are in accordance with previous findings.[10,22] Energy distributions for both carbon black and silica samples are shown in Figure 2. Shape and energy level of the ethane, propene, and 1-butene distributions are in line with results for hydrocarbons with a longer carbon chain (e.g., alkanes C5-C10 and cyclohexane) found in Refs. 23 and 24 by means of inverse gas chromatography. In addition, the same authors investigated adsorption of benzene (polar probe) on VN2. The shape of the resulting energy distribution closely resembles the one we obtained with CO_2. As expected, energy distributions shift to larger energies with increasing size of the gas molecules. Within measurement precision N339 and N550 are indistinguishable, confirming the universal, self-affine nature of carbon black surfaces.[7,10] For the silica surfaces, differences are more pronounced, showing a rather complex energy landscape with distinct maxima for CO_2. This indicates an energetically heterogeneous surface that may be related to patches of silanol groups on the silica surface being more sensitive for polar molecules.

TABLE I

MOLECULAR AREA σ CALCULATED ACCORDING TO EQ. 8 FOR ALL GASES[a]

	N_2	CO_2	Ethane	Propene	1-Butene
σ, nm^2	0.163	0.178	0.222	0.256	0.308
$S[\frac{m^2}{g}]/S_{BET}[\frac{m^2}{g}]$					
N339	85.0/86.9	39.2/53.6	69.2/72.7	65.2/67.8	61.0/64.6
N550	38.6/39.4	18.0/25.1	30.2/30.9	29.8/31.1	27.4/28.9
VN2	137.2/143.0	161.8/165.1	/	/	87.5/96.5
Z1165	150.9/156.9	227.5/229.0	/	/	68.6/77.1
$\langle W\rangle[\frac{kJ}{mol}]/W_s[\frac{J}{m^2}]$					
N339	8.2/0.08	14.9/0.14	18.5/0.14	20.5/0.13	23.6/0.13
N550	8.3/0.08	15.1/0.14	18.5/0.14	20.3/0.13	23.8/0.13
VN2	7.9/0.08	18.8/0.18	/	/	22.3/0.12
Z1165	8.5/0.09	19.5/0.18	/	/	21.7/0.12

[a] The value for CO_2 is taken from Ref. 20. Surface area S and mean interaction energy ⟨W⟩ are calculated according to Eq. 7. In addition, the BET surface area SBET and specific surface energy Ws = ⟨W⟩/(NA σ) are given.

As explained before, CO_2 seems to be much more attractive to silica than to carbon black. This can be seen well in Figure 3a, where mean adsorption energy is plotted against molecular area. Surprisingly, this effect is even more pronounced in the specific surface area, as shown in Figure 3b. For silica, the mean adsorption energy as well as specific surface area obtained with CO_2 is larger than the surface area and mean adsorption energy obtained with the smaller N_2 molecule. This might be due to the linear shape of CO_2 in combination with its larger quadrupole moment, favoring interaction with the hydroxylated (and thus polar) silica surface and probably allowing the molecule to penetrate easily into cavities. The electric quadrupole moment quantifies the ability of electrically neutral and unpolar particles to interact via coulomb forces due to charge inhomogeneities. In fact, the quadrupole moment of N_2 and CO_2 was found to be $-4.72 \cdot 10^{-40}$ Cm^2 and $-13.4 \cdot 10^{-40}$ Cm^2, respectively.[25] It has been shown that the dispersive component of the surface energy of hydroxylated silica ranges between 10%[23] and 50%[8] of the comparable carbon black, which exhibits almost purely dispersive interaction. Thus, it is reasonable to attribute the major part of the interaction energy to specific surface energy caused by the dipole-quadrupole interaction. From this point of view, the ratio of silica-CO_2 and silica-N_2 interaction energy should be comparable with the

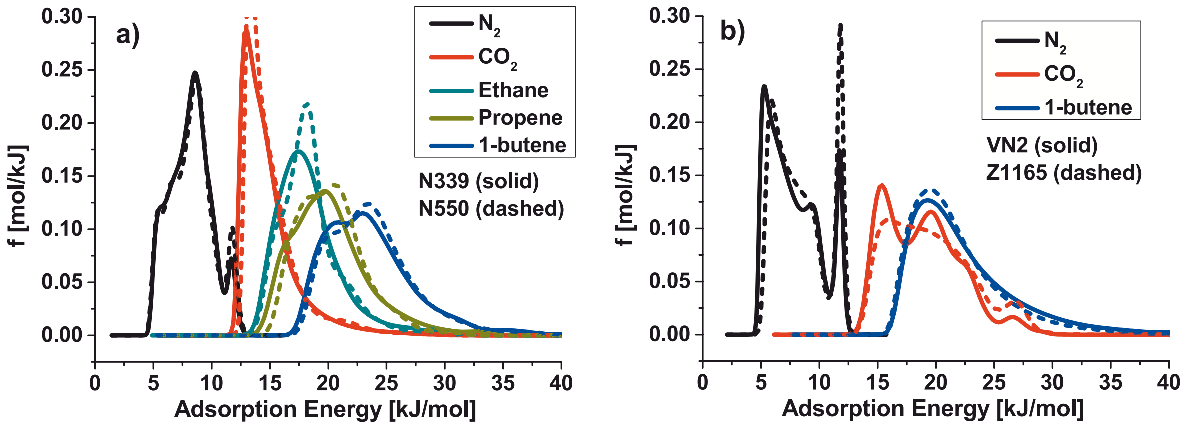

FIG. 2. — Normalized energy distributions for carbon black (a) and silica (b) samples. For all samples, energy distributions become broader and shift to larger energies with increasing size of gas molecules.

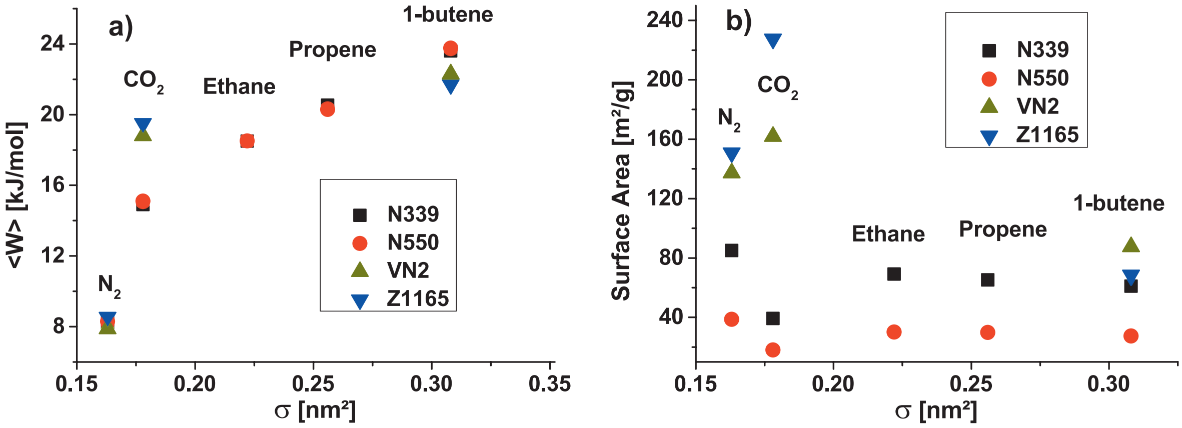

FIG. 3. — Mean adsorption energy ⟨W⟩ (a) and specific surface area *S* (b) against molecular area.

ratio of their quadrupole moments being 13.4/4.72 ≈ 284%. From the data in Table I, the ratio of interaction energies is found to be 18.8/7.9 ≈ 238% for VN2 and 19.5/8.5 ≈ 229% for Z1165 in fair agreement with the above expectation. The deviations may be due to the remaining dispersive interaction. This finding again highlights that the silica–polymer interaction is crucially affected by the charge distribution of the adsorbant: even a quadrupole moment, which represents weak short-range interaction, suffices to dominate the interaction over the disperse components. On the other hand, the same line of reasoning for carbon blacks N339 and N550 leads to a change of interaction energy, which should be (as a rough approximation) proportional to the ratio of the molecular areas of CO_2 and N_2, which is 0.178 nm^2/0.163 nm^2 ≈ 109%. The ratio calculated from Table I is 14.9/8.2 ≈ 15.1/8.3 ≈ 182% for both N339 and N550. This value seems to be too high, or in other words, the difference in CO_2 interaction energy between carbon black and silica is far smaller than their chemical compositions suggest. The problem may be resolved by noticing that adsorption sites where no adsorption takes place (e.g., because they are energetically not attractive) do not contribute to the energy distribution function at all. Looking at the specific surface energies, this assumption becomes reasonable: surprisingly, the CO_2 surface area of N339 and N550 is 44% and 47% of their N_2 surface area, respectively. Given that both molecules have roughly the same molecular area, this means that more than half of the adsorption sites available on both carbon blacks remain unoccupied by CO_2. Hence, the energy distribution is biased such that it includes only high-energy sites. These sites may be due to chemically bonded hydrogen and oxygen groups that survived the heating process. Studies by gas chromatography–mass spectrometry and SIMS have found a remarkable amount of up to 3% hydrogen and oxygen groups at various carbon black surfaces even after heating at 1173 K in an inert atmosphere.[26] As we heated carbon black up to 573.15 K, the amount of these groups may be higher in our samples. Possibly, these rather polar "impurities" act as nucleating points for CO_2, maybe even allowing local condensation/multilayer adsorption. This is supported by the following discussion about the samples' BET surface area measured with CO_2, revealing the great influence of self-interaction of CO_2.

In Figure 4b, the ratio of surface S determined by Eq. 7 and the BET surface S_{BET} is shown. It turns out that the BET surface is always slightly larger than its generalization S. Exceptions are the pairs carbon black/CO_2 and silica/1-butene, where S_{BET} is 30% and 10% larger than S, respectively. The main difference in S_{BET} and S is the inclusion of self-interaction via Eq. 3 in S, so the deviation may be traced back to highly self-interacting gas molecules, supporting the hypothesis of polar adsorption spots on carbon black, where CO_2 aggregates in consequence of its strong self-interaction. In contrast to the findings for carbon black, where $S(CO_2) < S(N_2)$, the CO_2 surface area of VN2 and Z1165 increases to 118% and 151% of its N_2 value, respectively. Inverting the

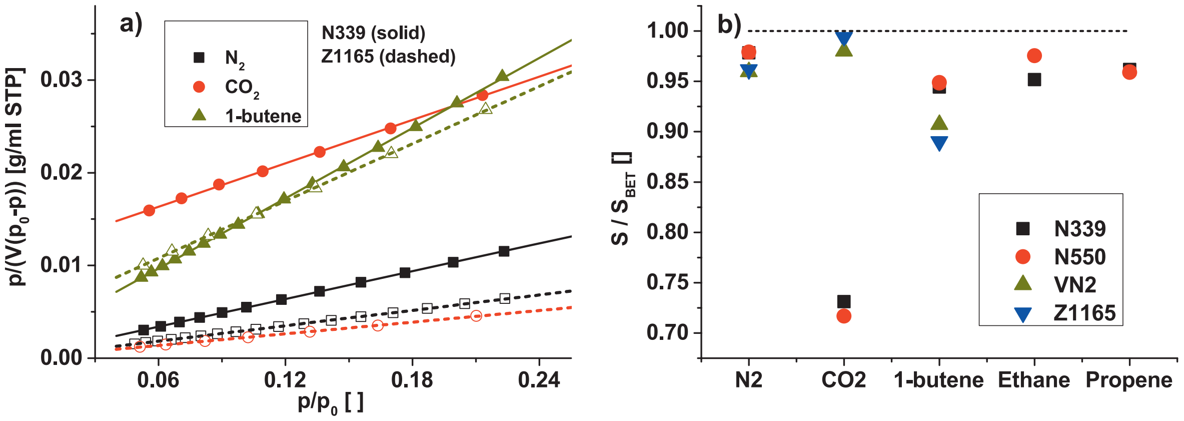

FIG. 4. — BET plots of selected samples (a) and ratio of surface area and BET surface area (b).

argumentation above, this indicates that nitrogen is unable to occupy all adsorption sites on silica, or stated reversely, that CO_2 is able to occupy adsorption sites not available to N_2 (possibly silanol groups). Nevertheless, it has to be kept in mind that the molecular area of CO_2 is relatively uncertain, reflected in a relatively wide spreading of literature values. In addition, the unknown arrangement of CO_2 molecules on the sample's surface should have a great influence on the effective molecular area because of its linear shape. A close arrangement comparable to the solid phase will decrease molecular area and thus the measured surface area. We want to point out that the increase in CO_2 surface area is especially pronounced for Z1165, so that it seems to be more polar than VN2. This finding is supported when looking at N_2 and 1-butene surface area. Compared with N_2, the 1-butene surface area of both silicas is greatly reduced, especially for Z1165. This can be explained again by unoccupied adsorption sites or by a different fractal surface roughness. The weight loss after 2 h heating at 105 °C taken from the data sheet of VN2 is 5.5%, while for Z1165, it was found to be 7%.[27] As the weight loss is attributed to water desorption, it is indicative of Z1165 being more polar, even if normalized by N_2 surface area of the samples.

The dependence of the specific surface area on molecular size can be quantified by a fractal dimension. In Figure 5a, the monolayer capacity $N_{m,g}$ is plotted against the molecular area of the adsorbant for both carbon blacks investigated. As carbon black exhibits a self-similar surface

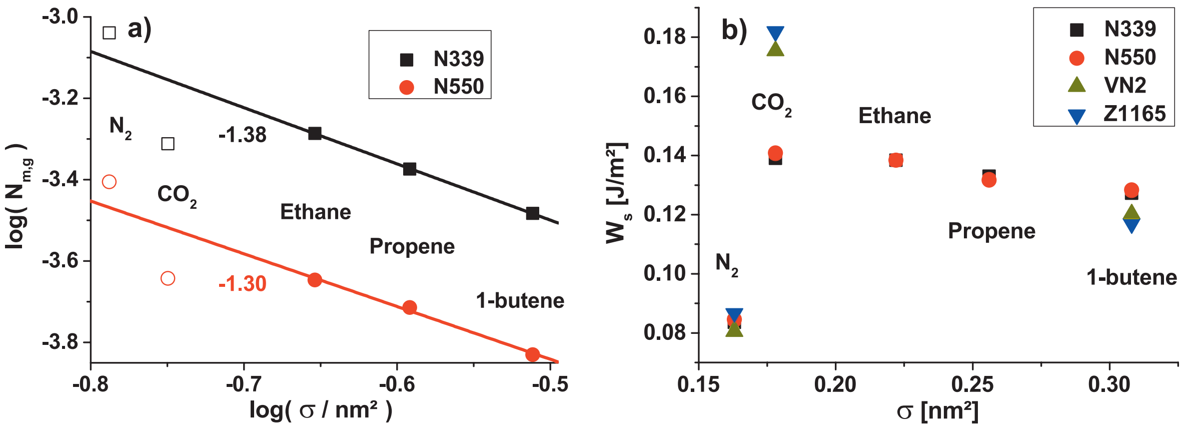

FIG. 5. — (a) Logarithmic monolayer capacity against logarithmic molecular area. The solid line is a linear fit over ethane, propene and 1-butene data delivering the surface fractal dimension. The open symbols are no hydrocarbons and are excluded from the fit. (b) Specific adsorption energy W_s against molecular area.

structure, the monolayer capacity should decrease according to[10]

$$\log(N_{\mathrm{m,g}}) = -\frac{D_{\mathrm{S}}}{2}\log\sigma + const.$$

where $2 \leq D_{\mathrm{S}} \leq 3$ is the surface fractal dimension. The fractal dimension was determined using the hydrocarbons ethane, propene, and 1-butene only, because of their similar interaction behavior. For silica, no adsorption data using ethane and propene were available, such that the fractal dimension cannot be determined. A fractal dimension of 2 corresponds to a flat surface, while a surface with a fractal dimension near 3 folds so much that it almost covers three-dimensional space. The fractal dimensions obtained are 2.76 ± 0.04 and 2.6 ± 0.2 for N339 and N550, respectively, in close agreement with the results from Schröder et al.[10]

To compare adsorption energies regarding polymer–filler and filler–filler interaction, the specific binding energy per unit area of coverage was calculated using $W_s = \langle W \rangle / (N_A\, \sigma)$. The results are shown in Figure 5b. It can be seen that the interaction energy of all hydrocarbons on carbon black is about $W_s \approx 0.13$ J/m^2. The cleavage energy of graphite planes was recently estimated[28] to be 0.37 J/m^2, representing an upper bound for the binding energy of carbon black particles. Although this energy is greater by a factor of 3, both energies are of the same order of magnitude, allowing the dispersion of carbon black into polymers with similar polarity as the gases investigated. It is worth noting that some authors believe chemical bonds between carbon black and polymers to be responsible for their great overall compatibility.[29] As we are investigating physical bonding only, this effect is out of the scope of this work. For N_2, a much smaller specific interaction energy is found on both type of fillers, indicating that it is less tightly bound independent of the dispersive or polar components of the filler. The very high specific surface energy $W_s \approx 0.18$ J/m^2 of CO_2 on silica is not surprising because of the strong quadrupolar interaction and possibly better coverage of the more polar surface constituents such as silanol groups. This fits the observation that silica is dispersible into polar polymers (e.g., polyethylene-oxide),[30,31] without further treatment of the silica surface. Surprisingly, the interaction energy of hydrocarbons on silica is $W_s \approx 0.12$ J/m^2 and is thus quite similar to their interaction energy with carbon black. Nevertheless, it is widely known that silica in unpolar polymers is hardly dispersible and forms large, stiff superstructures due to strong clustering.[32] For this reason, the problems of dispersing silica into unpolar polymers must be attributed to strong silica–silica interaction, governing silica clustering, although the polymer–silica interaction is on a similar level as the polymer–carbon black interaction. In fact, it has been shown that untreated silica particles move on long-time scales even in vulcanized (unpolar) rubber compounds,[33] whereas carbon black does not. Given these results, the great success of silica surface modification using silanes probably has to be interpreted more in terms of reducing the silica–silica affinity than increasing the polymer–silica interaction. Unfortunately, a value quantifying the binding energy of silica particles is hard to find because of dispersive and specific contributions as well as a surface chemistry (e.g., degree of hydroxylation) that is not well defined.

CONCLUSION

It has been shown that static gas adsorption is a powerful tool to characterize surfaces in several aspects on a molecular scale. Nitrogen surface areas are in good agreement with the literature and decrease with increasing size of probe molecules, proving the pronounced roughness of the samples. For both carbon blacks investigated, the surface fractal dimension is about 2.7. CO_2 adsorption measurement reveals that silica is more polar than carbon black, in accordance with its surface chemistry. In particular, Z1165 seems to be far more polar than VN2 silica in accordance with technical specifications. The great decrease in carbon black surface area when using CO_2 compared with nitrogen surface area is explained by incomplete CO_2 surface coverage, probably because of the remaining polar surface impurities. In addition, for the rather incompatible pair CO_2/carbon black, self-interaction of the gas molecules on the filler surface seems to be important. The difference in polarity may be investigated even better by using carbon monoxide (CO), which has a dipole moment and should therefore be more sensitive regarding filler polarity. Specific adsorption energy has been found to be constant for all hydrocarbons investigated and is very similar for carbon black and silica. The difference in specific adsorption energies of hydrocarbons on silica and carbon black is too small to explain their vastly different behavior in a polymer matrix. Thus, the greater self-interaction of polar silica particles than of carbon black seems to be the reason for increased phase separation, which in turn is responsible for the bad dispersibility and mechanical performance. Thus, the focus should possibly shift toward reducing the silica–silica interaction rather than improving polymer–silica affinity.

ACKNOWLEDGEMENTS

We thank the Arbeitsgemeinschaft industrieller Forschungsvereinigungen (AiF) grant 18079 BG for financial support and Frank Fleck for some measurements.

REFERENCES

[1] M. Alimardani, M. Razzaghi-Kashani, R. Karimi, and A. Mahtabani, RUBBER CHEM. TECHNOL. **89**, 292 (2016).

[2] H. Lorenz, M. Klüppel, and G. Heinrich, *ZAMM* **92**, 608 (2012).

[3] V. N. Khiêm and M. Itskov, *Int. J. Plast.* **90**, 96 (2017).

[4] J. Plagge and M. Klüppel, *Int. J. Plast.* **89**, 173 (2017).

[5] H. Wulf and J. Ihlemann, *Constit. Models Rubber IX* 305 (2015).

[6] S. M. Smith and D. S. Simmons, RUBBER CHEM. TECHNOL. **90**, 238 (2017).

[7] M. Klüppel, A. Schröder, and G. Heinrich, in *Physical Properties of Polymers Handbook,* Vol. 1076, J. E. Mark, Ed.; Springer, New York, 2007, Ch. 31.

[8] K. W. Stöckelhuber, A. Das, R. Jurk, and G. Heinrich, *Polymer* **51**, 1954 (2010).

[9] M.-J. Wang, S. Wolff, and J.-B. Donnet, RUBBER CHEM. TECHNOL. **64**, 559 (1991).

[10] A. Schröder, M. Klüppel, and R. H. Schuster, *Macromol. Mater. Eng.* **292**, 885 (2007).

[11] D. Bussmann, "Ruß-Kautschuk-Wechselwirkungen," Ph.D. Thesis, University of Hannover, 1992.

[12] J.-B. Donnet, *Carbon* 32, 1305 (1994).

[13] S. Wolff and M.-J. Wang, RUBBER CHEM. TECHNOL. **65**, 329 (1992).

[14] M. M. Möwes, F. Fleck, and M. Klüppel, RUBBER CHEM. TECHNOL. **87**, 70 (2014).

[15] I. Langmuir, *J. Am. Chem. Soc.* **40**, 1361 (1918).

[16] A. W. Adamson and A. P. Gast, *Physical Chemistry of Surfaces,* Interscience, New York, 1967.

[17] R. H. Fowler and E. A. Guggenheim, *Statistical Thermodynamics: A Version of Statistical Mechanics for Students of Physics and Chemistry*, University Press, 1952.

[18] B. J. Stanley and G. Guiochon, *J. Phys. Chem.* **97**, 8098 (1993).

[19] S. Brunauer and P. H. Emmett, *J. Am. Chem. Soc.* **59**, 2682 (1937).

[20] H. De Jonge and M. C. Mittelmeijer-Hazeleger, *Environ. Sci. Technol.* **30**, 408 (1996).

[21] P. Walker and M. Shelef, *Carbon* **5**, 7 (1967).

[22] S. Wolff, M.-J. Wang, and E.-H. Tan, RUBBER CHEM. TECHNOL. **66**, 163 (1993).

[23] M.-J. Wang and S. Wolff, RUBBER CHEM. TECHNOL. **65**, 715 (1992).

[24] M.-J. Wang and S. Wolff, RUBBER CHEM. TECHNOL. **65**, 890 (1992).

[25] C. Graham, J. Pierrus, and R. Raab, *Mol. Phys.* **67**, 939 (1989).

[26]J. Ayala, W. Hess, A. Dotson, and G. Joyce, RUBBER CHEM. TECHNOL. **63**, 747778 (1990).

[27]L. Guy, A. Monton, P. Jost, S. Goyard, and S. De Cayeux, "Paper Title," Paper X, presented at the Fall 184th Technical Meeting of the Rubber Division, ACS, Cleveland, October 2013.

[28]W. Wang, S. Dai, X. Li, J. Yang, D. J. Srolovitz, and Q. Zheng, *Nat. Commun. 6* (2015).

[29]P. Stickney and R. Falb, RUBBER CHEM. TECHNOL. **37**, 1299 (1964).

[30]D.-P. Wang, M.-Q. Yang, Z.-X. Dong, S.-Q. Bo, and X.-L. Ji, *Chin. J. Polymer Sci*. **31**, 1290 (2013).

[31]Q. Zhang and L. A. Archer, *Langmuir* **18**, 10435 (2002).

[32]T. A. Vilgis, G. Heinrich, and M. Klüppel, *Reinforcement of Polymer Nano-Composites: Theory, Experiments and Applications,* Cambridge University Press, Cambridge, 2009.

[33]F. Ehrburger-Dolle, I. Morfin, F. Bley, F. Livet, G. Heinrich, S. Richter, L. Piché, and M. Sut-ton, *Macromolecules* **45**, 8691 (2012).

[*Received June 2017, Revised December 2017*]

3.4 Outlook and Supplementary Information

As outlined in section 3.1, the model contains some uncommon mathematical concepts. First, the free energy density W_X contains non-elementary functions which are costly to evaluate and rarely implemented. Second, hysteresis is calculated by using convolutions which can only be evaluated by integrating the materials history. In commercial FE code and industrial application speed and stability are of crucial importance. For this reason this section deals with resource efficient approximations. Moreover, an extension of the model based on experimental findings on stress relaxation is presented.

3.4.1 A simpler free energy density integration

The calculation of the amplified energy density occurring in Eq. (19) of publication 1 is carried out as

$$W_X(I_1, X_{\max}, X_{\min}) = \int_{X_{\min}}^{X_{\max}} \mathrm{d}X \, P_X(X) \, W(X\bar{I}_1, X\bar{I}^*) \tag{3.1}$$

with the amplification factor distribution $P(X) \propto X^{-\chi}$ and amplified energy density of the non-affine tube model $W(X\bar{I}_1, X\bar{I}^*)$ defined by Eq. (2.25). It involves integrals of the form

$$\int \mathrm{d}X \, X^{-\chi} \frac{X}{1 - \frac{1}{n} X \, \bar{I}_1} \tag{3.2}$$

which can be solved analytically only by means of non elementary functions like incomplete beta functions or hypergeometric functions. For the sake of efficiency, the non-affine tube model given by Eq. (2.25) is reduced to a minimal functional form

$$W(\bar{I}_1, \bar{I}^*) = \frac{G_\mathrm{c}}{2} \left[\frac{\left(1 - \frac{1}{n}\right) \bar{I}_1}{1 - \frac{1}{\hat{n}} \bar{I}_1} + \log\left(1 - \frac{1}{n} \bar{I}_1\right) \right] + 2G_\mathrm{e} \, \bar{I}^* (-\beta) \tag{3.3}$$

$$\rightarrow \quad \hat{W}(\bar{I}_1, \bar{I}^*) = \frac{G_\mathrm{c}}{2} \frac{\bar{I}_1}{1 - \frac{1}{n} \bar{I}_1} + 2G_\mathrm{e} \, \bar{I}^* (-1) \tag{3.4}$$

where we assumed $n \gg 1$. Additionally, we assume sufficiently crosslinked networks ($\beta = 1$ [80, 81]). The $\log(\cdot)$ term is omitted, because for $n \gg 1$ and low strains $\log(1 - \bar{I}_1/n) \approx \bar{I}_1/n \approx 0$ and for large strains the $1/(1 - \bar{I}_1/n)$ term diverges faster than the corresponding logarithm. In the previous model the impact of less amplified domains was probably overestimated which is visible in the curvature of predicted virgin loading curves. This can be accounted for by introducing an offset parameter c in the distribution

$$\hat{P}(X) = (X + c)^{-\chi} \cdot \frac{\chi - 1}{(X_{\min} + c)^{1-\chi} - (X_{\max} + c)^{1-\chi}} \tag{3.5}$$

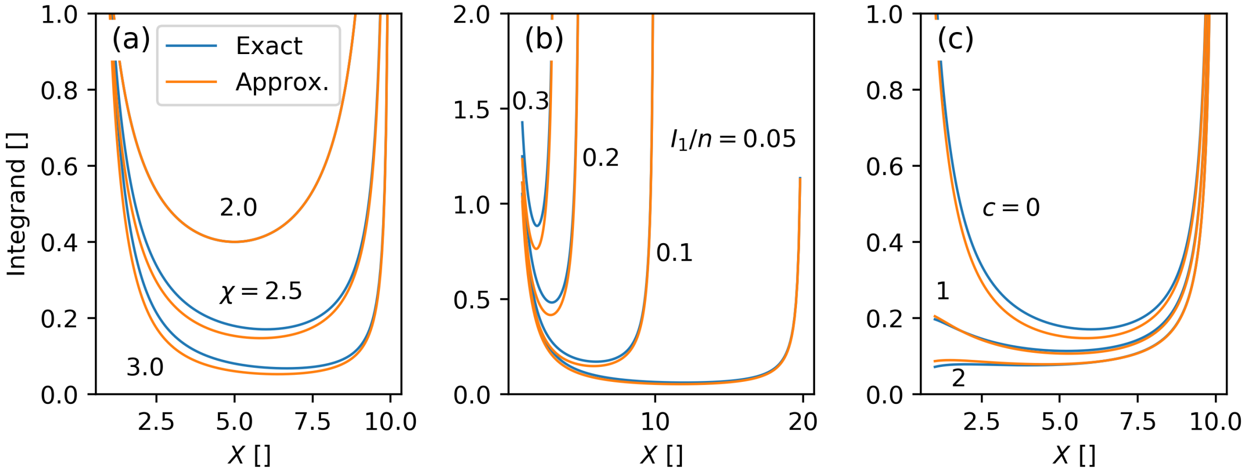

Figure 3.2: Check of the approximation given by Eq. (3.8). Default parameters are $\chi = 2.5$, $\bar{I}_1/n = 0.1$ and $c = 0$. Variations of these parameters are shown in (a), (b) and (c), respectively.

For $c = 0$ the original distribution $P(X)$ is recovered. The amplified free energy density is then defined as

$$\hat{W}_X(\bar{I}_1, X_{\max}, X_{\min}) = \int_{X_{\min}}^{X_{\max}} \mathrm{d}X\, \hat{P}_X(X)\, \hat{W}(X\bar{I}_1, X\bar{I}^*) \tag{3.6}$$

The integration can be simplified by taking a closer look on the problematic integrand

$$\int \mathrm{d}X\, (X+c)^{-\chi} \cdot \frac{X}{1 - \frac{X\,\bar{I}_1}{n}} = \int \mathrm{d}X\, \underbrace{(X+c)^{-\chi}\, X}_{f(X)} \cdot \underbrace{\frac{1}{1 - \frac{X\,\bar{I}_1}{n}}}_{g(X)} \tag{3.7}$$

For large $X \to n/\bar{I}_1$ the function $f(X)$ becomes small (if $\chi > 1$) and $g(X)$ diverges. In contrast, for small X, where $f(X)$ is largest, the second integrand $g(X)$ is close to 1. Altogether, the integral may be approximated by

$$\int \mathrm{d}X\, f(X) g(X) \approx \int \mathrm{d}X\, \left[f(X)\cdot 1 + f(n/\bar{I}_1)\cdot g(X)\right] \tag{3.8}$$

The approximation is evaluated in Fig. 3.2 and seems to reproduce the original behavior well. It can be expected that the remaining deviations are compensated by a slight change in fitting parameters. Using Eq. (3.8) the integration can be carried out analytically using elementary functions. The result is

$$\begin{aligned} \hat{W}_X(X_{\max}, X_{\min}) \approx \frac{1}{2}\,&\frac{1}{(X_{\min}+c)^{1-\chi} - (X_{\max}+c)^{1-\chi}} \cdot \\ \Bigg[\frac{G_\mathrm{c}\,\bar{I}_1 + 4\,G_\mathrm{e}\,\bar{I}^*}{\chi - 2} &\left((c+X_{\min})^{1-\chi}(c+(\chi-1)\,X_{\min}) - (c+X_{\max})^{1-\chi}(c+(\chi-1)\,X_{\max})\right) \\ &+ G_\mathrm{c}\,\frac{n^2(\chi-1)}{\bar{I}_1}\left(c + \frac{n}{\bar{I}_1}\right)^{-\chi} \log\left(\frac{\bar{I}_1\,X_{\min} - n}{\bar{I}_1\,X_{\max} - n}\right)\Bigg] \end{aligned} \tag{3.9}$$

From this, all elastic stress contributions can be calculated by suitable differentiation. It was implemented by Klein and Baaser into the FE software Abaqus and shown to be up to 4 times faster than the corresponding energy density with hypergeometric functions [89].

3.4.2 CONVOLUTION-FREE TIME INDEPENDENT HYSTERESIS

The convolution defined by Eq. (27) given in publication 1 requires storage of the whole deformational history of the sample. Additionally, it requires numerical integration for each timestep. This section is devoted to an alternative formulation using differential equations. The relaxation kernel

$$G(t) = 1/(1+t)^{\alpha} \tag{3.10}$$

coincides with the kernel used in Eq. (32) if $\alpha = 1$. It shall be approximated by a Prony series, such that

$$\frac{1}{(1+t)^{\alpha}} = \int_0^{\infty} \mathrm{d}\tau\, H(\tau)\, \mathrm{e}^{-\frac{t}{\tau}} \tag{3.11}$$

with a relaxation spectrum $H(\tau)$. According to the procedure used by Williams and Ferry [94] the first order approximation to the distribution $H(\tau)$ is obtained by converting the exponential to a step function

$$\mathrm{e}^{-\frac{t}{\tau}} \approx \begin{cases} 1 & \text{if} \quad t < \tau \\ 0 & \text{if} \quad t \geq \tau \end{cases} \tag{3.12}$$

Using this, Eq. (3.11) is rewritten as

$$\frac{1}{(1+t)^{\alpha}} \approx \int_t^{\infty} \mathrm{d}\tau\, H(\tau) \tag{3.13}$$

Differentiation on both sides gives an approximate expression for $H(t)$

$$-\frac{\alpha}{(1+t)^{\alpha+1}} \approx -H(t) \tag{3.14}$$

Inserting this into Eq. (3.11) gives

$$\frac{1}{(1+t)^{\alpha}} \approx \int_0^{\infty} \mathrm{d}\tau\, \frac{\alpha}{(1+\tau)^{\alpha+1}}\, \exp\left(-\frac{t}{\tau}\right) = \int_0^{1} \mathrm{d}n\, \exp\left(-\frac{t}{n^{-1/\alpha}-1}\right) \tag{3.15}$$

where the last step involves substitution of the integrand. Converting the integral to a sum we obtain

$$\frac{1}{(1+t)^{\alpha}} \approx \frac{1}{N-1} \sum_{n=1}^{N-1} \exp\left(-\frac{t}{(n/N)^{-1/\alpha}-1}\right) \tag{3.16}$$

Thus, power law relaxation is obtained by choosing relaxation times according to $\tau_n = (n/N)^{-1/\alpha} - 1$. The convolution with exponentials can be converted directly into a set of suitable differential equations. This is done in the framework of Greens functions, where solutions $u(t)$ of inhomogeneous differential equations can be expressed by convolution of Greens function (here: exponential) with the corresponding inhomogeneity $v(t)$. More formally

$$\dot{u} = -\frac{1}{\tau}u + \dot{v} \qquad \Leftrightarrow \qquad u(t) = \int_0^\infty \mathrm{d}t' \, \mathrm{e}^{-\frac{1}{\tau}(t-t')} v(t') \tag{3.17}$$

In Eq. (27) of publication 1 the convolution is carried out with respect to intrinsic time ς, which is running when stress changes. Expressing the corresponding kernel by exponentials gives

$$\frac{1}{1+\frac{\varsigma}{\sigma_c}} \approx \frac{1}{N-1}\sum_{n=1}^{N-1} \exp\left(-\frac{\varsigma}{\sigma_{\mathrm{c},n}}\right) \quad \text{with} \quad \sigma_{\mathrm{c},n} = \sigma_c \left(\frac{N}{n} - 1\right) \tag{3.18}$$

The equation can now be replaced by differential equations of the form

$$\frac{\mathrm{d}f_{\mathrm{hys},n}}{\mathrm{d}\varsigma} = -\frac{1}{\sigma_{\mathrm{c},n}} f_{\mathrm{hys},n} + \frac{\mathrm{d}f_{\mathrm{el}}}{\mathrm{d}\varsigma} \quad \text{and} \quad f_{\mathrm{hys}} = \frac{1}{N-1}\sum_{n=1}^{N-1} f_{\mathrm{hys},n} \tag{3.19}$$

These differential equations do not require storage of the materials history.

3.4.3 Stress Relaxation of Filled Elastomers

When holding filled elastomers at constant strain, stress usually decreases with time. Many authors have found that carbon black filled compounds relax logarithmically [33, 95]. The same was reported for semicrystalline polymers [31]. Theoretical investigations indicate that logarithmic stress relaxation may generally be explained by strongly interacting entities on the microscopic level [96]. Dynamic-Mechanical Analysis (DMA) measurements at small strains on SBR filled with up to 90 phr coupled silica have shown that the low-frequency modulus scales around $\sim \omega^{0.15}$, with a tendency towards lower exponents for the highly filled samples [97]. This corresponds to a slowly relaxing power law $\sim t^{-0.15}$ in the time domain, which is close to logarithmic relaxation.

In Fig. 3.3 the derivative of stress for carbon black (N339) filled EPDM with different sample geometries, filler amounts and temperatures is shown. Data was pretreated using a Savitzky-Golay filter to allow smooth differentiation. The derivative was taken to get rid of the additive constant which eventually represents the constant stress approached at large times. This was done, because an additive constant to a power law spoils the determination of slope in a log-log representation. For all samples the derivative of stress decayed close to $\mathrm{d}\sigma/\mathrm{d}t \propto t^{-1}$, irrespective of sample geometry, amount of filler, strain and temperature. This corresponds to a logarithmic stress decay $\sigma(t) \propto -\log(t)$. It is worth noting that, unlike a powerlaw, the logarithm $-\log(t)$ will never approach a constant value, which means that the sample would approach zero stress after sufficiently long time.

In the following logarithmic relaxation is derived from detachment of polymer chains from the filler surface. It shall be noted that, although the mathematics is temptingly simple, it is all but clear that polymer detachment is in fact responsible for the softening observed.

If one end of a polymer chain is adsorbed on the filler surface, while the other end is kept fixed at distance r, there is a retracting force $f(r, n)$, e.g. defined by the Gauss statistics given by Eq. (2.13). The number of statistical segments n only counts the segments in the free chain, because it can be

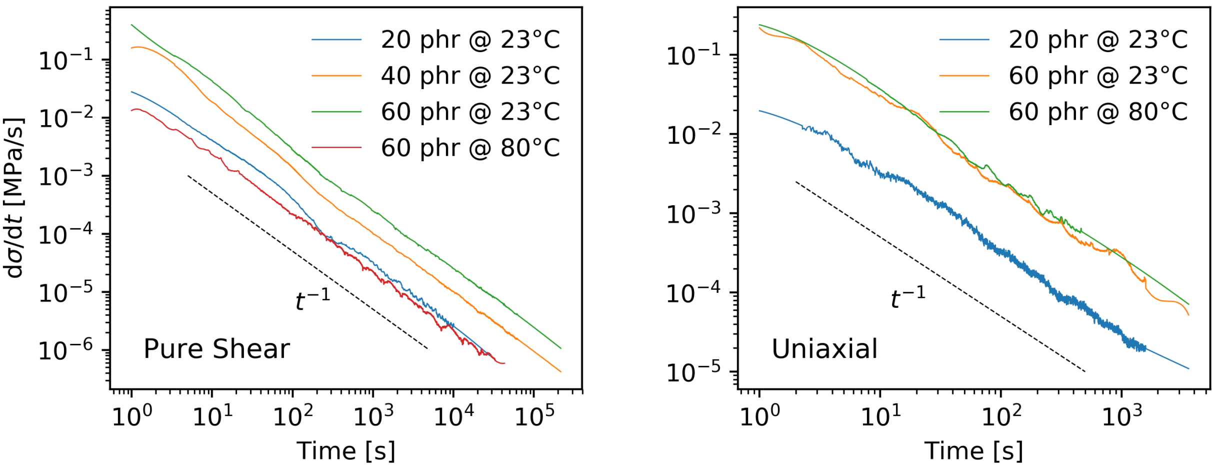

Figure 3.3: Stress decay of EPDM filled with different amounts of carbon black (N339) at different temperatures. The pure shear sample at 80 °C was stretched up to 50% strain, all other samples up to 120 % strain. The recipe can be found in tab. 1 of publication 1.

safely assumed that adsorbed segments will not contribute to the polymers elasticity. If chain segments desorb from the filler surface the chain will be relaxed. The change in force reads

$$\dot{f} = \frac{\mathrm{d}f}{\mathrm{d}n}\,\dot{n} \propto -\dot{n} \tag{3.20}$$

where $\mathrm{d}f/\mathrm{d}n < 0$, because an increase of polymer chain segments relaxes the chain (e g. for a Gauss chain we get $\frac{\mathrm{d}f}{\mathrm{d}n} \propto -\frac{r}{n^2} = -\frac{f}{n}$). The rate of detachment from the filler surface is identified with $\dot{n}$ and is approximated by Kramers escape rate out of the fillers attractive potential [98]

$$\dot{f} = \frac{\mathrm{d}f}{\mathrm{d}n}\,\dot{n} = \frac{\mathrm{d}f}{\mathrm{d}n}\,r_0 \exp\left(-\frac{E_\mathrm{b} - f\,d}{k_\mathrm{B}T}\right) \tag{3.21}$$

with r_0 [1/s] being the diffusivity without energy barrier E_b and d being a length scale quantifying the range of the attractive potential . This differential equation can be solved when approximating that $\frac{\mathrm{d}f}{\mathrm{d}n}$ is constant in time compared to the much more variable exponential term. For the Gauss chain with $\frac{\mathrm{d}f}{\mathrm{d}n} \propto -\frac{r}{n^2}$ the approximation becomes more precise, if r is constant (which is one of our prerequisites) and rather constant n. The latter will hold after large relaxation times.

With the initial condition $f(0) = f_0$ we get the solution of the differential Eq. (3.21) as

$$f(t) = f_0 - \frac{k_\mathrm{B}T}{d}\log\left[1 - \frac{r_0\,d}{k_\mathrm{B}T}\frac{\mathrm{d}f}{\mathrm{d}n}\mathrm{e}^{\frac{f_0\,d - E_\mathrm{b}}{k_\mathrm{B}T}}\,t\right] \tag{3.22}$$

$$\simeq A - B\,\log(t) \qquad \text{for large } t \tag{3.23}$$

with $A = \frac{E_\mathrm{b}}{d} - \frac{k_\mathrm{B}T}{d}\log\left(-\frac{r_0\,d}{k_\mathrm{B}T}\frac{\mathrm{d}f}{\mathrm{d}n}\right)$ and $B = \frac{k_\mathrm{B}T}{d}$. This is the desired result.

3.4.4 CONTINUOUS DAMAGE

According to section 3.4.3 filled and many crystallizing polymers exhibit logarithmic stress relaxation. Within the framework of publication 1, relaxation can be modeled as a decrease of the maximum amplification factor. Physically, the amplification factor may be related to shorter (and thus "stiffer") chains due to adsorption on filler particles, inclusion in crystals or geometric constraints imposed by the filler network on the polymer matrix. With the first mechanism in mind[§], it is easy to imagine that X could be antiproportional to the number of segments in a network chain partially adsorbed on a filler particle. If stress is applied, the most stretched chains, corresponding to the maximum amplification factor X_{max} desorb and relax. In analogy to section 3.4.3, the evolution of the maximum amplification factor can be written using Kramers escape rate [98, 99] as

$$\dot{X}_{\mathrm{max}} = r_+ - r_-(V\,\sigma_{\mathrm{max}}) = r_{0,+}\,\mathrm{e}^{-\frac{E_{\mathrm{b},+}}{k_{\mathrm{B}}T}} - r_{0,-}\,\mathrm{e}^{-\frac{E_{\mathrm{b},-} - V\,\sigma_{\mathrm{max}}}{k_{\mathrm{B}}T}} \approx r_0 \left(\mathrm{e}^{-\frac{E_{\mathrm{b}}}{k_{\mathrm{B}}T}} - \mathrm{e}^{-\frac{E_{\mathrm{b}} - V\,\sigma_{\mathrm{max}}}{k_{\mathrm{B}}T}} \right) \tag{3.24}$$

where r_+ [1/s] represents the hopping rate into a potential well, corresponding to an increase of amplification, and r_- is the force driven hopping rate out of the potential well, corresponding to decreasing amplification[¶]. Potential energy barriers are denoted $E_{\mathrm{b},\pm}$. The energy stored in the most stretched attached polymer $\sigma_{\mathrm{max}}\,V$ includes the corresponding stress σ_{max} and the excited volume V. The approximation done in Eq. (3.24) involves $r_{0,+} \approx r_{0,-} = r_0$ and $E_{b,+} \approx E_{b,-} = E_{\mathrm{b}}$. This ensures that $\dot{X}_{\mathrm{max}}(\sigma_{\mathrm{max}} = 0) = 0$, meaning that there is no change in maximum amplification factor when there is no applied force. Polymers will probably detach from the fillers surface under rather high load. This means that the stress measure σ_{max} just has to capture correctly the highly strained state. Looking at the energy density of the reduced non-affine tube model in Eq. (3.4) it becomes apparent that it may be modeled using the crosslink contribution only, because only the crosslink contribution is responsible for strain hardening. Stress σ_{max} is then approximated proportional to the crosslink contribution of the free energy density divided by a suitable strain measure Λ. The energy stored in the most stretched chains $V\,\sigma_{\mathrm{max}}$ can be expressed as

$$V\,\sigma_{\mathrm{max}} = V\,\frac{1}{c_1}\,\frac{1}{\Lambda}\,\frac{G_{\mathrm{c}}}{2}\,\frac{I_1\,X_{\mathrm{max}}}{1 - \frac{I_1\,X_{\mathrm{max}}}{n}} = \frac{1}{\tilde{c}_1}\,\frac{1}{\Lambda} k_{\mathrm{B}}T \frac{I_1\,X_{\mathrm{max}}}{1 - \frac{I_1\,X_{\mathrm{max}}}{n}} = \frac{1}{\tilde{c}_1}\,k_{\mathrm{B}}T \frac{\sqrt{I_1}\,X_{\mathrm{max}}}{1 - \frac{I_1\,X_{\mathrm{max}}}{n}} \tag{3.25}$$

where $\Lambda := \sqrt{I_1} = \sqrt{\lambda_1^2 + \lambda_2^2 + \lambda_3^2}$ is chosen to make the expression invariant to the choice of coordinate system and deformation state, and $\tilde{c}_1$ is a dimensionless proportionality constant. When the energy barrier is high compared to $k_{\mathrm{B}}T$ almost no jumping over the barrier occurs without external force. Formally, this corresponds to $r_0 \exp\left(-E_{\mathrm{b}}/k_{\mathrm{B}}T\right) \ll 1$ meaning that only the term scaled by

---

[§] It has to be noted again that there are a variety of other mechanism for stress softening under discussion. The calculation presented here selects chain desorption as a modeling paradigm. The same formalism could describe breakdown of filler structure at a certain load.

[¶] Physically, the force induced decrease in amplification is observable as Mullins effect. Accordingly, the increase of amplification may be physically identified with recovery of the Mullins effect as described in section 1.5.2.

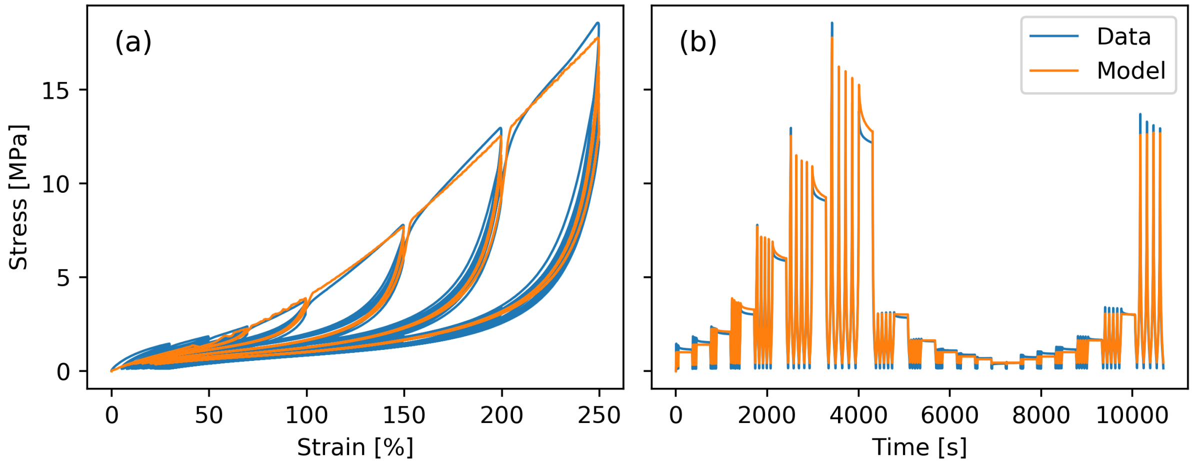

Figure 3.4: Model fit to peroxide cured EPDM filled with 50 phr N339 carbon black. The elastic response is derived from the free energy density given by Eq. (3.9) and the maximum amplification factor is evolved according to the continuous damage scheme defined by Eq. (3.26). Hysteresis is not modeled. Parameters are $G_\mathsf{c} = 0.11$ MPa, $G_\mathsf{e} = 0.20$ MPa, $n = 50.51$, $\chi = 3.16$, $c = 3.81$, $\tilde{c}_2 = 22.9$, $\tilde{c}_1 = 13.1$.

$V\,\sigma_{\max}$ survives. This allows to rewrite Eq. (3.24) in a simplified, more phenomenological form

$$\dot{X}_{\max} = -\frac{1}{\mathrm{s}}\exp\left(-\tilde{c}_2 + \frac{\frac{\sqrt{I_1}\,X_{\max}}{1-\frac{I_1\,X_{\max}}{n}}}{\tilde{c}_1}\right) \quad \text{with} \quad \tilde{c}_2 = \frac{E_\mathrm{b}}{k_\mathrm{B}T} - \log(r_0\cdot\mathrm{s}) \tag{3.26}$$

For numerical reasons it may be sensible to check that $X_{\max}$ never surpasses a maximum value:

$$X_{\max}(t) \equiv \min\left(X_{\max}(t), X_\infty\right) \qquad \text{with} \qquad X_\infty = \frac{n}{I_{1,\max}+\gamma} \tag{3.27}$$

where X_∞ is defined in analogy to Eq. (18) of publication 1. Otherwise the exponential occuring in Eq. (3.26) may generate extreme values which overstrain numerical integrators of the FE software. Eq. (3.26) was derived using many assumptions which may be physically questioned. It should be regarded as a physically motivated, heuristic expression, which generates logarithmic relaxation and softening while being compact and efficient. An example fit with continuous damage and using the simplified free energy density given by Eq. (3.9) is shown in Fig. 3.4. Integration of the amplification-defining evolution Eq. (3.26) was carried out numerically using an explicit Euler step without the regularization mechanism described in Eq. (3.27). Viscoelasticity and hysteresis are not included. The model fits the data fairly well, especially at large strains. Stress at low strains is slightly underestimated. This may be resolved when viscoelasticity is introduced. By including the exponential corresponding to r_+, which quantifies the regeneration rate of Mullins effect, the partial recovery observable in Fig. 3.4b at around 10000 s could probably be modeled.

If you're not confused, you don't understand things very well."

Charlie Munger

4

Self-Reinforcement due to Strain-Induced Crystallization

4.1 INTRODUCTION

Natural rubber exhibits unique properties in terms of wear and mechanical strength. Even unfilled it exhibits mechanical strength larger than many filled synthetic polymers. An example comparing NR to SBR using the same vulcanization system is provided in Fig. 4.1a and b. Although the response of both polymers is similar in the low strain regime, unfilled SBR fails below 5 MPa, while NR reaches up to almost 20 MPa.

At room temperature natural rubber is amorphous and highly elastic. But, as is widely known in industry, storage of uncured NR for long times significantly below room temperature results in a "hardening" of the material [100]. In fact, the corresponding timescale of crystallization was found to range between years at 14 °C [100] and hours at about -25°C, the latter being valid for both filled and unfilled compounds [101]. The introduction of chemical crosslinks was shown to greatly reduce crystallization speed [5]. When subjected to strain network chains are oriented and can undergo crystallization more easily [102], allowing natural rubber to crystallize in the temperature interval of 25°C-70°C where durable rubber components are needed. Except of NR only a few polymers exhibit this property, e. g. Hydrogenated Nitrile Butadiene Rubber (HNBR) with acrylonitrile content of about 35% [103, 104] and EPDM [105]. In tire industry it is common to blend natural rubber with high *cis* butadiene rubber (BR). With a *cis* content of up to 98 % the latter is able to crystallize at maximum speed at about -50 °C. Kang et al. investigated strain-induced crystallization (SIC) at room temperature in different blends of NR and BR via Wide Angle X-Ray Scattering (WAXS) [106]. While NR was clearly crystallizing under strain BR did not. An earlier study of Toki and coworkers revealed that temperature has to be reduced below 0 °C to observe SIC in BR [107]. Obviously, besides a regular structure, the thermodynamic parameters of the polymer have to be finely adjusted to allow SIC at technically relevant temperatures.

Most authors agree that SIC is responsible for NRs high strength [108]. Accordingly, there is a variety of theories, but no general consensus on the exact reinforcement mechanism. Some ideas involve

1. Strain-induced crystallites act similar to nanoscopic filler particles due to their small size [109].
2. Crystallites behave as multifunctional crosslinks, increasing network strength when strain is too large [110].
3. Crystallites are of fibrillar shape, forming in direction of strain. This is assumed to relax the surrounding matrix wherever strain is too large [111, 112].

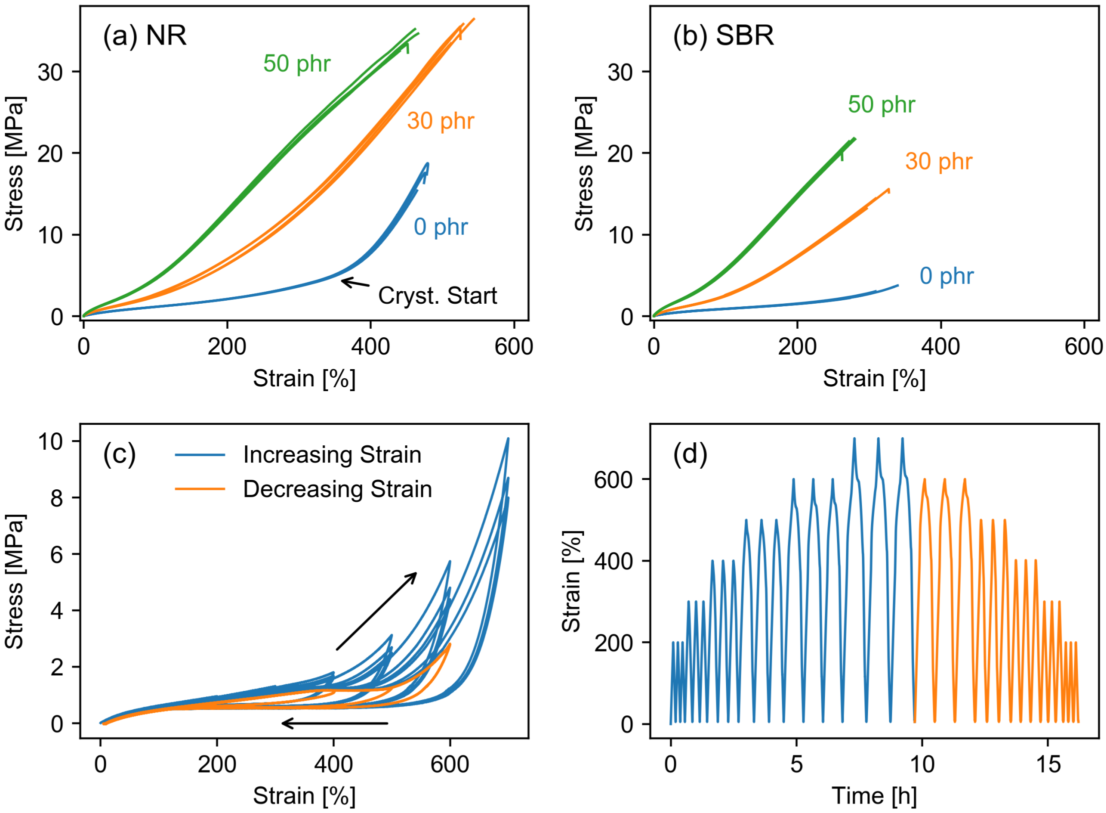

Figure 4.1: (a) Sulfur cured natural rubber filled with varying amount of carbon black N339. (b) SBR compounds with identical vulcanization system. The data was obtained by Matthias Wunde at DIK. (c) Slowly stretched NR cured with 1.0 phr sulfur and CBS during loading and unloading. The material shows softening comparable to Mullins effect for filled rubber. (d) Corresponding strain protocol.

These theories are non-exclusive, such that the emerging behavior of crystallite populations inside the material may be caused by a combination of all of them. Usually, SIC is investigated by means of WAXS which involves placing a stretching machine into a suitable X-Ray beamline. The experimental setup is rather complicated. Especially when high spatio-temporal resolution is required there is need for a sufficiently strong X-Ray source usually provided in large national accelerator facilities. The scattering pattern allows insight into the degree of crystallinity, the geometry of crystals, crystal orientation and even the orientation of the amorphous phase. The results can be summarized as follows

1. Crystal size parallel to stretching direction is around 10 nm but slightly depends on crosslink density. It could be related to the volume of an average network cell, so growth limitation due to network constraints seems to be reasonable. Moreover, it is rather independent of strain, while the remaining lateral dimensions slightly grow with strain. Fully grown crystals have a platelet-like shape [113–116]. The rather constant size of crystals gives rise to the assumption that an increase in crystallinity is mainly due to an increase in number of crystals [113].

2. Crystallization exhibits strong hysteresis with respect to strain. Onset is relatively independent on crosslink density at about 350% strain, while offset strain decreases with decreasing crosslink density. The hysteresis in crystallinity can be correlated to mechanical hysteresis of unfilled NR [32, 110, 115]. An example is shown in Fig. 2 and 6 of publication 4.

3. Despite the growth in non-stretching directions, the main part of crystallinity increase during stretching seems to be due to the formation of new crystals [113].

4. Crystal growth is probably induced by fibrillar crystal nuclei in direction of stretch [113, 117]. Electron microscopy has shown that chain folding of grown crystals is still possible at 900% strain [116].

5. Amorphous phase orientation is reduced when crystals appear. After SIC onset, it is almost constant during further loading. The effect is even more pronounced during unloading of the sample [111, 112]. Mechanically, this is visible as a stress plateau as can be seen in fig. 4.1c.

6. The introduction of fillers changes the shape of the crystallinity curve and shifts the on- and offset strains of SIC towards lower strains. This is attributed to strain amplification effects [110, 115].

7. In fracture mechanics, natural rubber based samples exhibit extraordinarily high crack resistance. They show crack deviation and “zigzag” like cracks in contrast to linear cracks observed in noncrystallizing polymers. Via WAXS it was observed that crystallinity strongly increases in the vicinity of the crack tip. The authors assume that the “zigzag” like path occurs from avoiding the crystalline region [118, 119]. Moreover, crack resistance increases under preload [120].

The present introduction covers just a fraction of the available literature. For more details the reader is referred to the upcoming works.

The first two publications in this chapter are devoted to the quantification of SIC by a newly developed method which is based on the comparison of true temperature and mechanically calculated temperature of the sample. The difference is attributed to the phase transition occuring during SIC. The first manuscript develops the foundations of the method. It is tested on uncured as well as silica- and carbon black filled natural rubber. Recently, an adaption of this work was published by Le Cam [121]. The second paper refines the method, delivering results quantitatively comparable to WAXS measurements. Moreover, the effect of filling degree and prestrain is analyzed. It is shown that fillers shift the onset of crystallization towards lower strains. The shape of crystallinity vs. strain curves changes from triangular to tube-like. Heterogeneous strain amplification is proposed to explain the phenomenon. This is in accordance with the assumption of an amplification factor distribution used in publication 1. Cyclic loading around high strains exhibits vanishing hysteresis, indicating that crystals grow and melt only partially in this strain regime instead of complete melting and successive nucleation.

The third work presents a microscopic theory on SIC during melting and formation of the last and first crystallites. It shows that a large amount of entropy is required for a chain to attach to a crystal, which was probably overlooked or mistakenly neglected by many authors. This may explain the constant crystal size in direction of stretch as well as the independence of SIC strain onset on crosslink density. A fit to an established dataset [32, 110, 122] shows that enthalpy of fusion depends slightly on crosslink density and differs at loading and unloading. The enthalpy of fusion is an important parameter for the evaluation concept presented in the previous publications, such that its dependency on material history should be taken into account in future works. In the end, the publication proposes a scheme for a life-cycle of an NR crystallite during a strain cycle in accordance with the hypothesis of incomplete crystal growth and melting when cycling at large strains.

Polymer 115 (2017) 12–20

Contents lists available at ScienceDirect

Polymer

journal homepage: www.elsevier.com/locate/polymer

Investigation of strain-induced crystallization of carbon black and silica filled natural rubber composites based on mechanical and temperature measurements

Reproduced with permission from Polymer, 2017, 115, 12-20.
https://doi.org/10.1016/j.polymer.2017.03.019

T. Spratte [a, b], J. Plagge [a], M. Wunde [a], M. Klüppel [a, *]

[a] *Deutsches Institut für Kautschuktechnologie e. V., Eupener Str. 33, D-30519, Hannover, Germany*
[b] *Faculty of Engineering, University of Kiel, Kaiser Str. 2, D-24143, Kiel, Germany*

ARTICLE INFO

Article history:
Received 22 December 2016
Received in revised form
22 February 2017
Accepted 11 March 2017
Available online 13 March 2017

Keywords:
Strain-induced crystallization
Self-reinforcement
Natural rubber
Carbon black
Silica
Silica-silane coupling

ABSTRACT

Strain-induced crystallization (SIC) in unfilled and carbon black or silica filled Natural Rubber (NR) with and without silane is investigated. The method introduced in this paper is based on measurements of the surface temperature during tensile test, whereby SIC is quantified by dividing the produced heat into different contributions, namely the dissipative heat, entropy-related reversible heat and crystallization enthalpy. It turns out that there is pronounced SIC in unfilled and carbon black filled NR, while silica/silane systems show less SIC. The degree of crystallinity correlates with the tensile strength of the samples. For silica/silane systems at the same strain level self-reinforcement by SIC is less pronounced possibly due to a lower crosslink density or strain amplification factor. Because of its simplicity, the method developed here is a promising option to investigate SIC on a broad experimental scale and provides an alternative access next to well-established methods like WAXS.

© 2017 Elsevier Ltd. All rights reserved.

1. Introduction

Strain-induced crystallization (SIC) is an important property of natural rubber (NR), which is a stereoregular polymer consisting of ~99.9% cis-poly-isoprene and thus can crystallize partially. If exposed to large strains, the polymer chains align in a more ordered way and entropy decreases supporting the formation of crystallites [1–3]. These crystallites can have fibrillar or lamellar shape [4] remaining quite small (roughly 10 nm) [5–7] and therefore may act in a similar way as nanoscopic fillers or physical cross-links. This implies a kind of self-reinforcement of the rubber which is believed to be the reason of its extraordinary toughness and tear resistance. Accordingly, NR plays a major role in rubber industry, especially for the production of truck tyres, because it strengthens the rubber in highly strained regions and therefore impedes the formation of cracks. Since the development of the green tyre technology for passenger cars, i.e. the replacement of carbon black by silica/silane filler systems, there is great interest in combining the unmatched wear properties of NR with the energy-saving potential of green tyres. Furthermore, silica/silane filled rubbers allow the design of tailor made viscoelastic properties for vibration control systems, since stiffness and dissipative losses can be tuned by the silane type used [8]. Unfortunately, in terms of wear properties, silane coupled NR/silica compounds perform worse than comparable carbon black filled compounds. The microscopic origin of this apparent incompatibility of NR and silica/silane filler systems is still unknown. One reason could be the presence of natural ingredients as proteins and phospholipids in NR, which could disturb the silica-silane reaction during the mixing process [9–11]. Another reason could be the lower crystallization efficiency in the presence of silica/silane filler systems, as recently conjectured from SIC measurements at variously filled NR samples [12], which may be related to a lower internal straining of the polymer chains due to less stable silica clusters in comparison to carbon black. Investigations of strain amplification in silica and carbon black filled rubbers have shown that the strain amplification factor at same filler loading is generally smaller for silica/silane systems delivering a lower stress level at large strains and a less pronounced Payne effect (comp. e.g. Fig. 10.18 in Ref. [28]). In addition, the crystallization degree depends on the dispersion state of the filler which may be much different for both filler systems.

---

* Corresponding author.
E-mail addresses: plagge.jan@gmail.com (J. Plagge), manfred.klueppel@DIKautschuk.de (M. Klüppel).

http://dx.doi.org/10.1016/j.polymer.2017.03.019
0032-3861/© 2017 Elsevier Ltd. All rights reserved.

The effect of filler on crystallization efficiency is a question of high technological relevance which will be addressed in the present paper. Thereby, we will refer to a new evaluation procedure for SIC based on temperature measurements at stretched samples. A number of measurement techniques, such as differential scanning calorimetry (DSC), nuclear magnetic resonance spectroscopy (NMR) and mainly wide-angle X-ray scattering (WAXS) are used by several authors [5–7,13–21] for the characterization of SIC. In particular, it was demonstrated by WAXS measurements that the size of the crystallites remains small on the nanoscale and increases only slightly after the onset of SIC. The crystallite length (L_{002} in stretching direction) was found in the range of 8–10 nm, almost independent of stretching ratio, while the lateral dimensions increase slightly with stretching ratio after the onset of SIC, from 4 to 8 nm (L_{200}) and 2–3 nm (L_{120}), respectively [6]. Similar results were obtained by other authors [5] and also for various carbon black and silica filled NR [7], indicating that the entanglement mesh size of the polymer network limits the crystal growth above the critical onset strain of SIC. Indeed, from the mean spacing of entanglements in the relaxed state, $d_0 = 5.14$ nm [22], the mesh size in stretching and lateral directions can be estimated by referring to the non-affine tube model of rubber elasticity, which was shown to fit the stress-strain response of unfilled NR in the non-SIC regime very well [23]. This model is based on a non-affine deformation law of entanglement spacing (in spatial direction i = 1, 2, 3), $d_i = d_0\,\lambda_i^{1/2}$, resulting from a partial relaxation of entanglements upon stretching. With this, the mesh size well above the onset of SIC, e.g. at stretching ratio $\lambda_1 = 6$, is obtained as $d_1 = 12.6$ and $d_2 = 3.3$ nm in stretching and lateral directions, respectively. Of cause this rough estimate assumes incompressibility and does not take the volume shrinkage into account appearing upon crystallization. Nevertheless, it is in fair agreement with the above cited results of crystallite size, confirming that the entanglement spacing of the polymer network limits the crystal growth in highly stretched NR. Note that more or less the same mesh size is realized for filled systems indicating that it limits crystal growth in the same manner.

According to WAXS measurements the onset of SIC at room temperature (20 °C) decreases slightly from 350% to 250% strain with increasing crosslink density of peroxide cured, unfilled NR [18] and decreases successively with filler loading down to 100% strain for highly filled NR [14,15]. It appears that in the presence of fillers, crystallization is amplified, since regions of polymer between non-deformable filler particles can be exposed to higher local strains than external strain. This results from hydrodynamic strain amplification that increases with filler concentration strain in analogy to the increase of viscosity of a liquid due to rigid inclusions [24,25] implying that the onset of SIC is shifted to smaller strain values. With increasing temperature, SIC is more and more suppressed and the onset of crystallization for unfilled and filled NR increases up to 500% and 200% strain at 60 °C, respectively [15]. In addition, the crystallization rate decreases significantly with increasing ambient temperature and the overall crystallinity decreases by about 80% if the temperature increases from 10 °C to 60 °C [15]. For sufficiently cured unfilled NR with $M_c < 7.000$ g/mol, the crystallization rate also decreases with crosslink density since the chain mobility decreases [5]. The chain orientation of unfilled and filled stretched NR networks has been estimated by measuring the line splitting of quadrupolar NMR spectra [15] and by evaluating the anisotropy of the amorphous halo obtained from WAXS measurements [13,16,19]. The data show that the orientation levels out just at the onset of SIC indicating that the chains in the vicinity of the crystals relax partly. This has been correlated with a softening effect of the mechanical stress due to additional free chain length associated with the chain alinement in the crystals [13,16]. In all measurements a pronounced hysteresis of SIC was found, almost independent of filler loading, which correlates with the mechanical hysteresis [13,15] and is mainly due to differences in melting and crystallization temperature [26]. The characteristic nucleation time of SIC at room temperature was found to be very small in the range of 20 ms [16,17]. Recently, the kinetics of crystal growth was investigated by WAXS measurements on harmonically and rapidly stretched unfilled and filled NR samples in the millisecond range [20,21,32]. It was found that the crystal growth can be well described by a diffusion-limited process with an Arrhenius-like thermal activation rate constant. The activation energies are in the range of 20–50 kJ/mol, reflecting the typical dynamics of entangled polymer chains. Dependent on temperature and final strain level, crystallite growth levels out almost completely after a few minutes. This is in contrast to the very large crystallization time of NR in the un-stretched state below crystallization temperature. The crystallization half-life time at 0 °C is about 260 h, but this value decreases significantly with strain showing already a half-life time of 110 h at 25% stretching [1]. Finally, we point out that the crystallization time of uncured NR in the un-stretched state is still about three orders of magnitude larger than for a high-cis polybutadiene rubber (BR) [2]. At present it remains unclear how this affects the SIC properties at large strains delivering the unique mechanical toughness and strength of NR, which is much lower for BR though the topological constraints due to entanglements are very similar for both rubbers.

In the present paper, SIC of NR is evaluated at relatively large strain rates of 0.5 s^{-1}, which is still slow compared to the characteristic nucleation time of SIC in the range of 20 ms. Uniaxial cyclic stress-strain measurements will be done at unfilled and carbon black or silica filled NR samples with and without silane coupling agent. Online temperature measurements performed with an IR camera will be used to evaluate the strain dependent crystallization of the samples, which is an exothermal process increasing the temperature. This will be distinguished from the entropy related heating due to the mechanical work done at the samples and the heat losses. In the next section a basic consideration of thermo-mechanical processes taking place in strain-crystallizing rubbers is reviewed and the evaluation procedure is explained.

2. Thermal heating of strain-crystallizing rubbers

Entropy elasticity is an essential property of rubber and describes the appearance of an entropic restoring force upon stretching. In the stretched state the polymer chains are aligned, which means that there are less possible conformations than in the relaxed state, where the entropy gains its maximum and the polymer chains form coils. Accordingly, for entropy elastic rubbers under adiabatic conditions the whole work done on the system is transferred into microscopic kinetic energy and no potential energy is stored. Thus the internal energy of entropy elastic systems is purely kinetic, being measurable as temperature [1,2]. In contrast, in steel mainly potential energy is stored upon stretching.

Considering the first law of thermodynamics:

$$dU = dW + dQ \tag{1}$$

for an adiabatic process ($dQ = 0$) and assuming no energetic contributions to the internal energy, it becomes clear, that all work done at the system will increase the sample temperature:

$$dU = c_p \rho dT_{\mathrm{mech}} = dW = \sigma d\varepsilon \tag{2}$$

Here, T_{mech} refers to the temperature increase due to mechanical work done on the system, σ is stress and ε engineering strain. The sample density ρ and heat capacity c_p are assumed to be independent of strain and temperature as listed in Table 1. For strain crystallizing rubbers the internal energy density also contains potential energy stored in the crystallites. Accordingly, it can be decomposed into the energetic contribution of crystallization and the entropic contribution:

$$\mathrm{d}U = \mathrm{d}U_{\mathrm{kin}} - \mathrm{d}U_{\mathrm{cryst}} \tag{3}$$

with

$$\mathrm{d}U_{\mathrm{kin}} = c_p \rho \mathrm{d}T_{\mathrm{IR}} \tag{4}$$

The subscript IR indicates, that this is the “true” temperature measured by the infrared camera. The negative sign in eq. (3) indicates that crystallization is an exothermal process. The release of crystallization energy leads to a reversible warming-up of the rubber, since the same amount of heat is consumed during melting of the crystallites under relaxation. The crystallization energy density can again be expressed in terms of density and heat capacity:

$$\mathrm{d}U_{\mathrm{cryst}} = c_p \rho \mathrm{d}T_{\mathrm{cryst}} \tag{5}$$

This delivers the temperature contribution of strain induced crystallization.

In reality adiabatic conditions are hard to realize and there is heat exchange with environment. In our case heat loss $\mathrm{d}Q_{\mathrm{loss}} = -\mathrm{d}Q$ is caused by thermal radiation and convection. The higher the temperature difference between sample and environment the larger the heat losses. This cooling effect is considered by noticing, that heat transfer from rubber to environment is, to first order, proportional to the temperature difference to ambient temperature $\Delta T = T_{\mathrm{IR}} - T_0$. In addition, heat transfer is proportional to the surface area S of the approximately two dimensional flat cuboid sample (Fig. 1) with dimensions a', b', c' and $c' \ll b' < a'$. For uniaxial loading $a' \sim \lambda$ and $b' \sim c' \sim 1/\sqrt{\lambda}$, such that we obtain:

$$S = 2(a' \cdot b' + b' \cdot c' + a' \cdot c') \approx 2a' \cdot b' \sim \lambda \frac{1}{\sqrt{\lambda}} = \sqrt{\lambda} \tag{6}$$

where $\lambda = 1 + \varepsilon$ is the strain ratio of the sample. Altogether, for cyclically strained rubbers lost energy can be calculated as an integral over time t:

$$Q_{\mathrm{loss}} = c_{\mathrm{p}} \rho T_{\mathrm{loss}} = a \int_0^t \Delta T(t') \sqrt{\lambda(t')}\, dt' + b \tag{7}$$

where a is a proportionality factor collecting heat-transfer constants and capacities and b is a constant collecting higher order terms and systematic errors, e. g. an offset of the infrared camera.

Reformulating the first law of thermodynamics, we can now write a temperature balance equation:

Table 1
Heat capacity and mass density of the sample pool.

Sample	c_p [J/g K]	ρ [g/cm^3]
NR	1.78	0.93
NR/N330	1.52	1.11
NR/U7000	1.55	1.14
NR/U7000 + Si69	1.57	1.14
SBR/N330	1.49	1.09

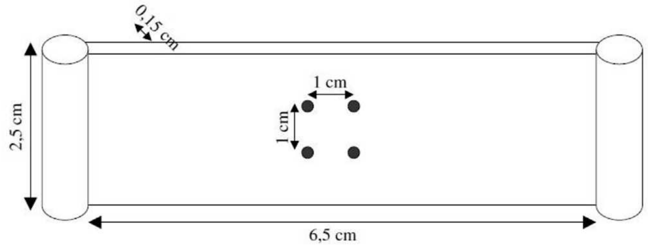

Fig. 1. Geometric shape of the tensile test samples. A square is marked in the middle by reflection points for evaluating the mean surface temperature by IR.

$$\mathrm{d}T_{\mathrm{cryst}} = \mathrm{d}T_{\mathrm{IR}} + \mathrm{d}T_{\mathrm{loss}} - \mathrm{d}T_{\mathrm{mech}} \tag{8}$$

or

$$T_{\mathrm{cryst}}(t) = T_{\mathrm{IR}}(t) + \int_0^t \left[a\, \Delta T\left(t'\right) \sqrt{\lambda\left(t'\right)} - \sigma\left(t'\right) \frac{\mathrm{d}\varepsilon\left(t'\right)}{\mathrm{d}t'} \right] \frac{\mathrm{d}t'}{c_{\mathrm{p}} \rho} + \frac{b}{c_{\mathrm{p}} \rho} \tag{9}$$

Since at room temperatures no crystallites are present at zero strain, T_{cryst} is zero at these points: $T_{\mathrm{cryst}}(\varepsilon = 0) = 0$. So the equation can be rewritten for zero strain:

$$0 = T_{\mathrm{IR}}(\varepsilon = 0) + T_{\mathrm{loss}}(\varepsilon = 0) - T_{\mathrm{mech}}(\varepsilon = 0) \tag{10}$$

The free parameters a and b can be fitted such, that this equation is fulfilled at each point where $\varepsilon = 0$.

3. Experimental

3.1. Materials

Four batches of purified natural rubber (Pale Crepe) have been prepared in an internal mixer containing different filler systems: 50 phr carbon black N330, 50 phr silica (Ultrasil U7000, Evonik) without silane, 50 phr silica with 4.17 phr silane coupling agent TESPT (Si69) and an unfilled sample. Additionally, all samples contain activator (3 phr ZnO and 1 phr stearic acid), antioxidant (1 phr IPPD), accelerator (1.5 phr CBS) and cross-linker (1.5 phr sulphur). For comparison, a solution styrene-butadiene rubber (S-SBR) filled with 50 phr N330 and cured with 1.2 phr sulphur as well as 2.0 phr CBS was prepared.

Vulcanization curves have been recorded for each batch and the cross-linking was done by compression moulding at 160 °C up to the t_{90} time obtained by vulcameter measurements. A sketch of the shape of the tensile test samples used for temperature measurements can be seen in Fig. 1. The dimensions are 2.5 cm width, 6.5 cm length and 0.15 cm thickness.

The heat capacities and densities of all materials have been determined with differential scanning calorimetry (DSC) and buoyancy measurements with a pycnometer, respectively. The results for the samples used are listed in Table 1.

3.2. Instruments and procedures

A mechanical analysis of the different samples has been performed by standard tensile test with S2-type samples (Zwick UPM-03). For this purpose 3 tensile specimens per batch have been stretched until fracture and the stress-strain curves have been recorded. In addition, cyclic stress-strain measurements with 5 cycles first up to 300% and then 450% strain were performed with

S3A-type samples in a heating chamber at 23 °C, 60 °C and 100 °C. The strain was measured via an optical system consisting of two cameras tracking fixed light reflection points on the samples. The velocity of the machine was 200 mm/s corresponding to a stretching rate of about 0.15 s^{-1}.

The influence of filler type on the crystallization process has been investigated by periodic stretching of the samples shown in Fig. 1 over four cycles from the relaxed state to 350% strain for the filled and 600% strain for the unfilled rubber, respectively. To minimize thermal losses, the cross-head velocity was chosen to be as fast as possible, 2000 mm/min, corresponding to a strain rate of 0.5 s^{-1}. At the turning points the tensile testing machine decelerates and accelerates again, delivering a more or less pronounced relaxation of the samples (compare Fig. 4). A thermal imaging camera (Jenoptic Vario Therm) was used to record the behaviour of surface temperature with a sampling rate of 1 Hz. The camera was positioned in a distance of 1 m from the sample and operated with an emissivity coefficient of $\varepsilon^* = 1$. It is known, that the emission of black rubber is close to black body radiation, e. g. $\varepsilon^* = 0.95$ [27]. Since the exact value is not known, we rely on absorption of the measurement error into constant b in eq. (7). Fig. 2 shows an example of two infrared images at different strain values. Four light reflection points were glued on the samples in a square of 1 cm × 1 cm to indicate a reference area. Consequently, the average surface temperature in this area was calculated.

4. Results and discussion

Fig. 3 shows the stress-strain curves up to rupture of the investigated NR composites at room temperature with 50 phr filler in comparison to unfilled NR. It shows that the stress level as well as the tensile strength of the samples strongly depends on filler type. As expected, the best mechanical performance is observed for the sample filled with carbon black, which is the standard industrial filler e.g. for truck tire tread compounds. For the NR/silica/silane system stress values and also the tensile strength are lower though the maximum strain is somewhat larger. The worst mechanical performance among the reinforced samples is found for the NR/silica system without silane coupling agent.

Examples of stress-strain curves (unfilled and CB filled) obtained under fast repeated cycling at 0.5 s^{-1} are shown in Fig. 4, whereby the strain history is depicted in the inset. Both curves have in common that the first cycle shows the strongest hysteresis compared to the following ones. This behaviour is especially significant for the carbon black filled samples and is related to stress softening due to the irreversible breakdown of the filler network also denoted Mullins-effect [28,29]. Furthermore, rearrangement of the filler network during the first cycle results in a significantly larger release of energy than in the later cycles.

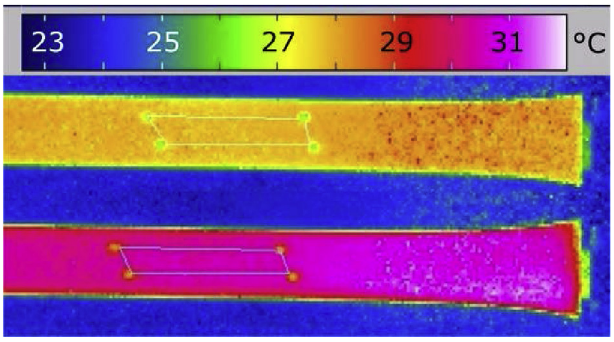

Fig. 2. Infrared images of two differently elongated states. The four reflection points marking the area for evaluating the mean surface temperature are visible.

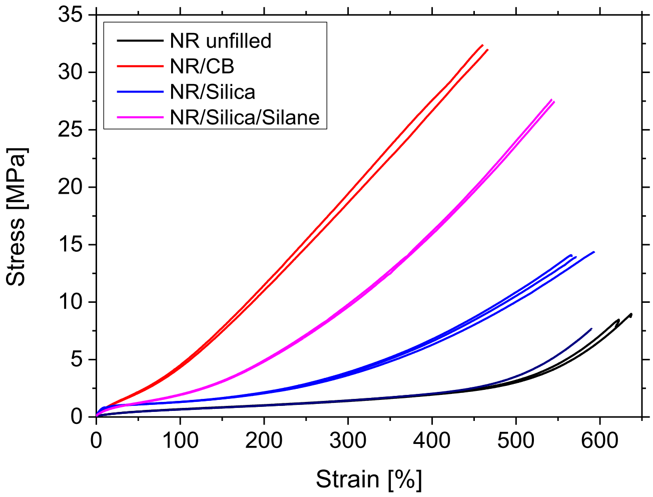

Fig. 3. Stress-strain curves at 0.15 s^{-1} up to rupture of variously filled and unfilled NR samples, as indicated.

Integration of the measured stress-strain curves shown in Fig. 4 yield the energy density, whereby the area in the hysteresis loops represents the energy dissipated irreversibly as heat due to internal friction. In addition heat is stored reversibly in the entropy-elastic stretched polymer chains. The stored and dissipated heat results in an increase of sample temperature, which can be calculated from the work integral via division by sample density ρ and heat capacity c_p Accordingly, the mechanical work done on the rubber delivers a temperature increase T_{mech} if no heat loss is considered:

$$T_{\mathrm{mech}}(t) = \sum_i \mathrm{sign}(\dot{\varepsilon}_i) \int_0^{\varepsilon_i} \frac{\sigma}{\rho\, c_p} d\varepsilon \quad \text{with} \quad \mathrm{sign}(\dot{\varepsilon}) = \pm 1 \text{ for } \dot{\varepsilon} \gtrless 0 \tag{11}$$

Here, each half-cycle is integrated separately with different sign, taking into account that part of the stored energy is retrieved during retraction of the samples. Note that the corresponding integration over time used in eq. (9) delivers the changing sign for stretching and retraction direction in agreement with eq. (11). The temperature $T_{\mathrm{mech}}(t)$ calculated with eq. (11) from the measured stress-strain cycles is shown in Fig. 5 for various samples. In addition, the detected IR-temperature is shown. It appears that the measured surface temperature shows an analogous behaviour compared to the mechanically calculated temperature. In particular, the first peak, which represents the first stress-strain cycle, shows the highest rise in temperature. However, the mechanically calculated temperature shows some difference: the maximum temperature increases with each cycle and is systematically higher than the measured temperature. This is due to heat losses into the surrounding, which are not considered in the calculation under adiabatic conditions. The heat losses and the corresponding loss temperatures are calculated with eq. (7) and fitted such, that the sum of the measured IR temperature and the loss temperature are equals the mechanical temperature of the relaxed samples at $\varepsilon = 0$ (eq. (10)).

The results in Fig. 5 show, that the measured temperature corrected by temperature loss (IR + loss) is higher than the one calculated from mechanical hysteresis. Since T_{mech} contains both the irreversible dissipative contribution and the reversible contribution arising from entropic changes during stretching of the rubber, the additional third contribution must be related to SIC. The

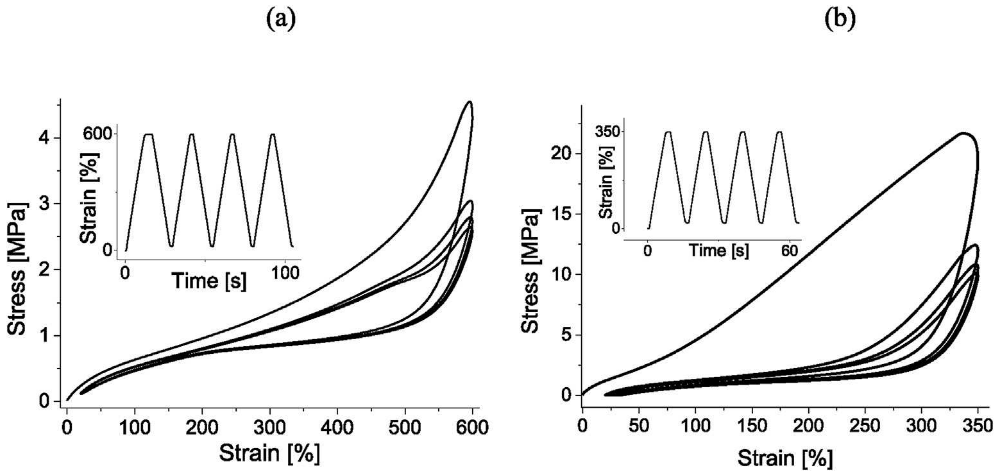

Fig. 4. Stress-strain cycles for unfilled (a) and carbon black filled NR (b) at 0.5 s^{-1} up to 600% and 350%, respectively. Strain histories are shown in the inset.

degree of crystallization $K(t)$ is calculated by transforming the temperature deviation T_{cryst} from eq. (9) to the SIC related energy via heat capacity and density and dividing it by the crystallization enthalpy of the polymer component per unit volume (excluding filler):

$$K(t) = \frac{\rho c_p T_{\text{cryst}}(t)}{\left(1 - \Phi_{\text{filler}}\right) \Delta H_{\text{cryst,NR}}} \tag{12}$$

Here, ρ and c_{p} are given in Table 1 and Φ_{filler} represents the filler volume fraction. The crystallization energy of natural rubber is approximated by the enthalpy of fusion $\Delta H_{\text{cryst,NR}} = 61\ \text{J/cm}^3$ [30]. This approximation is justified by a relative change in volume of about $\Delta V_{a-c} \approx -10\%$ from amorphous to crystalline state, which is based on an estimated volume change of highly elongated NR of about 3% and approximately 30% degree of crystallinity [1,31]. The internal pressure lies in the range of $p \approx 20$ MPa, such that $p\ V_{a-c} \approx -2\ \text{J/cm}^3$. As this is most probably an overestimation we assume $\Delta H_{\text{cryst,NR}}$ and the crystallization energy to be roughly the same within the range of experimental errors. We point out that this approach neglects surface tension effects of the molten-crystalline interface. Including them would require detailed knowledge about the amount and shape of crystallites, which isn't available. Moreover it is known, that NR exhibits a maximum crystallinity of about 30%. As $\Delta H_{\text{cryst,NR}}$ was derived comparing WAXS to DSC data there are necessarily surface effects included in the value.

The calculated degree of crystallization is plotted in dependence of strain for the second, third and fourth cycle in Fig. 6. Obviously, all samples show a pronounced crystallinity, which depends on the filler type. Similar to the mechanical data shown in Fig. 4 also the crystallinity exhibits a hysteresis, i.e. the crystallinity obtained for the up-cycle to maximum elongation differs from the back cycle to the relaxed state. The fact that the crystallinity during stretching is lower than during retraction indicates that the melting of crystallites happens delayed compared to the formation of crystallites. Metastable states during formation and melting of crystallites have been proposed as a possible reason for unstretched polymers [26]. Furthermore, the onset of crystallization seems to be roughly the same for all filled samples and is located at around 200% elongation. For the unfilled sample it appears at about 420% strain. This indicates that the polymer chains between the non-deformable filler particles are exposed to locally higher strain than the external strain and that the details of the filler are of minor importance concerning SIC onset. The silica filled sample without silane coupling shows significantly less crystallization (4%) compared to the other samples, while carbon black filled NR shows the highest degree of crystallization (10%) followed by the silica/silane system (8%). This ranking agrees with the findings of Chenal et al. [7], though the silica-polymer coupling had a weaker influence on crystallinity. The results also agree regarding carbon black filled samples which show a slightly increased crystallinity compared to (coupled) silica filled ones. Our data indicate that the maximum crystallinity of the filled samples scales roughly with the stress level at 350% strain of the tensile test data shown in Fig. 3, which is mainly attributed to differences in strain amplification [28]. However, it is not clear from these findings whether strain amplification by non-deformed filler units is the only mechanism governing SIC. The increased stress level may also be attributed to a higher apparent crosslink density due to additional polymer-filler couplings. We point out that this is expected to reduce the crystallinity, because a smaller mash size should hinder SIC. This is confirmed by unfilled NR, which tends to exhibit lower crystallinity at higher degrees of crosslinking at fixed strain [5,7].

A systematic deviation from the thermo-mechanical model of Section 2 is the "negative crystallinity" observed in Fig. 6, which is clearly seen in the medium stretching regime for the unfilled but also for the filled samples. It could be an effect of non-entropic energetic contributions whereby potential energy is stored, e.g. rotation of carbon bonds, temporary network bonds or stretching of filler clusters, although the latter case seems to be of minor importance, since the problem occurs for unfilled NR, as well. Temporary network bonds are less favorable in stretched states, because each bond represents an additional crosslink, thus lowering the entropy. A further reason for energy-elastic contributions could be attractive chain interactions close to the crosslinks, which are separated upon stretching, or long time relaxation mechanisms due to slowly relaxing network defects, which act similar to temporary network bonds. The "negative SIC" might also shift the onset of crystallization to somewhat larger values compared to the crystallization onset found with the WAXS method at 350% strain for sulfur cured unfilled NR and 150% strain for 50 phr carbon black filled NR, both at 40 °C [15]. The obtained maximum crystallinities of about 9% at 600% strain for unfilled NR and about 10% at 350% strain for carbon black filled NR differ from the majority of WAXS studies showing larger crystallinities by a factor of up to 2 [6,15]. However, also from WAXS investigations large deviations of crystallinity are found by various authors using different evaluation procedures, e.g. 10% at 600% strain for unfilled

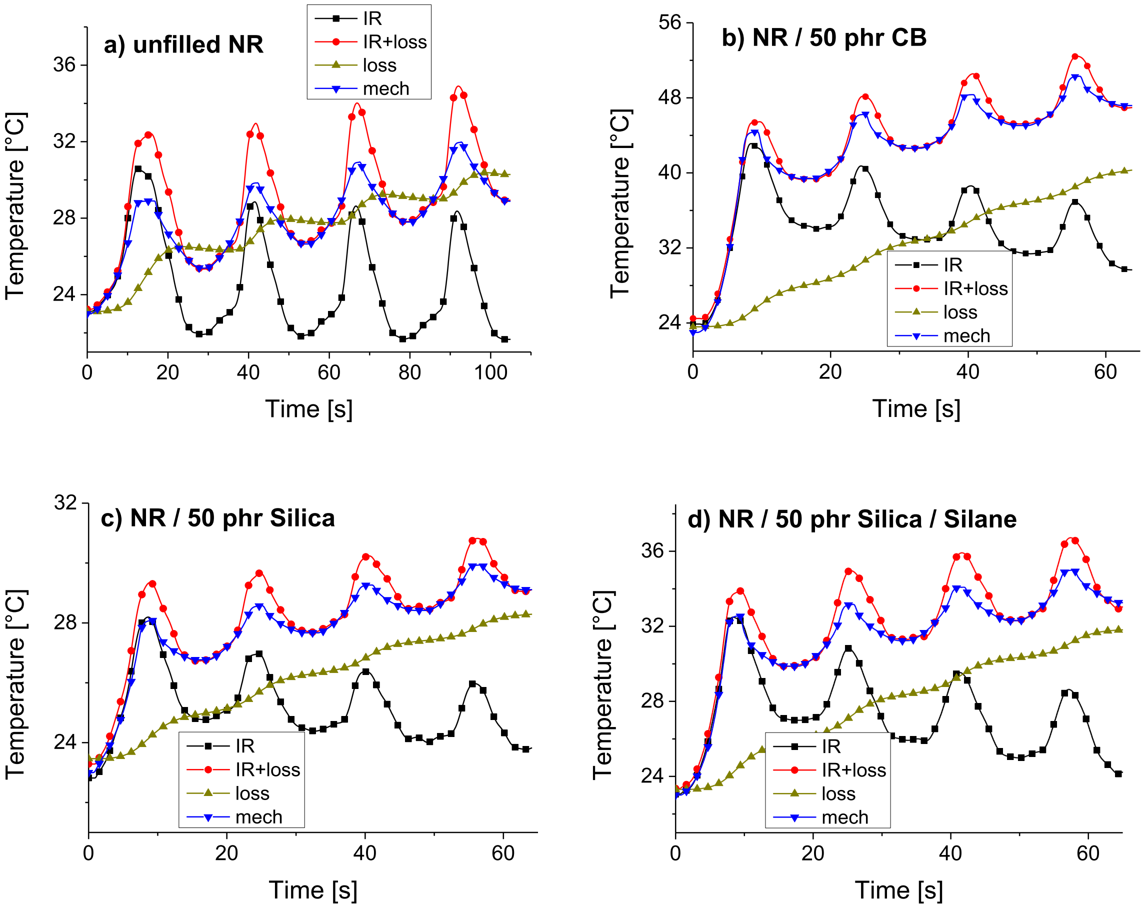

Fig. 5. Temperature variations for unfilled and filled NR samples, as indicated, measured by infrared camera (IR) as compared to mechanical evaluations (mech) calculated with eq. (11), loss temperatures (loss) calculated according to eq. (7) and fitted such, that the sum of IR and loss temperature (IR + loss) equals the mechanical temperature (mech) at the minima where $\varepsilon = 0$ (eq. (10)). The difference between temperature (IR + loss) and (mech) is a measure of crystallinity, which is positive due to the exothermal character of SIC.

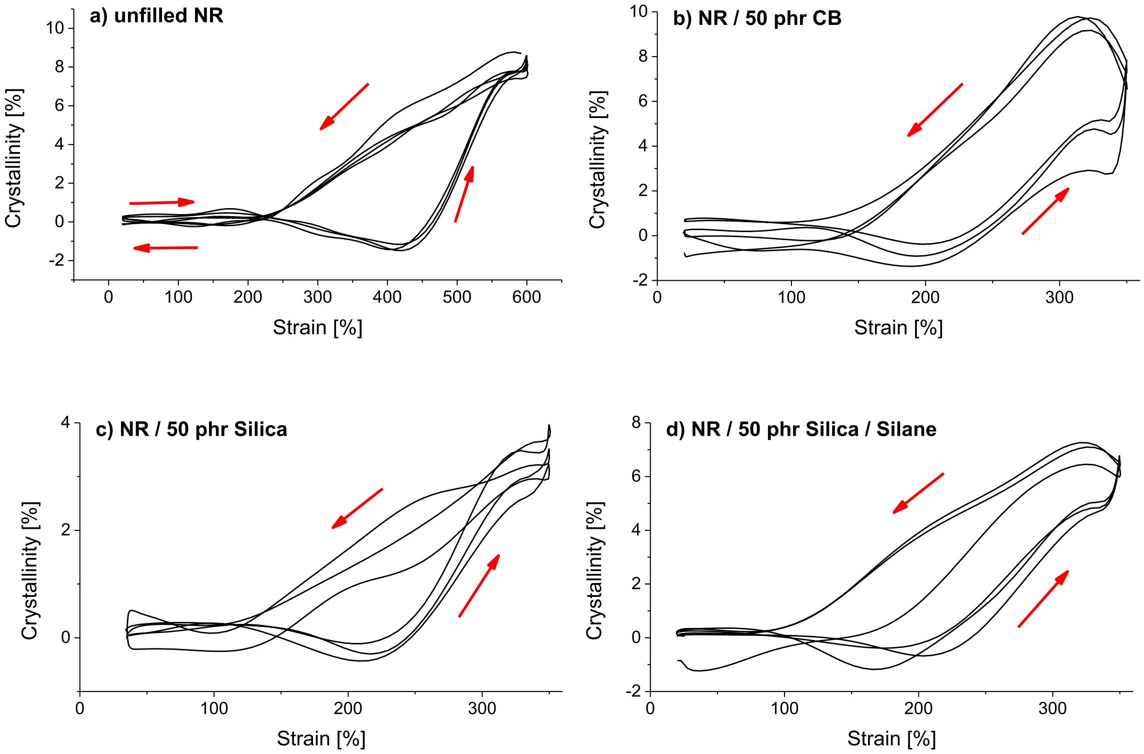

Fig. 6. Degree of crystallinity vs. strain under cyclic loading for variously filled NR samples, as indicated.

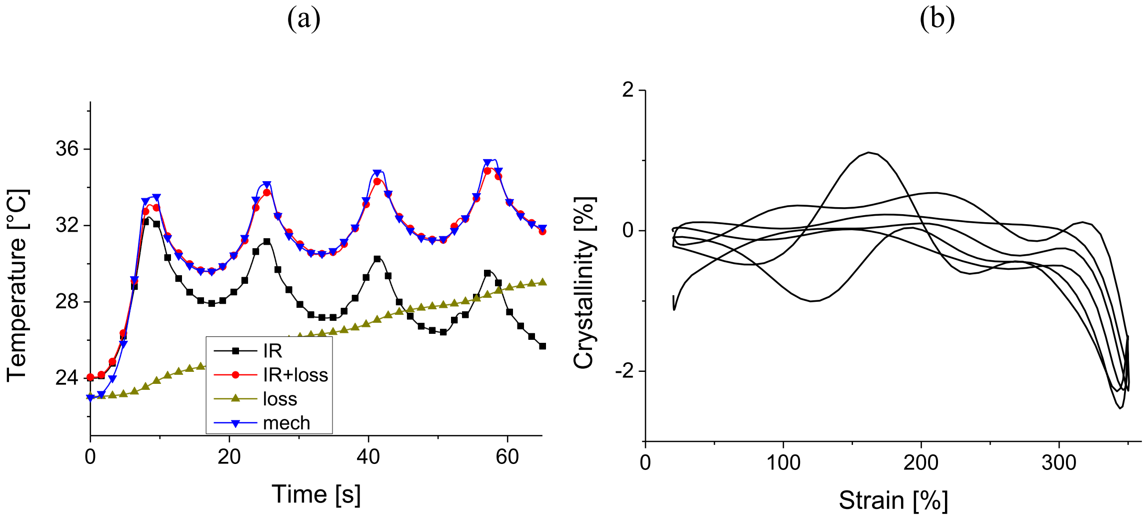

Fig. 7. Measured and calculated temperature contributions as in Fig.5(a) and degree of crystallinity vs. strain (b) for S-SBR with 50 phr carbon black.

NR [14], which agrees fairly well with our estimate. In addition, the energetic contribution mentioned may be a systematic offset, shifting the whole crystallinity curve to lower values.

The differences between our data from IR-measurement and WAXS data from different authors can also result from the different NR types used. A purified, high molar mass type (Pale Crepe) was used in our studies while other authors applied non-purified standard NR types with reduced chain length (SMR, SVR, SIR…) or the high molar mass type (RSS1). Also, many WAXS studies use strain rates up to 2 decades slower than in the present work, which could explain a larger crystallinity, although SIC is reported to take place on generally small timescales compared to our deformation speed [16,17,32]. Due to the fast deformation rates we used in our studies, an increase of sample temperature up to 20 °C takes place (see Fig. 5), which in turn suppresses crystallization. A temperature shift from 20 °C to 40 °C in unfilled natural rubber has been reported to decrease crystallinity from 16% to about 12% [13]. We point out, that the pronounced increase in crystallinity for the carbon-black and silica/silane systems at maximum strain can be related to the fast relaxation processes at the upper turning point of each cycle. At these points the testing machine has to slow down to allow a continuous change of direction, which yields a strong decrease in stress (due to relaxation) at almost constant strain (see Fig. 4). It is clear, that this relaxation process should dissipate energy, but isn't captured immediately by the work integral, since $d\varepsilon \approx 0$ at the turning points (see eq. (11)). Hence at these points calculated temperatures will stay below reality, generating an overestimation of crystallinity. On the other side, the strong mechanical relaxation of the samples can also be a result of the crystallization process itself, since the strong chain alinement in the crystals implies relaxation of the surrounding chains. This softening effect of the mechanical stress due to additional free chain length, associated with the strong orientation of chain segments in the crystals [13,16,19], can considered to be an important homogenization mechanism in highly stretched polymer domains, possibly delivering the extraordinary ultimate properties of strain-crystallizing elastomers. It compares to the stress homogenization mechanism in highly reinforcing filled rubbers, where stress peaks in a more or less heterogeneously cross-linked rubber matrix are balanced by the rupture of filler clusters [28,29].

The S-SBR compound with carbon black shows no significant SIC, as can be seen in Fig. 7. Indeed, for the statistical co-polymer S-SBR no crystallinity is expected, confirming the applied procedure. The observed deviations from zero in Fig. 7b) below 300% strain are in the range of experimental errors, while the negative peak above 300% strain seems to be a systematic deviation. This compares to the negative crystallinity contributions in Fig. 6, indicating that the thermo-mechanical approach in Section 2 exhibits some insufficiencies at medium and high strains as previously discussed.

The SIC-induced stress softening effect discussed above can be observed in more detail by referring to the temperature dependent stress-strain cycles for carbon black and silica/silane filled natural rubber shown in Fig. 8. Here, the fifth cycles of repeated stretching from 50% up to 300% and afterwards from 50% up to 450% are compared for 23 °C, 60 °C and 100 °C. A closer look on the mechanical data shows that with increasing temperature the mean initial slope of stress-strain cycles increases, which can be related to the entropic character of rubber elastic stress, being proportional to the absolute temperature. In addition, the hysteresis decreases significantly with increasing temperature since SIC is suppressed at high temperatures. The remaining hysteresis at 100 °C becomes significantly smaller and is probably related to the filler alone. However, we also observe that the stress-strain cycles at medium strain become more flat with decreasing temperature. This SIC-induced stress softening effect is associated with additional free chain length in consequence of chain alinement during the formation of crystals [13]. Especially for the large cycles, the stress in the down-cycle is more or less plateau–like between 100% and 300% strain, indicating that the chain stretching remains almost constant during melting of the crystals in the retraction phase. A further effect is the upturn of stress-strain cycles at large strain, which appears at smaller strain with decreasing temperature. This stress hardening effect is related to the finite extensibility of network chains and seems to be affected by the formation of crystals, as well, since more crystals deliver shorter chains. Accordingly, the upturn is more-steep for strain crystallizing polymer networks since the apparent chain density increases when crystallites are formed. For both filler types, carbon black and silica/silane, a quite similar qualitative behaviour is observed in Fig. 8. However, the stress level is about a factor 2 smaller for the silica/silane system. This indicates that the strain amplification factor resulting from hard-rigid filler structures in both system is also similar since SIC is controlled by the internal strain of the rubber matrix. Accordingly, the different stress level seems to be related to a lower cross-linking density of the silica/silane system, though the same vulcanization system was used. A reason could be a

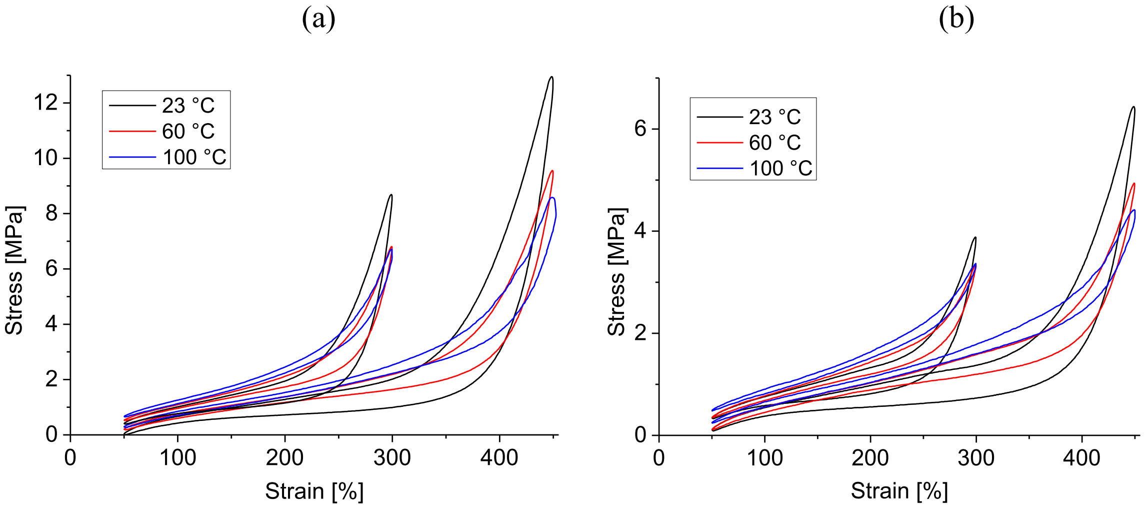

Fig. 8. Stress-strain cycles of carbon black (a) and silica/silane filled NR (b) at 0.15 s^{-1} for three temperatures, as indicated. Only fifth cycles of stretching up to 300% and 450% are shown.

pronounced adsorption and interaction of the accelerator CBS with the silica surface delivering a reduced cross-linking density compared to carbon black. Whether this interpretation is correct or not will be investigated in future tasks.

We finally point out that the evaluation method for SIC developed in this paper is based on simple thermodynamic assumptions and does not refer to a microscopic picture of crystallite formation, growth and melting. One major advantage of the method presented here is its simplicity and the fact that it works based on a small number of assumptions. With this method we're unable to distinguish crystal amount and crystal size, we only measure the total crystalline fraction. A first microscopic theory of SIC based on entropy elasticity has been developed about 70 years ago by Flory [33]. Recently, this concept was extended in a phase field model by Laghmach et al. [34] by focusing on topological constraints to quantify effects of entanglements and cross-links on the crystallite growth. In this work, surface tension effects play a central role implying that additional assumptions about crystal dimensions and shape are required. An advanced microscopic concept of SIC must take into account the nucleation and growth of the crystals differing from the melting process, which possibly can explain the complex stress-strain cycles of unfilled and filled NR in dependence of crosslink density and temperature (comp. Fig. 8). So far, such theory is still missing though it is strongly demanded for a better understanding of high performance technical rubber goods based on strain crystallizing elastomers.

5. Summary and conclusions

It has been shown that on-line temperature measurements during cyclic tensile testing of unfilled and filled NR together with the evaluation of mechanical work done at the systems can be used to characterize the degree of strain-induced crystallization (SIC). The mechanical work consists of a purely elastic part and a dissipated energy part that both can be calculated by integration of the stress-strain-curves. The former delivers a temperature increase upon stretching due to the entropic origin of rubber elasticity that is fully reversible upon retraction. The latter one is equal to the dissipated heat which is consequently converted into an irreversible increase of temperature. Considering a correction of heat losses into the surrounding, the difference in calculated and corrected temperature can be finally converted into a degree of crystallinity. A drawback of this method is the appearance of a negative degree of crystallinity for medium strains, which could be explained by energetic elastic contributions not captured by the purely entropy elastic model.

The results obtained from this evaluation procedure demonstrate that the onset of crystallization is roughly the same for all filled NR samples. The carbon black filled NR shows the highest degree of crystallization followed by the silica/silane system at equal strain level, while silica filled NR without silane coupling agent shows the lowest crystallinity. The maximum crystallinity of the filled samples at 350% strain correlates with the stress level of the tensile test data during first stretching. A lower self-reinforcement by SIC for the silica/silane system compared to carbon black at the same strain level is also concluded from temperature dependent stress-strain cycles, which can be related to a lower crosslink density and/or less strain amplification by non-deformed filler units. For carbon black filled S-SBR samples no crystallinity is detected in the range of experimental errors, confirming the applied procedure. The SIC evaluation method developed here is a promising option to investigate synergetic interactions between filler networking and SIC, especially to understand the poorer fatigue and wear properties of silica/silane filled NR composites compared to carbon black filled NR.

Acknowledgements

We thank the Deutsche Forschungsgemeinschaft (DFG, grant KL 1409/9-1) for funding.

References

[1] L.R.G. Treloar, The Physics of Rubber Elasticity, Clarendon Press, Oxford, 1975.
[2] U. Eisele, Introduction to Polymer Physics, Springer, Berlin, Heidelberg, N. Y., 1995.
[3] B. Ozbas, S. Toki, B.S. Hsiao, B. Chu, R.A. Register, I.A. Aksay, D.H. Adamson, Strain-induced crystallization and mechanical properties of functionalized graphene sheet-filled natural rubber, J. Polym. Sci. part B Polym. Phys. 50 (10) (2012) 718–723.
[4] G.S.Y. Yeh, K.Z. Hong, Strain-induced crystallization, Part III: theory, Polym. Eng. Sci. 19 (6) (1979) 395–400, http://dx.doi.org/10.1002/pen.760190605.
[5] J.-M. Chenal, L. Chazeau, L. Guy, Y. Bomal, C. Gauthier, Molecular weight between physical entanglements in natural rubber: a critical parameter during strain-induced crystallization, Polymer 48 (2007) 1042–1046, http://dx.doi.org/10.1016/j.polymer.2006.12.031.
[6] N. Candau, R. Laghmach, L. Chazeau, J.-M. Chenal, C. Gauthier, T. Biben, E. Munch, Strain-induced crystallization of natural rubber and cross-link

densities heterogeneities, Macromolecules 47 (2014) 5815–5824.

[7] J.M. Chenal, C. Gauthier, L. Chazeau, L. Guy, Y. Bomal, Parameters governing strain induced crystallization in filled natural rubber, Polymer 48 (23) (2007) 6893–6901.

[8] L. Ladouce-Stelandre, Y. Bomal, L. Flandin, D. Labarre, Dynamic-mechanical properties of precipitated silica filled rubber: influence of morphology and coupling agent, Rubber Chem. Technol. 76 (2003) 145–159.

[9] S.S. Sarkawi, Nano-reinforcement of Tire Rubbers: Silica Technology for Natural Rubber, PhD-Thesis, University of Twente, Enschede, the Netherlands, 2013.

[10] Sarkawi, S. S., Dierkes, W. K., Noordermeer J.W.M., “Filler-to-filler and filler-to-rubber interaction in silica-reinforced natural rubber”, Proceedings KHK, 26.-28. 11., Hannover, 2014.

[11] Y. Tanaka, L. Tarachiwin, Recent advances in structural characterization of natural rubber, Rubber Chem. Technol. 82 (2009) 283–314.

[12] T. Spratte, Entwicklung eines Messverfahrens zur Charakterisierung von Dehnungskristallisation in Naturkautschuk, Bachelor Thesis, University of Kiel, Germany, 2015.

[13] P.-A. Albouy, A. Vieyres, R. Perez-Aparicio, O. Sanseau, P. Sotta, The impact of strain-induced crystallization on strain during mechanical cycling of cross-linked natural rubber, Polymer 55 (2014) 4022–4031, http://dx.doi.org/10.1016/j.polymer.2014.06.034.

[14] K. Brüning, K. Schneider, G. Heinrich, In-situ structure characterization of rubber during deformation and fracture, in: W. Grellmann, et al. (Eds.), Fracture Mechanics and Statistical Mechanics of Reinforced Elastomeric Blends'', Lecture Notes in Applied and Computational Mechanics 70, Springer, Berlin, Heidelberg, N.Y, 2013.

[15] J. Rault, J. Marchal, P. Judeinstein, P.A. Albouy, Stress-induced crystallization and reinforcement in filled natural rubbers: ^{2}H NMR study, Macromolecules 39 (24) (2006) 8356–8368, http://dx.doi.org/10.1021/ma0608424.

[16] P.-A. Albouy, G. Guillier, D. Petermann, A. Vieyres, O. Sanseau, P. Sotta, A stroboscopic X-ray apparatus for the study of the kinetics of strain-induced crystallization in natural rubber, Polymer 53 (15) (2012) 3313–3324.

[17] N. Candau, L. Chazeau, J.M. Chenal, C. Gauthier, J. Ferreira, E. Munch, C. Rochas, Characteristic time of strain induced crystallization of crosslinked natural rubber, Polymer 53 (13) (2012) 2540–2543.

[18] Y. Ikeda, Y. Yasuda, S. Makino, S. Yamamoto, M. Tosaka, K. Senoo, S. Kohjiya, Strain-induced crystallization of peroxide-crosslinked natural rubber, Polymer 48 (2007) 1171–1175.

[19] A. Vieyres, R. Peresz-Aparicio, P.-A. Albouy, O. Sanseau, K. Saalwächter, D.R. Long, P. Sotta, Sulfur-cured natural rubber elastomer networks: correlating cross-link density, chain orientation, and mechanical response by combined techniques, Macromolecules 46 (2013) 889–899.

[20] K. Brüning, K. Schneider, S. Roth, G. Heinrich, Kinetics of strain-induced crystallization in natural rubber: a diffusion controlled rate law, Polymer 72 (2015) 52–59.

[21] K. Brüning, In-situ Structure Characterization of Elastomers during Deformation and Fracture, PhD Thesis, TU Dresden, Germany, 2014.

[22] L.J. Fetters, D.J. Lohse, R.H. Colby, Chain dimensions and entanglement spacings'', Chap. 25, in: J.E. Mark (Ed.), Physical Properties of Polymers Handbook, Springer Science +Busyness Media, LLC, 2007.

[23] M. Klüppel, H. Menge, H. Schmidt, H. Schneider, R.H. Schuster, Influence of preparation conditions on network parameters of sulfur cured natural rubber, Macromolecules 34 (2001) 8107–8116.

[24] A. Einstein, Eine neue Bestimmung der Moleküldimensionen, Ann. Phys. 324 (1906) 289–306.

[25] J. Domurath, M. Saphiannikova, A. Gilles, G. Heinrich, Modelling of stress and strain amplification effects in filled polymer melts, J. Newt. Fluid Mech. 171 (2012) 8–16.

[26] G. Strobl, The Physics of Polymers, Springer, Berlin, Heidelberg, N. Y., 2007.

[27] Luukkonen, A., Sarlin, E., Villman, V., Hoikkanen, M., Vippola, M., Kallio, M., Lepistö, T. (2009). “Heat generation in dynamic loading of hybrid rubber-steel composite structure” proceedings: international conference on composite materials (pp. 27–31).

[28] T.A. Vilgis, G. Heinrich, M. Klüppel, Reinforcement of Polymer Nano-composites, Cambridge University Press, Cambridge, New York, 2009, ISBN 978-0-521-87480-9.

[29] H. Lorenz, M. Klüppel, G. Heinrich, Micro-structure based modeling and FE-implementation of filler-induced stress softening and hysteresis of reinforced rubbers, ZAMM, Z. Angew. Math. Mech. 92 (2012) 608–631.

[30] H.G. Kim, L. Mandelkern, Multiple melting transitions in natural rubber, J. Polym. Sci. Part A2 Polym. Phys. 10 (6) (1972) 1125.

[31] L.R.G. Treloar, Transactions of the Faraday Society, 37, 84, 1941.

[32] K. Brüning, K. Schneider, S. Roth, G. Heinrich, Kinetics of strain-induced crystallization in natural rubber studied by WAXD: dynamic and impact tensile experiments, Macromolecules 45 (2012) 7914–7919.

[33] P.J. Flory, Thermodynamics of crystallization in high polymers. I. Crystallization induced by stretching, J. Chem. Phys. 15 (1947) 397–408.

[34] Laghmach, et al., J. Chem. Phys. 142 (2015) 244905.

Polymer Testing 66 (2018) 87–93

Contents lists available at ScienceDirect

Polymer Testing

journal homepage: www.elsevier.com/locate/polytest

Test Method

Determining strain-induced crystallization of natural rubber composites by combined thermography and stress-strain measurements

J. Plagge*, M. Klüppel

Deutsches Institut für Kautschuktechnologie e. V., Eupener Str. 33, 30519 Hannover, Germany

ARTICLE INFO

Keywords:
Strain induced crystallization
Natural rubber
Filler reinforcement
Thermography

ABSTRACT

Strain induced crystallization is essential to the physicochemical properties of polymer materials, but is difficult to investigate, as it usually requires X-ray sources in combination with stretching machines. We improve and validate a recently developed method which allows the calculation of the crystallinity index using easily available thermography and stress-strain data. For natural rubber, the method is shown to be reproducible and delivers results quantitatively comparable to spectroscopic methods such as wide angle X-ray scattering. The incorporation of different amounts of carbon black is shown to increase the level of crystallization and to change the shape of the strain-crystallization curves. Additionally, crystallinity during partial retraction is investigated and reveals that crystallization characteristics change at sufficiently high strain.

1. Introduction

Strain-Induced-Crystallization (SIC) is a well-known phenomenon observable in many polymers. The most prominent example may be natural rubber (NR), where SIC is assumed to be responsible for its outstanding mechanical properties [13–15]. While NR works fine filled with carbon black, comparable silica filled compounds perform less well, especially in terms of wear. The reason for that is still under discussion and may be related to depression of SIC and/or inadequate choice of coupling agents [7].

HNBR with ACN content larger than roughly 35% and high level of hydrogenization is able to crystallize under strain [12], while NBR is not. This indicates that HNBRs great mechanical strength is also due to SIC. Apart from that, SIC may occur in many other polymers (among them EPDM).

In contrast to crystallization in unstretched polymers, which is easy to quantify by methods such as DSC [6] or XRD, the evaluation of SIC requires much larger experimental effort. The problems start with constructing a sample holder, which allows setting precise strains or stresses, but fits the DSC machine or X-ray beam. When using X-ray, the distinction between amorphous- and crystalline diffraction pattern is difficult, because the amorphous background becomes anisotropic under strain [5].

Recently, we have shown that SIC can be quantified by combining mechanical characterization and thermography [8]. The method presented was able to capture the characteristics of SIC but lacked accuracy and precision. In this work, we present crucial improvements which increase reproducibility to a level comparable or superior to X-ray measurements. In contrast to DSC and most X-ray applications, it can be carried out online at almost arbitrarily high speed. Additionally, the interplay of SIC and filler, as well as SIC during partial unloading, are investigated.

1.1. Evaluation procedure

The energy of crystallization is determined by balancing the mechanical energy input W, internal energy U and heat exchange with environment Q. The internal energy can be split up into an kinetic part, which measures the excitation of the microscopic degrees of freedom such as vibration, translation and rotation in terms of heat capacity c_p, density ρ, sample temperature T and the energy stored in potentials. The latter is identified with the energy gain from crystallization and is labeled U_c. In differential form, the first law of thermodynamics (given per volume) is written as

$$c_p\rho\, \mathrm{d}T - \mathrm{d}U_c = \mathrm{d}W + \mathrm{d}Q \tag{1}$$

where the negative sign of U_c indicates, that crystallization is an exothermal process. The total crystallization energy is calculated by rearranging Eq. (1)

$$U_c = \int (c_p\rho\, \mathrm{d}T - \mathrm{d}W - \mathrm{d}Q) \tag{2}$$

The parameterization of the integral is best done by measurement time t. For the mechanical energy inserted into the sample per volume

---

[*] Corresponding author.
E-mail address: jan.plagge@dikautschuk.de (J. Plagge).

https://doi.org/10.1016/j.polymertesting.2017.12.021
Received 14 November 2017; Accepted 18 December 2017
Available online 11 January 2018
0142-9418/ © 2018 Elsevier Ltd. All rights reserved.

**Reproduced with permission from
Polymer Testing, 2018, 66, 87-93.
https://doi.org/10.1016/j.polymertesting.2017.12.021**

we get

$$W(t) = \int \mathrm{d}W = \int_{0}^{t} \mathrm{d}t' \sigma(t') \dot{\lambda}(t') \tag{3}$$

with σ and λ being appropriate stress and strain measures (e. g. engineering stress and strain). The greatest uncertainty in the present treatment comes from the heat exchange with the environment. Heat flow is to a first order proportional to the temperature difference from the environment $\Delta T(t) = T(t) - T_0(t)$, where $T_0(t)$ is environment temperature and to the surface area S of the sample. For a cuboid sample volume with dimensions $x_1 \times x_2 \times x_3$, we have a surface area $S = 2x_1x_2 + 2x_2x_3 + 2x_3x_1$. For a platelet-like sample with $x_1 > x_2 \gg x_3$ this simplifies to $S \simeq 2x_1x_2$.

In the case of uniaxial strain with $\lambda_1 = \lambda,\ \lambda_2 = \lambda_3 = 1/\sqrt{\lambda}$ and $x_1 \propto \lambda_1,\ x_2 \propto \lambda_2$ we get $S \propto \sqrt{\lambda}$.

The heat exchange with environment per volume is then given as

$$Q(t) = \int \mathrm{d}Q = -\int_{0}^{t} \mathrm{d}t' a(t') \left(T(t') - T_0(t')\right) \sqrt{\lambda(t')} \tag{4}$$

with $a(t)$ being an unknown proportionality factor. Note that it has the dimension of W/(m^3 K). It can be compared to the heat transfer coefficient α usually given in W/(m^{2}K) by multiplying by the thickness of the sample $\alpha = d\ a$. From Eq. (2) the total energy of crystallization reads

$$U_c(t) = \int_{0}^{t} \mathrm{d}t' [c_p\rho\ \dot{T}(t') - \sigma(t')\,\dot{\lambda}(t') + a(t')(T(t') - T_0(t'))\,\sqrt{\lambda(t')}\,] \tag{5}$$

The quantities c_p and ρ are experimentally accessible (and may even be made temperature dependent). Sample temperature $T(t)$ and ambient temperature $T_0(t)$ are measured directly by an infrared camera. From this, the unknown function $a(t)$ can be determined if the energy stored in crystallites at a specific point in time is known. For natural rubber and many other strain crystallizing polymers, crystallinity is zero at zero strain and ambient temperature. If t_i denote the points in time where crystallinity is zero, we have $U_c(t_i) \approx 0$ for all t_i. This implies that:

$$\begin{aligned} 0 \approx \Delta U_c(t_{i+1}, t_i, a_i) &= U_c(t_{i+1}) - U_c(t_i) \\ &= \int_{t_i}^{t_{i+1}} \mathrm{d}t' [c_p\rho\ \dot{T}(t') - \sigma(t')\,\dot{\lambda}(t') + a_i\,(T(t') - T_0(t'))\,\sqrt{\lambda(t')}\,] \end{aligned} \tag{6}$$

Note that we set $a(t) = a_i$ for t in the interval $[t_i, t_{i+1}]$. If ambient temperature was not measured over time, as is the case for some of our measurements, it can be treated similarly: $T_0(t) \to T_{0,i}$ in $[t_i, t_{i+1}]$. Equation (6) can be solved for a_i (and $T_{0,i}$) by suitable numerical methods. In fact, a_i (and $T_{0,i}$) should be functions smoothly varying in time. For this reason, the solution for a_i (and $T_{0,i}$) of

$$0 \approx \left|\Delta U_c(t_{i+1}, t_i, a_i)\right| + C\left(\frac{a_i - a_{i-1}}{a_{i-1}}\right)^2 \tag{7}$$

is determined (an equivalent term for $T_{0,i}$ is added, if necessary). The variable $C > 0$ defines the strength of smoothing/regularization. For $C = 0$, the algorithm optimizes the a_i such, that $\Delta U_c(t_{i+1}, t_i, a_i) = 0$, even if this involves highly fluctuating a_i and overshooting calculated temperatures inside a cycle. Introducing C enforces solutions which both tolerate small deviations from $\Delta U_c(t_{i+1}, t_i, a_i) = 0$ due to inexact assumptions and smoothly varying a_i. For $C \gg 1$ the algorithm will neglect ΔU_c and generate constant a_i. In this work $C = 10$, because in this regime a_i as well as crystallinity cycles are smooth and do not vary much with variation of C. The total energy of crystallization can then be composed from the discretized function a_i (and $T_{0,i}$)

$$\begin{aligned} U_c(t) = \sum_{t_i \le t} \int_{t_i}^{\min(t,t_{i+1})} \mathrm{d}t' [c_p\rho\ \dot{T}(t') - \sigma(t')\,\dot{\lambda}(t') \\ + a_i(T(t') - T_0(t'))\,\sqrt{\lambda(t')}\,] \end{aligned} \tag{8}$$

where the minimum function is a formality which takes into account that the measurement doesn't have to end with zero crystallinity.

From equation (8), we can calculate the crystallinity index as

$$K(t) = \frac{U_c(t)}{(1 - \Phi_{\text{filler}})\Delta H_{\text{cryst}}} \tag{9}$$

with the filler volume fraction Φ_{filler} and enthalpy of fusion ΔH_{cryst} for the pure polymer, which is close to the energy of fusion due to small volume changes and internal pressures on phase transition. From Eq. (2), we can see that the temperature of a non-crystallizing polymer ($U_c(t) = 0 \quad \forall\ t$) is calculated according to

$$T_{nc}(t) = \frac{W(t) + Q(t)}{\rho\ c_p} \tag{10}$$

which will be useful later to visually compare the true sample temperature (from thermography) to the hypothetical one of a non-crystallizing polymer. The difference is proportional to $U_c(t)$, and thus a direct measure of crystallinity.

For reliable determination of SIC, two conditions regarding sample geometry have to be fulfilled. First, the surface to volume ratio has to be small to avoid heat exchange with environment, which is corrected only approximately. Second, an inhomogeneous temperature profile and heat buildup inside the sample due to inserted mechanical energy have to be avoided. This can be achieved by reducing the sample dimensions. To fulfill both conditions, the timescale of heat diffusion has to be in the same range as the timescale of the experiment. It can be estimated by assuming a single temperature deviation in the middle of the sample $x = 0$. The solution of the heat diffusion equation.

$$\frac{\partial T}{\partial t} - \kappa\frac{\partial T}{\partial x^2} = 0 \text{ and } T(x, 0) = \delta(x)$$

With the Dirac delta distribution $\delta(x)$ gives the solution

$$T(x, t) = \frac{1}{\sqrt{4\pi\kappa\ t}}\mathrm{e}^{-\left(\frac{x^2}{4\kappa\ t}\right)}$$

which is called the fundamental solution (or Greens function) of the heat diffusion equation. Looking at the exponent, we see that the timescale of diffusion scales as $\tau \approx x^2/(4\kappa)$. For rubber, $\kappa \approx 1.5{\cdot}10^{-7}$ m^2/s [11]. As we have heat sinks/sources on both sides of the sample, we have to take half of the sample thickness for x. With $x = d/2 \approx 1{\cdot}10^{-3}$ m we get $\tau \approx 1.7$ s, which is of the same order of magnitude as the time required for one deformation cycle. In addition, the temperature homogeneity depends on the radiating boundary condition:

$\frac{\partial T}{\partial x} = -h\ (T - T_0)$ for $x = d/2$ (sample surface).

With $h = \alpha/(\kappa\ c_p\ \rho)$, where α is the heat transfer coefficient that can be set to $\alpha = a{\cdot}d \approx 40$ W/(m^2 K), which is a common value for rubber [11] and is also found in the results section. Using $c_p\ \rho \approx 1.7$ J/(cm^3 K) (see Table 1), we get $h \approx 160$ 1/m. From this, we can extrapolate the maximum temperature deviation in the middle of the sample by

$$\Delta T \approx h(T - T_0){\cdot}\frac{d}{2} \approx 170\frac{1}{\text{m}}{\cdot}10\ \text{K}{\cdot}10^{-3}\ \ \text{m}= 1.7\ \text{K}$$

where we assumed a temperature difference from sample surface to environment of 10 K.

The 1.7 K represent an upper bound, as the temperature profile is more flat than linear extrapolation from the samples' borders.

2. Experimental

Vulcanizates based on natural rubber (pale crepe), Standard

Table 1
Heat capacity and density of the compounds investigated.

Rubber	Sulfur/CBS [phr]	Filler [phr]	c_p [J/g K]	ρ [g/cm^3]	$c_p\,\rho$ [J/cm^3 K]
NR (SVR)	1.5/1.5	0	1.62	0.943	1.53
NR (pale crepe)	1.0/1.0	0	1.64	0.942	1.54
NR (pale crepe)	1.5/1.5	0	1.61	0.945	1.52
NR (pale crepe)	1.0/1.0	20 (N339)	1.51	1.019	1.54
NR (pale crepe)	1.0/1.0	40 (N339)	1.40	1.082	1.51
NR (pale crepe)	1.0/1.0	60 (N339)	1.35	1.136	1.53
SBR	1.5/1.5	50 (N330)	1.36	1.136	1.54

Vietnam Rubber (SVR) and Styrene-Butadiene Rubber (SBR) were prepared. Additives were 3 phr (parts per hundred rubber) zinc oxide, 1 phr stearic acid and 1.5 phr *N*-isopropyl-*N*-phenyl-*p*-phenylendiamine (IPPD) as ageing protection. As filler, 20 phr, 40 phr or 60 phr N339 carbon black was added. The compounds were cured with 0.5, 1.0 or 1.5 phr sulfur and same amount *N*-cyclohexylbenzothiazole-2-sulphenamide (CBS). Curing was done in a heated press at 150 °C up to $t_{90\%}$ time, which is defined as the time where 90% of vulcameter stress is reached.

Strip samples with approximate dimensions $100 \times 15 \times 2\,\mathrm{mm}^3$ were stretched at 2000 mm/min ($\dot{\varepsilon} \approx 0.4$ /s) using a Zwick universal testing machine. Temperature profiles were recorded using a micro-epsilon TIM640 IR camera operated with an emissivity factor of 0.95. The temperature was averaged over a rectangular area within the front side of the sample. For some measurements, room temperature was recorded by placing black paper next to the sample inside the field of view of the camera. Note, that sample cooling given by Eq. (4) crucially depends on the temperature difference from room temperature. For this reason, the latter should be tracked near the sample. Additionally, the same device should be used to account for systematic errors involved in temperature determination by IR cameras. A schematic representation of the sample setup is shown in Fig. 1.

Heat capacity and density were measured via DSC and a pycnometer, respectively, at 23 °C. They are given in Table 1.

3. Results and discussion

First, an example of the method described in the theory section is presented. In Fig. 2 the crystallinity evolution of a 1.5 phr sulfur/CBS cured SVR rubber is shown. The sample was drawn several times to 450% strain. The corresponding stress-strain curve was used to calculate a hypothetical temperature according to Eq. (10). Obviously, the hypothetical temperature is often lower than the measured one, indicating crystallization. By means of Eq. (10) the crystallinity index is determined using an enthalpy of fusion of 61 J/cm^3 [2]. Ambient temperature was fitted. With increasing strain, crystallinity remains zero up to roughly 350%. Then, crystal nucleation sets in and induces rapid growth of the crystallinity index. In the mechanical data, this is visible as a kink. When decreasing strain, crystals successively melt until the last crystal melts at about 180% strain.

To validate reproducibility, 3 SVR samples were punched out of the same vulcanizate and measured successively up to 450% strain. As shown in Fig. 3, there are minor deviations in maximum crystallinity, whereas on- and offset are nearly constant. They were determined by fitting lines to the linear slopes during loading and unloading. Maximum crystallinity is found to be (14.3 ± 1.0) %, on- and offset are $(351 \pm 3)\,\%$ and $(181 \pm 8)\,\%$, respectively. Similar compounds investigated by WAXS at same strain yield $\sim$11% crystallinity (TSR 20, 1.2 phr sulfur, 1.9 phr CBS) [9], $\sim$14% crystallinity (SMR, 1.5 phr sulfur, 2 phr CBS) [19] and $\sim$11.5% crystallinity (1.2 phr sulfur, 1.2 phr accelerator) [4]. For more precise quantification of the uncertainty a greater series of samples is required.

In Fig. 4, the method was applied to SBR cured with 1.5 phr sulfur and CBS and filled with 50 phr N330 carbon black. SBR is unable to crystallize due to steric hindrances and will be used as a benchmark for this reason. In Fig. 4b, the calculated and measured temperatures are shown. The calculated temperature is systematically higher than the measured one. This can possibly be explained by intramolecular energy elastic contributions like twisting and torsion of bonds, which aren't accounted for in our model. For this reason, the crystallinity equivalent (using the enthalpy of fusion of NR, to allow comparison) becomes negative. The force fraction $|f_e/f|$ of energy elasticity of SBR and NR is usually found to be between 0 and 0.2 [17]. Nevertheless, the maximum deviation from zero is about -2% crystallinity at peak stress, including eventual stress softening effects and uncertainties of DSC and density measurements. This is a consequence of the relatively large amount of energy involved in crystallization, reducing the relative error due to unknown energy elastic contributions. It is worth noting that the measurement speed was increased during measurement (see Fig. 2b). The resulting crystallinity equivalent seems to be independent of speed, indicating the validity of the calculation of $Q(t)$.

To further investigate the effect of measurement speed on crystallization and to validate the fitting of ambient temperature, a single sample made up of natural rubber (pale crepe), cured with 1.0 phr sulfur and CBS stretched to 500% strain several times. This was done successively at a measurement speed of 0.5 m/min, 1.0 m/min and 2.0 m/min, corresponding to stretching rates of roughly 0.1 1/s, 0.2 1/s and 0.4 1/s. The result with fitted ambient temperature is shown in Fig. 5a. By decreasing measurement speed, the degree of crystallinity increases. Even although the majority of crystals forms on the timescale of ms [3], it is known that crystallinity increases slowly on the timescale of seconds [1]. It is worth noting that the increase in crystallinity is particularly pronounced close to the melting (decreasing strain). This indicates that larger, and thus more stable, crystallites may form at lower speeds. Nevertheless, two alternative explanations can be given:

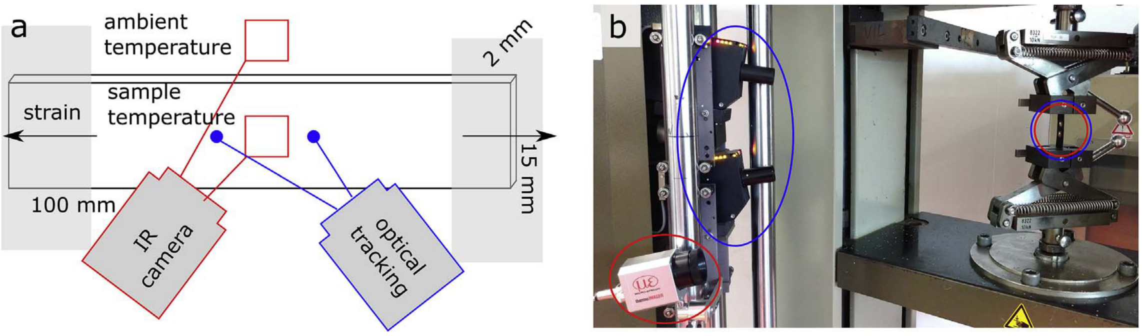

Fig. 1. (a) Schematic representation of the measurement setup and (b) experimental realization.

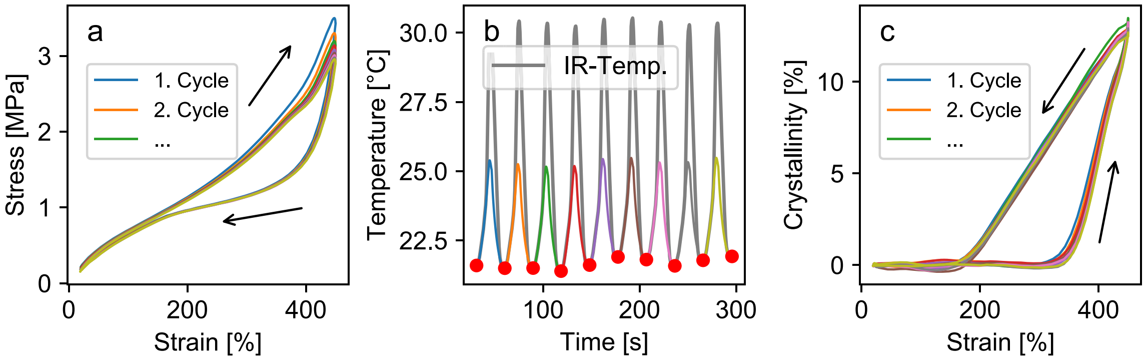

Fig. 2. (a) Stress-strain data of sulfur cured SVR rubber, (b) calculated temperature profile (color) and measured sample temperature (grey). Red dots indicate points of zero crystallization, where $\boldsymbol{Q}(\boldsymbol{t})$ is reset. (c) Degree of crystallinity. (For interpretation of the references to color in this figure legend, the reader is referred to the Web version of this article.)

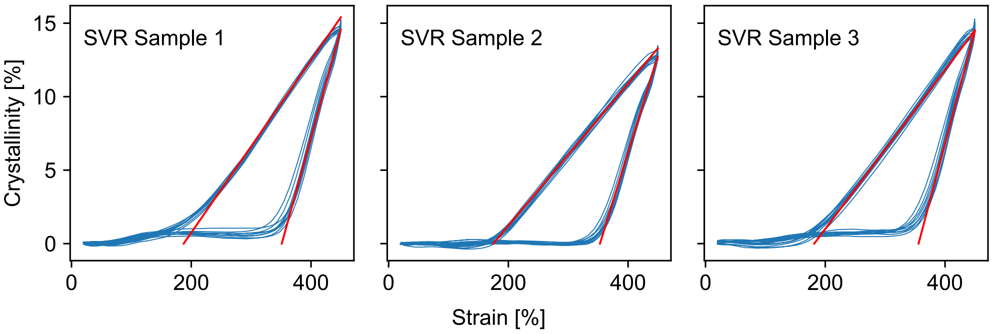

Fig. 3. Crystallinity of 3 sulfur cured, unfilled SVR samples punched out of the same vulcanizate. Sample 2 corresponds to the example shown in Fig. 2. The red lines are used to determine crystallization on- and offset strain. (For interpretation of the references to color in this figure legend, the reader is referred to the Web version of this article.)

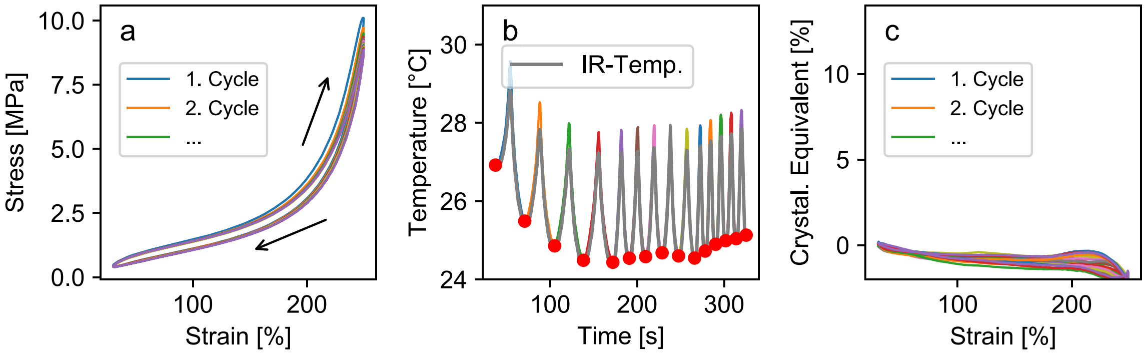

Fig. 4. (a) Stress-strain data of sulfur cured, 50 phr N330 filled SBR, (b) calculated temperature profile (color) and measured sample temperature (grey). Red dots indicate points of zero crystallization, where $\boldsymbol{Q}(\boldsymbol{t})$ is reset. (c) Equivalent degree of crystallinity using the enthalpy of fusion of natural rubber. (For interpretation of the references to color in this figure legend, the reader is referred to the Web version of this article.)

By decreasing the measurement speed, the average sample temperature is closer to room temperature due to increased time to exchange heat with the environment. WAXS studies carried out by Rault et al. [4,19] show that a temperature shift of 10 °C may change the degree of crystallinity by up to one fifth of its value. Thus, the observed increase in crystallinity may be explained by a lower sample temperature. This can be checked by carrying out measurements at elevated ambient temperature and reduced speed.

Additionally, the calculation of heat exchange $Q(t)$ is only approximate and the error will increase with increasing measurement time (to the next minimum, where $Q(t)$ is set to the correct value).

In Fig. 5b, crystallinity of the same data was evaluated using measured ambient temperature $T_0(t)$. The result is almost identical to Fig. 5a, indicating that fitting T_0 gives a very good approximation. This is supported in Fig. 5c and d Where the $T_{0,i}$ and $T_0(t)$ as well as the corresponding coefficients a_i are shown to be similar.

The method also allows analysis of crystallinity for stress-strain cycles which do not end with zero crystallinity. Nevertheless, it has to be ensured that the corrective term $Q(t)$ is reset sufficiently often to allow for precise determination of heat exchange. For this reason, it is crucial to go to low strains after a certain period of time.

In Fig. 6, an unfilled natural rubber (pale crepe) cured with 1.5 phr sulfur/CBS was drawn to different increasing strain levels 5 times each. Then, strain was decreased according to the same protocol. Finally, the sample was drawn 5 times from 450% to 500%, then from 400% to 500%, and so on. In between, the correction was reset by going from 500% to 30% strain. The strain-time protocol is also shown in Fig. 6b. Red dots denote reset points.

The stepwise increase in maximum strain reveals that crystallites appear around 300% maximum strain (green curve in Fig. 6c), which is clearly below the large strain onset of crystallization commonly found to be around 350% [3,5]. Mechanically, this goes along with an increase in hysteresis as well as the occurrence of stress softening. On further increasing maximum strain, the crystallization onset shifts to larger strains, while the offset remains almost fixed slightly below 200%. In contrast, during unloading (decreasing strain), the onset remains constant. Mechanically, all cycles are enclosed by an enveloping curve during unloading, such that the shift in crystallization onset

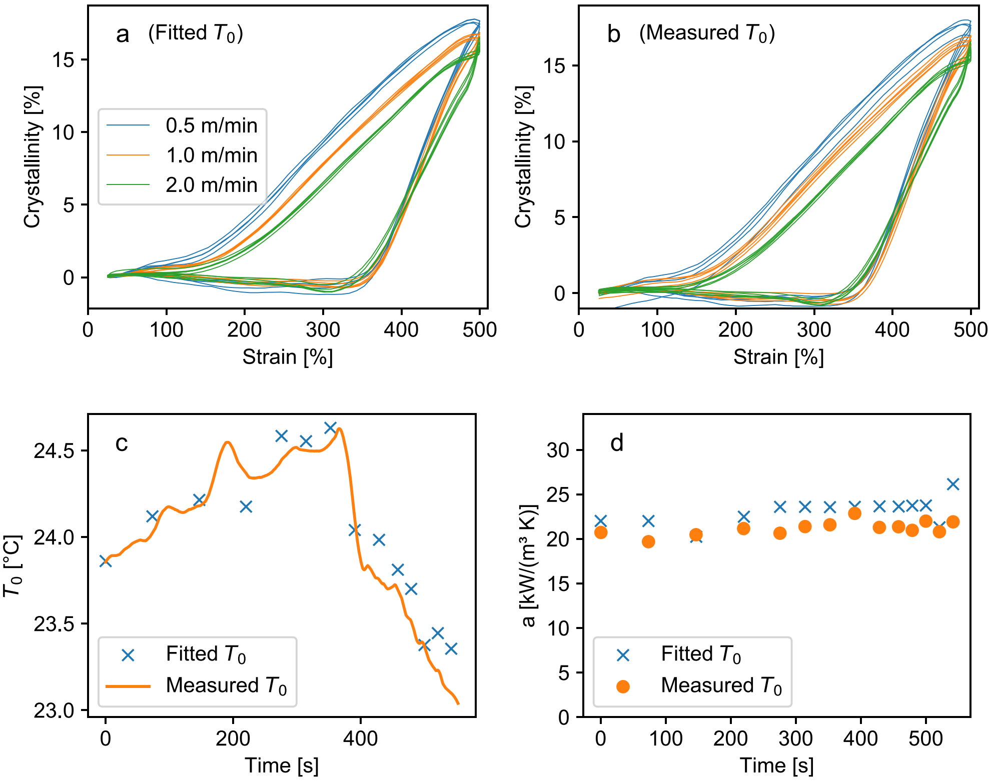

Fig. 5. (a) Measurement speed variation for an unfilled natural rubber (Pale Crepe), crosslinked with 1.0 phr sulfur/CBS. Ambient temperature T_0 fitted. (b) Same plot, but using measured ambient temperature. (c) Comparison of fitted and measured ambient temperature. (d) Comparison of heat transfer coefficient α for fitted and measured ambient temperature.

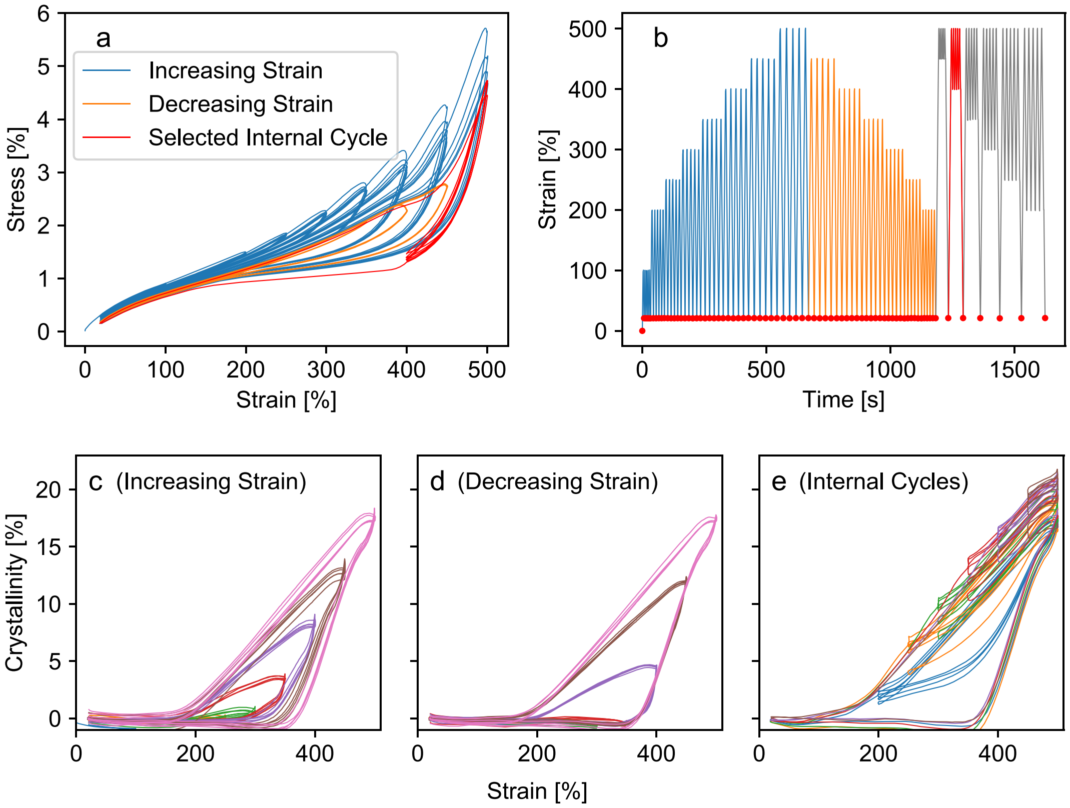

Fig. 6. (a, b) Stress-strain measurement of natural rubber (Pale Crepe) cured with 1.5 phr sulfur/CBS. The red dots denote the strain minima, where crystallinity is zero. (c, d, e) Crystallinity for the increasing and decreasing strain part, as well as internal cycles. (For interpretation of the references to color in this figure legend, the reader is referred to the Web version of this article.)

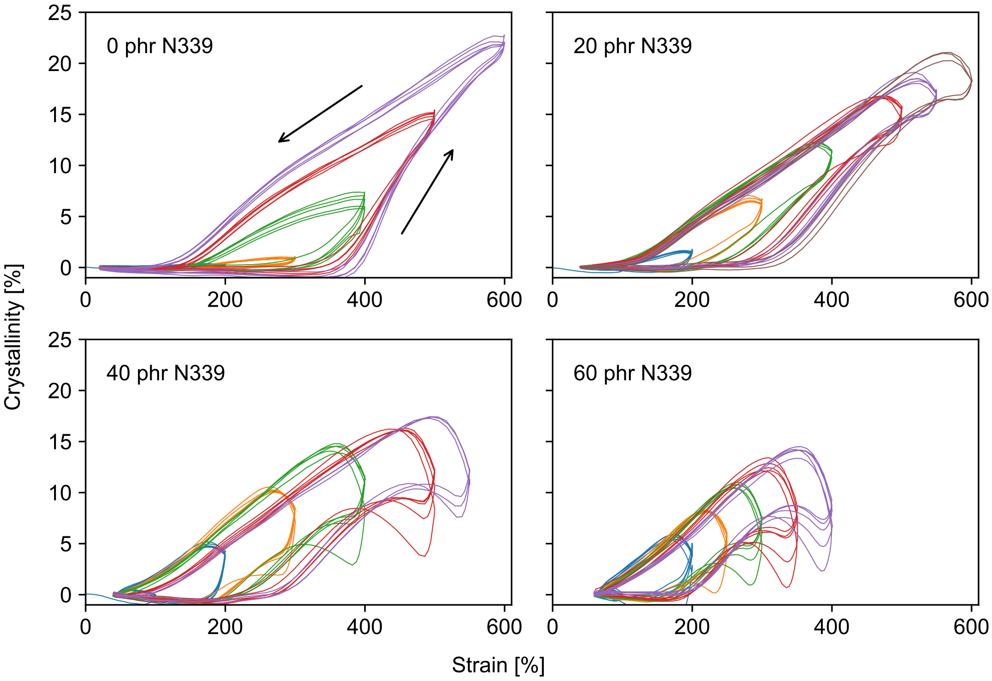

Fig. 7. Crystallinity of natural rubber (Pale Crepe) crosslinked with 1.0 phr sulfur/CBS for varying amount of N339 carbon black.

might be due to stress softening.

Surprisingly, the crystallinity during internal cycles shown in Fig. 6e exhibits far less hysteresis. For low strain amplitudes (e. g. from 450% to 500%) hysteresis seems to vanish. Similar results were found by means of WAXS [9]. This indicates that either crystallites are melting only partially and continuously grow again during loading, or that the timescale of nucleation is much smaller than the timescale of the experiment. Additionally, the five internal cycles don't collapse onto one line, but exhibit a trend towards larger crystallinity. This finding may be explained by continuing crystallization, decreasing sample temperature or uncertainties in the dissipation correction (because of the relatively infrequent reset points). Nevertheless, at larger amplitudes (e. g. from 200% to 500%) the cycles collapse again, such that continuing crystallization is most probable. Mechanically, this hypothesis is supported by a lower stress level with decreasing strain (see red cycle in Fig. 6a). The height of the retracting stress plateau was explained by the degree of crystallization [16].

The impact of filler loading on SIC is investigated in Fig. 7. There, crystallization of natural rubber (pale crepe) crosslinked with 1.0 phr sulfur/CBS filled with 0, 20, 40 and 60 phr N339 carbon black is presented. Without any filler, crystallinity evolves similarly as shown in Fig. 6c. Filled with 20 phr of filler, the samples crystallinity curve changes from triangular shape towards a more tube-like shape. Probably, this is due to different strain levels within the sample as a consequence of spatially heterogeneous strain amplification. In fact, a recently proposed model is able to precisely describe the mechanical behavior of rubber using this assumption [10].

The turning point at maximum strain is less sharp, such that maximum crystallinity seems to be reached on the way back slightly below maximum strain. Indeed, such results were found using WAXS [4]. For 40 and 60 phr carbon black this trend continues. Additionally, crystallinity seems to decrease close to maximum strain. As can be seen in the figure, this effect becomes smaller with every stress-strain cycle. We think that this is related to the pronounced mechanical relaxation of sufficiently filled elastomer composites, which possibly involves energy elastic contributions not accounted for up to now. With increasing amount of filler, the crystallization onset shifts to larger strains. In principle, this allows the calculation of a strain amplification factor. As this quantity depends on maximum applied strain, this is rather complex and out of the scope of this work. In Fig. 8, the maximum of the crystallinity curve with respect to filler loading at different strain levels is presented. Take into account that the maximum of crystallinity does not coincide with maximum strain for the filled samples. The degree of crystallinity of the unfilled sample is close to the value ~17% at 550% strain obtained in Ref. [4] for a slightly different compound (1.2 phr sulfur and accelerator). Crystallinity increases with increasing filler loading in accordance with literature [4,18], but saturates and eventually decreases afterwards. The filler loading of saturation decreases with increasing strain. This also indicates that, at low strains, the filler network locally overstretches large parts of the network, thus increasing the average crystallinity. At larger strains, the corresponding constraints break down and the network more and more resembles the unfilled sample. Finally, the presence of carbon black may hinder crystallization, resulting in a decrease of crystallinity with more filler.

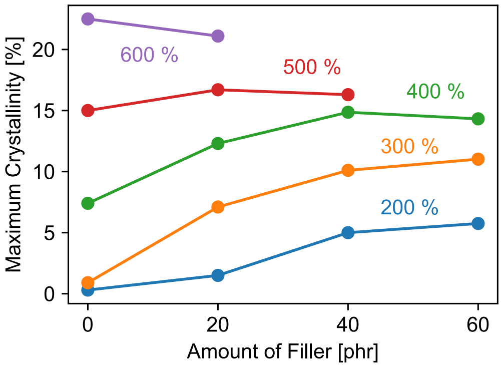

Fig. 8. Maximum of crystallinity for different strain levels and amounts of carbon black. Data taken from Fig. 7.

For the 60 phr N339 measurement, it is all but clear that crystallinity is zero at minimum strain. Because of this, the measurement has to be interpreted with care.

4. Conclusions

A method to determine SIC from thermography and mechanical data is presented. It was shown to be reproducible and accurate, delivering reliable and fast information about different types of NR, differently crosslinked and filled. It may easily be used on other polymers. The method works fine with or without knowledge of ambient temperature. Speed has a significant influence on the measured degree of crystallinity. It has to be clarified whether this is due to continuing crystallization or non-ideal measurement conditions. Mechanical stress softening also impacts crystallization behavior. Additionally, crystallization during incomplete cycles exhibits reduced hysteresis and increases with time. The latter effects are rarely studied and deserves further investigation. Crystallization of filled samples can also be quantified, showing a transition from triangular-shape crystallinity curves to tube-like curves. This is interpreted in terms of differently amplified domains. We want to highlight, that the whole evaluation procedure can also be carried out in a heated cabinet to investigate SIC at arbitrary temperatures. This will be treated in future works.

Acknowledgements

This work has been supported by the community project “Reinforcement mechanisms of NR/Silica composites”.

References

[1] K. Brüning, K. Schneider, S.V. Roth, G. Heinrich, Kinetics of Strain-induced Crystallization in Natural Rubber: a Diffusion-controlled Rate Law Polymer vol. 72, Elsevier, 2015, pp. 52–58.

[2] H.-g. Kim, L. Mandelkern, Multiple Melting Transitions in Natural Rubber Journal of Polymer Science Part A-2: Polymer Physics vol. 10, Wiley Online Library, 1972, pp. 1125–1133.

[3] N. Candau, L. Chazeau, J.-M. Chenal, C. Gauthier, J. Ferreira, E. Munch, C. Rochas, Characteristic Time of Strain Induced Crystallization of Crosslinked Natural Rubber Polymer vol. 53, Elsevier, 2012, pp. 2540–2543.

[4] J. Rault, J. Marchal, P. Judeinstein, P. Albouy, Stress-induced Crystallization and Reinforcement in Filled Natural Rubbers: 2H NMR Study Macromolecules vol. 39, ACS Publications, 2006, pp. 8356–8368.

[5] A. Vieyres, R. Pérez-Aparicio, P.-A. Albouy, O. Sanseau, K. Saalwächter, D.R. Long, P. Sotta, Sulfur-cured Natural Rubber Elastomer Networks: Correlating Cross-link Density, Chain Orientation, and Mechanical Response by Combined Techniques Macromolecules vol. 46, ACS Publications, 2013, pp. 889–899.

[6] J.-M. Chenal, L. Chazeau, Y. Bomal, C. Gauthier, New Insights into the Cold Crystallization of Filled Natural Rubber Journal of Polymer Science Part B: Polymer Physics vol. 45, Wiley Online Library, 2007, pp. 955–962.

[7] K. Sengloyluan, K. Sahakaro, W. Dierkes, J. Noordermeer, Silane grafted natural rubber and its compatibilization effect on silica-reinforced rubber tire compounds, Express Polym. Lett. 11 (2017) 11.

[8] T. Spratte, J. Plagge, M. Wunde, M. Klüppel, Investigation of Strain-induced Crystallization of Carbon Black and Silica Filled Natural Rubber Composites Based on Mechanical and Temperature Measurements Polymer vol. 115, Elsevier, 2017, pp. 12–20.

[9] N. Candau, R. Laghmach, L. Chazeau, J.-M. Chenal, C. Gauthier, T. Biben, E. Munch, Strain-induced Crystallization of Natural Rubber and Cross-link Densities Heterogeneities Macromolecules vol. 47, ACS Publications, 2014, pp. 5815–5824.

[10] J. Plagge, M. Klüppel, A physically based model of stress softening and hysteresis of filled rubber including rate-and temperature dependency, Int. J. Plast. 89 (2017) 173–196.

[11] J. Fritzsche, M. Klüppel, Simulation of the internal sample temperature of rubber components during cyclic deformation KGK, Kautschuk, Gummi, Kunststoffe, Hüthig 64 (2011) 44–51.

[12] G. Severe, J.L. White, Physical Properties and Blend Miscibility of Hydrogenated Acrylonitrile-butadiene Rubber Journal of Applied Polymer Science vol. 78, Wiley Online Library, 2000, pp. 1521–1529.

[13] G. Hamed, H. Kim, A. Gent, Cut Growth in Vulcanizates of Natural Rubber, Cis-polybutadiene, and a 50/50 Blend during Single and Repeated Extension Rubber Chemistry and Technology vol. 69, (1996), pp. 807–818.

[14] M. Tosaka, Strain-induced Crystallization of Crosslinked Natural Rubber as Revealed by X-ray Diffraction Using Synchrotron Radiation Polymer Journal vol. 39, Nature Publishing Group, 2007, p. 1207.

[15] B. Huneau, Strain-induced Crystallization of Natural Rubber: a Review of X-ray Diffraction Investigations Rubber Chemistry and Technology vol. 84, (2011), pp. 425–452.

[16] S. Trabelsi, P.-A. Albouy, J. Rault, Crystallization and Melting Processes in Vulcanized Stretched Natural Rubber Macromolecules vol. 36, ACS Publications, 2003, pp. 7624–7639.

[17] James E. Mark (Ed.), Physical Properties of Polymers Handbook, vol. 1076, Springer, New York, 2007.

[18] J.-M. Chenal, C. Gauthier, L. Chazeau, L. Guy, Y. Bomal, Parameters Governing Strain Induced Crystallization in Filled Natural Rubber Polymer vol. 48, Elsevier, 2007, pp. 6893–6901.

[19] P.-A. Albouy, A. Vieyres, R. Pérez-Aparicio, O. Sanséau, P. Sotta, The Impact of Strain-induced Crystallization on Strain during Mechanical Cycling of Cross-linked Natural Rubber Polymer vol. 55, Elsevier, 2014, pp. 4022–4031.

Reproduced with permission from Macromolecules 2018, 51, 3711-3721. Copyright 2018 American Chemical Society.

Macromolecules

Article

Cite This: *Macromolecules* 2018, 51, 3711−3721

A Theory Relating Crystal Size, Mechanical Response, and Degree of Crystallization in Strained Natural Rubber

J. Plagge* and M. Klüppel

Deutsches Institut für Kautschuktechnologie e.V., Eupener Str. 33, 30519 Hannover, Germany

ABSTRACT: It is widely believed that the extraordinary mechanical properties of natural rubber (NR) are mainly caused by its ability to crystallize at large strains. While several authors believe crystallites working equivalent to nanoscopic filler particles in terms of amplification and filler networking, recent works have identified a crystal-induced strain regulation process as a possibility to explain its outstanding properties. We present a theory that is able to quantitatively describe crystal formation and melting in stretched NR in dependence of temperature and cross-link density. The theory gives reasons for the constant crystals length observed in NR and answers the question why crystallization onset strain is independent of cross-link density. It is tested on the data set of Trabelsi (2003), Albouy (2005), and Rault (2006) reproducing stress−strain data, degree of crystallinity, and crystal sizes at different temperatures using a physically well-defined set of parameters. Additionally, a scheme for NR crystallization involving linear and folded chain crystals is drawn.

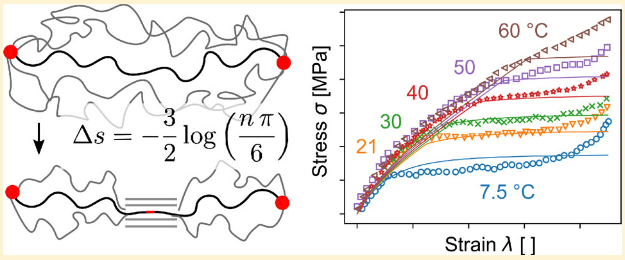

INTRODUCTION

Natural rubber (NR) is a crucial ingredient to a great variety of rubber goods, most importantly to heavy duty rubber articles like truck tires or belts. Its unmatched mechanical properties in terms of wear and tear strength are believed to be due to strain-induced crystallization (SIC) and/or due to natural ingredients like proteins and phospholipids.[1,2] If NR is exposed to large strains, the conformational entropy of polymer chains is reduced, allowing the formation of small crystallites. The crystallization kinetics and crystallite size evolution as well as total crystalline fraction were extensively analyzed by means of wide-angle X-ray spectroscopy (WAXS). The crystallites' length parallel to stretching direction was found to be constant around 10 nm for both filled and unfilled elastomers, slightly depending on cross-link density.[3−6] The crystals volume could be related to the volume of an average network mesh cell, defined by cross-link spacing,[7] indicating that cross-links or trapped entanglements limit crystal growth. Additionally, the length of the crystallites seems to be rather independent of applied strain.[5−7] With increasing strain, crystallites slightly grow in directions perpendicular to strain, but the main part of additional total crystallinity is due to the formation of new crystallites.[3] The morphology of strain-induced crystals is still not totally clear. Electron microscopic pictures obtained at room temperature suggest chain folding crystallites even at high strains.[6] Nevertheless, many authors assume fibrillar nuclei,[3,8] probably allowing the growth of chain folded crystals on their surface.

Without strain, NR crystallizes on the time scale of hours around −25 °C, and the total fraction of crystals in cured as well as uncured NR was found to be limited at about 40%.[9] In contrast, SIC occurs on time scales of roughly 20 ms at room temperature, which is fast compared to time scale of typical mechanical experiments. The time scale of SIC can be described by a diffusion-controlled rate law.[10,11] Comparable to many other polymers, the phase transition of NR exhibits great hysteresis: Crystals need high strain to appear but melt at much lower strains. In analogy to cold crystallization, many authors refer to this process as supercooling.[7,12,13] Surprisingly, the onset strain for crystallization appears to be almost independent of strain,[5,7,14] while offset strain increases with increasing cross-link density. The second observation can easily be explained with a larger size of crystals for loose networks, increasing the melting temperature according to the Gibbs−Thomson equation.[15] The first observation conflicts classical rubber elasticity theory, as pointed out by Flory,[13] and is still a matter of dispute. Tosaka[2] assumes network heterogeneities to be responsible for this effect. The reason why SIC increases the mechanical strength of NR is still under discussion. Because of their size, crystallites may act as multifunctional cross-links[12] or nanoscopic fillers.[16] Recently, the evaluation of the WAXS amorphous halo allowed to determine amorphous polymer orientation.[17,18] The results indicate that after crystallization onset the amorphous polymer phase has constant average orientation, irrespective of strain. On a mechanical level this is visible as a stress plateau. The authors refer to this effect as a strain regulation process.[18] Similar results were found by NMR measurements.[12] Many observations are collected in the review of Huneau.[19]

There is a great variety of theories aiming to describe SIC. The famous approach of Flory[13] treats rubber in a single Gauss chain picture and the crystal as linear, weighing their respective

Received: January 24, 2018
Revised: April 26, 2018
Published: May 7, 2018

© 2018 American Chemical Society

DOI: 10.1021/acs.macromol.8b00177

entropic and energetic contributions. It correctly describes temperature dependency of crystallization but fails in reproducing the mechanical response of NR and the dependence on cross-link density. Gaylord[20] followed a similar approach but introduced folded crystals. Several other models deal with different assumptions on crystal geometry and relation to the polymer matrix. Kroon[21] and Mistry[22] developed semiempirical constitutive models allowing to reproduce whole hysteresis cycles. These models are based on a splitting of the rubber matrix into crystalline and elastic phases in a similar way as presented here but differ in the treatment of the evolution of the crystalline phase. An overview about existing theories of SIC is found in ref 8. In this work we present a new microscopic theory that treats SIC in a simple but physically reasonable way. It aims to answer some of the remaining questions concerning SIC of natural rubber. (1) Why do crystals always have the same length, irrespective of strain and temperature? (2) Why is crystallization onset strain rather independent of cross-link density? (3) What is the morphology of NR crystals? (4) What is the life- cycle of a crystallite during cyclic loading? The model is fitted to the excellent data set of Trabelsi,[7] Albouy,[23] and Rault,[12] providing mechanical and WAXS data for different compounds at several temperatures.

■ A MICROSCOPIC THEORY OF SIC

The theory section is split into five parts. First, Flory's theory is shortly reviewed, focusing on his assumptions and the difference to the present work. Afterward, some general calculations concerning serial connections of Gaussian chains are performed. Then, the entropy cost of attaching a chain to a crystal is calculated. Using this result, a linear network of crystalline and noncrystalline chains is investigated. It turns out that the whole linear network can be described by one replacement chain. In the end the transition to continuum mechanics is done by averaging the replacement chain over three directions in space. The three modeling steps are visualized in Figure 2.

Flory's Theory.[13] Flory's theory on SIC paved the way for numerous other microscopic theories. His theory is based on the assumptions that (i) crystallization occurs in thermodynamic equilibrium, (ii) the formation of crystal nuclei induces negligible changes in entropy, (iii) crystallites are all oriented in stretching direction, (iv) each chain traverses the crystal in the direction of stretching, and (v) Gaussian statistics is employed despite its obvious deficiencies at large strains. Additionally, he implicitly assumes that (vi) the network can be described by a continuously crystallizing representative chain. Commenting on this, he expressed concerns:[13] "This interpretation of λ [remaining amount of amorphous chain] may be reasonably satisfactory for low degrees of crystallinity, but it is beset with doubts, partly of intuitive origin, when a substantial fraction of the material becomes crystalline. A literal extension [...] to the system as a whole would imply that nucleation is restricted to the initial crystallization interval, further crystallization thereafter being restricted to longitudinal growth of existing crystallites."

The model presented below takes over assumptions i, iii, iv, and v, mainly for the sake of analytically feasible calculations but also to avoid unnecessary assumptions, even though the assumption of equilibrium necessarily requires to distinguish thermodynamic parameters for loading and unloading. It is worth noting here that the terminus equilibrium is used in the context of a locally stable state. If the system would be always in the global free energy minimum, hysteresis would be impossible by construction (without introducing explicit dissipative mechanisms). Assumption ii and vi are dropped and replaced by the result that crystal nucleation costs a significant amount of entropy. Building on this, it is shown that spawning of fully grown individual crystals is thermodynamically more favorable than growth of existing ones. It will be shown that a linear array of individual crystals is mathematically equivalent to a replacement chain with a growing crystallite but a chain-length-dependent entropy of fusion.

Serial Connections of Gaussian Chains. The probability distribution of the end-to end vector $\vec{r}$ of an ideal polymer chain with segment length b and number of statistical segments n is given by the well-known Gauss approximation[15]

$$P(r) = \left(\frac{3}{2\pi n b^2}\right)^{3/2} \exp\left(-\frac{3}{2}\frac{r^2}{nb^2}\right) \tag{1}$$

The nontranslational part of chain entropy is defined as the logarithm of accessible states Ω, which is given by

$$\begin{aligned} S &= k_B \log \Omega = k_B \log(C_f^n P(r)) \\ &= n s_f + k_B\left(\frac{3}{2}\log\left(\frac{3}{2\pi n b^2}\right) - \frac{3}{2}\frac{r^2}{nb^2}\right) \end{aligned} \tag{2}$$

with C_f counting the number of conformations each segment may take in the melt and $s_f = k_B \log C_f$ being the corresponding entropy.

For the sake of more compact notation we define the unit length to be $b = 1$ and $k_B = 1$, converting the final results back to SI units.

Now we serially connect two ideal chains with end to end vectors r_1 and r_2 and number of statistical segments m_1 and m_2. Both end-to-end vectors may be reduced in length by the constants c_1 and c_2, which will later be identified with crystal lengths. The deformational entropy (neglecting the term containing s_f for the time being) of both chains then reads

$$-\frac{3}{2}\frac{(r_1 - c_1)^2}{m_1} + \frac{3}{2}\log\left(\frac{3}{2m_1\pi}\right) - \frac{3}{2}\frac{(r_2 - c_2)^2}{m_2} + \frac{3}{2}\log\left(\frac{3}{2m_2\pi}\right) \tag{3}$$

Fixing the end-to-end distance to $r_1 + r_2 = R$ and maximizing the entropy (with respect to the remaining internal coordinate, e.g., r_1) then yields

$$-\frac{3}{2}\frac{(R - (c_1 + c_2))^2}{m_1 + m_2} + \frac{3}{2}\log\left(\frac{3}{2m_1\pi}\right) + \frac{3}{2}\log\left(\frac{3}{2m_2\pi}\right) \tag{4}$$

This equation can be applied recursively to give the generalization of an arbitrary number of serially connected chains in equilibrium

$$\begin{aligned} \sum_i \left(-\frac{3}{2}\frac{(r_i - c_i)^2}{m_i} + \frac{3}{2}\log\left(\frac{3}{2m_i\pi}\right)\right) &\equiv -\frac{3}{2}\frac{(R - \sum_i c_i)^2}{\sum_i m_i} \\ &+ \sum_i \frac{3}{2}\log\left(\frac{3}{2m_i\pi}\right) \end{aligned} \tag{5}$$

where the $\equiv$ indicates that the equation holds in equilibrium only.

Attachment of a Chain to a Crystal. Equation 4 represents the entropy of two chains with end-to-end distance

R reduced by c_1 and c_2. The $c_j = \eta\gamma_j n_j$ (where j is 1 or 2 here) are the lengths of crystals in stretching direction, with γ_j being the degree of crystallization of the corresponding chain ranging from 0 to 1. The strain reduction parameter η quantifies which fraction of the crystalline polymer spans distance in the direction of strain. For example, $\eta = 1$ corresponds to fibrillar (linear) crystals in direction of strain, whereas $\eta = 1/3$ corresponds to chains folded one time. The $m_j = n_j - \gamma_j n_j$ represent the remaining segments in the amorphous chain part. Inserting these expression into eq 4 gives

$$-\frac{3}{2}\frac{(R - (\eta\gamma_1 n_1 + \eta\gamma_2 n_2))^2}{(n_1 - \gamma_1 n_1) + (n_2 - \gamma_2 n_2)} + \frac{3}{2}\log\left(\frac{3}{2(n_1 - \gamma_1 n_1)\pi}\right) + \frac{3}{2}\log\left(\frac{3}{2(n_2 - \gamma_2 n_2)\pi}\right) \tag{6}$$

If a chain with n segments crystallizes and generates two subchains on each side of the crystallite while maintaining the same end-to-end distance, the condition $n_1 + n_2 = n$ has to be fulfilled. At fixed η, maximization of entropy gives $\gamma = \gamma_1 = \gamma_2$ and $n_1 = n_2 = n/2$. This means that the crystal will preferably spawn in the middle of a chain with equally sized remaining amorphous chains on each side. This is visualized in Figure 1.

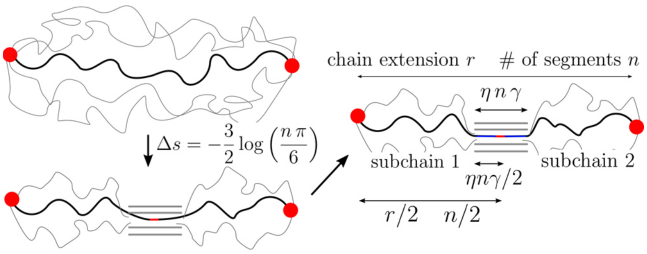

Figure 1. Sketch of the attachment of a single chain between two network nodes (red dots) to a preexisting or emerging crystal. Forcing the chain to be at the crystals surface reduces the number of possible conformations (gray lines) and consequently the entropy of the chain. Afterward, the subchains integrate into the crystal.

From the maximization of eq 6 we get the deformational entropy of a chain (composed of two subchains) that is attached to a crystal of length $\eta\gamma n$:

$$s_c = -\frac{3}{2}\frac{(r - \eta\gamma n)^2}{n(1 - \gamma)} + 3\log\left(\frac{3}{n(1 - \gamma)\pi}\right) \tag{7}$$

In contrast, the entropy of an unattached chain with number of segments n and end-to-end distance r is given as

$$s_0 = -\frac{3}{2}\frac{r^2}{n} + \frac{3}{2}\log\left(\frac{3}{2n\pi}\right) \tag{8}$$

Note that for an infinitesimal crystal $\gamma = 0$ we get the entropy cost for forcing the chain to make a detour to a specific point in space (crystal surface)

$$s_c(\gamma = 0) - s_0 = -\frac{3}{2}\log\left(\frac{n\pi}{6}\right) \tag{9}$$

showing that the mere attachment of the chain requires a large amount of entropy, even if the crystal is in direction of stretch. This is visualized in Figure 1 and contradicts Flory's theory, who assumed that there is no entropy change upon attachment of a chain to a crystal (see above). To the best of our knowledge, he and many other authors of the time neglected the change in conformational entropy due to chain attachment because they focused on the r-dependent part of entropy ($\sim -3/2\, r^2/n$) only, where a randomly placed cross-link (new crystal) only changes the overall entropy at strains deviating from the strain of its formation.[24] Instead, this simple calculation confirms the intuitive idea that the chain looses conformational entropy if it anchors at a crystal surface.

From a Single Chain to a Linear Network. Using eqs 8 and 7, the total deformational entropy of a one-dimensional linear network of k chains of which k_c are crystalline can be expressed as

$$S_D = \sum_{i=1}^{k_c} s_{i,c} + \sum_{i=k_c+1}^{k} s_{i,0} \tag{10}$$

$$S_D = \sum_{i=1}^{k_c}\left[-\frac{3}{2}\frac{(r_i - \eta\gamma_i n_i)^2}{n_i(1 - \gamma_i)} + 3\log\left(\frac{3}{n_i(1 - \gamma_i)\pi}\right)\right] + \sum_{i=k_c+1}^{k}\left[-\frac{3}{2}\frac{r_i^2}{n_i} + \frac{3}{2}\log\left(\frac{3}{2n_i\pi}\right)\right] \tag{11}$$

The network is visualized in Figure 2a. By introducing the discrete step function ($H[n] = 1$ for $n \geq 0$ and $H[n] = 0$ otherwise), we can combine the r-dependent sums of crystalline and noncrystalline chains

$$S_D = \underbrace{\sum_{i=1}^{k}\left[-\frac{3}{2}\frac{(r_i - H[k_c - i]\eta\gamma_i n_i)^2}{n_i(1 - H[k_c - i]\gamma_i)}\right]}_{(a)} + \underbrace{\sum_{i=1}^{k_c} 3\log\left(\frac{3}{n_i(1 - \gamma_i)\pi}\right) + \sum_{i=k_c+1}^{k}\frac{3}{2}\log\left(\frac{3}{2n_i\pi}\right)}_{(b)} \tag{12}$$

Assuming an equilibrated network, we can use eq 5 to bunch together the r-dependent terms collected in eq 12a

$$\sum_{i=1}^{k}\left[\frac{3}{2}\frac{(r_i - H[k_c - i]\eta\gamma_i n_i)^2}{n_i(1 - H[k_c - i]\gamma_i)}\right] \equiv \frac{3}{2}\frac{(R - \sum_i H[k_c - i]\eta\gamma_i n_i)^2}{\sum_i n_i(1 - H[k_c - i]\gamma_i)} = k\frac{3}{2}\frac{(r - \eta\gamma n)^2}{n(1 - \gamma)} \tag{13}$$

where $R = \sum_{i=1}^{k} r_i$ is the (fixed) total elongation of the linear network. The average replacement chain (see Figure 2b) is defined by the average quantities

$$r = \frac{1}{k}R \qquad \nu = \frac{\sum_i H[k_c - i]\gamma_i n_i}{\sum_i n_i} \qquad n = \frac{1}{k}\sum_{i=1}^{k} n_i \tag{14}$$

which tells us that network crystallinity ν may be continuously increasing, even though experimental results clearly show that individual crystals form spontaneously. The latter observation is taken into account by the step function $H[k_c - i]$, switching on the crystallinity of chain i if it belongs to the crystalline fraction. r is the average end-to-end distance of a network chain, and n is the average number of segments. We point out that eq 14 may be seen as a justification of numerous approaches in the literature, which model continuously growing crystals within the chain.[8,13,20,22] An extension of the model could involve varying η, depending on the direction of the chain relative to the crystal. The serial connection of an ensemble of chains differently likely to crystallize would be a natural explanation for the nonlinear shape of crystallization curves close to SIC onset and offset.

While eq 12a can be expressed exactly by average quantities, the log terms in eq 12b have to be evaluated using assumptions. Approximating the number of segments and the microscopic single chain crystallinity by their respective averages $n_i = n$ and $\gamma_i = \gamma$, we get

$$\sum_{i=1}^{k_{\mathrm{c}}} 3\log\left(\frac{3}{n_i(1-\gamma_i)\pi}\right) + \sum_{i=k_{\mathrm{c}}+1}^{k}\frac{3}{2}\log\left(\frac{3}{2n_i\pi}\right) \tag{15}$$

$$\approx \frac{3}{2}\left((k_{\mathrm{c}}-k)\log(2) - 2k_{\mathrm{c}}\log(1-\gamma) + (k+k_{\mathrm{c}})\log\left(\frac{3}{n\pi}\right)\right) \tag{16}$$

The crystallinity of the network ν is the product of microscopic single-chain crystallinity γ and fraction of crystalline chains k_{c}/k, so that $\nu = \gamma k_{\mathrm{c}}/k$. The latter equation can be used to eliminate k_{c}:

$$k\frac{3}{2\gamma}\left((\nu-\gamma)\log(2) - 2\nu\log(1-\gamma) + (\nu+\gamma)\log\left(\frac{3}{n\pi}\right)\right) \tag{17}$$

In general, less than 40% of the chains are incorporated in the crystal, such that $\gamma < 0.4$ and $\log(1-\gamma) \approx -\gamma$. Using this approximation, we get

$$k\frac{3}{2}\left(2\nu + \nu\frac{1}{\gamma}\log\left(\frac{6}{n\pi}\right) + \log\left(\frac{3}{2n\pi}\right)\right) \tag{18}$$

The simplifications derived above are used to simplify the total deformational entropy of the (linear) network S_{D} given by eq 12. The total deformational entropy of the replacement chain $s_{\mathrm{D}} = S_{\mathrm{D}}/k$ then reads

$$s_{\mathrm{D}} = -\frac{3}{2}\frac{(r-\eta\nu n)^2}{n(1-\nu)} + \frac{3}{2}\left(2\nu + \nu\frac{1}{\gamma}\log\left(\frac{6}{n\pi}\right) + \log\left(\frac{3}{2n\pi}\right)\right) \tag{19}$$

where $\nu \leq \gamma$ because $\nu = \gamma$ corresponds to the case where every network chain is crystalline ($k_{\mathrm{c}} = k$). In the limit of zero network crystallization $\nu = 0$ we obtain the usual Gauss chain

$$s_{\mathrm{D}}(\nu = 0) = -\frac{3}{2}\frac{r^2}{n} + \frac{3}{2}\log\left(\frac{3}{2n\pi}\right) \tag{20}$$

We would like to highlight that eq 19 allows to calculate the deformational entropy of a replacement chain with total degree of crystallinity ν, which is composed of noncrystalline chains and crystalline chains with microscopic chain crystallinity γ. The difference between ν and γ is illustrated in Figure 2. As this theory assumes thermodynamic equilibrium, the free energy of the system shall be minimized with respect to the microscopic degree of crystallinity γ. Investigating the deformational entropy of the replacement chain given by eq 19 in the interval $\gamma \in [0, 1]$ it becomes obvious that the free energy will be minimal for $\gamma \to 1$. This means that crystalline chains would not have any amorphous segments anymore. As outlined in the Introduction, it is widely known that NR crystals are limited in size at about 10 nm and size scales roughly with mesh size defined by cross-link spacing. Additionally, for fibrillar crystals, 10 nm corresponds to roughly ten incorporated statistical segments (assuming a statistical segment size of $b = 0.934$ nm[25]), which is far less than the typical number of 50−150 segments between cross-links usually observed for natural rubber.

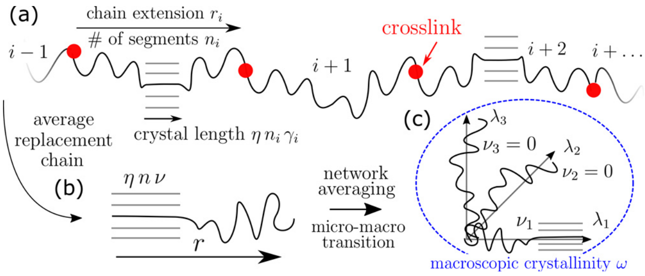

Figure 2. Visualization of the three modeling steps: (a) building a linear network of partially crystalline chains; (b) replacement by an average chain; (c) taking into account spatial distribution of chains and expressing crystallinity in terms of measurable, continuum crystallinity.

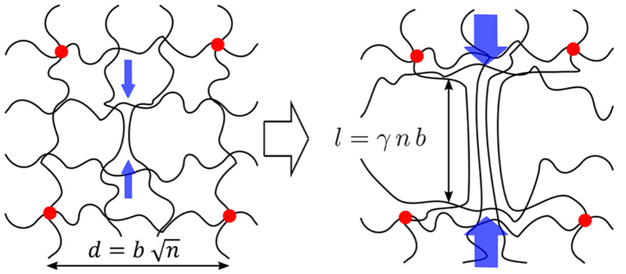

Figure 3. Illustration of the repelling entropic potential s_{P}. Small crystal nuclei are not hindered by the entropic potential originating from entangled and cross-linked chains (small blue arrows). If the crystal becomes too large, the entropic potential will prevent further crystal growth (large blue arrows).

Obviously, crystal growth is limited by processes not captured up to now. It is assumed that crystals are hindered in growth by surrounding chains because entanglements and cross-links have to be pushed out of it. This is visualized in Figure 3. We collect the influence of the surrounding by introducing a repelling entropic potential. The potential is proportional to the number of crystalline chains k_{c}. The remaining is expanded into a Taylor series, giving $S_{\mathrm{P}}(x) = k_{\mathrm{c}}(\kappa_0 + \kappa_1 x + \kappa_2/2\, x^2 + \ldots)$ where x is a measure for crystal length. The latter has to be dimensionless because otherwise higher order terms in the expansion would give arbitrary powers of dimensions. Two length scales are available to make x dimensionless: the segment length b, which will most certainly not affect crystal growth, and the network mesh size $d = \sqrt{n}\, b$, which was successfully related to crystal size as pointed out in the Introduction. The latter is chosen, defining $x = l/d = \eta\gamma n b/(\sqrt{n}\, b)$. There should be no entropy penalty for zero length crystals, so that $S_{\mathrm{P}}(x = 0) = 0$. Moreover, when holding the number of crystalline chains k_{c} constant, the repelling force opposed to growth should be vanishing for small crystals, which gives $\frac{\mathrm{d}S_{\mathrm{P}}}{\mathrm{d}x}(x = 0) = 0$. These conditions imply $\kappa_0 = \kappa_1 = 0$. The remaining potential is capped above quadratic order. We set $\kappa \equiv \kappa_2$. For the replacement chain the potential s_{P} is given by (in SI)

$$s_{\mathrm{P}} = \frac{S_{\mathrm{P}}}{k} \simeq \frac{1}{k} k_{\mathrm{c}} \kappa \left(\frac{l}{d}\right)^2 = \frac{\nu}{\gamma} \kappa \left(\frac{\eta \gamma n b}{\sqrt{n}\, b}\right) = \nu \kappa \eta^2 \gamma n \tag{21}$$

where we used the definition of $\nu = k_{\mathrm{c}}/k\gamma$ to eliminate k_{c}. The dimensionless quantity κ is an unknown fit parameter. It should be a measure for the amount of constraints opposed to crystal growth, e.g., entanglement density. Additionally, it may be related to the fact that larger crystals require a larger detour for chains not ideally aligned in crystal direction. Given this, eq 21 should represent a good approximation in consideration of limited knowledge of the detailed processes involved.

Altogether, the total entropy of the replacement chain is composed of the deformational entropy s_{D} defined by eq 19, the repelling entropic potential s_{P}, and the conformational entropy s_{C} resulting from the degrees of freedom of each noncrystalline segment. The latter is given in analogy to eq 2 as

$$s_{\mathrm{C}} = s_f \frac{1}{k} \left(\sum_{i=1}^{k_{\mathrm{c}}} (1 - \gamma_i) n_i + \sum_{i=k_{\mathrm{c}}+1}^{k} n_i \right) = s_f (1 - \nu) n \tag{22}$$

with s_f being the entropy of fusion of one statistical polymer segment. Moreover, the enthalpy gain due to crystal formation is

$$h_{\mathrm{C}} = h_f \frac{1}{k} \sum_{i=1}^{k_{\mathrm{c}}} n_i \gamma_i = h_f \nu n \tag{23}$$

with the enthalpy of fusion per segment h_f.

Equilibrium is defined by the free energy f. It is composed of

$$f = h_{\mathrm{C}} - T(s_{\mathrm{D}} + s_{\mathrm{C}} + s_{\mathrm{P}}) \tag{24}$$

$$= -h_f \nu n - T[-\frac{3}{2} \frac{(r - \eta \nu n)^2}{n(1 - \nu)} + \frac{3}{2} \left(2\nu + \nu \frac{1}{\gamma} \log\left(\frac{6}{n\pi}\right) + \log\left(\frac{3}{2n\pi}\right) \right) + (1 - \nu) s_f n - \nu \kappa \eta^2 \gamma n] \tag{25}$$

$$= -\nu n \theta + T\left(\frac{3}{2} \log\left(\frac{2n\pi}{3}\right) - s_f n \right) + T \frac{3}{2} \frac{(r - \eta \nu n)^2}{n(1 - \nu)} \tag{26}$$

where (in SI)

$$\theta = h_f - k_{\mathrm{B}} T \left(\frac{s_f}{k_{\mathrm{B}}} + \eta^2 \kappa \gamma - \frac{3}{n} + \frac{3}{2\gamma n} \log\left(\frac{n\pi}{6}\right) \right) = h_f - \tilde{s}_f T \tag{27}$$

collects all terms scaling with network crystallinity ν, despite its effect on the strain term. Take into account that the entropy punishment due to crystal formation ($\sim\log(n\pi/6)/n$) decreases with the number of segments n. To compare the obtained entropy of fusion with literature, it is useful to define the effective entropy of fusion as follows:

$$\tilde{s}_f = s_f + k_{\mathrm{B}} \left(\eta^2 \kappa \gamma - \frac{3}{n} + \frac{3}{2\gamma n} \log\left(\frac{n\pi}{6}\right) \right) \tag{28}$$

which corrects the entropy of fusion of one segment by the entropy lost due to decreasing mobility of the remaining chain and the repelling potential.

Micro–Macro Transition. The transition to a polymer network is carried out by splitting up the network into three orientational domains as shown in Figure 2c and assuming affine deformation. The first one is directed into the direction of maximum strain λ_1, while the two other ones are perpendicular. The end to end vectors of the domains are deformed affinely from their length at zero strain: $r_i = \lambda_i r_0$. Each domain may be crystalline with crystallinity fraction ν_i. The average free energy is then given as

$$\langle f \rangle = \frac{1}{3} (f(r_0 \lambda_1, \nu_1) + f(r_0 \lambda_2, \nu_2) + f(r_0 \lambda_3, \nu_3)) \tag{29}$$

$$= \frac{1}{3} \left(-\theta n \sum_{i=1}^{3} \nu_i + T \sum_{i=1}^{3} \frac{3}{2} \frac{(r_0 \lambda_i - \eta \nu_i n)^2}{n(1 - \nu_i)} + 3T \left(\frac{3}{2} \log\left(\frac{2n\pi}{3}\right) - s_f n \right) \right) \tag{30}$$

we can easily see that the crystallinity of the whole sample can be identified by $\omega = \frac{1}{3}(\nu_1 + \nu_2 + \nu_3)$. We will call ω continuum crystallinity from now on. Experimental results show that crystals are highly oriented in direction of strain,[7] such that it appears reasonable to assume that only the domain in direction of strain is crystalline. This can be formalized as $\nu_2 = \nu_3 = 0$, thus giving $\nu_1 = 3\omega$. The r-dependent part of eq 30 can be simplified as

$$\frac{1}{3} \sum_{i=1}^{3} \frac{3}{2} \frac{(r_0 \lambda_i - \eta \nu_i n)^2}{n(1 - \nu_i)} \simeq \frac{1}{3} \left(\frac{3}{2} \frac{(r_0 \lambda_1 - \eta \nu_1 n)^2}{n(1 - \nu_1)} + \frac{3}{2} \frac{(r_0 \lambda_2)^2}{n} + \frac{3}{2} \frac{(r_0 \lambda_3)^2}{n} \right) \tag{31}$$

$$\approx \frac{1}{2} \frac{(r_0 \sqrt{{\lambda_1}^2 + {\lambda_2}^2 + {\lambda_3}^2} - \eta \nu_1 n)^2}{n(1 - \nu_1)} \tag{32}$$

where the latter approximation is exact for strains below crystallization onset ($\nu_1 = 0$) and becomes more precise for $\lambda_1 \gg \lambda_2 \approx \lambda_3$, which is usually fulfilled above crystallization onset for uniaxial strain. The approximation was done to make the model invariant to rotation of the coordinate system. Using $r_0 = \sqrt{n}$, the average free energy then reads (in SI)

$$\langle f \rangle = -\omega n \theta(\gamma) + k_{\mathrm{B}} T \left(\frac{3}{2} \log\left(\frac{2n\pi}{3}\right) - s_f n \right) + k_{\mathrm{B}} T \frac{3}{2} \frac{\left(\sqrt{\frac{n I_1}{3}} - \sqrt{3} \eta \omega n \right)^2}{n(1 - 3\omega)} \tag{33}$$

with $I_1 = {\lambda_1}^2 + {\lambda_2}^2 + {\lambda_3}^2$ being the first strain invariant known from continuum mechanics. The average free energy $\langle f \rangle$ can be minimized with respect to the degree of crystallinity of individual chains γ to get a measure for the length of the crystallites. Quantities defining the minimum of the free energy density will be denoted with an asterisk from now on. Note that $\theta(\gamma)$ incorporates all dependencies on γ. Minimization gives (in SI)

$$\gamma^* = \frac{1}{\eta} \sqrt{\frac{3}{2\kappa n} \log\left(\frac{n\pi}{6}\right)} \rightarrow l^* = b \eta n \gamma^* = b \sqrt{\frac{3n}{2\kappa} \log\left(\frac{n\pi}{6}\right)} \tag{34}$$

with l^* being the length of the crystal. Take into account that l^* is independent of the first strain invariant $I_1 = \lambda^2 + 2/\lambda$ and temperature T. In fact, numerous studies have shown the length in stretching direction of the crystallite to be insensitive to strain, although the remaining dimensions weakly depend on it.[3−5] Additionally, the extension of crystallites was shown to be almost independent of temperature.[6]

Note also that the enthalpy of fusion does not appear in the equation, too. This is because the length is solely determined by balancing the entropic need for long crystals (because of the entropy punishement of chain attachment) and the entropy loss due to displacement of the surrounding network.

The continuum crystallinity ω measuring the number of crystalline chains is still unknown. Inserting γ^* and minimizing the averaged free energy $\langle f \rangle$ with respect to ω gives (in SI)

$$\omega^* = \frac{1}{3}\left(1 - \sqrt{\frac{(\sqrt{I_1} - \eta\sqrt{n})^2}{\eta^2 n + \frac{2\theta(\gamma^*)}{3k_B T} n}}\right) \tag{35}$$

Crystallization starts when ω^* becomes larger than 0. From $\omega^*(I_1^*) = 0$, we get the crystallization onset strain in terms of the first invariant (in SI)

$$I_1^* = n\left(\eta - \sqrt{\eta^2 + \frac{2\theta(\gamma^*)}{3k_B T}}\right)^2 \tag{36}$$

The total free energy density of the network $F(I_1)$ can be calculated from the average free energy given by eq 33 by multiplication with the number density of elastically active chains ν_c. This is the central quantity of this work, as its minimum defines the materials behavior. Before crystallization onset at I_1^* crystallization is $\omega = 0$, afterward $\omega = \omega^*(I_1)$:

$$F(I_1) = \begin{cases} \nu_c \langle f \rangle(\omega = 0) & \text{for } I_1 < I_1^* \\ \nu_c \langle f \rangle(\omega = \omega^*, \gamma = \gamma^*) & \text{for } I_1 \geq I_1^* \end{cases} \tag{37}$$

where the first case is equivalent to the neo-Hookean material model. Stress is derived from the given free energy density using continuum mechanical methods (see e.g. ref 26).

RESULTS AND DISCUSSION

To validate the model described in the previous section, we use data obtained by Trabelsi,[7] Albouy,[23] and Rault.[12] They investigated the same natural rubber recipes containing 2 g of stearic acid, 5 g of ZnO, and 1 g of antioxidant (6PPD) per 100 g of natural rubber. The rubber was cross-linked semiefficiently using 0.8, 1.2, and 2.0 g of sulfur and accelerator (CBS) for samples I, II, and III, respectively. The number of monomers between two cross-links has been determined via swelling to be 335, 238, and 145, respectively.

In contrast to the authors, we will use the number of statistical segments instead of the number of monomers between cross-links. Using the molar mass of NR statistical segments $M_s = 128.6$ g/mol[27] and the molar mass $M_m = 68.12$ g/mol of isoprene, we can assume that a segment consists on average of $M_s/M_m = 1.89$ isoprene units. Thus, we get the number of statistical segments $n_1 = 177$ for sample I, $n_2 = 126$ for sample II, and $n_3 = 77$ for sample III.

Alignment measurements[12] indicate that first crystallites grow into stretching direction, such that we set the strain reduction factor $\eta = 1$. *Until otherwise noted, we will keep this assumption.* This also means that the crystallizing chains are assumed to be aligned perfectly in direction of stretch. Usually, crystallization occurs at large strains (aligning the chains), such that this approximation feels appropriate.

The authors performed extensive WAXS studies during static and dynamic loading at different temperatures. They determined the crystal sizes in stretching direction (l_{002}) at room temperature for all three samples[7] as well as crystallization onset and offset strain, degree of crystallinity, and the mechanical response.

Their data are now evaluated in three steps. (1) Experimental crystal size is fitted to eq 34 to determine its sole fitting parameter κ, which scales the entropy punishment due to crystal growth. Using this parameter (2) the model is fitted to SIC onset and offset strains of all samples and different temperatures using eq 36. This allows to determine all thermodynamic parameters of the model and to deduce information about crystal geometry. The model is fully determined, then. Finally, (3) the parameters obtained are used to calculate the mechanical response and degree of crystallinity around crystallization onset and offset.

The fit of step 1 is shown in Figure 4, together with crystal sizes obtained by other authors,[3,4] determining $\kappa = 4.76$. Segment length of NR was set to $b = 0.934$ nm.[25] The accuracy of the fit retrospectively justifies the choice of the entropic potential given in eq 21.

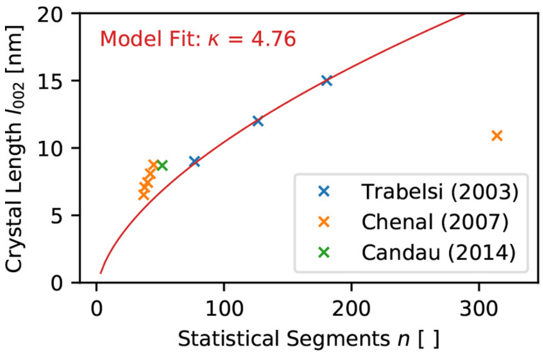

Figure 4. Crystal length $l^* \equiv l_{002}$ in stretching direction vs chain length in statistical segments obtained by various authors. The model fit to data from Trabelsi[7] given by eq 34 is also shown. The curve is fully determined by the parameter $\kappa = 4.76$.

Additionally, the authors determined the onset and offset strain at different temperatures by extrapolating the crystallinity curve to zero (sample I)[12] or by investigating the kinks in the stress−strain curve (sample II).[23] Onset and offset at room temperature for samples I, II, and III were extracted from the data provided by Trabelsi.[7] The onset and offset strains were converted to the first invariant using the assumption of perfect uniaxial loading: $I_1^* = \lambda^{*2} + 2/\lambda^*$. The data obtained is fitted to eq 36 to determine the remaining model parameters: The entropy of crystal formation per segment s_f is assumed to be the same during crystal melting (offset) and crystal formation (onset), as it should be independent of crystal size and geometry. In contrast, the enthalpy of fusion per segment h_f may be influenced by crystal size because larger crystallites are less impacted by surface energy. Thus, h_f is set free for onset and offset and each sample. It will be related to crystal size later. The parameter κ scaling the entropy punishment due to growth of crystallites is set to the value obtained in Figure 4 for all samples and crystal melting/formation. Data and fit are shown in Figure 5. The model fits the data rather good, except at low temperatures. There it has to be taken into account that the SIC offset at temperatures $\lesssim$20 °C were sometimes

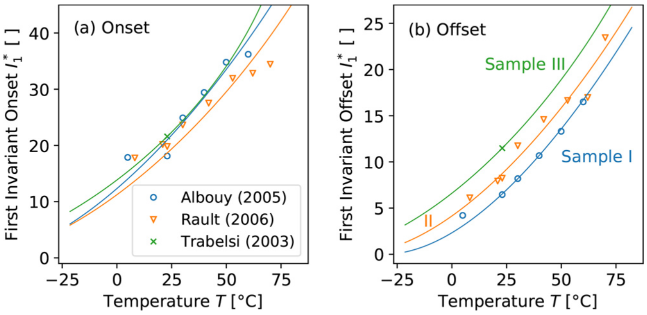

Figure 5. (a) Onset strain of SIC measured[7,12,23] for differently cross-linked samples I−III at different temperatures and converted to the first strain invariant $I_1^* = \lambda^{*2} + 2/\lambda^*$. The solid lines correspond to a fit to eq 36. (b) Same for the offset of SIC. It has to be kept in mind that deviations of data and model strain appear squared due to the definition of I_1.

extrapolated by the authors due to inverse yielding effects (which will be discussed later), and the crystallization mechanism may already resemble cold crystallization.[6] Thus, the corresponding data points involve some uncertainties. From the enthalpy and entropy of fusion per segment the corresponding macroscopic quantities (per gram of sample) can be calculated according to

$$H_f = \frac{N_A}{M_s} h_f \quad S_f = \frac{N_A}{M_s} s_f \quad \tilde{S}_f = \frac{N_A}{M_s} \tilde{s}_f \tag{38}$$

with Avogadro's constant N_A and the molar mass of statistical segments $M_s = 128.6$ g/mol.[27] The effective entropy of fusion $\tilde{S}_f$ is calculated from the corresponding microscopic value given by eq 28. All converted fitted result are given in Table 1. It is crucial to note that H_f as presented here is an effective value including surface tension. It can be expressed as follows:

$$H_f = H_{f,0}\left(1 - \frac{2l(a+b)\sigma + 2ab\sigma_e}{H_{f,0}abl}\right) \tag{39}$$

where $H_{f,0} = 65.3$ J/g is the bulk enthalpy of fusion determined on the un-cross-linked melt,[28] l is crystal length, a and b are the remaining cuboid dimensions, σ is the lateral surface energy, and σ_e is the end surface energy (where chains leave) of the crystallite. WAXS data suggest that NR crystallites are of platelet-like shape with l constant respective strain while a and b increase with proceeding crystallization. Additionally, it is found that $b \approx a/3$.[3,4] Using the latter, we can solve eq 39 for a

$$a = \frac{8l\sigma}{(H_{f,0} - H_f)l - 2\sigma_e} \tag{40}$$

Knowing l from the data of Trabelsi[7] (see Figure 4) for each specimen, we can use eq 40 to determine the lateral size of the crystal close to nucleation and melting. The lateral free surface energy of unstrained purified NR melts, crystallized by cooling below the equilibrium melting point, was estimated by Kawahara[29] to be $\sigma = 0.013$ J/m^2. While the lateral interface of strain-induced crystals and lamellar crystals usually occurring in the quenched melt is probably similar, the end surface energy σ_e may be different because crystals in the melt usually are of lamellar type and SIC crystals do not fold to the same extent. For un-cross-linked NR it was estimated by the same authors to be $\sigma_e = 0.024$ J/m^2. Gros et al.[30] argue that end surface energy for strain crystallizing, cross-linked NR is close to zero. Thus, the end surface energy is rather uncertain, such that we calculate a using both $\sigma_e = 0.024$ J/m^2 and $\sigma_e \approx 0$. The result is given in Table 1 as well. It turns out that the crystal dimensions $a \approx 4.5$ nm and $b \approx a/3 \approx 1.5$ nm at crystallization onset are rather independent of cross-link density. This indicates that always the same amount of chains participate in forming the nucleus, although nucleus length l depends on cross-link density. As the number of chains initially available for nucleation should be independent of cross-link density (on a scale much smaller than mesh size), this results feels intuitively correct. It is a direct consequence of the larger entropy punishment for chain attachment at larger cross-link densities; otherwise, a larger network strain (at constant SIC onset strain) would have to be compensated by smaller, less stable nuclei with a smaller net enthalpy of fusion, when holding onset strain constant.

In previous models a larger network strain (for higher cross-linked samples) would result in a smaller SIC onset strain. This was already pointed out by Flory[13] and other authors[19] and seemed to contradict experimental evidence.

We also see from Table 1 that crystal dimensions prior to melting are larger than shortly after SIC onset. Moreover, crystal dimensions increase with decreasing cross-link density. This indicates that the last melting crystals perfected their ordering. Crystal sizes close to onset and offset as given in Table 1 roughly coincide with the dimensions at onset and offset strain observed by Candau.[3]

The entropy of fusion of uncured NR of NR can be calculated from the literature data using $0 = H_{f0} - T_m S$, where melting temperature is $T_m = 309$ K.[29] The result $S = 0.211$ J/(g K) is 5−10% off from the effective entropy of fusion $\tilde{S}_f$ given in Table 1.

It has to be kept in mind that all results given in Table 1 are derived using many assumptions, especially the micro−macro transition may be questioned: In eq 33 the factor $\sqrt{3}$ directly emerges from splitting the network in three representative chains in each direction of space. Changing the averaging process will change this factor and scale h_f and s_f accordingly.

Using eq 37 and the parameters defined in Table 1, the mechanical response can be derived. The number of elastically active chains is computed via $\nu_c = \rho/(M_s n)$ with $\rho \approx 0.92$ g/cm^3 being the density of natural rubber. The results are

Table 1. Collection of the Fitting Results Originating from Figures 4 and 5[a]

sample	1	2	3
	fixed parameters		
n	177	126	77
η	1		
κ	4.76 (from Figure 4)		
	fitted parameters		
H_f up [J/g]	38.0	38.3	37.6
H_f down [J/g]	44.3	43.3	42.1
S_f [J/(g K)]	0.129		
	calculated parameters		
a up [nm]	4.1 (4.7)	4.2 (5.1)	4.1 (5.2)
a down [nm]	5.4 (6.5)	5.1 (6.4)	4.9 (6.5)
$\tilde{S}_f$ [J/(g K)]	0.184	0.191	0.203

[a] The lateral crystal sizes a are derived from the corresponding enthalpy of fusion H_f during onset (up) and offset (down) via eq 40. The surface tension is set to $\sigma_e = 0$ ($\sigma_e = 0.024$ J/cm^2).

compared to experimental data for samples I and II in Figure 6. At intermediate temperatures and strains below strain hardening the model reproduces the experiment fairly well. The deviations at low temperatures may be traced back to invalid model assumptions (partial "cold crystallization") and/or errors due to extrapolation of crystallization offset. At high temperatures probably a smaller fraction of polymer is able to undergo SIC, preventing a complete stress homogenization and thus the "melting stress plateau" observable during unloading. For sample II a complete deformation cycle is shown in Figure 6b. While the stress plateau during release is described fairly well, the decrease in stress upon beginning of SIC is overestimated. Probably, the network and crystallites need some additional driving force to rearrange for perfect stress homogenization.

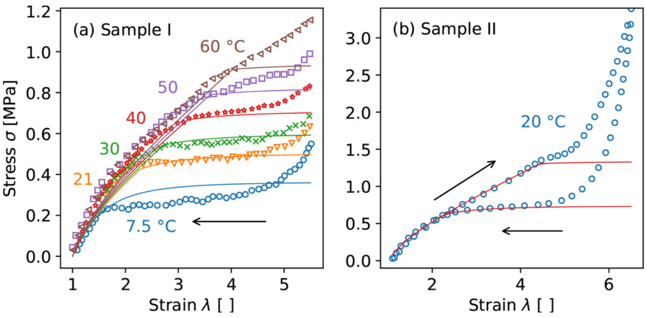

Figure 6. (a) Mechanical response during unloading of sample I (data from ref 23) and corresponding response derived from eq 37 and the parameters given in Table 1. (b) Mechanical response of sample II (data from ref 12) and calculated response for onset and offset of SIC.

Similarly, the degree of crystallinity can be calculated using eq 35 and the parameters from Table 1. The result and comparison to data of sample II is shown in Figure 7. In Figure 7b the model prediction is shown up to the value of crystallinity, which is possible without chain folding. It is defined by $\gamma = l/(nb) = 0.091$, 0.102, and 0.125 for samples I, II, and III, respectively. The formula assumes that every chain of contour length nb passes one time through a crystal. For small crystallinities, the model predicts the experimental data fairly well, given the numerous assumption involved. At larger crystallinities the model fails because larger and thus more stable crystallites may change the overall crystallization mechanism (see discussion later).

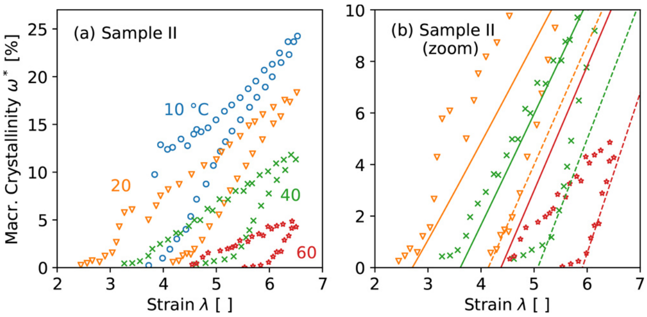

Figure 7. (a) Crystallinity of sample II at different temperatures (taken from ref 12). (b) Same data and crystallinity reproduced from eq 35 using parameters from Table 1 for onset (dashed) and offset (solid) of SIC. Data for 10 °C is omitted for better visibility.

Now the effect of crystal phase morphology on degree of crystallinity is investigated. As explained in the Theory section, $\eta = 1$ corresponds to fibrillar crystals aligned in stretching direction. For $\eta < 1$ just a fraction of the crystalline chain reduces strain of the amorphous phase; e.g., $\eta = 1/3$ corresponds to chains folded one time. A value below 1 may be beneficial when the surrounding network hinders further fibrillar (linear) crystal growth, but additional crystalline fraction will give a net negative free energy. This may happen when crystals become large enough to allow energetically attractive chain folding on the surface. The thermodynamic validity of chain folding is determined by the free energy density given by eq 33. The energetical minimum depends crucially on enthalpy of fusion h_f, which is in turn related to the dimensions of the crystallites via eq 40 (using $\sigma_e \approx 0$). Minimization with respect to η analytically requires much effort, such that we do it numerically. Varying the size of the crystal a the minimum of eq 33 with respect to ω and η for different strains λ is shown in Figure 8. Again, minimum quantities ω^* and η^* are indicated by an asterisk. Two things become obvious. (1) For all strains above crystallization onset $\lambda \approx 4.5$ crystallinity increases upon increasing the crystals dimensions. At a critical crystal dimensions, which is lower than the crystals size a determined close to crystallization offset (see Table 1), all curves discontinuously jump to maximum crystallinity, indicating a kind of phase transition. The critical crystal dimension is a function of temperature and almost independent of strain, consistent with results from X-ray and electron microscopy obtained by Luch and Yeh,[31] who stated "These results strongly suggests that temperature (...) is the primary, if not the only, variable which directly decides lamellar stability, although applied stress and/or strain may affect the rate and ease with which lamellae form". Interestingly, for strains below crystallization onset $\lambda \approx 4.5$ the phase transition occurs discontinuously if crystals are sufficiently large, their critical size depending on strain. (2) The explanation is given by the observation that up to critical crystal size a the optimum strain reduction parameter η^* equals 1, corresponding to linear crystals. After surpassing the threshold it discontinuously jumps to a constant smaller value, see Figure 8b. The larger the strain, the larger the remaining η^*. In fact, η^* is chosen such that the deformational entropy $\sim(\sqrt{nI_1} - 3\eta\omega n)^2$ becomes zero. In reality, there will always be a remaining deformational entropy because also chain folding crystallites are restricted by the surrounding matrix. Additionally, the formation of loops requires additional entropy,[32] which is not taken into account. To conclude, it may be said that the derivations above indicate

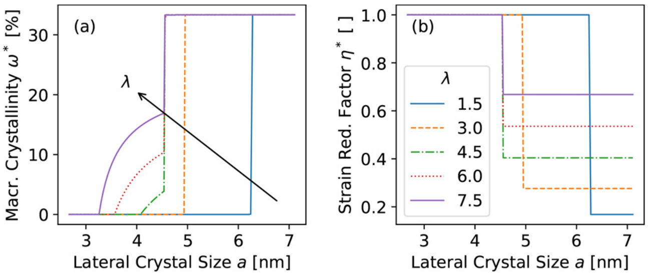

Figure 8. (a) Continuum crystallinity ω^* and (b) strain reduction factor η^* corresponding to the minimum of free energy (eq 33) at different strains λ and crystal sizes a for sample II. Remaining parameters are taken from Table 1 (using $\sigma_e = 0$), and temperature is set to 23 °C. Above a critical crystal dimension, which is independent of strain, crystallinity increases and chains are folding.

that chain folding becomes possible when crystals are sufficiently large. There will certainly be no discrete jump to maximum crystallinity (as found here) because this would require recrystallization of the total fibrillar crystals to lamellar type. Instead, lamellar chains may grow on top of the fibrillar nucleus, such that the quantitative values in Figure 8 have to be interpreted with care.

Now a scheme of NR crystallization is drawn. Take into account that the model derived above is strictly valid only near crystallization onset and offset, where the enthalpy of fusion was fitted. Thus, many of the observations below are deduced from combining results and experience from the modeling with careful interpretation of the large amount of literature data available on the topic.

- Upon increasing strain the entropy punishment for crystal formation decreases. At onset strain $\lambda \approx 4.5$ first crystals consisting of a few chains are thermodynamically stable. Onset strain is largely independent of n because the entropy punishment (per segment) for attaching to a crystal becomes smaller for longer chains, compensating for the lower network strain. The entropy punishment for crystal attachment also explains why full-length crystals appear: It is thermodynamically more favorable to grow one crystal as long as possible than to grow two smaller ones because the attachment cost has to be paid only once. Formally, this results from the minimization of eq 33 with respect to microscopic (single chain) crystallinity γ at fixed macroscopic crystallinity ω, giving γ as large as possible, only restricted by the repelling entropic potential s_P. Macroscopic crystallinity ω is proportional to the number of crystalline chains k_c and single chain crystallinity γ. Thus, at constant macroscopic crystallinity, an increasing microscopic crystallinity goes along with a decrease of crystalline chains.
- By further increasing strain crystals increase in number and rapidly thicken. The thickening in directions perpendicular to stretching as well as the increase in number of crystals was shown via WAXS by various authors.[3,4] This happens because the enthalpy gain for attaching to an already present crystal is larger than forming a new one. With increasing crystal size the effective enthalpy of fusion per segment increases until the threshold visualized in Figure 7 is reached, where the linear crystals may act as a nucleus for folded chain crystals. We will refer to the degree of crystallinity defining the point as crystallinity threshold from now on. Luch et al. found fibrillar crystals in un-cross-linked natural rubber at −28 °C at strains up to 900%.[6] Although experiments evaluated here were done at a much larger temperature, network strain will certainly be much larger due to cross-linking. We argue that the transition to chain folding has to set in when the crystallinity of the crystallizable polymer fraction approaches γ, meaning that all crystallizable polymer traverses a fibrillar crystal one time. To increase crystallization further, the polymer necessarily has to fold. Indeed, numerous WAXS studies on moderately cross-linked samples[3,7,12,23] and calorimetric approaches[33,34] clearly show a kink in the crystallinity curve for loading as well as unloading at about 6 ± 3% crystallinity, dependent on cross-link density.[3,7,18] Mechanically, these points seem to correspond to the beginning/end of the stress plateau. Presumably this happens because folded chain crystals are not equally effective in regulating strain and the regulation process is overcompensated by the increase in cross-link density due to crystal formation, as originally proposed by Flory.[13] Candau[3] investigated incomplete stretching cycles. If the lower strain limit of a strain cycle is larger than the crystallinity threshold, the crystallinity curve shows almost no hysteresis. Similar effects can be seen in crystallinity curves obtained by thermography.[34] A vanishing hysteresis is indicative of continuous attachment/detachment to crystals instead of new crystals spawning and disappearing. In that sense, crystallization above the crystallinity threshold may be similar to "cold crystallization" in unstretched polymers[31] with nuclei already present (explaining the faster crystallization rate and vanishing hysteresis). The model presented here is unable to reproduce the kink, created by chain folding, because a change in strain reduction factor η goes along with complete recrystallization of the crystal. A crystal consisting of a fibrillar nucleus with chains folded on top cannot be modeled using this framework.
- During strain release the chain folded crystalline parts melt first. The last folded chain detaches at roughly the same degree of crystallinity as the first folded chain attached because the thermodynamic stability of chain folded crystals depends only on crystal size (and thus on chains included in crystals, which scales with ω) and not on strain. This is deduced from the result of Figure 8.
- Below crystallization threshold crystals are only stable due to the strain regulation effect. Whenever strain is released, the need for crystalline chains vanishes and they detach. Most probably, this will induce the melting of the corresponding crystallites, as chain detachment decreases the overall stability of the crystal. We suggest that during unloading larger domains of comparably high crystallinity are present than during loading, which is closer to the global free energy minimum, yields a more effective strain regulation effect, and could explain the inverse yielding observable in loosely cross-linked samples.[7] This is also supported by the fact that crystal size obtained by the model close to SIC offset is larger than at SIC onset, as shown in Table 1. Thus, the large hysteresis both in crystallinity and strain can be safely attributed to a supercooling effect.

■ CONCLUSION

A physically simple model of SIC was presented. Despite its obvious simplifications (e.g., restriction to Gauss chains without finite extensibility), it is able to reproduce stress, degree of crystallinity, and length of the crystallites. The crucial difference to previous works is the consideration of entropy punishment for attachment to a crystal, which seems to resolve the mystery, that SIC onset is independent of strain. Also, it takes into account the relationship of single chain microscopic crystallinity and measurable macroscopic crystallinity. The corresponding calculation shows that a series of individual crystals may be approximated by a continuously growing crystal, justifying the foundation of many other models. Concerning the questions posed in the introduction the following answers can be given: (1) Crystals always have the same length because it is determined by the purely entropic competition between forming a crystal as large as possible and the repelling entropic force of the surrounding matrix. As both contributions scale with temperature the thermodynamic equilibrium is independent of it. The consistency of the modeling approach indicates that the repelling entropic potential does not depend on strain. It is worth investigating if this is truly the case. (2) Crystallization onset strain is rather independent of cross-link density because higher network strain in dense networks is compensated by a larger punishment for chains attaching to the crystal. (3) Modeling results and comparison with experiments in the literature show that chain folding is almost indispensable for the large values of crystallinity usually found. Motivated by a phase transition found in the model we propose that chains fold on the surface of fibrillar crystals, when the latter are sufficiently large. This also naturally explains why strain hardening occurs: Chain folded crystals span less distance per segment spent, thus regulating strain less effectively. (4) At onset strain crystal nuclei made up of a few stretched chains emerge, the number of chains being independent of cross-link density. These crystals thicken until chain folding becomes possible and folded chains attach to the surface. At unloading, folded chains detach rather continuously from the crystal surface. Afterward, fibrillar crystals successively melt. Between crystal formation and melting crystals may rearrange such that the strain regulation process becomes most effective. We believe that the latter effect is the predominant reason for NRs toughness because it will automatically homogenize the mechanical load in the rubber material. SIC will certainly increase the effective cross-link density of the material. Presumably, this also affects the particularly strong strain hardening of NR compounds[7,13] followed by the stress plateau. The increase in cross-link density is not taken into account up to now and will be a task for future works.

■ AUTHOR INFORMATION

Corresponding Author

*E-mail: jan.plagge@dikautschuk.de (J.P.).

ORCID

J. Plagge: 0000-0002-6650-4653

Notes

The authors declare no competing financial interest.

■ REFERENCES

(1) Amnuaypornsri, S.; Sakdapipanich, J.; Toki, S.; Hsiao, B. S.; Ichikawa, N.; Tanaka, Y. Strain-induced crystallization of natural rubber: effect of proteins and phospholipids. *Rubber Chem. Technol.* **2008**, *81*, 753−766.

(2) Tosaka, M. Strain-induced crystallization of crosslinked natural rubber as revealed by X-ray diffraction using synchrotron radiation. *Polym. J.* **2007**, *39*, 1207.

(3) Candau, N.; Laghmach, R.; Chazeau, L.; Chenal, J.-M.; Gauthier, C.; Biben, T.; Munch, E. Strain-induced crystallization of natural rubber and cross-link densities heterogeneities. *Macromolecules* **2014**, *47*, 5815−5824.

(4) Chenal, J.-M.; Chazeau, L.; Guy, L.; Bomal, Y.; Gauthier, C. Molecular weight between physical entanglements in natural rubber: a critical parameter during strain-induced crystallization. *Polymer* **2007**, *48*, 1042−1046.

(5) Chenal, J.-M.; Gauthier, C.; Chazeau, L.; Guy, L.; Bomal, Y. Parameters governing strain induced crystallization in filled natural rubber. *Polymer* **2007**, *48*, 6893−6901.

(6) Luch, D.; Yeh, G. Morphology of strain-induced crystallization of natural rubber. I. Electron microscopy on uncrosslinked thin film. *J. Appl. Phys.* **1972**, *43*, 4326−4338.

(7) Trabelsi, S.; Albouy, P.-A.; Rault, J. Crystallization and melting processes in vulcanized stretched natural rubber. *Macromolecules* **2003**, *36*, 7624−7639.

(8) Dargazany, R.; Khiêm, V. N.; Poshtan, E. A.; Itskov, M. Constitutive modeling of strain-induced crystallization in filled rubbers. *Phys. Rev. E* **2014**, *89*, 022604.

(9) Chenal, J.-M.; Chazeau, L.; Bomal, Y.; Gauthier, C. New insights into the cold crystallization of filled natural rubber. *J. Polym. Sci., Part B: Polym. Phys.* **2007**, *45*, 955−962.

(10) Candau, N.; Chazeau, L.; Chenal, J.-M.; Gauthier, C.; Ferreira, J.; Munch, E.; Rochas, C. Characteristic time of strain induced crystallization of crosslinked natural rubber. *Polymer* **2012**, *53*, 2540−2543.

(11) Brüning, K.; Schneider, K.; Roth, S. V.; Heinrich, G. Kinetics of strain-induced crystallization in natural rubber: a diffusion-controlled rate law. *Polymer* **2015**, *72*, 52−58.

(12) Rault, J.; Marchal, J.; Judeinstein, P.; Albouy, P. Stress-induced crystallization and reinforcement in filled natural rubbers: ^{2}H NMR study. *Macromolecules* **2006**, *39*, 8356−8368.

(13) Flory, P. J. Thermodynamics of crystallization in high polymers. I. Crystallization induced by stretching. *J. Chem. Phys.* **1947**, *15*, 397−408.

(14) Tosaka, M.; Murakami, S.; Poompradub, S.; Kohjiya, S.; Ikeda, Y.; Toki, S.; Sics, I.; Hsiao, B. S. Orientation and crystallization of natural rubber network as revealed by WAXD using synchrotron radiation. *Macromolecules* **2004**, *37*, 3299−3309.

(15) Strobl, G. R. *The Physics of Polymers: Concepts for Understanding Their Structures and Behavior*; Springer Science & Business Media: 2007.

(16) Flory, P. J. *Principles of Polymer Chemistry*; Cornell University Press: 1953.

(17) Vieyres, A.; Perez-Aparicio, R.; Albouy, P.-A.; Sanseau, O.; Saalwachter, K.; Long, D. R.; Sotta, P. Sulfur-cured natural rubber elastomer networks: correlating cross-link density, chain orientation, and mechanical response by combined techniques. *Macromolecules* **2013**, *46*, 889−899.

(18) Albouy, P.-A.; Vieyres, A.; Pérez-Aparicio, R.; Sanséau, O.; Sotta, P. The impact of strain-induced crystallization on strain during mechanical cycling of cross-linked natural rubber. *Polymer* **2014**, *55*, 4022−4031.

(19) Huneau, B. Strain-induced crystallization of natural rubber: a review of X-ray diffraction investigations. *Rubber Chem. Technol.* **2011**, *84*, 425−452.

(20) Gaylord, R. A theory of the stress-induced crystallization of crosslinked polymeric networks. *J. Polym. Sci., Polym. Phys. Ed.* **1976**, *14*, 1827−1837.

(21) Kroon, M. A constitutive model for strain-crystallising rubber-like materials. *Mech. Mater.* **2010**, *42*, 873−885.

(22) Mistry, S. J.; Govindjee, S. A micro-mechanically based continuum model for strain-induced crystallization in natural rubber. *Int. J. Solids Struct.* **2014**, *51*, 530−539.

(23) Albouy, P.-A.; Marchal, J.; Rault, J. Chain orientation in natural rubber, Part I: The inverse yielding effect. *Eur. Phys. J. E: Soft Matter Biol. Phys.* **2005**, *17*, 247−259.

(24) Scanlan, J. Cross-link breakdown and re-formation in strained polymer networks. *Trans. Faraday Soc.* **1961**, *57*, 839−845.

(25) Mark, J. E. *Physical Properties of Polymers Handbook*; Springer: 2007; Vol. *1076*.

(26) Holzapfel, G. A. Nonlinear solid mechanics. Wiley: Chichester, **2000**, *24*.

(27) Fetters, L.; Lohse, D.; Colby, R. *Physical Properties of Polymers Handbook*; Springer: 2007; pp 447−454.

(28) Kim, H.-G.; Mandelkern, L. Multiple melting transitions in natural rubber. *Journal of Polymer Science Part A-2: Polymer Physics* **1972**, *10*, 1125−1133.

(29) Kawahara, S.; Takano, K.; Yunyongwattanakorn, J.; Isono, Y.; Hikosaka, M.; Sakdapipanich, J. T.; Tanaka, Y. Crystal nucleation and growth of natural rubber purified by deproteinization and trans-esterification. *Polym. J.* **2004**, *36*, 361−367.

(30) Gros, A.; Tosaka, M.; Huneau, B.; Verron, E.; Poompradub, S.; Senoo, K. Dominating factor of strain-induced crystallization in natural rubber. *Polymer* **2015**, *76*, 230−236.

(31) Luch, D.; Yeh, G. S. Strain-induced crystallization of natural rubber. III. Reexamination of axial-stress changes during oriented crystallization of natural rubber vulcanizates. *J. Polym. Sci., Part B: Polym. Phys.* **1973**, *11*, 467−486.

(32) Reiter, G.; Strobl, G. R. *Progress in Understanding of Polymer Crystallization*; Springer: 2007; Vol. *714*.

(33) Le Cam, J.-B. Strain-induced crystallization in rubber: A new measurement technique. *Strain* **2018**, *54*, e12256.

(34) Plagge, J.; Klüppel, M. Determining strain-induced crystallization of natural rubber composites by combined thermography and stress-strain measurements. *Polym. Test.* **2018**, *66*, 87−93.

4.5 Outlook and Supplementary Information

The publications presented above present techniques for the quantification and modeling approaches for the understanding of SIC in natural rubber. Even though an explanation for constant SIC onset strain and crystal size was presented there are many open questions.

Strain hardening going along with SIC as observed in Fig. 4.1c is not understood. The increase of effective crosslink density due to bundling of chains in crystals offers an intuitive explanation [102, 110], but opens new questions: It is all but clear how to relate the crystalline fraction to crosslink density. Moreover, it has to be clarified which physical quantity determines the onset of strain hardening, as SIC induced crosslinking and hardening competes with the strain regulation process. Chain folding crystals at high strains could shift the balance towards crosslinking, but there is little evidence except the works of Luch and coworkers [116, 123, 124] and the theoretical investigations presented above.

The role of finite chain extensibility needs further discussion, too. Although Flory rejected the idea in his early works [102] almost complete chain stretching would naturally induce strain hardening. In particular, crystal growth decreases the number of free chain segments and shortens the amorphous chain. On the other hand a highly stretched chain would make the formation of crystals in stretching direction even more beneficial.

Crosslink density heterogeneities were proposed by Candau et al. [113] to explain the successive appearance of crystals of almost uniform size with strain: Wherever local strain is high enough, crystals will spawn. When increasing strain, the less crosslinked domains begin to crystallize. Although crosslink density heterogeneities will certainly play a role, it may be of minor importance for the understanding of SIC in natural rubber: The formation of crystals will decrease matrix strain in the surrounding which was neglected by Candau and coworkers. The strain equilibration following this process will prevent locally larger strains. The work presented above suggests that SIC controls strain such that it is internally constant. This is, during retraction, in accordance with experimental findings.

Non-equilibrium states are common in polymer melts. In cold crystallization, crystal geometry and crystallization kinetics is highly dependent on the materials history [58]. This is attributed to the highly viscous character of the material due to entanglements. In this context, the large hysteresis in crystallinity occuring during SIC is not surprising: Crystals prior to melting are larger and more stable than shortly after formation, as derived in publication 5. Nevertheless, this concept does not provide an explanation for the experimental fact that SIC onset is usually followed almost directly by the strain hardening regime, while during retraction a pronounced plateau with greatly reduced stress appears. In the following a scheme is presented which allows to explain the hysteresis cycle by the emergent strain-reduction potential of crystal agglomerations.

At crystallization onset strain crystals become locally favorable. This means that crystals will spawn randomly within the matrix, wherever strain is large enough and chains are directed appropriately. These crystals locally reduce matrix strain, but their effect is limited to their immediate

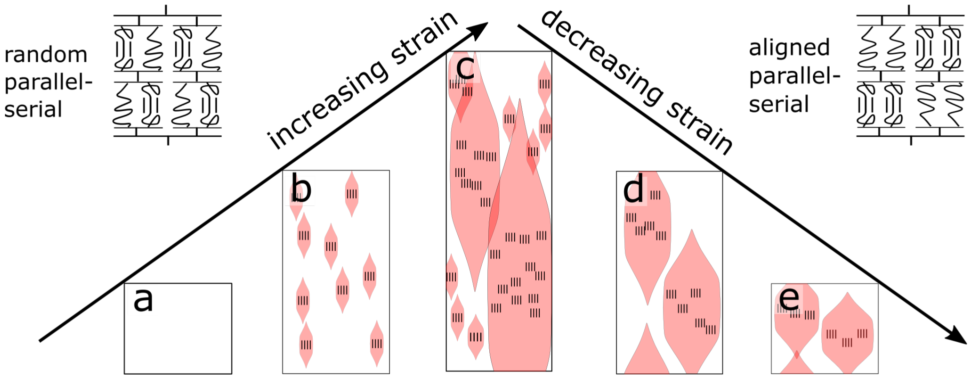

Figure 4.2: Sketch of the proposed hysteresis-generating crystallization mechanism. Red areas are reduced in local strain due to the presence of crystals. (a) During loading there are no crystals at low strains. (b) Above crystallization onset, first strain-induced crystals appear in the matrix wherever local strain and polymer configuration admits it. This corresponds to a random parallel-serial connection of crystalline and non-crystalline chains, preventing a pronounced stress plateau/strain regulation effect. (c) Upon further stretching, enough crystals spawned to form larger crystalline domains. In parallel configuration, these crystals are able to control strain of larger parts of the material. (d) During unloading, isolated crystals melt first. The larger crystalline domains stay intact, because they reduce matrix strain most effectively, thus decreasing the free energy. (e) Crystalline domains stay intact at strains where crystals were not present during loading because overall free energy is lower.

surrounding. An equivalent spring network would consist of random parallel-serial connections. For this reason, the crosslinking effect dominates and the material hardens. During strain hardening crystals continue to spawn randomly. If there are enough crystals close together, they may synergetically control strain of larger domains. This can be envisioned as crystalline chains connected in serial to the amorphous part on a larger scale. For this reason these collection of crystals will survive lower strains during unloading and generate a stress plateau. In fact, Trabelsi et al. could distinguish the crystalline and amorphous parts of quasistatically released NR by eye and named the phenomenon “inverse yielding effect” [32]. The whole process is sketched in Fig. 4.2. In the scope of thermodynamics, the state during unloading is closer to equilibrium even though the crystal arrangement is less random. The entropy loss due to non-random arrangement of crystals is compensated by an overall lower matrix strain.

Fig. 4.1c shows that NR exhibits behavior similar to Mullins effect. During first loading (enveloping virgin curve) the onset of SIC at about 350% strain is directly followed by strain hardening, whereas the mechanical cycles of the softened material show a pronounced plateau after SIC onset. In the scope of the mechanism presented above this indicates that the material remembers the thermodynamically ideal configuration of crystals. In fact, Sommer and coworkers have found via molecular dynamics simulations that remains of crystals may survive heating above the melting transition and self-seed crystals when cooled again [125, 126].

5

Conclusion and Outlook

The physical mechanism of polymer reinforcement was analyzed by means of different experimental as well as modeling approaches. Filler surface area and energy distribution were analyzed using static gas adsorption and automatized data evaluation. A new physically motivated constitutive material model for filled elastomers was developed. The model consciously avoids to explain rubber explanation by a specific mechanism. Instead, it assumes rubber to consist of several differently amplified domains which break down and reaggregate less amplified under load. Hysteresis was modeled by structures breaking and reforming under load. The breakdown is described by force driven diffusion over a potential barrier. The model fits data in different deformational states, at different speeds and temperatures very well. The mathematics was designed such that it is portable to FE code. Remaining flaws concerning exotic and inefficient mathematics were resolved in this work. Moreover, a physically reasonable scheme on the basis of detaching chains for continuous damage effects was elaborated and tested. A model fit to samples deformed at different speeds and temperature shows that the energy barrier related to hysteresis is about 100 kJ/mol. Consequently, polymer-filler investigation was quantified via static gas adsorption and automatized data evaluation using different polymer-analogue gases. The binding energy of ethane and propene to carbon black was found to be around 20 kJ/mol, showing that segments of about 5 monomers detaching and attaching to the filler surface could be responsible for hysteresis. Previous results concerning the surface fractal dimension of carbon black were confirmed. Silica exhibits a much higher surface occupation and adsorption energy than carbon black when probing with quadrupolar CO_2 molecules. In contrast, the interaction energy with hydrocarbons is similar for both carbon black and silica. Although uncoupled silica tends to aggregate in an unpolar matrix the latter result indicates that the better reinforcing potential of carbon black cannot be attributed exclusively to a better physical interaction.

Self reinforcement due to strain induced crystallization was measured by comparing the heating caused by deformation to the true temperature which originates also from melting and crystallization inside the material. The method was shown to be a fast and cost efficient alternative to established scattering experiments. The crystallinity vs. strain curve of carbon black filled samples differs in shape from the curve of unfilled samples, suggesting heterogeneous strain amplification as assumed in the amplification model presented in publication 1. Moreover, hysteresis in degree of crystallinity is reduced when cycling around strains above crystallization onset strain. A theory was developed, which explains the occurrence of many small crystals of uniform size by the fact that chains pay entropy to attach to a crystal, but crystals are limited in growth by the surrounding matrix. The same mechanism may answer the long standing question, why strain induced crystallization starts at the same strain for differently crosslinked samples. The model allows to reproduce the degree of crystallinity and mechanical data fairly well and delivers hints for a fibrillar-lamellar phase transition at high degrees of crystallinity.

The results presented in this thesis give rise to many new questions. Some of them are outlined below.

- Mullins effect of carbon black filled rubber is reversible at temperatures above room temperature. Regeneration starts to speed up at temperatures above 100 °C [127]. Moreover, as also found in this work, physical interaction of classical diene rubbers is similar to carbon black and silica, but the reinforcing effect of carbon black is much higher. This suggests that chemical binding of polymer and carbon black may play a crucial role. Bound rubber studies [127] and squalene-fullerene model systems show [128] that chemical bondings exist under thermo-oxidative conditions. Nevertheless, the authors are uncertain concerning their role in rubber reinforcement. It needs to be clarified, whether Mullins effect originates from chain slippage, caused by breaking physical bonds, chain desorption ultimately limited by the strength of chemical bonds or different mechanism like carbon black cluster breakage [47, 129]. This question may be addressed by detailed Mullins effect recovery measurements. Heat flux during recovery may be detectable using Dynamic Scanning Calorimetry (DSC) and could offer insight into the exact temperature and energy scales of the reactions involved. Squalene-carbon black model compounds could help to quantify the amount of chemical bonds and their strength in vitro.

- The origin of logarithmic stress relaxation is not understood. Successive chain desorption was proposed as a mechanism in this work and the resulting equations generate the desired behavior. Nevertheless, an experimental verification is still lacking and another mechanism, e. g. breakdown of filler structure, could prove to be the main cause [33, 47]. Moreover it would need to be clarified, whether chains desorb continuously or single chains are teared off the fillers surface, giving the logarithmic stress decay only as a collective behavior.

- The theory about SIC presented in this work reveals that enthalpy of fusion of NR crystals differs between loading and unloading. This has to be taken into account in the thermomechanical evaluation scheme. Additionally, the latter has to be calibrated using WAXS or similar techniques in parallel on the same sample.

- Altogether, a general concept for rubber reinforcement does not exist. While the increase in modulus, often referred to as amplification, may be understood via filler networking and hydrodynamic amplification, the increase in elongation and stress at break is not understood. Several concepts exist which often refer to local energy dissipation mechanisms [37, 130].

> Probably the proposed self reinforcement mechanism of natural rubber due to local strain regulation may serve as a guiding line to understand filler reinforcement. It is tempting to use the analogy of crystals giving additional chain length by spanning distance more effectively and fillers relaxing the chain by desorption of chain segments.

These question may serve as a starting point for future works. I hope that this thesis contributed to obtain a coherent picture of rubber reinforcement.

Bibliography

[1] E. D. Keoke and K. M. Porterfield, *Encyclopedia of American Indian contributions to the world: 15,000 years of inventions and innovations.* Infobase Publishing, 2009.

[2] L. A. González, *Etnocidio y resistencia en la Amazonía peruana*, vol. 69. Univ de Castilla La Mancha, 2003.

[3] H.-D. Feger, “Geschichte und wirtschaftliche Entwicklung des Kautschuks,” Master’s thesis, Innsbruck, 1973.

[4] F. Röthemeyer and F. Sommer, *Kautschuktechnologie: Werkstoffe-Verarbeitung-Produkte.* Carl Hanser Verlag GmbH Co KG, 2013.

[5] A. Gent, S. Kawahara, and J. Zhao, “Crystallization and strength of natural rubber and synthetic cis-1, 4-polyisoprene,” *Rubber Chemistry and Technology*, vol. 71, no. 4, pp. 668–678, 1998.

[6] N. Nakajima, *Science and practice of rubber mixing.* iSmithers Rapra Publishing, 2000.

[7] M. Krejsa and J. Koenig, “A review of sulfur crosslinking fundamentals for accelerated and unaccelerated vulcanization,” *Rubber Chemistry and Technology*, vol. 66, no. 3, pp. 376–410, 1993.

[8] K. Hummel, W. Scheele, and K. Hillmer, “Zur Kenntnis der Vulkanisation hochelastischer Polymerisate. 34 mitt.: Die Vulkanisation des Naturkautschuks durch Dicumylperoxyd in Abwesenheit von Zusatzstoffen,” *Kautschuk u. Gummi*, vol. 14, p. 171, 1961.

[9] R. C. Keller, “Peroxide curing of ethylene-propylene elastomers,” *Rubber Chemistry and Technology*, vol. 61, no. 2, pp. 238–254, 1988.

[10] L. Loan, “Mechanism of peroxide vulcanization of elastomers,” *Rubber Chemistry and Technology*, vol. 40, no. 1, pp. 149–176, 1967.

[11] E. Geberth and M. Klüppel, “Effect of carbon black deactivation on the mechanical and electrical properties of elastomers,” *Macromolecular Materials and Engineering*, vol. 297, no. 9, pp. 914–922, 2012.

[12] ASTM D6556 - 17: Standard Test Method for Carbon Black - Total and External Surface Area by Nitrogen Adsorption.

[13] ASTM D2414 - 17: Standard Test Method for Carbon Black - Oil Absorption Number (OAN).

[14] T. A. Vilgis, G. Heinrich, and M. Klüppel, *Reinforcement of polymer nano-composites: theory, experiments and applications.* Cambridge University Press, 2009.

[15] Rauline (to Michelin & Cie.). EP Patent 0, 501, 227.

[16] A. Payne, "The dynamic properties of carbon black-loaded natural rubber vulcanizates. Part I," *Journal of Applied Polymer Science*, vol. 6, no. 19, pp. 57–63, 1962.

[17] L. Chazeau, J. Brown, L. Yanyo, and S. Sternstein, "Modulus recovery kinetics and other insights into the payne effect for filled elastomers," *Polymer composites*, vol. 21, no. 2, pp. 202–222, 2000.

[18] W. Fletcher and A. Gent, "Apparatus for the measurement of the dynamic shear modulus and hysteresis of rubber at low frequencies," *Rubber Chemistry and Technology*, vol. 26, no. 1, pp. 181–187, 1953.

[19] A. Payne and G. Kraus, "Reinforcement of elastomers," *Interscience, New York*, vol. 69, 1965.

[20] G. Heinrich, M. Klüppel, and T. A. Vilgis, "Reinforcement of elastomers," *Current opinion in solid state and materials science*, vol. 6, no. 3, pp. 195–203, 2002.

[21] C. G. Robertson and X. Wang, "Isoenergetic jamming transition in particle-filled systems," *Physical review letters*, vol. 95, no. 7, p. 075703, 2005.

[22] G. Kraus, C. Childers, and K. Rollmann, "Stress softening in carbon black reinforced vulcanizates. strain rate and temperature effects," *Rubber Chemistry and Technology*, vol. 39, no. 5, pp. 1530–1543, 1966.

[23] R. Hentschke, "The payne effect revisited," *eXPRESS Polymer Letters*, vol. 11, no. 4, p. 278, 2017.

[24] D. Steinhauser, M. Möwes, and M. Klüppel, "Carbon black networking in elastomers monitored by simultaneous rheological and dielectric investigations," *Journal of Physics: Condensed Matter*, vol. 28, no. 49, p. 495103, 2016.

[25] M. Kluppel, R. H. Schuster, and G. Heinrich, "Structure and properties of reinforcing fractal filler networks in elastomers," *Rubber Chemistry and Technology*, vol. 70, no. 2, pp. 243–255, 1997.

[26] L. B. Tunnicliffe, A. G. Thomas, and J. J. Busfield, "Effects of surface deactivation of carbon black on thermomechanical sensitivity of filler networks in rubber compounds," *Macromolecular Materials and Engineering*, vol. 301, no. 10, pp. 1202–1210, 2016.

[27] K. Stöckelhuber, S. Wießner, A. Das, and G. Heinrich, "Filler flocculation in polymers–a simplified model derived from thermodynamics and game theory," *Soft matter*, vol. 13, no. 20, pp. 3701–3709, 2017.

[28] H. Bouasse and Z. Carrière, "Sur les courbes de traction du caoutchouc vulcanisé," in *Annales de la Faculté des sciences de Toulouse: Mathématiques*, vol. 5, pp. 257–283, 1903.

[29] L. Mullins, “Softening of rubber by deformation,” *Rubber Chemistry and Technology*, vol. 42, no. 1, pp. 339–362, 1969.

[30] L. Mullins and N. Tobin, “Stress softening in rubber vulcanizates. Part I. Use of a strain amplification factor to describe the elastic behavior of filler-reinforced vulcanized rubber,” *Journal of Applied Polymer Science*, vol. 9, no. 9, pp. 2993–3009, 1965.

[31] K. Hong, A. Rastogi, and G. Strobl, “A model treating tensile deformation of semicrystalline polymers: quasi-static stress- strain relationship and viscous stress determined for a sample of polyethylene,” *Macromolecules*, vol. 37, no. 26, pp. 10165–10173, 2004.

[32] S. Trabelsi, P.-A. Albouy, and J. Rault, “Crystallization and melting processes in vulcanized stretched natural rubber,” *Macromolecules*, vol. 36, no. 20, pp. 7624–7639, 2003.

[33] F. Ehrburger-Dolle, I. Morfin, F. Bley, F. Livet, G. Heinrich, S. Richter, L. Piché, and M. Sutton, “XPCS investigation of the dynamics of filler particles in stretched filled elastomers,” *Macromolecules*, vol. 45, no. 21, pp. 8691–8701, 2012.

[34] G. Machado, G. Chagnon, and D. Favier, “Induced anisotropy by the mullins effect in filled silicone rubber,” *Mechanics of Materials*, vol. 50, pp. 70–80, 2012.

[35] J. Diani, M. Brieu, and P. Gilormini, “Observation and modeling of the anisotropic visco-hyperelastic behavior of a rubberlike material,” *International Journal of Solids and Structures*, vol. 43, no. 10, pp. 3044–3056, 2006.

[36] M. Itskov, E. Haberstroh, A. Ehret, and M. Vohringer, “Experimental observation of the deformation induced anisotropy of the mullins effect in rubber,” *KGK-Kautschuk Gummi Kunststoffe*, vol. 59, no. 3, pp. 93–96, 2006.

[37] J. Diani, B. Fayolle, and P. Gilormini, “A review on the mullins effect,” *European Polymer Journal*, vol. 45, no. 3, pp. 601–612, 2009.

[38] F. Laraba-Abbes, P. Ienny, and R. Piques, “A new ‘tailor-made’ methodology for the mechanical behaviour analysis of rubber-like materials: II. Application to the hyperelastic behaviour characterization of a carbon-black filled natural rubber vulcanizate,” *Polymer*, vol. 44, no. 3, pp. 821–840, 2003.

[39] Z. Rigbi, “Reinforcement of rubber by carbon black,” in *Properties of Polymers*, pp. 21–68, Springer, 1980.

[40] F. Fleck, V. Froltsov, and M. Klüppel, “Polymer-filler interphase dynamics and reinforcement of elastomer nanocomposites,” *Soft Materials*, vol. 12, no. sup1, pp. S121–S134, 2014.

[41] F. Bueche, “Molecular basis for the Mullins effect,” *Journal of Applied Polymer Science*, vol. 4, no. 10, pp. 107–114, 1960.

[42] A. Blanchard and D. Parkinson, “Breakage of carbon-rubber networks by applied stress,” *Industrial & Engineering Chemistry*, vol. 44, no. 4, pp. 799–812, 1952.

[43] N. Suzuki, M. Ito, and F. Yatsuyanagi, “Effects of rubber/filler interactions on deformation behavior of silica filled sbr systems,” *Polymer*, vol. 46, no. 1, pp. 193–201, 2005.

[44] R. Houwink, “Slipping of molecules during the deformation of reinforced rubber,” *Rubber Chemistry and Technology*, vol. 29, no. 3, pp. 888–893, 1956.

[45] V. N. Khiêm and M. Itskov, “An averaging based tube model for deformation induced anisotropic stress softening of filled elastomers,” *International Journal of Plasticity*, vol. 90, pp. 96–115, 2017.

[46] T. Kojima and M. Koishi, “Influence of filler dispersion on mechanical behavior with large-scale coarse-grained molecular dynamics simulation,” *Technische Mechanik*, vol. 38, no. 1, pp. 41–54, 2018.

[47] H. Lorenz, M. Klüppel, and G. Heinrich, “Microstructure-based modelling and FE implementation of filler-induced stress softening and hysteresis of reinforced rubbers,” *ZAMM*, vol. 92, no. 8, pp. 608–631, 2012.

[48] J. Plagge and M. Klüppel, “A physically based model of stress softening and hysteresis of filled rubber including rate-and temperature dependency,” *International Journal of Plasticity*, vol. 89, pp. 173–196, 2017.

[49] Y. Shinohara, H. Kishimoto, K. Inoue, Y. Suzuki, A. Takeuchi, K. Uesugi, N. Yagi, K. Muraoka, T. Mizoguchi, and Y. Amemiya, “Characterization of two-dimensional ultra-small-angle x-ray scattering apparatus for application to rubber filled with spherical silica under elongation,” *Applied Crystallography*, vol. 40, no. s1, pp. s397–s401, 2007.

[50] K. Hagita, H. Morita, M. Doi, and H. Takano, “Coarse-grained molecular dynamics simulation of filled polymer nanocomposites under uniaxial elongation,” *Macromolecules*, vol. 49, no. 5, pp. 1972–1983, 2016.

[51] L.-H. Cai, S. Panyukov, and M. Rubinstein, “Hopping diffusion of nanoparticles in polymer matrices,” *Macromolecules*, vol. 48, no. 3, pp. 847–862, 2015.

[52] C. A. Grabowski and A. Mukhopadhyay, “Size effect of nanoparticle diffusion in a polymer melt,” *Macromolecules*, vol. 47, no. 20, pp. 7238–7242, 2014.

[53] H. Wulf and J. Ihlemann, “Simulation of Mullins effect and relaxation due to self-organization processes in filled rubber,” *Constitutive Models for Rubber IX*, p. 305, 2015.

[54] G. T. Mase, R. E. Smelser, and G. E. Mase, *Continuum mechanics for engineers.* CRC press, 2009.

[55] G. A. Holzapfel, “Nonlinear solid mechanics,” vol. 24, 2000.

[56] K. S. Pitzer, “Potential energies for rotation about single bonds,” in *Molecular Structure And Statistical Thermodynamics: Selected Papers of Kenneth S Pitzer*, pp. 58–65, World Scientific, 1993.

[57] T. Kawakatsu, *Statistical physics of polymers: an introduction.* Springer Science & Business Media, 2013.

[58] G. R. Strobl, *The Physics of Polymers: Concepts for Understanding Their Structures and Behavior.* Springer Science & Business Media, 2007.

[59] W. Kuhn and F. Grün, "Beziehungen zwischen elastischen Konstanten und Dehnungsdoppelbrechung hochelastischer Stoffe," *Kolloid-Zeitschrift*, vol. 101, no. 3, pp. 248–271, 1942.

[60] J. E. Mark, *Physical properties of polymers handbook.* Springer, 2007.

[61] R. Rivlin, "Large elastic deformations of isotropic materials. IV. Further developments of the general theory," *Philosophical Transactions of the Royal Society of London A: Mathematical, Physical and Engineering Sciences*, vol. 241, no. 835, pp. 379–397, 1948.

[62] G. Marckmann and E. Verron, "Comparison of hyperelastic models for rubber-like materials," *Rubber Chemistry and Technology*, vol. 79, no. 5, pp. 835–858, 2006.

[63] V. Litvinov, W. Barendswaard, and M. Van Duin, "The density of chemical crosslinks and chain entanglements in unfilled EPDM vulcanizates as studied with low resolution, solid state 1H NMR," *Rubber Chemistry and Technology*, vol. 71, no. 1, pp. 105–118, 1998.

[64] M. Klüppel and G. Heinrich, "Network structure and mechanical properties of sulfur-cured rubbers," *Macromolecules*, vol. 27, no. 13, pp. 3596–3603, 1994.

[65] S. Kastner, "Theorie der Polymernetzwerke mit behinderter Fluktuation I. Zustandsintegral, freie Energie und Frontfaktor bei behinderter Fluktuation der Vernetzungspunkte," *Colloid Polym. Sci.*, vol. 259, pp. 499–507, 1981.

[66] H. M. James and E. Guth, "Theory of the elastic properties of rubber," *The Journal of Chemical Physics*, vol. 11, no. 10, pp. 455–481, 1943.

[67] J. Hermans, "Deformation and swelling of polymer networks containing comparatively long chains," *Transactions of the Faraday Society*, vol. 43, pp. 591–600, 1947.

[68] P. J. Flory, "Statistical mechanics of swelling of network structures," *The Journal of Chemical Physics*, vol. 18, no. 1, pp. 108–111, 1950.

[69] F. T. Wall and P. J. Flory, "Statistical thermodynamics of rubber elasticity," *The Journal of Chemical Physics*, vol. 19, no. 12, pp. 1435–1439, 1951.

[70] P. J. Flory, "Molecular theory of rubber elasticity," *Polymer journal*, vol. 17, no. 1, pp. 1–12, 1985.

[71] G. Ronca and G. Allegra, "An approach to rubber elasticity with internal constraints," *The Journal of Chemical Physics*, vol. 63, no. 11, pp. 4990–4997, 1975.

[72] S. F. Edwards, "The statistical mechanics of polymers with excluded volume," *Proceedings of the Physical Society*, vol. 85, no. 4, p. 613, 1965.

[73] B. Erman and P. J. Flory, “Relationships between stress, strain, and molecular constitution of polymer networks. Comparison of theory with experiments,” *Macromolecules*, vol. 15, no. 3, pp. 806–811, 1982.

[74] G. Marrucci, “Rubber elasticity theory. A network of entangled chains,” *Macromolecules*, vol. 14, no. 2, pp. 434–442, 1981.

[75] R. J. Gaylord, “The constant volume tube model of rubber elasticity,” *Polymer Bulletin*, vol. 8, no. 7, pp. 325–329, 1982.

[76] R. Ball, M. Doi, S. Edwards, and M. Warner, “Elasticity of entangled networks,” *Polymer*, vol. 22, no. 8, pp. 1010–1018, 1981.

[77] R. Deam and S. F. Edwards, “The theory of rubber elasticity,” *Philosophical Transactions of the Royal Society of London A: Mathematical, Physical and Engineering Sciences*, vol. 280, no. 1296, pp. 317–353, 1976.

[78] S. Edwards and T. Vilgis, “The effect of entanglements in rubber elasticity,” *Polymer*, vol. 27, no. 4, pp. 483–492, 1986.

[79] G. Heinrich and E. Straube, “A theory of topological constraints in polymer networks,” *Polymer Bulletin*, vol. 17, no. 3, pp. 247–253, 1987.

[80] M. Klüppel and J. Schramm, “A generalized tube model of rubber elasticity and stress softening of filler reinforced elastomer systems,” *Macromolecular Theory and Simulations*, vol. 9, no. 9, pp. 742–754, 2000.

[81] G. Heinrich and M. Kaliske, “Theoretical and numerical formulation of a molecular based constitutive tube-model of rubber elasticity,” *Computational and Theoretical Polymer Science*, vol. 7, no. 3/4, pp. 227–241, 1997.

[82] S. Edwards and T. A. Vilgis, “The tube model theory of rubber elasticity,” *Reports on Progress in Physics*, vol. 51, no. 2, p. 243, 1988.

[83] A. Einstein, “Eine neue Bestimmung der Moleküldimensionen,” *Ann. Phys.*, vol. 324, pp. 289–306, 1906.

[84] G. Huber and T. A. Vilgis, “Universal properties of filled rubbers: Mechanisms for reinforcement on different length scales,” *Kautschuk Gummi Kunststoffe*, vol. 52, no. 2, pp. 102–107, 1999.

[85] M. Klüppel, “The role of disorder in filler reinforcement of elastomers on various length scales,” in *Filler-Reinforced Elastomers/Scanning Force Microscopy*, pp. 1–86, Springer, 2003.

[86] R. Raghunath, D. Juhre, and M. Klüppel, “A physically motivated model for filled elastomers including strain rate and amplitude dependency in finite viscoelasticity,” *International Journal of Plasticity*, vol. 78, pp. 223–241, 2016.

[87] D. Besdo, C. Hohl, and J. Ihlemann, “Abaqus implementation and simulation results of the morph constitutive model,” in *Constitutive Models for Rubber*, vol. 4, p. 223, Taylor & Francis Group, London, 2005.

[88] H. Lorenz and M. Klüppel, “Microstructure-based modelling of arbitrary deformation histories of filler-reinforced elastomers,” *Journal of the Mechanics and Physics of Solids*, vol. 60, no. 11, pp. 1842–1861, 2012.

[89] D. K. Klein and H. Baaser, *FEM Imlementierung eines Modells zur Entfestigung gefüllter Elastomere*. Bachelors thesis, TH Bingen, 2018.

[90] S. Brunauer and P. H. Emmett, “The use of low temperature van der waals adsorption isotherms in determining the surface areas of various adsorbents,” *Journal of the American Chemical Society*, vol. 59, no. 12, pp. 2682–2689, 1937.

[91] *BELSORP-max Instruction Manual.*

[92] R. C. Weast, ed., *Handbook of Chemistry and Physics.* CRC Press, 65 ed., 1984.

[93] L. Fetters, D. Lohse, and R. Colby, “Chain dimensions and entanglement spacings,” in *Physical properties of polymers handbook*, pp. 447–454, Springer, 2007.

[94] M. L. Williams and J. D. Ferry, “Second approximation calculations of mechanical and electrical relaxation and retardation distributions,” *Journal of Polymer Science Part A: Polymer Chemistry*, vol. 11, no. 2, pp. 169–175, 1953.

[95] A. Stevenson and R. Campion, “Engineering with rubber: How to design rubber components,” *Gent, AN, Ed*, 2001.

[96] B. Huisman and A. Fasolino, “Logarithmic relaxation due to minimization of interactions in the burridge-knopoff model,” *Physical Review E*, vol. 74, no. 2, p. 026110, 2006.

[97] I. Ivaneiko, V. Toshchevikov, M. Saphiannikova, K. Stöckelhuber, F. Petry, S. Westermann, and G. Heinrich, “Modeling of dynamic-mechanical behavior of reinforced elastomers using a multiscale approach,” *Polymer*, vol. 82, pp. 356–365, 2016.

[98] P. Hänggi, P. Talkner, and M. Borkovec, “Reaction-rate theory: fifty years after kramers,” *Reviews of modern physics*, vol. 62, no. 2, p. 251, 1990.

[99] H. Kramers, “Physica (utrecht), 7, 284–304,” *CrossRef CAS*, 1940.

[100] L. A. Wood and N. Bekkedahl, “Crystallization of unvulcanized rubber at different temperatures,” *Journal of Applied Physics*, vol. 17, no. 5, pp. 362–375, 1946.

[101] J.-M. Chenal, L. Chazeau, Y. Bomal, and C. Gauthier, “New insights into the cold crystallization of filled natural rubber,” *Journal of Polymer Science Part B: Polymer Physics*, vol. 45, no. 8, pp. 955–962, 2007.

[102] P. J. Flory, “Thermodynamics of crystallization in high polymers. I. Crystallization induced by stretching,” *The Journal of Chemical Physics*, vol. 15, no. 6, pp. 397–408, 1947.

[103] G. Severe and J. L. White, “Physical properties and blend miscibility of hydrogenated acrylonitrile-butadiene rubber,” *Journal of applied polymer science*, vol. 78, no. 8, pp. 1521–1529, 2000.

[104] K. Narynbek Ulu, M. Dragicevic, P.-A. Albouy, B. Huneau, A.-S. Beranger, and P. Heuillet, “Strain-induced crystallization ability of hydrogenated nitrile butadiene rubber,” in *Constitutive Models for Rubber X*, pp. 8–10, 2017.

[105] J. Plagge, T. Spratte, M. Wunde, and M. Klüppel, “Thermo-mechanical properties of strain-crystallizing elastomer nanocomposites,” in *Constitutive Models for Rubber*, vol. 10, pp. 489–494, Taylor & Francis Group, London, 2017.

[106] M. K. Kang, H.-J. Jeon, H. H. Song, and G. Kwag, “Strain-induced crystallization of blends of natural rubber and ultra high cis polybutadiene as studied by synchrotron x-ray diffraction,” *Macromolecular Research*, vol. 24, no. 1, pp. 31–36, 2016.

[107] S. Toki, I. Sics, B. S. Hsiao, S. Murakami, M. Tosaka, S. Poompradub, S. Kohjiya, and Y. Ikeda, “Structural developments in synthetic rubbers during uniaxial deformation by in situ synchrotron x-ray diffraction,” *Journal of Polymer Science Part B: Polymer Physics*, vol. 42, no. 6, pp. 956–964, 2004.

[108] B. Huneau, “Strain-induced crystallization of natural rubber: a review of x-ray diffraction investigations,” *Rubber Chemistry and Technology*, vol. 84, no. 3, pp. 425–452, 2011.

[109] P. J. Flory, *Principles of polymer chemistry.* Cornell University Press, 1953.

[110] J. Rault, J. Marchal, P. Judeinstein, and P. Albouy, “Stress-induced crystallization and reinforcement in filled natural rubbers: ^{2}H NMR study,” *Macromolecules*, vol. 39, no. 24, pp. 8356–8368, 2006.

[111] A. Vieyres, R. Pérez-Aparicio, P.-A. Albouy, O. Sanseau, K. Saalwächter, D. R. Long, and P. Sotta, “Sulfur-cured natural rubber elastomer networks: correlating cross-link density, chain orientation, and mechanical response by combined techniques,” *Macromolecules*, vol. 46, no. 3, pp. 889–899, 2013.

[112] P.-A. Albouy, A. Vieyres, R. Pérez-Aparicio, O. Sanséau, and P. Sotta, “The impact of strain-induced crystallization on strain during mechanical cycling of cross-linked natural rubber,” *Polymer*, vol. 55, no. 16, pp. 4022–4031, 2014.

[113] N. Candau, R. Laghmach, L. Chazeau, J.-M. Chenal, C. Gauthier, T. Biben, and E. Munch, “Strain-induced crystallization of natural rubber and cross-link densities heterogeneities,” *Macromolecules*, vol. 47, no. 16, pp. 5815–5824, 2014.

[114] J.-M. Chenal, L. Chazeau, L. Guy, Y. Bomal, and C. Gauthier, "Molecular weight between physical entanglements in natural rubber: a critical parameter during strain-induced crystallization," *Polymer*, vol. 48, no. 4, pp. 1042–1046, 2007.

[115] J.-M. Chenal, C. Gauthier, L. Chazeau, L. Guy, and Y. Bomal, "Parameters governing strain induced crystallization in filled natural rubber," *Polymer*, vol. 48, no. 23, pp. 6893–6901, 2007.

[116] D. Luch and G. Yeh, "Morphology of strain-induced crystallization of natural rubber. I. Electron microscopy on uncrosslinked thin film," *Journal of Applied Physics*, vol. 43, no. 11, pp. 4326–4338, 1972.

[117] R. Dargazany, V. N. Khiêm, E. A. Poshtan, and M. Itskov, "Constitutive modeling of strain-induced crystallization in filled rubbers," *Physical Review E*, vol. 89, no. 2, 2014.

[118] S. Trabelsi, P.-A. Albouy, and J. Rault, "Stress-induced crystallization around a crack tip in natural rubber," *Macromolecules*, vol. 35, no. 27, pp. 10054–10061, 2002.

[119] D. J. Lee and J. A. Donovan, "Microstructural changes in the crack tip region of carbon-black-filled natural rubber," *Rubber Chemistry and Technology*, vol. 60, no. 5, pp. 910–923, 1987.

[120] N. Saintier, G. Cailletaud, and R. Piques, "Cyclic loadings and crystallization of natural rubber: An explanation of fatigue crack propagation reinforcement under a positive loading ratio," *Materials Science and Engineering: A*, vol. 528, no. 3, pp. 1078–1086, 2011.

[121] J.-B. Le Cam, "Strain-induced crystallization in rubber: A new measurement technique," *Strain*, vol. 54, no. 1, 2018.

[122] P.-A. Albouy, J. Marchal, and J. Rault, "Chain orientation in natural rubber, part I: The inverse yielding effect," *The European Physical Journal E: Soft Matter and Biological Physics*, vol. 17, no. 3, pp. 247–259, 2005.

[123] D. Luch and G. Yeh, "Morphology of strain-induced crystallization of natural rubber. Part II. X-ray studies on cross-linked vulcanizates," *Journal of Macromolecular Science, Part B: Physics*, vol. 7, no. 1, pp. 121–155, 1973.

[124] D. Luch and G. S. Yeh, "Strain-induced crystallization of natural rubber. III. Reexamination of axial-stress changes during oriented crystallization of natural rubber vulcanizates," *Journal of Polymer Science Part B: Polymer Physics*, vol. 11, no. 3, pp. 467–486, 1973.

[125] C. Luo and J.-U. Sommer, "Coexistence of melting and growth during heating of a semicrystalline polymer," *Phys. Rev. Lett.*, vol. 102, p. 147801, Apr 2009.

[126] J. Sommer and C. Luo, "Molecular dynamics simulations of semicrystalline polymers: Crystallization, melting, and reorganization," *Journal of Polymer Science Part B: Polymer Physics*, vol. 48, no. 21, pp. 2222–2232.

[127] P. Stickney and R. Falb, “Carbon black-rubber interactions and bound rubber,” *Rubber Chemistry and Technology*, vol. 37, no. 5, pp. 1299–1340, 1964.

[128] F. Cataldo, “A model compound study about carbon black and diene rubber interaction: The reactivity of C60 fullerene with squalene,” *Fullerene science and technology*, vol. 8, no. 3, pp. 153–164, 2000.

[129] H. Lorenz, J. Meier, and M. Klüppel, “Micromechanics of internal friction of filler reinforced elastomers,” *LNACM*, no. 51, 2010.

[130] E. Ducrot, Y. Chen, M. Bulters, R. P. Sijbesma, and C. Creton, “Toughening elastomers with sacrificial bonds and watching them break,” *Science*, vol. 344, no. 6180, pp. 186–189, 2014.

A

Appendix

A.1 Curriculum Vitae

Personal data

Name	Jan Plagge
Date and place of birth	08.11.1988, Eckernförde
Nationality	german

Occupational experience

05.2014 – 07.2018	Ph. D. research • Deutsches Institut für Kautschukechnologie e. V., department Material Concepts and Modeling
01.2014 – 04.2014	Scientific coworker • Georg-August University Göttingen, Institute for Theoretical Physics

Higher education

05.2012 – 12.2013	Master of Science Physics, Georg- August University Göttingen • Institute for Theoretical Physics, work group Claus Heussinger *"Viscoelastic Properties of Semiflexible Polymer Networks"*
10.2008 – 05.2012	Bachelor of Science Physics, Georg- August University Göttingen • Institute for Theoretical Physics, work group Claus Heussinger *"Diffusionsverhalten granularer Materie"*, with distinction
10.2010 – 03.2011	Erasmus exchange program • Université Claude Bernard Lyon 1
06.2008	Abitur • Herderschule Rendsburg

Honors and Awards

2016	IRCO Best Paper Student Award • International Rubber Conference 2016, Kitakyushu

A.2 Own Literature

Own Literature Included in this Thesis

1. J. Plagge and M. Klüppel, ”A Theory Relating Crystal Size, Mechanical Response and Degree of Crystallization in Strained Natural Rubber,” *Macromolecules*, vol. 51, no. 10, pp. 3711–3721, 2018.
2. J. Plagge and M. Klüppel, ”Investigation of Carbon Black and Silica Surface Structure by Static Gas Adsorption with Various Gases,” *Rubber Chemistry and Technology*, accepted, 2018.
3. J. Plagge and M. Klüppel, ”Determining strain-induced crystallization of natural rubber composites by combined thermography and stress-strain measurements,” *Polymer Testing*, vol. 66, pp. 87–93, 2018.
4. J. Plagge and M. Klüppel, ”A physically based model of stress softening and hysteresis of filled rubber including rate-and temperature dependency,” *International Journal of Plasticity*, vol. 89, pp. 173–196, 2017.
5. T. Spratte, J. Plagge, M. Wunde, and M. Klüppel, ”Investigation of strain-induced crystallization of carbon black and silica filled natural rubber composites based on mechanical and temperature measurements,” *Polymer*, vol. 115, pp. 12-20, 2017.

Own Literature not Included in this Thesis

1. J. Plagge and M. Klüppel, ”A Hyperelastic Physically Based Model for Filled Elastomers Including Continuous Damage Effects and Viscoelasticity,” in *Constitutive Models for Rubber*, Taylor & Francis Group, London, vol. 10, pp. 559–565, 2017.
2. J. Plagge, A. Lang, M. Klüppel, and A. Stoll, ”Influence of thermal Aging on mechanical and tribological Properties of Roller Compounds based on EPDM,” *KGK–Kautschuk Gummi Kunststoffe*, vol. 70, pp. 31–37, 2017.
3. J. Plagge, A. Fischer, and C. Heussinger, ”Viscoelasticity of reversibly crosslinked networks of semiflexible polymers,” *Phys. Rev. E*, vol. 93, no. 6, pp. 062502, 2016.
4. M. Klüppel, M. Möwes, A. Lang, J. Plagge, M. Wunde, F. Fleck, and C. W. Karl, ”Characterization and application of graphene nanoplatelets in elastomers,” in *Designing of Elastomer Nanocomposites: From Theory to Applications*, Springer International Publishing, pp. 319–360, 2016.
5. J. Plagge and M. Klüppel, ”Application of a micro-structure based model to thermally aged filler reinforced elastomer compounds,” in *Constitutive Models for Rubber*, Taylor & Francis Group, London, vol. 9, pp. 23–27, 2015.
6. J. Plagge and C. Heussinger, ”Melting a granular glass by cooling,” *Phys. Rev. Lett.* vol. 110, no. 7, pp. 078001, 2013.

A.3 CONTRIBUTIONS TO CONFERENCES

1. J. Plagge, M. Klüppel, “Measuring strain-induced crystallization of filled and unfilled natural rubber by thermography, stress and strain,” *PolyMerTec 2018*, 06.2018, Merseburg
2. J. Plagge, T. Spratte, M. Wunde, M. Klüppel, “Thermo-Mechanical Evaluation of Strain-Induced-Crystallization of Natural rubber Composites,” *TireTec 2018*, 02.2018, Hannover
3. J. Plagge, M. Klüppel, “A Hyperelastic Physically Based Model for Filled Elastomers Including Continuous Damage Effects and Viscoelasticity,” *ECCMR 2017*, 08.2017, München
4. J. Plagge, A. Lang, P. Stratmann, A. Stoll, M. Klüppel, “Verbesserung der Gebrauchs- und Verschleißeigenschaften von gummierten Walzen,” *DKG Jahrestagung*, 06.2017, Nürnberg
5. J. Plagge, M. Klüppel, “Modeling Time- and Temperature Dependent Nonlinear Response of Filled Rubbers based on Physical Principles,” *ICMM 5*, 06.2017, Rome
6. J. Plagge, M. Klüppel, “Theoretical Investigation and Quantification of Strain Induced Crystallization by Linking Thermal and Mechanical Data,” *International Ph. D. Seminar*, 05.2017, Dresden
7. J. Plagge, M. Klüppel, “Quantification of Strain Induced Crystallization by Thermo-Mechanical Analysis,” *KHK 2016*, 11.2016, Hannover
8. J. Plagge, M. Klüppel, “A New Microstructure Based Model for the Response of Filler Reinforced Elastomers Including Temperature and Rate Dependence,” *IRC 2016*, 10.2016, Kitakyushu
9. J. Plagge, M. Klüppel, “Entwicklung eines temperatur- und ratenabhängigen physikalisch motivierten Modells für verstärkte Elastomere,” *Arbeitskreis Stoffgesetze*, 05.2016, Hannover
10. J. Plagge, M. Klüppel, “Development of a new physical model for the response of reinforced elastomers including temperature and rate dependence,” *ECCMR 2015*, 03.2016, Regensburg
11. J. Plagge, M. Klüppel, “Application of a micro-structure based model to thermally aged filler reinforced elastomer compounds,” *DPG Jahrestagung 2015*, 08.2015, Prague
12. J. Plagge, M. Klüppel, “Application of a micro-structure based model to filler reinforced elastomer compounds, *DPG Frühjahrstagung*,” 03.2015, Berlin
13. (Poster) J. Plagge, A. Jain, R. Schuster, U. Giese, M. Klüppel, “Investigation of Polymer-Filler Interaction with Static Gas Adsorption and IGC,” *IRC 2015*, 07.2015, Nürnberg
14. (Poster) J. Plagge, F. Fleck, A. Lang, M. Möwes, M. Klüppel, “Energy-Efficient Elastomers,” *ZFM Summer School 2014*, 10.2014, Hannover